Aus der Klinik für Strahlentherapie und Radioonkologie
der Medizinischen Fakultät Mannheim
(Direktor: Prof. Dr. med. Frank Anton Giordano)

Retinal Imaging with Compact Custom Phase Plates and Two-Photon Imaging Methods

Inauguraldissertation
zur Erlangung des Doctor scientiarum humanarum (Dr. sc. hum.)
der
Medizinischen Fakultät Mannheim
der Ruprecht-Karls-Universität
zu
Heidelberg

vorgelegt von
Gopal Swamy Jayabalan

aus
Kumbakonam, India
2023

Dekan: Prof. Dr. med. Sergij Goerdt
Referent: Prof. Dr. Dr. h.c. Frederik Wenz

TABLE OF CONTENTS

Page

LIST OF ABBREVIATIONS

2D	Two-dimensional
3D	Three-dimensional
AMD	Age-related macular degeneration
ANSI	American National Standards Institute
AOSLO	Adaptive optics scanning laser ophthalmoscope
APD	Avalanche photodiode
ART	Automatic real-time tracking
ARVO	Association for Research in Vision and Ophthalmology
CCD	Charge-coupled device
CMOS	Complementary metal-oxide-semiconductor
cSLO	Confocal scanning laser ophthalmoscope
CNV	Choroidal neovascularization
DNIRA	Delayed near infrared analysis
DR	Diabetic retinopathy
FA	Fluorescein angiography
FAF	Fundus autofluorescence
FOV	Field of view
FWHM	Full width at half maximum
HMO	High-magnification objective
HOAs	Higher-order aberrations
HRT	Heidelberg Retinal Tomograph
IACUC	Institutional Animal Care and Use Committee
ICGA	Indocyanine green angiography
ICNIRP	International Commission on Non-radiation Protection
IEC	International Electrotechnical Commission
ISO	International organization for standardization
MEMS	Microelectromechanical systems
MPE	Maximum permissible exposure
MSI	Mask structured ion exchange
MTF	Modulation transfer function
NA	Numeric aperture
NIR	Near-infrared
OCT	Optical coherence tomography
OCTA	Optical coherence tomography angiography
OTF	Optical transfer function
PMT	Photomultiplier tube
PSF	Point Spread Function
RIS	Refractive Index Shaping
RMS	Root mean square
RPE	Retinal pigment epithelium
SHG	Second-harmonic generation
SHS	Shack-Hartmann Sensor
SLO	Scanning laser ophthalmoscope
SRT	Selective retina therapy
TPEF	Two-photon excited fluorescence
TUNEL	Terminal deoxynucleotidyl transferase dUTP nick end labeling
UV	Ultraviolet

1 INTRODUCTION

One of the significant concerns in ophthalmology is preserving vision, as even a minor loss in visual acuity can greatly impact the quality of life. Fundus imaging has become an essential part of retinal examination for diagnostic and monitoring purposes since the invention of the first ophthalmoscope in 1851 by Hermann von Helmholtz[1]. In recent years, many advanced retinal imaging techniques have emerged to provide new insights into the pathogenesis of retinal diseases. A wide range of clinical instruments, such as slit lamps, fundus cameras, direct and indirect handheld ophthalmoscopes, confocal scanning laser ophthalmoscope (cSLO), optic nerve head analyzer, ultrasonography, and optical coherence tomography (OCT), are widely used in clinics for early diagnosis and monitoring of retinal diseases[2]. However, significant effort is still needed to develop new retinal imaging techniques at a cellular level. For example, retinal cell dysfunction and loss are common in most retinal diseases and can lead to significant visual loss. It is believed that the significant loss of photoreceptors and retinal ganglion cells is also a primary cause of age-related macular degeneration (AMD) and glaucoma. The current clinical instruments do not provide cellular-level imaging of this cell dysfunction or loss. Conventional fundus cameras have a limitation in axial resolution to image different layers of the retina, and standard OCT limits transverse resolution to evaluate individual retinal cells[3]. As the retina is part of the central nervous system and has highly specialized neuronal cell types, most retinal cells have limited or no capacity for self-renewal or tissue regeneration. Therefore, non-invasive in vivo imaging for early detection of morphological changes at the cellular or subcellular level is essential to better understand the pathogenesis and progression of these diseases and detect them earlier before irreversible cell death occurs.

Retinal imaging at the cellular level is challenging as the instrument must have a lateral resolution that approaches the size of a cell to distinguish neighboring cells within the same focal plane, as well as the ability to penetrate through absorbers and scatter in the eye, perform optical sectioning, be fast, sensitive, and generate contrast. Similarly, the camera must have sufficient resolution and contrast to visualize individual cells. Handheld ophthalmoscopes and fundus cameras can observe the gross anatomical features of the retina over large areas, but they do not provide clinically relevant information at a cellular level. cSLO and OCT devices have a better effective resolution than fundus cameras[4-7]. They have been widely implemented for various clinical applications, including the detection of the biomarkers of diabetic retinopathy (DR), AMD, and glaucoma. Despite these technological advancements, imaging of the retina at a cellular level is still limited by optical aberrations, which limit the lateral resolution. The human eye is not a perfect optical system, and ocular aberrations impair vision and retinal image quality[8-11]. Although defocus and astigmatism can be corrected by eyeglasses, higher-order aberrations (HOAs) need to be corrected to enable high-resolution imaging of the retina. Smirnov proposed the idea of correcting the HOAs in the human eye with customized contact lenses in the early 1960s. Later in 1997, Liang et al. successfully corrected the HOAs providing normal eyes with supernormal optical quality allowing imaging of the retina at a microscopic scale[8]. Since then, adaptive optics has been implemented by numerous research groups for high-resolution imaging of the retina. The aberrations can be compensated by integrating adaptive optics, enabling visualization of cone photoreceptors, rod photoreceptors, and leucocytes. In vivo retinal imaging of these structures helps to non-invasively monitor the retinal

functions, the progression of retinal diseases, and the efficacy of therapies at a microscopic spatial scale[12].

Adaptive optics has been combined with techniques such as scanning laser ophthalmoscopy (SLO), fundoscopy, and OCT. Adaptive optics systems typically consist of a wavefront sensor and a deformable mirror. The wavefront sensor measures aberrations induced by the optical system and eye, and the deformable mirror corrects these aberrations by physically changing the surface shape to match the measured aberration. Thus, adaptive optics enables an aberration-free or diffraction-limited system[13-18]. However, the cost and complexity of adaptive optics ophthalmoscopes currently obstruct their clinical use[15]. To overcome this limitation, non-adaptive optics ophthalmoscope at low cost have been developed to visualize cone photoreceptors and nerve fiber bundles. In healthy eyes with ideal optics, microscopic retinal structures can be resolvable without the need for adaptive optics[19-21]. However, the resolution and image quality of non-adaptive optics ophthalmoscopes are not as good as adaptive optics ophthalmoscopes, and cone photoreceptors can only be visualized in healthy eyes with minimal ocular aberrations and smaller pupil sizes[22-25]. Yet, the foveal cone and rod photoreceptors can only be seen using adaptive optics ophthalmoscopes. The distance between cones in the fovea is much smaller than in other parts of the retina, and non-adaptive optics systems do not have the resolution to visualize these receptors in the fovea. The center-to-center spacing of cones in the fovea is typically 2.6±0.2 micrometers, and at nasal and temporal retina, the center-to-center spacing between cones increased to approximately to an average of 14-16 micrometers. Rod photoreceptors are distributed unevenly throughout the retina, with a higher concentration in the peripheral areas, and an average spacing of about 2-3 micrometers[26].

Multiphoton microscopy is another widely used retinal imaging technique in research that allows for cellular-level imaging of the retina. It uses lasers to stimulate the fluorescence of specific cells or molecules within the retina, allowing for the visualization of specific cellular and molecular processes. These techniques have greatly advanced our understanding of the retina at the cellular level. Two-photon microscopy is a similar technique to multiphoton microscopy. The main difference between two-photon microscopy and multiphoton microscopy is the number of photons used to excite the fluorescence. In two-photon microscopy, only two photons are required to excite the fluorescence, while in multiphoton microscopy, multiple photons are required. This difference in the number of photons used allows for the visualization of different depths within the tissue and the ability to study different structures or processes within the tissue.

Two-photon retinal imaging has become a promising tool in ophthalmology for research purposes due to its greater penetration and superior resolution of microstructures[27-30]. Two-photon and confocal imaging techniques use lasers to excite the fluorescent molecules within the tissue and detect the emitted light, which can be used to produce high-resolution images. The main difference between confocal and two-photon imaging is the way they produce images. Confocal imaging uses a single laser beam and a pinhole in front of the detector to block the out-of-focus light, resulting in a two-dimensional (2D) image of a thin section of the tissue. A series of 2D images can be combined to form a three-dimensional (3D) image. In contrast, two-photon imaging uses a pulsed laser beam, and the emitted light is collected by the detector without a pinhole, resulting in a 3D image of the entire tissue. The major difference is the type of laser used, confocal imaging typically uses a continuous wave laser, while two-photon uses a femtosecond laser that produces extremely short pulses of light. The use of femtosecond lasers in two-photon imaging allows for the absorption of two photons of light simultaneously, which results in the excitation of fluorophores at a much deeper

depth within the tissue. This technique offers the potential for better anatomical resolution of retinal cells and better detection of autofluorescence patterns of the retina. For instance, Fundus autofluorescence (FAF) imaging, which is widely used, has the limitation of providing low-resolution images of intracellular and extracellular lipofuscin. It can detect changes in the retinal pigment epithelium (RPE) only when there is a significant decrease in lipofuscin concentration. TPEF imaging is an effective method for detecting early changes in lipofuscin distribution and providing structural and functional information of the retina. Furthermore, several native fluorophores like NAD(P)H, all-trans retinol and derivatives, melanin, and elastin have been reported as a source of fluorescent signals in TPEF retinal imaging[31-38]. These fluorophores can be efficiently excited and visualized at the near-infrared (NIR) optical window by TPEF. Moreover, many of these native fluorophores have excitation maxima in the ultraviolet/ short-visible range, which raises concerns about optical safety. And these native fluorophores can be excited and detected by two-photon technique. TPEF imaging could be used to visualize the structure and function of RPE[36, 38], ganglion cells[39], and could be a powerful technique for in vivo detection and monitoring of retinal disease progression[31-35]. Nevertheless, the retina is vulnerable to injury from radiation and the unknown tissue response to femtosecond laser obstructs the two-photon retinal imaging clinical use.

1.1 Motivation and Hypothesis of this Thesis

This thesis aims to improve the retinal image quality at a cellular level for early detection and diagnosis of retinal diseases. To achieve this goal, the thesis will evaluate a compact aberration compensation unit with "*phase plates*" in a cSLO device to establish improvement in retinal imaging at a cellular level. In the second part, a fluorescent imaging technique called "*two-photon imaging*" will be evaluated on animal models to determine the potential of two-photon retinal imaging for cellular level imaging and the safe use of a two-photon SLO prototype for retinal imaging.

Aberrations of the human eye play a significant role in degrading the visual and retinal image quality. Although cSLO with OCT imaging is commonly employed in clinical routine for diagnostic purposes, the resolution of the retinal images is limited due to aberrations of the eye. Despite the high resolution at a cellular level with adaptive optics, these systems are not widely available in clinics due to system complexity, cost, and operative effort. Even non-adaptive optics systems which can capture the retinal microstructures are only beneficial for subjects with smaller pupils. These challenges acted as the motivation for this work. The goal of this study is to enhance the precision of diagnostic and therapeutic procedures by providing clearer and more detailed images of the retina for patients with ocular aberrations and larger pupils, specifically those with HOAs. To accomplish this, the phase plates will be tested with a clinical cSLO device to assess the improvement in retinal image quality. Incorporating aberration compensation into a clinically established device would enhance retinal image quality and enable the early identification of retinal diseases. This could lead to a better understanding of the structure and function of the retina and may provide new insights into how it can be affected by various diseases and conditions. An implementation in a clinically established device could also increase accessibility for patients in eye clinics, facilitating a better understanding of retinal anatomy and pathology.

The hypothesis for retinal imaging with phase plates is that the wavefront detection technology, which has been widely used for refractive surgeries, can be used to customize the procedure for individual eyes[40-43]. Also, the same technique is combined with the aberration correction unit in the adaptive optics system to improve the retinal image quality. Likewise, it is rational to use a “*phase plate*” to compensate for the

wavefront aberrations to facilitate high-quality image to capture detailed images of the retina. It can potentially improve the overall efficacy of resolution and contrast of retinal images and the lateral resolvable detail with a clinical cSLO without adaptive optics.
Although the phase plates were used in the past with the SLO to compensate for HOAs[44-49] and recently to increase the retinal image sharpness[50], the visualization of microstructures was not achieved. With current advancements in technology, the use of phase plates in non-adaptive optics systems can now enable direct observation of retinal microstructures, allowing for analysis of their integrity and pathological abnormalities. This can lead to a more compact and cost-effective adaptive optics system that can be easily incorporated into clinical cSLO devices.
Furthermore, a high-resolution imaging device with the best image quality is also vital to reveal the potential source responsible for the onset of the disease rather than monitoring the secondary effects. For example, in the aging eye, vision is compromised by an increased incidence of age-related degenerative diseases[51, 52]. AMD is a significant cause of visual impairment worldwide, especially in the elderly. The global projected new cases of early AMD would be 32.44 million for the year 2030 and 39.05 million by 2050[53]. AMD affects the macula, and there is a lack of effective treatments since the precise origins and mechanisms that trigger this multifactorial disease are not extensively identified. Therefore, any new imaging technique that can yield high in vivo structural and functional information of the fundus with the potential to provide new insights into its pathogenesis would help to understand the AMD better. In clinics, the cSLO with OCT imaging is widely used to quantify retinal health based on its fluorescence properties. Fluorescein angiography (FA) is mainly performed to confirm neovascularization's presence. Indocyanine green angiography (ICGA) is performed to diagnose and guide treatment in patients with AMD. FAF allows visualization of the pathological and functional state of the retina by highlighting defects and alterations in the RPE that remained unrevealed by fundus photography or direct ophthalmoscopy[54-58]. FAF imaging is valuable in diagnosing and monitoring dynamic changes of RPE-related diseases but also helps identify and classify characteristic atrophy patterns in the search for cross-correlations to other pathologies and possibly genetic factors of influence. However, current fluorescence imaging tools could not resolve the RPE on a cellular level. It is partly owing to a lack of adequate resolution and strongly scattered or absorbed blue excitation light in the different layers of the human eye. These limits FAF measurements to the mapping of topographic distribution in search of areas of relative hyper- or hypo-autofluorescence.
These challenges acted as the motivation for studying the retina with the two-photon scanning laser ophthalmoscope since the TPEF provides a substantially increased sensing depth and reduced photodamage as compared with the single-photon technique (confocal technique). As a second-order effect, the fluorescence emission depends on the square of the excitation intensity. Consequently, two-photon absorption is only confined to the focal plane, resulting in an intrinsic three-dimensional diffraction-limited resolution providing highly selective optical sectioning in thick tissue without the practical constraints on resolution implied by a confocal pinhole. These unique characteristics of TPEF and the transparency of the human eye to NIR light, nonlinear retinal imaging has huge potential in developing novel high-resolution diagnostic methods in ophthalmology for the study of RPE-related metabolic alterations on cellular and subcellular level, to enhance the understanding of the normal and diseased retina.
One of the practical limitations of two-photon imaging is that it is typically limited to a relatively small field of view (FOV) since the two-photon absorption process requires a very high intensity of light, which can only be achieved over a small area. As the size of the FOV increases, the intensity of the light must be reduced to avoid damaging the

retina. This reduction in intensity can limit the resolution and sensitivity of the imaging system. Another challenge of two-photon imaging is that it can be sensitive to photobleaching, which can limit the duration of image acquisition and make it difficult to image larger areas. The intention of the study is to determine the likelihood of TPEF in animal models with a 30-degree FOV and the laser power required to provide structural and functional information on the retina for a potential non-invasive in vivo application. This will allow the direct observation of malignant changes on a cellular level preceding degenerative retinal pathologies and help to design effective therapies at the early stages of the disease. Furthermore, TPEF imaging in human eyes is crucial since the tissue responses to short-pulsed lasers are unknown. The lasers used in two-photon imaging can be damaging to the eye, so it is not currently considered safe for use in human eyes. This motivated us to evaluate the ultrashort pulsed laser effects on the retina in animal models to determine the maximum permissible exposure (MPE) for the safe use of lasers for retinal imaging with the two-photon technique. The feasibility of two-photon technology for retinal imaging concerning laser safety is needed to promote two-photon usage in clinics.

1.2 Optical Aberrations

The principle of image formation by the human eye is the same as that of optical systems, such as a camera. The cornea refracts image-forming light, and the light is focused on the retina by the lens. It is well known that the human eye is not a perfect optical system. In this section, optical aberrations of the human eye are briefly summarized.

1.2.1 Aberrations in the Optical System

Aberrations are imperfections in the optical system. Optical components can create errors in an image even if it is made of the finest materials without any defects. Generally, the aberration occurs when light from one point of an object does not converge into (or does not diverge from) a single point after transmission through the system. The optical systems need to be corrected to compensate for the aberration. The optical aberrations are divided into two classes,

- Monochromatic aberrations
- Chromatic aberrations

Monochromatic Aberration

Monochromatic aberrations are caused by geometry (the shape of the lens or mirror). These include the aberrations at reflecting surfaces of any colored light and at refracting surfaces of monochromatic light of a single wavelength. These include:

- Piston and tilt
- Defocus aberration
- Astigmatism aberration
- Coma aberration
- Spherical aberration
- Distortion
  - Barrel distortion
  - Pincushion distortion
  - Mustache distortion

Chromatic Aberration

More than 300 years ago, Newton demonstrated that white light is composed of different colors of light by passing it through a prism, which caused the light to spread out into a spectrum of colors. The concept of light as a wave and the understanding of it being composed of multiple wavelengths was developed later in the 19th century by scientist like Thomas Young and Augustin-Jean Fresnel. Chromatic aberration is caused by a lens having different refractive indices for different wavelengths of light. As a result, the light will be refracted differently as a function of wavelength. The light with a shorter wavelength is refracted more than with a longer wavelength. Consequently, lenses will not image light all in one place, as shown in Figure 1.1.

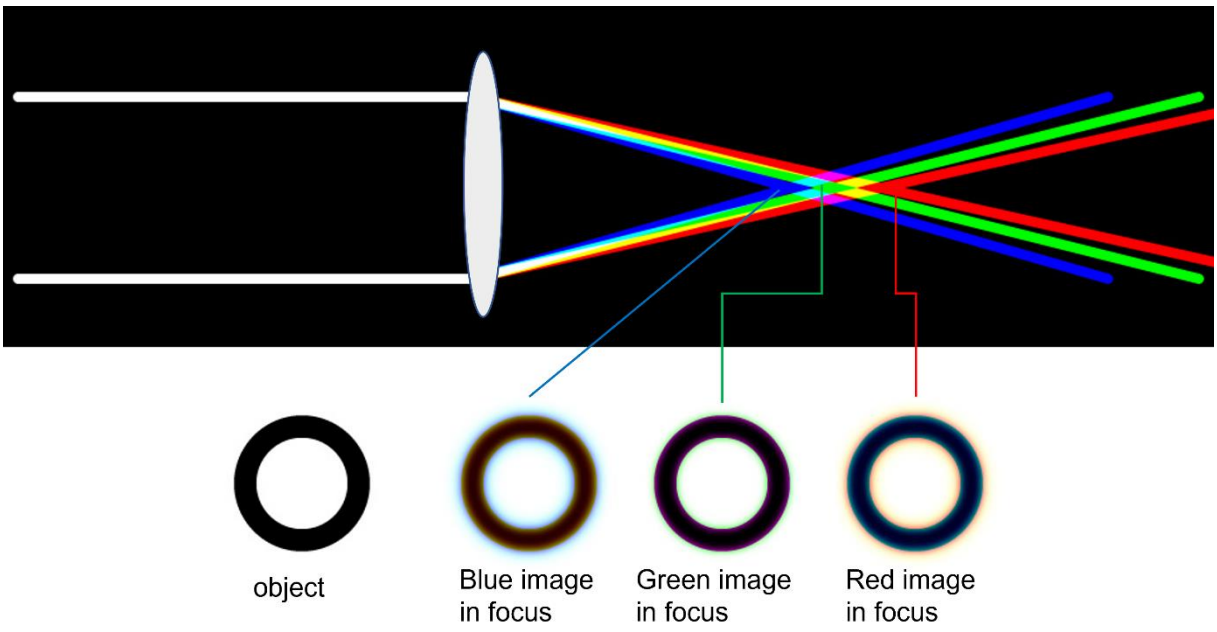

Figure 1.1. Axial chromatic aberration. Shorter wavelength light (blue) is more refracted than the longer wavelength light (red)[59].

1.2.2 Optical Aberrations of the Human Eye

The inability to provide diffraction-limited performance arises from optical imperfections in the eye. As an optical system, the eye focuses the incoming light rays on the retina. Any imperfections in focusing the light on the retina will cause the light rays to deviate, and these deviations are referred to as optical aberrations. The eye's monochromatic aberrations degrade the vision and retinal image quality for pupil size larger than 2 mm[60]. The monochromatic aberrations occur due to changes in the shape of the tear film, cornea, and lens. Chromatic aberration of the eye arises due to the different index of refraction of an eye for different wavelengths of light.
The eye suffers from several specific optical aberrations. The appearance of visual complaints such as halos, glare, and double vision are correlated with the initiation of optical aberrations. Refractive errors such as myopia (near-sighted), hyperopia (far-sighted), and astigmatism are common in the average population. These aberrations are called lower-order or second order, which can be corrected with eyeglasses, contact lenses, or refractive surgery. These aberrations make up about 90% of aberrations in the eye[40]. The other not visually significant lower-order aberrations are known as first-order aberrations, such as prisms and zero-order aberrations (Piston).

HOAs are a relatively small component, comprising about 10% of the eye's total aberrations[41], and increase with age, and mirror symmetry exists between the right and the left eyes[61]. There are numerous HOAs, of which coma, trefoil, and spherical aberration are of clinical interest. *Coma* is the distortion in the image formation and occurs when the light rays entering the optical systems are not parallel to the optic axis, and common in patients with decentered corneal grafts, keratoconus, and decentered laser ablations. *Spherical aberration* is an imaging imperfection that occurs when the light rays from the edges of a lens or mirror focus on a shorter distance than the light rays from the center. It is the cause of low light myopia and commonly increases after LASIK (laser-assisted in situ keratomileusis) and surface ablation. It results in halos around point images. HOAs are more complex than lower-order aberrations, and these aberrations produce vision errors such as difficulty seeing at night, glare, halos, blurring, starburst patterns, or double vision.

1.2.3 Wavefront Approach to Aberrations of the Eye

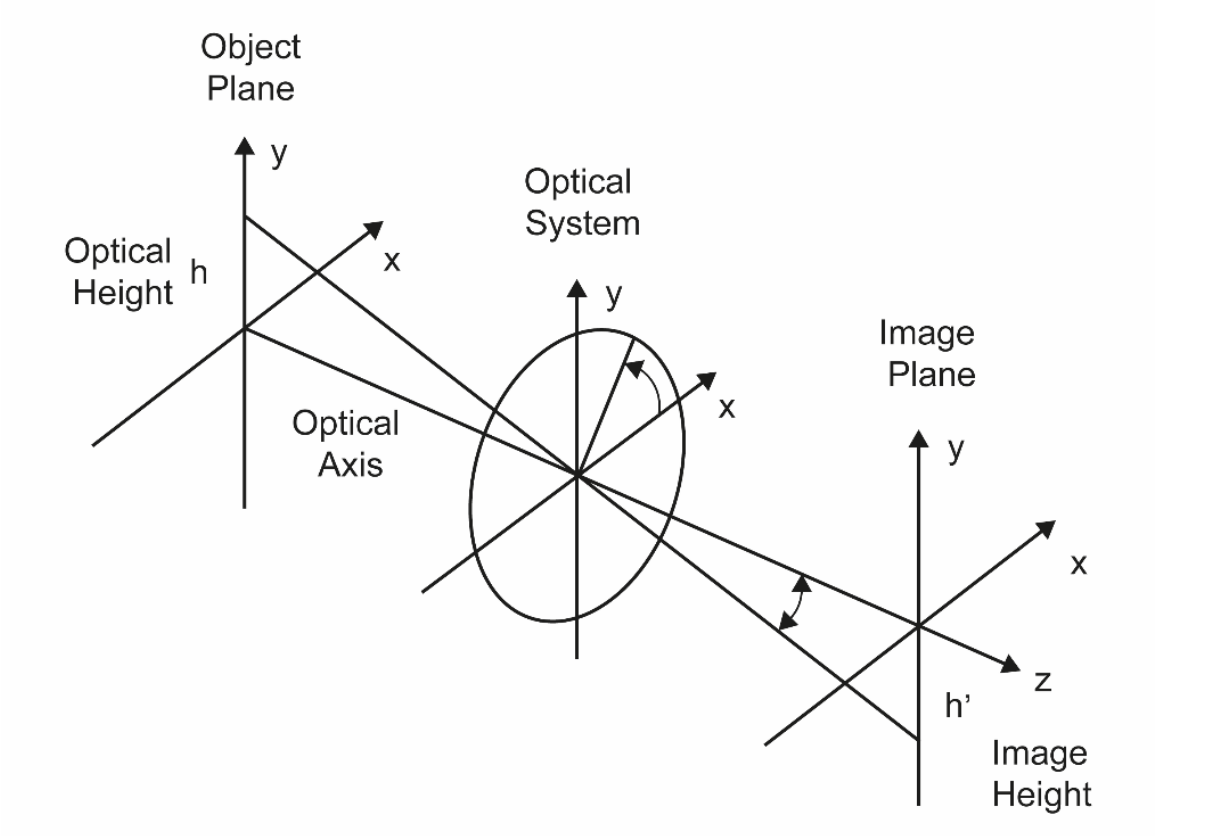

Figure 1.2. Optical imaging system with right-handed coordinates

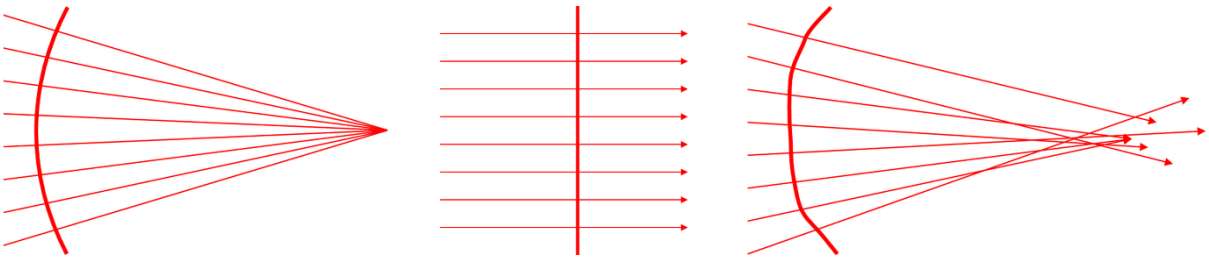

Figure 1.3. Wavefront aberrations. Ideal spherical wavefront (a), ideal planar wavefront (b), aberrated wavefront (c)

A typical optical imaging system consists of an object plane, an optical system, and an image plane, as shown in Figure 1.2. Right-handed coordinate systems are constantly employed. A wavefront is a surface over which an optical disturbance has a constant phase and is always perpendicular to the rays. The wavefront aberration (or aberrations of the eye) is the optical path length difference along rays between the actual wavefront and the ideal wavefront at the exit pupil. The distance in micrometers between the actual and ideal wavefront is the wavefront aberration. The shape of the wavefront can be either spherical or planar in an aberration-free optical system (Figure 1.3).

1.2.4 Quantitative Expression of Ocular Aberrations

Zernike Polynomials

The most common method to classify the shapes of aberration maps is to consider each map as the sum of fundamental shapes or basic functions. In ophthalmology, the wavefront aberrations are expressed using a series of Zernike polynomials (Table 1.1). The benefit of expressing the aberrations in Zernike's polynomials is that the polynomials are independent of each other, and the coefficient gives the wavefront errors[62].

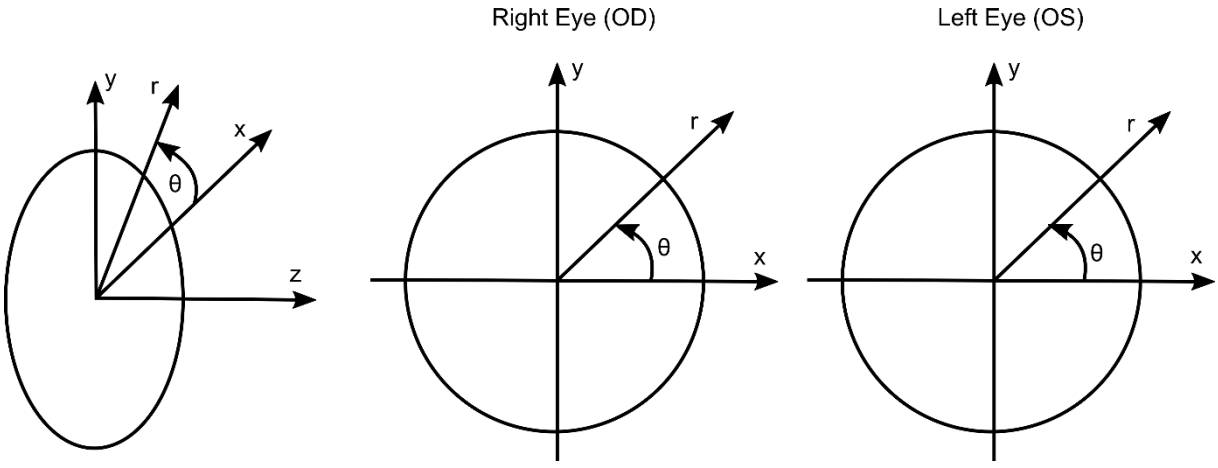

Figure 1.4. Ophthalmic coordinate system

A Zernike polynomial is a complete set of functions orthogonal over the unit circle (Figure 1.4) and parameterized by a dimensionless radial parameter ρ and a dimensionless meridional parameter θ. It is designated by a non-negative radial integer index *n* and a signed meridional index *m*. Each Zernike polynomial is the product of three terms, a normalization term, a radial term, and a meridional term. The following equation gives it.

$$Z_n^m(\rho,\theta) = N_n^m R_n^{|m|}(\rho)\cos(m\theta) \text{ for } \mathrm{m} \geq 0, 0 \leq \rho \leq 1, 0 \leq \theta \leq 2\pi$$

$$Z_n^{-m}(\rho,\theta) = -N_n^m R_n^{|m|}(\rho)\sin(m\theta) \text{ for } \mathrm{m} < 0, 0 \leq \rho \leq 1, 0 \leq \theta \leq 2\pi$$

Equation 1.1

for a given *n: m* can only take on values *-n*, *-n*+2, *-n*+4…. *N*

N_n^m is the normalization factor and is given by

$$N_n^m = \sqrt{\frac{2(n+1)}{1+\delta_{m0}}} \qquad \delta_{m0} = 1 \text{ for m} = 0, \delta_{m0} = 0 \text{ for } m \neq 0$$

Equation 1.2

$R_n^{|m|}(\rho)$ is the radial polynomial and is given by

$$R_n^{|m|}(\rho) = \sum_{s=0}^{(n-|m|)/2} \frac{(-1)^s\,(n-s)!}{s!\,[0.5(n+|m|)-s]!\,[0.5(n-|m|)-s]!}\,\rho^{n-2s}$$

Equation 1.3

Standard Wavefront Error Description

The wavefront error of an eye is the optical path length, i.e., the product of the geometric length (the physical distance the light travels) and the refractive index of the medium, between a plane wavefront in the eye's entrance pupil and the wavefront of light exiting the eye from a point source on the retina. It is specified as a function of (x, y) or (ρ, θ) coordinates of the entrance pupil. Wavefront errors are measured in an axial direction from the pupil plane towards the wavefront. By convention, the wavefront error is set to zero at the pupil center by subtracting the central value from values at all other pupil locations. The wavefront is described using the Zernike polynomial functions, as shown in equation 1.4.

$$W(\rho,\theta) = \sum_{n,m} c_n^m Z_n^m\,(\rho,\theta)$$

Equation 1.4

where *c* denotes the Zernike's amplitudes or coefficients and *Z* the polynomials.

Root Mean Square Wavefront Error

The quantitative comparisons between different eyes and conditions are expressed as root mean square (RMS). The RMS wavefront error for the human eye is computed as the square root of the variance of the wavefront error function. Piston and tilt are usually excluded from the calculation since they correspond to lateral displacements of the image rather than image degradation. The following equation 1.5 defines RMS error.

$$RMS = \sqrt{\frac{\iint_{pupil}[W\,(x,y) - \bar{W}]^2\,dx\,dy}{A}}$$

Equation 1.5

where *A* is the area of the pupil and $\bar{W}$ is the mean wavefront optical path difference. If the wavefront function is expressed in terms of normalized Zernike coefficients, the RMS value is equal to the square root of the sum of the squares of the coefficients with radial indices n ≥ 2.

$$RMS = \sqrt{\sum_{n\geq 2, all\ m} (c_n^m)^2}$$

Equation 1.6

Table 1.1 Zernike polynomials up to 4th order[63]

Symbol	Polar form	Common name	Plots
Z_0^0	1	Piston	
Z_1^{-1}	$2\rho\sin(\theta)$	Vertical tilt	
Z_1^1	$2\rho\cos(\theta)$	Horizontal tilt	
Z_2^{-2}	$\sqrt{6}\rho^2\sin(2\theta)$	Oblique astigmatism	
Z_2^0	$\sqrt{3}(2\rho^2-1)$	Defocus	
Z_2^2	$\sqrt{6}\rho^2\cos(2\theta)$	Vertical astigmatism	
Z_3^{-3}	$\sqrt{8}\rho^3\sin(3\theta)$	Oblique trefoil	
Z_3^{-1}	$\sqrt{8}(3\rho^3-2\rho)\sin(\theta)$	Vertical coma	
Z_3^1	$\sqrt{8}(3\rho^3-2\rho)\cos(\theta)$	Horizontal coma	
Z_3^3	$\sqrt{8}\rho^3\cos(3\theta)$	Horizontal trefoil	
Z_4^{-4}	$\sqrt{10}\rho^4\sin(4\theta)$	Oblique quadrafoil	
Z_4^{-2}	$\sqrt{10}(4\rho^4-3\rho^2)\sin(2\theta)$	Oblique secondary astigmatism	
Z_4^0	$\sqrt{5}(6\rho^4-6\rho^2+1)$	Primary spherical	
Z_4^2	$\sqrt{10}(4\rho^4-3\rho^2)\cos(2\theta)$	Vertical secondary astigmatism	
Z_4^4	$\sqrt{10}\rho^4\cos(4\theta)$	Horizontal quadrafoil	

Point Spread Function

The aberration of the human eye negatively impacts the retinal image quality. Fourier optics has been introduced in ophthalmology to characterize the effects of aberrations. One of those techniques is the point spread function (PSF), which defines the propagation of electromagnetic radiation or other imaging waves from a point source or point object. In incoherent imaging systems such as fluorescent microscopes, telescopes, or optical microscopes, the image formation process is linear and described by linear system theory. A convolution equation usually formulates the process.

$$Image = PSF \otimes Object$$

Equation 1.7

Image: image generated by the optical system,

PSF: point spread function of the optical system,

Object: object,

⊗: convolution operator.

Figure 1.5. Image formation process. The final image generated by the optical system can be described as a mathematical convolution of the object with the PSF of the optical system.

Figure 1.5 shows the image formation process of the optical system. The final image created by the system is the convolution of the object, which will be imaged with the system's point spread function. Due to the imperfection of the optical system, the image is normally blurred. The optical properties of the eye can be characterized by the wavefront error function, which can be described by a series of Zernike polynomials. The image of a point object formed by the optical system is the PSF or impulse response. It is defined as

$$PSF\ (x,y) = \frac{1}{\lambda^2 d^2 A_p}\left\| FT\ \{\ p(x,y).e^{-i\frac{2\pi}{\lambda}W(x,y)}\}\right\|^2$$

Equation 1.8

FT: Fourier transform operator.

D: distance from the exit pupil to image.

A_p: area of the exit pupil.

p (x, y): defines the exit pupil's shape, size, and transmission.

$e^{-i\frac{2\pi}{\lambda}W(x,y)}$accounts for phase deviations of the wavefront from a reference sphere

W (x, y): wavefront aberrations function at the exit pupil.

It is also possible to calculate the modulation transfer function (MTF) of the human eye, which is the modulus of the optical transfer function (OTF). MTF is normally used to characterize the resolution and performance of an imaging system and is also known as spatial frequency response. The following equation gives the mathematical formulas:

$$OTF\left(s_x, s_y\right) = \frac{FT\left\{PSF\right\}}{FT\left\{PSF\right\}|\, s_x = 0, s_y = 0}$$

Equation 1.9

$$MTF\left(s_{x,} s_y\right) = \left\|OTF\left(s_x, s_y\right)\right\|$$

Equation 1.10

$\left(s_x, s_y\right)$ are in units of cycles per radian.

Strehl Ratio

The Strehl ratio measures the effect of aberrations in reducing the maximum or peak value of the PSF. The definition of the Strehl ratio is the ratio of the observed peak intensity at the detection plane of a telescope or other imaging systems from a point source compared to the theoretical maximum peak intensity of a perfect imaging system working at the diffraction limit. The Strehl calculation is based on complex mathematics, and a simple empirical expression gives a very close approximation of the Strehl ratio in terms of the RMS wavefront error:

$$Strehl\ ratio \cong e^{-(2\pi\sigma)^2}$$

Equation 1.11

where, σ is the root-mean-square deviation of the wavefront measured in wavelengths.

1.3 Overview of Clinical Ophthalmic Devices

"One picture is worth a thousand words."

Retinal imaging devices have played a crucial role in ophthalmic examination and diagnosis for over a century. The invention of the first ophthalmoscope by Hermann von Helmholtz in 1851 marked the beginning of the quest for quantitative in vivo images of the ocular fundus for diagnostic and monitoring purposes. Over time, the technology has evolved from simple photographs to more advanced and specialized digital recording methods. These recordings provide quantitative and reproducible information on retinal health over time and are essential in the diagnosis and monitoring of various retinal diseases.

Fundus Photography

The fundus camera is a widely used retinal imaging device in clinics for fundus imaging (Figure 1.6). It is an extension of indirect ophthalmoscopy, in which a photographic film or digital camera records the images. The advantage of using a fundus camera over direct or indirect ophthalmoscopy is that the images can be stored and reviewed later for monitoring disease progression. Fundus photographs aids physicians in identifying the retinal changes and planning appropriate diagnosis and treatment. However, fundus photography has limitations in terms of depth discrimination and high-resolution retinal imaging. To overcome these limitations, color filters and blocking specific

wavelengths can be used to image specific retinal structures. The fundus camera can perform various modes such as color photography, red-free fundus photography, angiography (FA and ICGA), and simultaneous stereo fundus photos.

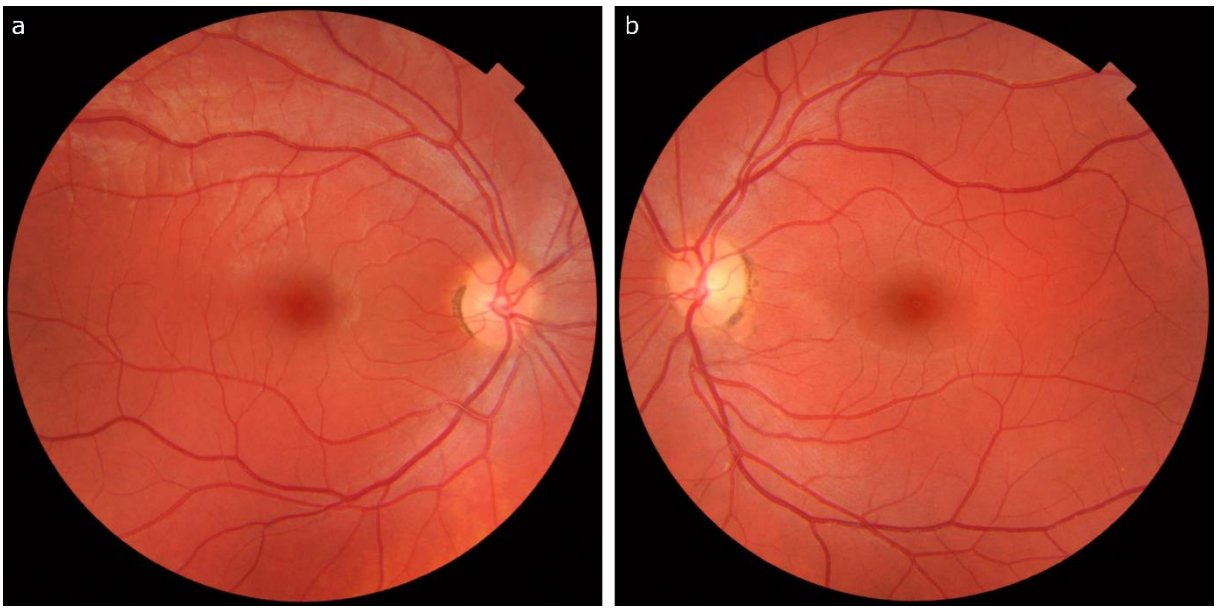

Figure 1.6. Fundus photography of the right eye (a) and left eye (b)[64]

Scanning Laser Ophthalmoscope

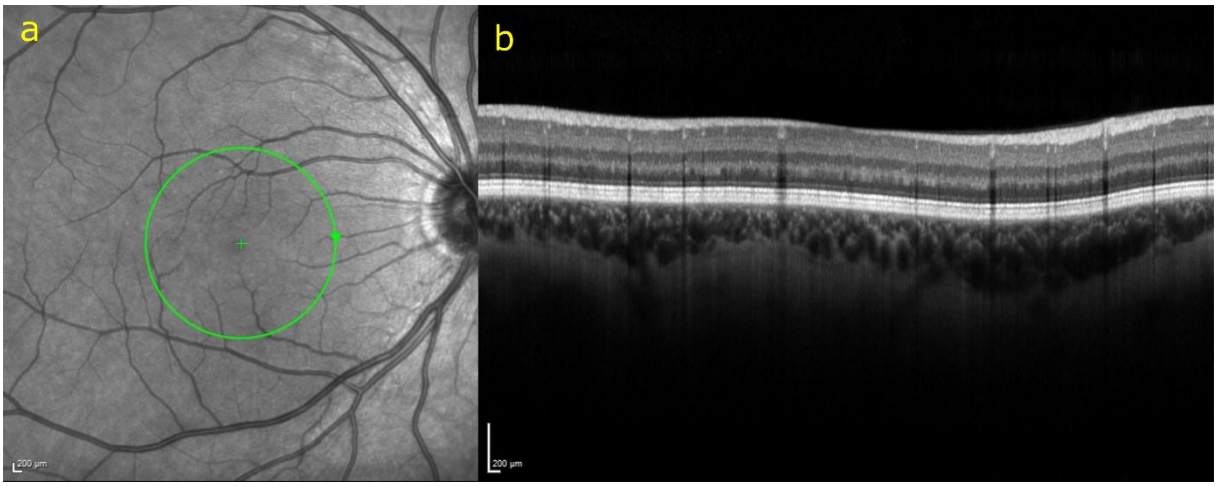

Figure 1.7. The Heidelberg Engineering SPECTRALIS device captures both cSLO (a) and OCT (b) images of the retina. The green circle in the cSLO image (a) indicates the position of the corresponding OCT image (b).

A SLO uses a laser beam of light that is directed onto the retina, which is then scanned across the surface of the eye to create a detailed image. A solution to depth discrimination in retinal imaging is provided by the cSLO. It is based on the confocal imaging technique and offers high contrast and detailed retina images (Figure 1.7a). The cSLO allows optical sectioning of a 3D retina by blocking the light originating from the out-of-focus plane, improving the depth and resolution. A confocal pinhole enhances the contrast of the images before the detector, which stops the scattered light from the unwanted retinal layers[65, 66]. The cSLO principle is described in detail in section 1.3.2. The SLO can provide qualitative and quantitative 3D retinal images and become an essential tool in ophthalmic clinics.

Optical Coherence Tomography

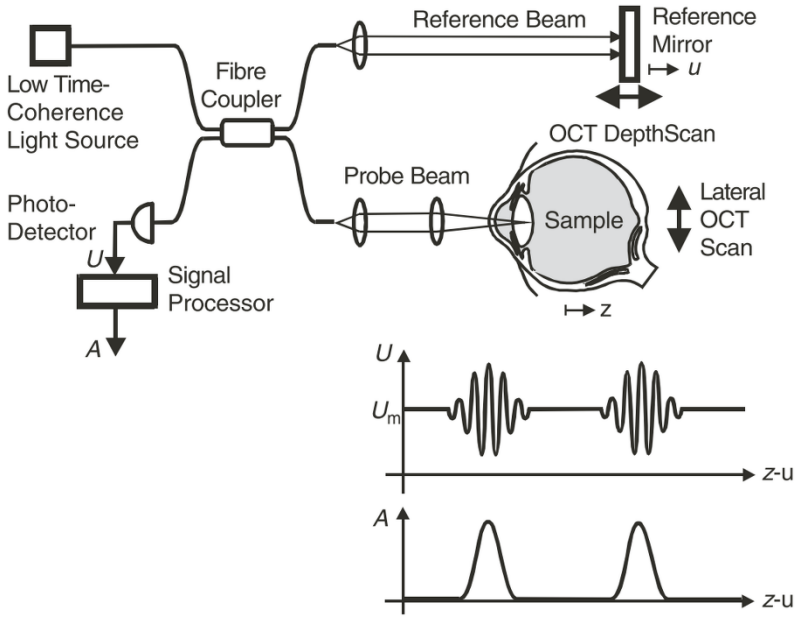

Figure 1.8. Illustration of the principle of OCT[67]

Further improvement in depth resolution was achieved by OCT. The depth resolution of an OCT system refers to its ability to distinguish between structures or layers that are close together in the tissue being imaged. OCT is a non-contact imaging technique that provides high-resolution cross-sectional retina images[67]. Light reflected from the retina is interfered with that of a reference beam. A low-coherence light source is desired to observe the reflected light from retinal layers since the coherence length of the light determines the depth resolution. The coherence length is a measure of the distance over which the light waves maintain a stable phase relationship, and it determines the minimum distance that can be resolved by the system. Scanning is employed to image the retina's different depths and lateral locations. Figure 1.8 illustrates the principle of OCT. In ophthalmology, OCT has become a clinical workhorse due to the capability of providing cross-section retinal images at a micrometer resolution which were previously imaged only in excised samples[68, 69]. Recent advances in OCT support ophthalmologists in assessing the vascular health of the retina without dye injection[70]. Optical coherence tomography angiography (OCTA) generates volumetric angiography images in seconds and provides 3D visualization of perfused vasculature of the retina and choroid.

1.3.1 Need for High-Resolution Retinal Imaging

High resolution retinal imaging is important for the early detection and diagnosis of a wide range of retinal diseases, such as AMD, DR and glaucoma, which can lead to serious vision loss if not detected and treated early. High resolution images allow for the detection of small changes or abnormalities in the retina that may indicate the presence of a disease, enabling earlier diagnosis and treatment and improving the chances of preserving vision. Additionally, high resolution images allow for more accurate monitoring of the progression of a disease, which can help guide treatment decisions. However, a significant issue with in vivo retinal imaging is the blur introduced by eye optics, including the diffraction caused by the small size of the pupil under bright light conditions and the HOAs that occur in larger pupil sizes. These aberrations limit the resolution of the imaging devices and must be measured and corrected for high-resolution

retinal imaging. Despite the technical advancements, resolving the retinal structures at a microscopic scale remains a challenge in a clinical setting. Adaptive optics can be used to visualize retinal structures at a cellular level, but it is not widely available in clinics due to its complexity, cost, and operational effort. Therefore, correcting aberrations is crucial in our quest to increase the image quality at a cellular level in a clinical device.

1.3.2 Confocal Scanning Laser Ophthalmoscopy

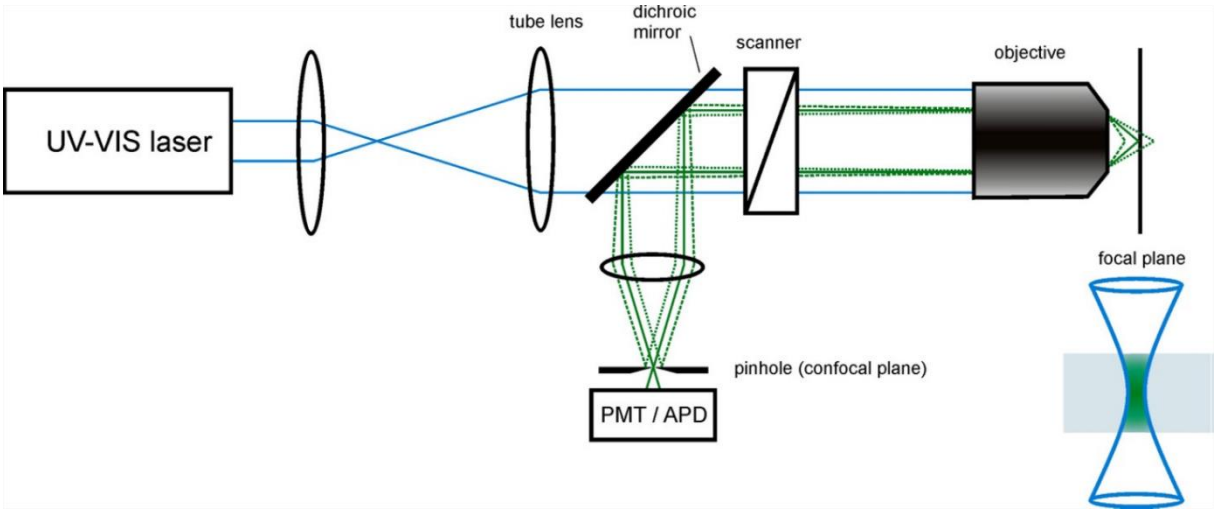

Figure 1.9. The basic setup of a fluorescence confocal laser scanning microscope. The excitation path is blue, and the fluorescence emission path is green[71].

In a conventional microscope, the object is imaged by a magnifying lens simultaneously and parallel to all objects in one plane. In contrast, in a scanning microscope, the focused spot of the light moves over the sample in a defined raster pattern and images only one object point at a time. This way, the detector serially collects the reflected or fluorescent light (intensity measurement) from the same volume to build a digital image. However, the limitations of such scanning systems are their resolution and depth of focus. The signals from the planes above and below the focal planes produce a strong background, degrade the image quality, and subsequently restrict an application for 3D imaging. To overcome this limitation confocal scanning microscope was introduced. A significant advantage of confocal microscopy is the ability to collect light only from a single plane. Minsky first described and patented the confocal principle in 1961 to reduce the scattered light from the sample under inspection[72]. The key benefit of a confocal microscope is the pinhole, which is placed conjugate to the object plane of the microscope with its center located on the optical axis. This only detects light signals from the sample in focus and blocks the out-of-focus signal. Furthermore, the technological advancement in illumination light sources and detection systems made confocal laser scanning microscopy an invaluable tool in research[73, 74]. The basic optical layout of confocal laser scanning microscopy in epifluorescence is shown in Figure 1.9. The objective lens focuses the laser light onto the sample, and a dichroic mirror spectrally separates the excited fluorescence from the illuminated area. The reflected or fluorescent light from the sample is collected and focused as a confocal point onto the detector pinhole positioned in front of the photodetector (usually a photomultiplier tube (PMT) or avalanche photodiode (APD)). The fluorescence intensity is then converted from an analog signal into a pixel value by an analog to digital converter.
Different scanner arrangements are possible to move the laser light across the sample. Besides tandem scanning and stage scanning, the most popular way to raster scan in

confocal microscopy is the beam scanning or flying spot method, which uses two mirrors to change the beam angle. If the rotational axis of the mirrors coincides with the optical axis, a pair of scanning mirrors moves the laser beam across the focal plane in the x-y- direction. The biggest challenge of a fast 2D scanning system requires a fast-scanning direction. A fast line scan rate is necessary to achieve frame rates greater than 15 Hz while maintaining a sufficiently high line density for square pixels. i.e., same pixel separation in x- and y- direction. In addition to the high speed, the optical scan angle and the size of the scan pupil need to be carefully balanced. Resonant scanners or polygon scanners can meet these demanding specifications. The straight lines in Figure 1.9 show the optical path for an object in the focal plane. The light emanating from a plane above or below the focal plane (dashed lines) arrives at the detector pinhole as a defocused blur; only the central region is detected and contributes to the image. In this way, the system discriminates against features that do not lay in the focal region of the objective. The larger the defocus distance, the weaker the detected signal. This property is the primary reason for the popularity of confocal microscopes. It allows image detail from one specific volume by choosing the focal position in thick translucent samples (optical sectioning). It reconstructs its 3D structure by a stack of sections at different depths without necessarily mechanically slicing the object. Acquisition and visualization are generally computer-controlled by appropriate software.
In a perfect optical system, the resolution is restricted by the numerical aperture (NA) of optical components and the wavelength of light, both incident (excitation) and detected (emission). In a typical fluorescence microscope, contrast is determined by the number of photons collected from the specimen, the signal's dynamic range, optical aberrations of the imaging system, and the number of picture elements (pixels) per unit area in the final image. The properties of the intensity PSF in the image plane as well as in the axial direction are critical factors in determining the resolution of a microscope. The intensity PSF of a confocal can be described as the probability of a fluorescence photon emitted at a point(v,u). The illumination PSF denoted as $h_{il}(v,u)$ and the detection PSF is denoted as $h_{det}(\frac{v}{\beta},\frac{u}{\beta})$. The effective PSF of a confocal microscope is given by:

$$h_{confocal}(v,u) = h_{il}(v,u).h_{det}(\frac{v}{\beta},\frac{u}{\beta}) = h_{il}^2(v,u)$$

Equation 1.12

The factor $\beta = \frac{\lambda_{fl}}{\lambda_{il}}$ is the ratio of the illumination to the fluorescence wavelength. The value of β is 1 approximately. The quadratic dependence of the PSF has two main consequences, to make the width of the PSF smaller, resulting in a resolution improved by a factor of 1.4, and to reject fluorescence from molecules that are not in focus. Assuming a uniform illumination, the full width at half maximum (FWHM- resolution or spread of a peak in a spectrum or plot) resolution of an ideal confocal microscope depends on both the excitation and emission wavelength and can be expressed as

$$\Delta_r = 0.37 \frac{\overline{\lambda}}{NA}$$

Equation 1.13

$$\Delta_z = 1.28 \frac{\overline{\lambda}}{NA^2}$$

Equation 1.14

in a lateral and axial direction, respectively. $\bar{\lambda}$ is mean wavelength.

$$\bar{\lambda} = \sqrt{2}\,\frac{\lambda_{il}\,\lambda_{fl}}{\sqrt{{\lambda_{il}}^2 + {\lambda_{fl}}^2}}$$

Equation 1.15

The above considerations are based on the concept of an ideal point illumination and point detection. In practice, the pinholes are of finite size, and the confocal PSF must be convolved with the respective illumination and detection pinhole functions. The detection pinhole, however, sets a practical limit to the effect achieved confocal resolution and is always a trade-off between resolution and signal strength. A pinhole considerably smaller than the Airy pattern only marginally improves resolution and blocks most of the light intensity, whereas a larger pinhole primarily degrades depth resolution. A good compromise must be achieved for a pinhole size of 1–2 Airy units[75].

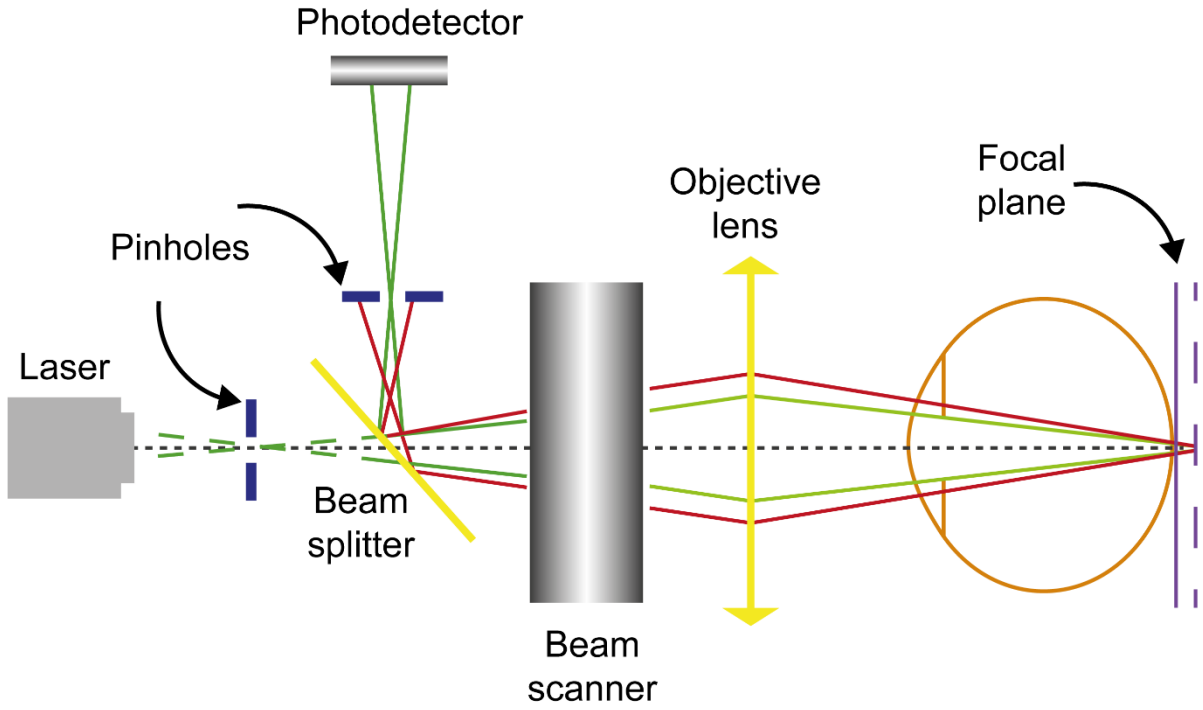

Figure 1.10. Schematic diagram of confocal scanning laser ophthalmoscope

Confocal scanning laser ophthalmoscope (cSLO) is a retinal imaging technique that utilizes the principles of the confocal scanning laser microscope. The main difference between cSLO and a traditional confocal microscope is that in cSLO, the eye's optics serve as the objective lens (Figure 1.10). As a result, the optical resolution of cSLO is limited by the anatomy of the human eye itself. Like any conventional microscope, diffraction limits the minimum spot size of the focused laser in the object plane. The NA of an optical system characterizes the range of angles (half cone angle θ, measured against the optical axis) over which the system can accept or emit light. It is also a measure of the optical resolution in a diffraction-limited system. For the human eye, it is defined by:

$$\mathrm{NA_{eye}} = n_{vitr.} \cdot \sin(\theta) = n_{vitr.} \cdot \sin\left(\frac{\mathrm{D}}{2 \cdot f_p}\right) = n_{vitr.} \cdot \frac{\mathrm{D}}{2 \cdot f_p} = \frac{\mathrm{D}}{2 \cdot f_{eye}}$$

Equation 1.16

where $n = 1.336$ is the refractive index of the vitreous, D the pupil diameter, f_p the posterior focal length of the emmetropic eye ($f_p = 22.3\mathrm{mm}$), and f_{eye} the anterior focal length determines the retina's lateral scaling parameters.
For undilated pupils, the maximum NA_{eye} is about 0.09 ($\mathrm{D} = 3\ \mathrm{mm}$), and it can be increased by a factor of 2-3 by dilating the pupil to $\mathrm{D} = 6 - 8\ \mathrm{mm}$. However, due to the limited optical quality of the eye and the substantial increase of the optical aberrations in the periphery, the wavefront distortions result in a larger focal volume on the retina and thus decrease the optical resolution compared to undilated pupils. To exploit the full diffraction-limited resolution for dilated pupils, an adaptive optical element must be used to compensate for the distortions of the optical wavefront of the individual eye. With this concept, the lateral resolution can be increased by a factor of 2-3 and the axial resolution even by a factor of 4-9 compared to undilated pupils. The cSLO is now a well-established tool in clinical routine. cSLO generates high-contrast images and can perform optical slicing through weakly scattering media, making it ideal for imaging the multi-layered retina.

1.4 Adaptive Optics in Ophthalmology

The pursuit for optically perfect vision has been a major focus in the field of ophthalmology over the last twenty years, leading to the development of wavefront-guided laser refractive surgery. More than 25 years ago, the Shack-Hartmann method was used to demonstrate the first in vivo measurement of the eye's wave aberrations at the University of Heidelberg[76-78]. This allowed for the continuous measurement of ocular aberrations and the use of adaptive optics to correct these aberrations in ophthalmoscopy. This has led to the development of various new diagnostic and treatment modalities such as AOSLO and adaptive optics OCT. The limits of human vision can be assessed by using adaptive optics. Although there are many methods to measure ocular aberrations, Shack-Hartmann is considered the most acceptable method to precisely measure the aberrations in the human eye and is generally employed in clinical aberrometers. In 1989, Drs. Dreher, Bille, and Weinreb attempted to measure and correct monochromatic aberrations using an active mirror to correct ocular aberrations and provided improved depth resolution retinal images using a SLO[77]. The clinical adoption of the Shack-Hartmann wavefront sensor to measure eyes wave aberration was demonstrated in the early 1990s at the University of Heidelberg, in Prof. Bille's laboratory, with Dr. Liang working as a graduate student[78]. This led to the important development of closed-loop adaptive optics systems for ophthalmology. Later, with Dr. Williams at the University of Rochester, Dr. Liang built the first closed-loop adaptive optics system that could correct HOAs of the eye and achieve a supernormal vision and visualization of single cells in the human retina[13]. With advancements in these technologies, wavefront-guided laser refractive surgery was introduced as a clinical treatment for refractive correction[79]. The wavefront technology has advanced significantly in recent years, allowing for accurate measurements and diagnoses of HOAs. This had led to the development of wavefront-designed glasses, contact lenses, intraocular implants, and wavefront-guided laser vision correction. Additionally, fundus cameras, SLO, OCT, and two-photon ophthalmoscopy have incorporated adaptive optics to achieve a diffraction-limited imaging system[14, 47, 80].

1.4.1 Principle of Aberration Measurement

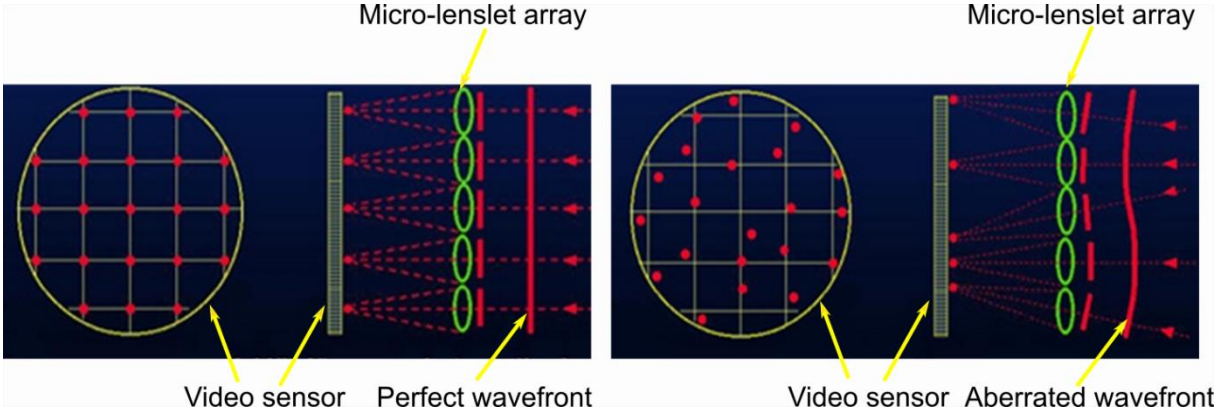

Figure 1.11. Left: Incident plane wave resulting in a square grid of spots. Right: Distorted wavefront causes lateral displacement of spots.

In recent years, three aberration measurement devices have been developed: the thin-beam ray tracing aberrometer, the Tscherning aberrometer, and the Shack-Hartmann method. The principle of operation of the Shack-Hartmann wavefront sensor is demonstrated in Figure 1.11. On the left-hand side, the processing of an ideal plane wave is depicted, where the incident plane wave results in a square grid of spots in the focal plane of the micro-lens array. On the right-hand side, the image of a distorted wavefront is shown, which causes lateral displacements of the spots on the CCD array. By analyzing the spot pattern, the shape of the incident wavefront can be reconstructed using appropriate curve-fitting algorithms. More than twenty-five years ago, the first detailed study of the application of wavefront technology for the assessment of the refractive properties of the human eye was conducted. Zernike coefficients were calculated from the wavefront measurements, and the wavefronts emerging from the eyes were reconstructed.
Figure 1.12 illustrates how a lens-array works. An incident planar wavefront results in a square grid of spots (green), but an aberrated wavefront generates a distorted pattern in the focal plane of the lens array (red). By comparing the lateral displacements of the spots in the two patterns, the distorted wavefront can be reconstructed using appropriate curve fitting algorithms. This process results in a series of Zernike coefficients that can be used for further analysis.

Figure 1.12. Principle of WaveScan™ measurements. The ideal wavefront is represented as a regular grid of spots coded in green, while the distorted wavefront is given by an irregular grid of dots coded in red.

1.4.2 Adaptive Optics Retinal Imaging

Adaptive optics technology aims to correct the ocular aberrations to enhance the performance of the optical systems[15, 18, 81]. Modern adaptive optics retinal imaging systems typically use a wavefront sensor, a wavefront corrector to shape the wavefront, and a computer controller to control the interaction between the wavefront sensor and the corrector. An alternative to this approach is a sensorless adaptive optics, which eliminates the need for a wavefront sensor and computational adaptive optics, which eliminates the need for a wavefront sensor and corrector.
The adaptive optics systems with the wavefront sensor and corrector are widely used for human retinal imaging[14, 15, 80, 82-88]. These system measures the eye's optics with a wavefront sensor and then corrects the eye's wavefront using a wavefront corrector. The advantage of this technique is the robustness and simplicity of system operation. The eye's wavefront aberrations are typically determined based on the observation that different points in the pupil focus on the same location in the image plane in a diffraction-limited imaging system. It is not the same in the presence of optical aberrations; each pupil position does not focus on the same location (See Figure 1.11). A widely used method to measure the aberrations is the Shack-Hartmann method. The Shack-Hartmann sensor (SHS) provides a simple and robust way to quantify the wavefront aberrations. The Shack-Hartmann wavefront sensor is an array of small lenses (lenslets) arranged such that each one focuses collimated light onto an area of the sensor, typically a charged-coupled device (CCD) or complementary metal-oxide-semiconductor (CMOS) camera. In a typical setup, the retina is illuminated by a point source of light. The light rays exiting the pupil will be parallel when there are no aberrations in the eye. But when the aberrations are present, the rays originating will not be similar as they exit the eye. The light from the retina is then re-imaged back onto the SHS, which is typically optically conjugate to the eye's pupil. A series of spots will be created on the CCD. The SHS is typically a slope sensor sensitive to the spatial derivative of the wavefront since the bright spot on the sensor for each lenslet depends on the local slope of the wavefront across the lenslet. The control software computes rapidly and continuously the wavefront deviations[88]. The SHS is simple and efficient, but its limited spatial resolution can be a problem in high spatial frequency aberrations. Other wavefront sensors such as the pyramid sensor have been investigated[89-91], but they have not been widely adopted due to complexity and the need for more light for wavefront sensing. In general, most of the light returning from the retina is directed to the imaging detectors, and only a small amount of light is used for wavefront measurements and corrections.
The wavefront corrector's purpose is to vary light's time delay (optical path length) over space and can be done in reflection or transmission mode. The wavefront corrector can be placed conjugate to the eye pupil but is not a requirement. Wavefront correctors are characterized by their spatial resolution and the amplitude of the aberrations they can correct (stroke). Other factors such as speed, reflectivity or transmissivity, surface quality, polarization properties, and linearity of control from location to location across corrector are essential. Different types of wavefront correctors are available, each with their own limitations. The liquid crystal phase plates are one wavefront connector composed of oriented molecules with varying indexes of refraction in one direction compared to another. An electric field can alter the orientation of these molecules as a function of position; thus, the time delay for light passing through them can vary over space. The liquid crystal display can be set up only to change the phase and not the amplitude as a phase modulator to vary the delay of light over space[92-94]. The advantage of liquid crystal phase plates is that they can correct aberrations with spatial

frequency and are easily programmable and relatively inexpensive. However, the wavelength dependency and the polarization effects limit the liquid crystal phase plates used in retinal imaging systems. Both cornea and retina exhibit birefringence and thus polarization of light returning from the eye[95-97]. This decreases the light efficiency of the imaging systems as well as limits the flexibility of the system. The most widely used wavefront corrector in adaptive optics systems is the deformable mirrors. These include piezoelectric deformation of glass, MEMS (microelectromechanical mirrors), and electrostatic and electromagnetic mirrors[98-102]. The piezoelectric mirrors work by using a piezoelectric stack to deform a glass surface. Due to their high costs, they have been replaced for ophthalmic imaging. Electromagnetic deformable mirrors have excellent surface properties and large strokes, but they are also costly. Researchers have explored alternative techniques like woofer-tweeter design and wavefront doubler design to reduce the cost of the deformable mirror[103]. The MEMS mirror has a high actuator count and are less expensive, but limited amounts of stroke can be imposed. Despite this, the MEMS has been widely used in adaptive optics systems due to their cost-effectiveness for clinical systems. Combining adaptive optics with SLO increases the contrast of retinal imaging and allows high-resolution retinal images at 2 µm resolution in the living human eye. This enables cellular and sub-cellular visualization of retinal structures. Adaptive optics techniques can also be combined with a single photon, two-photon fluorescence, and fluorescence lifetime imaging to provide information on specific molecular events[104-109].

1.5 Two-Photon Excited Fluorescence Imaging

Fluorescence imaging has become an effective imaging tool in ophthalmology for the non-invasive monitoring of retinal disease. The lipofuscin in RPE cells is strongly autofluorescent upon blue light excitation. Its fluorescent properties permit direct visualization of retinal health, becoming a useful diagnostic tool for AMD. This overview covers the principles of fluorescence imaging, including single and two-photon excitation, two-photon fluorescence microscopy, and laser-tissue interactions related to the research in chapters 4 and 5.

1.5.1 Fluorescence

Fluorescence is a type of luminescence that occurs when a molecule, called a fluorophore, absorbs light. This absorption causes the electrons in the molecule to become excited to a higher energy state. The excited electrons then return to their ground state by emitting a longer wavelength, lower energy photon. This process is illustrated in a Jablonski diagram (Figure 1.13) which shows the major molecular pathways of a fluorophore. The lowest energy state, the ground state, is denoted by S0. For most organic molecules, this state is an electronic singlet, in which all electrons have opposite spins. For any molecule, several excited states (S1, S2, . . .) exist depending on the total electron energy. Each electron state is further subdivided into several vibrational and rotational states with distinct energy levels. At room temperature, most molecules exist in the ground's lowest vibrational state; hence, the excitation process usually originates from this energy level. A molecule is excited from its ground state to an excited state upon absorption of a photon of energy,

$$E = h\nu = h\,\frac{c}{\lambda}$$

Equation 1.17

where h is Planck's constant (6.626 × 10^{-34} Js), c is the speed of light in vacuum (3 × 10^8 m/s), v is the frequency and λ wavelength of the incoming photon.
Excitation of molecules can occur through physical means, such as the absorption of light, as well as chemical or mechanical means. Luminescence is the spontaneous emission of light while returning to the ground state. The excitation caused by the absorption of photons is called photoluminescence. Photoluminescence can be either fluorescence or phosphorescence, depending on the electronic configuration of the excited and emission pathways. Fluorescence is the ability of some atoms and molecules to absorb photons of specific energy and re-emit them at a longer wavelength (lower energy) after a short time interval, typically on the nanosecond time scale. This is known as the fluorescence lifetime. Phosphorescence, on the other hand, differs from fluorescence in that it involves an electronic transition pathway (intersystem crossing) into the excited triplet state, resulting in a much longer excited state lifetime, ranging from milliseconds to hundreds of seconds[110].
The molecules can transit from the ground state (lower energy) to the excited state (higher energy) by absorption of photons with an energy equal to the energy difference between the excited and ground state. This electronic excitation can occur through linear or nonlinear absorption. Linear absorption is when a molecule is excited from the ground state to an excited state by a single photon and is called single photon absorption. Nonlinear absorption occurs when two or more photons with less energy than a single photon are combined to bridge the energy gap needed for excitation. Two-photon absorption is the most widely used nonlinear excitation in biomedical research, in which two photons with half the energy of single photon absorption are combined to excite the molecule[111, 112]. From the electronically excited state, the molecule can return to the electronic ground state either by non-radiative relaxation, emitting a photon with a longer wavelength (fluorescence), or by phosphorescence after intersystem crossing (Figure 1.13).
Fluorescence microscopy relies on the ability of the object of interest to fluoresce when illuminated with excitation light. This can be achieved by labeling specific cellular or subcellular compounds with exogenous fluorophores that are specially synthesized for this purpose. Additionally, many biological substances have inherent fluorophores, known as autofluorescence, that can be used to monitor the physiological state of tissue without the need for labeling. Fluorescence imaging only highlights the objects of interest, providing intrinsic selectivity and contrast[113].

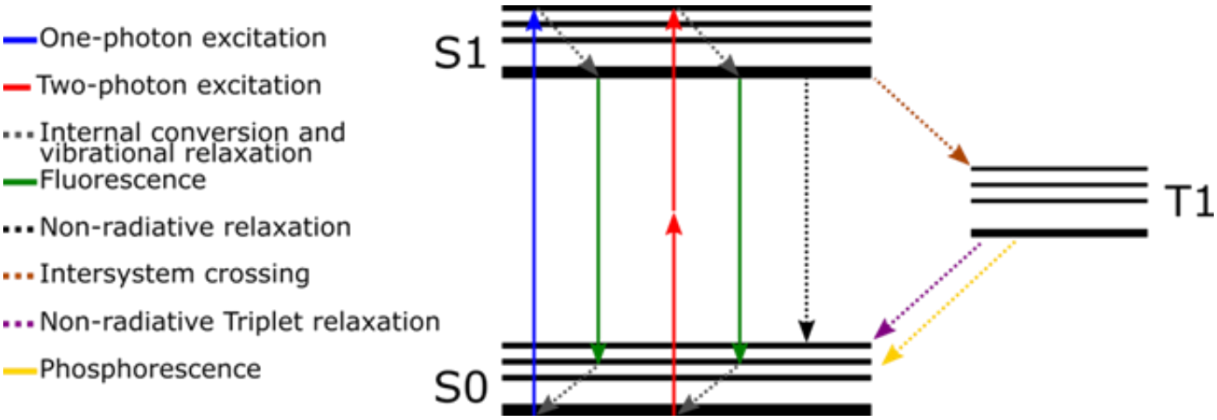

Figure 1.13. Jablonski Diagram illustrates the molecular pathways of a fluorophore during single-photon excitation fluorescence, two-photon excitation fluorescence, internal conversion and vibrational relaxation, non-radiative relaxation, intersystem crossing, and phosphorescence[71].

1.5.2 Two-Photon Excited Fluorescence Microscopy

In 1931 Maria Göppert-Mayer first theoretically predicted that the excited molecule state produced by the absorption of a single photon could be reached upon simultaneous absorption of two lower energy, or longer wavelength, photons in the same quantum event, a process called two-photon excitation[71, 112]. The timescale for simultaneousness is determined by the timescale for molecular energy fluctuations at photon energy scales, as determined by Heisenberg's uncertainty principle, which is on the order of 10^{-16} s. The energy sum of both photons is equivalent to the one required for single-photon excitation, such that:

$$\lambda_{1P} \approx \left(\frac{1}{\lambda_A} + \frac{1}{\lambda_B}\right)^{-1}$$

Equation 1.18

where, λ_{1P} is the wavelength needed to promote a fluorescent molecule to the excited state in single-photon mode. The wavelengths of the two simultaneously absorbed photons do not have to be necessarily the same but usually are for practical reasons (as they come from the same excitation light source)

$$\lambda_A = \lambda_B \approx 2\lambda_{1P}$$

Equation 1.19

In 1961, the first two-photon excited fluorescence emission in a CaF_2:Eu^{2+} crystal was demonstrated by Kaiser and Garrett[114]. In 1990 Denk and his team were the first to apply this technology to scanning laser microscopy and introduced it to biological applications[27]. Since then, TPEF microscopy has become a powerful tool for biological research and live sciences for non-invasive fluorescence microscopy of thick tissues and live animals with still unexplored potential[115].
Two-photon excitation efficiency is several orders of magnitude lower than single-photon excitation and is confined to a small region where the light is sharply focused. The intensity of two-photon fluorescence is related to the number of photons absorbed per fluorophore (n_{abs}), which depends on multiple factors, such as the square of the power of incident light (P_{avg}) and the two-photon absorption cross-section for the fluorophore (σ), the pulse width (τ_p) and the pulse repetition rate of the laser (f_p). The objective lens is used to focus the light onto the sample and parameters such as the NA and wavelength of incident light (λ_{exc}) also determine the efficiency of two-photon absorption. Thus, the probability of two photons absorbed per unit pulse per fluorophore is given by[27]

$$n_p \approx \sigma \frac{P_{avg}^2}{\tau_p f_p^2} \left(\frac{NA^2}{hc\ \lambda_{exc}}\right)^2$$

Equation 1.20

where h is Planck's constant and c speed of light. Dispersion is a phenomenon in which the phase velocity of a wave is coupled to its frequency resulting in wavelength dependent refractive indices in optical media. The laser pulse duration is inversely proportional to the two-photon signal generation; reducing the laser pulse duration would result in increased two-photon signal generation. In practice, however, short pulses lead to higher dispersion which must be compensated. The temporal profile of the laser pulse is directly related to its spectral bandwidth. Therefore, shorter pulses are more

vulnerable to dispersion effects leading to broadened pulses and less efficient two-photon excitation if not compensated[116, 117].

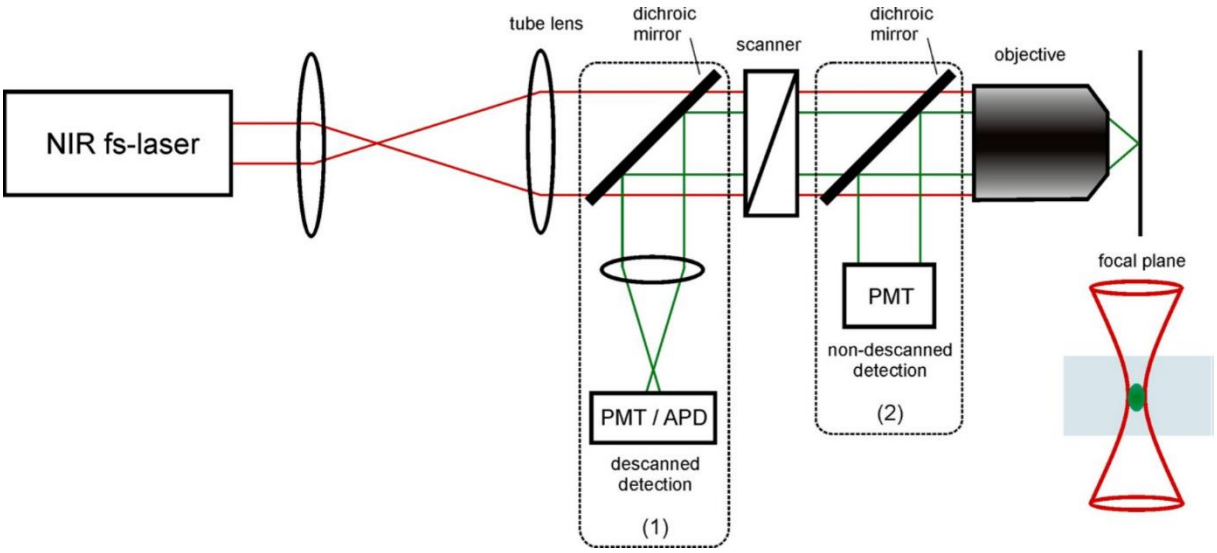

Figure 1.14. Basic two-photon excited fluorescence microscope setup, showing the excitation (red) and fluorescence emission (green) paths for both descanned (1) and non-descanned (2) detection. The fluorescence emission is intrinsically localized to the vicinity of the focal spot[71].

The considerable impact of TPEF microscopy is mainly derived from its unique property of localized excitation, which leads to new imaging characteristics that are both qualitative and quantitative. As the emission of two-photon fluorescence is quadratically dependent on the excitation intensity, two-photon absorption is only confined to the vicinity of the focal plane where the light intensity is highest. This in contrast to single-photon fluorescence, where absorption occurs through the entire illumination cone even while only imaging a single plane. The use of TPEF microscopy is beneficial for bioimaging applications because of its unique property of localized excitation. This results in several advantages such as intrinsic 3D diffraction-limited resolution that allows for optical sectioning in thick tissues without the need for a confocal pinhole to filter out-of-focus background fluorescence. Additionally, wide-field detectors can be used in combination with a non-descanned optical emission path for higher collection efficiency in scattering tissues, as all fluorescence photons that originate from the focal plane are considered useful signal[118]. Furthermore, the use of NIR light improves the penetration depth of the illumination light in thick biological samples, up to one millimeter[119], due to less scattering and absorption outside the focal plane[120, 121]. The use of NIR excitation light also allows access to a range of fluorescent indicators that would otherwise require ultraviolet (UV) lasers for single-photon excitation in combination with specialized UV optics.

In TPEF microscopy, photobleaching and photodamage may occur in the focal plane where photo interaction takes place, and consequently, tissue viability is increased. However, due to the lack of efficient single-photon endogenous cellular absorbers in the spectral range from about 700 nm to 1100 nm, NIR TPEF microscopy is considered less phototoxic[122] compared to single-photon fluorescence microscopy allowing for imaging of living organisms over extended periods without compromising viability[123].

The basic setup of a TPEF microscope is shown in Figure 1.14. Like in confocal laser scanning microscopy, the focused excitation laser beam is raster scanned across the specimen. However, due to the nonlinear character of the excitation, the fluorescence is only emitted from a thin focal plane, and spatially resolved detection is not required. This means that a confocal pinhole before the detector is not needed. A dichroic mirror

is used to spectrally separate excitation and emission light. The large spectral separation gap between excitation and fluorescence emission allows for efficient signal collection and simplifies the detection of multiple fluorophores in the same sample. The absence of a confocal pinhole makes several epifluorescence detections schemes possible: In Figure 1.14(1), the fluorescence signal is descanned and projected to a point detector that can be a PMT or an APD, which has higher quantum efficiencies than conventional PMTs and are favorable at low fluorescence levels[124].
This setup allows for the implementation of an optional detector pinhole, which can improve resolution but also reduces signal strength, a trade-off that is not typically desirable in TPEF microscopy, where emitted photons are often scarce. Additionally, the optical path is simplified and superior fluorescence collection for deep tissue imaging is achieved through non-descanned detection (Figure 1.14(2)). The emitted radiation is collected without passing through the scanning mirrors using a large-area PMT. As a result, ballistic and scattered photons collected by the objective reach the detector, contributing to the overall acquired signal. In confocal microscopy, axial sectioning can be improved by spatially filtering the emitted fluorescence signal at the detection plane. However, this also reduces fluorescence yield as fluorescence photons suffering from chromatic aberrations and strong scattering are blocked and cannot reach the detector[115]. In contrast, axial and lateral confinement in TPEF is an intrinsic property of the nonlinear excitation process, eliminating the need for spatially filtering the signal with a pinhole.
In TPEF, the effective point spread function (PSF_{TP}) can be described by the square of the illumination[125] (PSF_{ill})

$$PSF_{TP} = (PSF_{ill})^2 \approx PSF^2\left(\frac{v}{2}, \frac{u}{2}\right)$$

Equation 1.21

with $v = k(NA)r$, $u = k(NA)^2 z$ and assuming $\frac{\lambda_{ill}}{2} \approx \lambda_{fl}$, v/2 and u/2 denoting an about doubled illumination wavelength in contrast to single-photon excitation.

Considering full illumination of the back aperture of the microscope objective (beam diameter > back aperture diameter), the diffraction-limited resolution for TPEF can be approximated by the FWHM of a Gaussian fit to the squared illumination PSF. Lateral (Δr) and axial fitted (Δz) squared intensity PSF profiles are described as follows[110, 111]

$$\Delta r = \begin{cases} \dfrac{0.320\sqrt{2ln2}\lambda}{NA}, & NA \leq 0.7 \\ \dfrac{0.325\sqrt{2ln2}\lambda}{NA^{0.91}}, & NA \geq 0.7 \end{cases}$$

Equation 1.22

$$\Delta z = 0.532\sqrt{2ln2}\lambda\left(\frac{1}{n - \sqrt{n^2 - NA^2}}\right)$$

Equation 1.23

where NA is the numerical aperture of the objective lens, λ the excitation wavelength, and n denotes the refractive index of the immersion medium.

1.5.3 Retinal Light Damage

Light is necessary for vision, but it can also cause damage to the eye. The retina is particularly vulnerable to injury from radiation due to its imaging characteristics. Hazardous retinal effects can occur from optical radiation in the visible and NIR regions as it is transmitted through the ocular media with little loss of intensity, which is also referred to as the retinal hazard region. Wavelengths outside of this spectral band are primarily absorbed in the cornea and lens. Therefore, special considerations on laser safety play an essential role in applying light non-invasively to the eye.
Laser-induced damage may occur due to interactions of heat, thermoacoustic transients, photochemical processes, and non-linear effects. The degree of damage may also depend on wavelength, pulse duration, image size, irradiance, and radiant exposure. Absorption of optical radiation is considered one of the main reasons for laser-induced damage to tissue. For example, when intense light is focused on the retina, melanin granules of the RPE absorb most of the optical radiation reaching the retina. Melanin is the optically most dense absorbing layer, making RPE the most sensitive and vulnerable site upon radiation exposure. The retina absorbs very little radiation in the NIR range compared to visible light, reducing the relative effectiveness of causing retinal injury. Absorption happens at an atomic or molecular level and is specific to wavelength, and thus the wavelength determines which tissue a particular laser beam is liable to damage[126].
Photothermal damage occurs due to the transfer of radiant energy, or photons, from light to retinal tissue. As previously discussed, molecules can transition from the ground state (lower energy) to the excited state (higher energy) by absorbing photons with an energy equal to the energy difference between the excited and ground state. Molecules' vibrational and rotational quantum states predominate over excitation states for longer wavelengths in the visible spectrum and near-infrared (600-1400 nm). This increase in mean kinetic energy is dissipated as molecules collide and their temperature increases[127-129]. The ability of light to cause an increase in mean kinetic energy is inversely proportional to the wavelength of the light and is described by equation 1.17. The shorter the wavelength, the higher the temperature for a given exposure time. Irreversible retinal thermal damage typically occurs if the ambient temperature in the retina is raised by at least 10°C. Cells may undergo apoptosis secondary to lower-level thermal damage (55-58°C), apoptosis and necrosis for more severe levels of thermal damage (60-80°C), and immediate cell death secondary to more severe thermal exposure (72°C or higher). Thermal damage can cause denaturing of proteins, loss of molecular tertiary structure, and fluidization of membranes on a cellular and molecular level[130, 131]. Thermal damage tends to occur in the visible spectrum's blue, green, and red regions and depend on the chromophore's absorption spectrum[132]. Melanin, the most effective RPE absorber, will more readily absorb photothermal energy. The most common clinical example of photothermal damage to the retina is laser treatments such as transpupillary thermotherapy, laser photocoagulation, and micro-pulse diode laser. These laser treatments are used for various disease states, including diabetic retinopathy, retinal oedema, retinopathy of prematurity, tumors of the choroid and retina, retinal tears, and retinal detachments.
Photomechanical damage denotes tissue damage due to mechanical compressive or tensile forces generated by energy's rapid introduction into the RPE melanosomes. Photomechanical damage is believed to be caused by high irradiances in the range of megawatts or terawatts per cm squared and exposure times in the range of nanoseconds to picoseconds. The introduction of energy occurs more rapidly than the relaxation time needed to relieve the mechanical stress produced in the tissue by

thermoelastic expansion, resulting in micro cavitation bubbles, which are toxic to the RPE and other cells. These compressive and tensile forces generate sonic transients or shock waves that can also result in permanent damage to the RPE or photoreceptors. The amount of damage is related to the delivery rate and energy absorbed[129, 133-141]. The most common clinical application of photomechanical damage in ophthalmology is radiation from the Nd: YAG laser, typically used to create an iridotomy in patients with closed-angle glaucoma or cause retraction of an opacified posterior lens capsule in patients after cataract surgery.

Photochemical damage is the most probable cause of hazards by ophthalmic instruments[142-144] and is the most widely studied light damage due to its ability to cause damage under ambient conditions. The damage occurs when a photosensitizer absorbs the light, that is, a chromophore, which upon photoexcitation to photoexcited singlet state undergoes intersystem crossing and forms a transient excited triplet state. The excited triplet state is long-lived, allowing for interaction with other molecules producing free radicals or singlet oxygen energy from the photosensitizer in the triplet state to molecular oxygen. Photochemical damage demonstrates delayed onset following light exposure; in the retina, this delay may be several hours. Retinal photochemical damage can be of two types depending on the action spectra, duration of exposure, and the irradiance energy required to cause the damage[145]. The first type of damage corresponds well with the absorption spectrum of the visual pigments. On the other hand, the action spectra of light damage to the retina under conditions where rhodopsin is completely bleached suggest that there is a shift in the site of damage from the outer rod segment at short wavelengths to the pigment epithelium at longer (>470 nm) wavelengths[146, 147], suggesting that there are at least two other mechanisms responsible for photodamage. The second type of damage is considered to originate in the RPE[148, 149] and appears to correlate with endogenous melanin and lipofuscin granules. Since such damage occurs at the shorter wavelength end of the visible spectrum, it is often referred to as ‘blue light damage.’ Furthermore, this second type of damage appears to be oxygen dependent.

There are several methods for assessing light damage[150-152]: psychophysical (reduction in visual field, color defects), electroretinographic (reduction in rod function), physiological (e.g., disruption of the blood-retina barrier), morphological (e.g., mitochondrial swelling, aggregation of melanosomes observed as hypopigmentation, disorganization of the RPE layer, apoptosis of photoreceptors and RPE cells) and biochemical (e.g., loss of rhodopsin, decreased activity of several enzymes, oxidation of retinal proteins, lipid peroxidation, and loss of docosahexaenoic fatty acids).

Nonlinear effects can also cause laser-induced damage. With the introduction of pulsed lasers in ophthalmology, the short-pulsed with high peak-power (i.e., Q-switched, or mode-locked lasers) may give rise to tissue damage with a different combination of induction mechanisms. The energy is delivered in a short time with high irradiance, resulting in rapid temperature rise that converts the liquid components of their cells to gas. In most cases, these phase changes are so rapid that they are explosive, and the cells rupture. Short pulses produce photoacoustic damage (< 1 ns) and are associated with various nonlinear mechanisms such as laser-induced optical breakdown, self-focusing, and two-photon absorption leading to blue light injury radiation which further reduces the energy level to cause retinal injury compared to longer pulse durations[126]. Furthermore, other nonlinear optical mechanisms play a role in retinal injury in the sub-nanosecond region.

Laser safety thresholds limit the maximum level of exposure of the eye to laser sources. There are several guidelines established for the safe use of lasers by the International Commission on Non-radiation Protection (ICNIRP)[153], the International

Electrotechnical Commission (IEC)[126], and the American National Standards Institute (ANSI)[154], International organization for standardization (ISO). These guidelines assist with protection against laser hazards. For example, the ANSI standards define an MPE value in units of radiant exposure (J/cm^2) or irradiance (W/cm^2) for direct ocular exposure to optical radiation without adverse effects. It is based on the best knowledge available from actual biological injury thresholds gained from numerous experimental studies (mainly on monkeys and rabbits) that incorporate the above injury considerations for different combinations of exposure (interaction) duration, wavelength, and retinal spot size in a conservative way.

1.6 Thesis Synopsis and Outline

This thesis presents two methods for improving the quality of retinal images: confocal retinal imaging with phase plates and two-photon retinal imaging. Current clinical instruments often have limitations in resolution and contrast, which makes it difficult to visualize small structures and details within the retina, leading to challenges in diagnosing and treating retinal diseases. To address these limitations, the thesis evaluates the use of a custom phase plate to compensate for ocular aberrations and improve image quality and conducts basic research on animal models using two-photon imaging to provide high-resolution images at a cellular level with less photo-damage. Additionally, the thesis evaluates the feasibility of two-photon retinal imaging with regards to laser safety and studies the effects of ultrashort pulsed lasers on retinal tissue.
This thesis is organized as follows:
Chapter 2 deals with the design and technical implementation of phase plates in a cSLO. The focus is on the establishment of a compact custom phase plate to compensate for the aberrations of the human eye and the evaluation of image quality and aberration compensation.
Chapter 3 evaluates the improvement in retinal imaging at a microscopic scale using phase plates on both mydriatic and non-mydriatic eyes. The retinal images with phase plates are compared to those obtained using adaptive optics systems, and the limits of retinal imaging and aberration compensation with phase plates are determined.
Chapter 4 presents TPEF retinal imaging in animal models, including the use of autofluorescence imaging with two-photon excitation and simultaneous two-photon fluorescein angiography and indocyanine green angiography to characterize retinal and choroidal vessels.
Chapter 5 evaluates the effects of a two-photon laser (ultrashort pulse) on the retina, using rat retinas at various laser exposure levels and with different laser parameters. The results are verified using confocal reflectance imaging, two-photon fluorescein angiography, immunohistochemistry, and are correlated to the IEC 60825-1 laser safety standard.
Chapter 6 summarizes the findings of this work and their implications.

It should be noted that certain sections of this thesis have been paraphrased from previously published self-publications[155-158] at the time of submitting this thesis.

2 CUSTOM PHASE PLATES FOR ABERRATION COMPENSATION

In this chapter, we present a novel and cost-effective adaptive optics unit that utilizes custom phase plates to correct ocular aberrations and enhance image quality in clinical scanning laser ophthalmoscope (cSLO) devices. The human eye is not a perfect optical system and suffers from various aberrations that can degrade image quality and visual performance. Wavefront sensing techniques have led to a deeper understanding of the effects of wavefront aberrations on visual performance, and it has been shown that correcting HOAs improves visual performance and retinal image quality. Conventional eyeglasses and contact lenses can only correct lower-order aberrations, but not HOAs. Our proposed technique utilizes a phase plate designed with Zernike polynomials to correct both lower and HOAs in the human eye with a single plate. We also demonstrate how these phase plates can be integrated into a clinically available cSLO device.

2.1 Materials and Methods

This study aimed to evaluate the use of custom phase plates for compensating ocular aberrations and improving image quality in cSLO devices. The study was conducted at the Medical Faculty Mannheim and Heidelberg Engineering laboratories, and consisted of the following phases:

Phase 1: The ocular aberrations of five volunteers were measured using a commercial aberrometer (iDesign, Abbott Medical Optics Inc., USA) by a trained clinician at the Eye clinic Heidelberg, Germany (Augenpraxisklinik Heidelberg, Germany). Zernike coefficients were used to simulate the effect of aberrations on image quality and its compensation using Zemax (OpticStudio, ANSYS Inc., USA) software. The PSF, MTF, and wavefront compensation were simulated and evaluated to understand the effect of aberration compensation with phase plates.

Phase 2: Phase plates were fabricated with the measured ocular aberrations by Smart Micro-optical Solutions (SMOS), Walldorf, Germany. The PSF, MTF, and wavefront compensation were measured from the phase plates using an optical bench setup. The data were then compared to the computationally simulated measurements with Zemax to validate the effectiveness of the manufacturing process.

Phase 3: The lower-order aberrations compensation with phase plate was evaluated by producing a phase plate compensating only for astigmatism to evaluate the performance and manufacturing process.

Phase 4: The positioning of phase plates for retinal imaging is crucial for aberration compensation, and this was evaluated using a cSLO. A compact compensation unit with phase plates for retinal imaging was established.

Phase 5: The ocular aberrations were evaluated using three different ocular aberrometers to find the optimal aberrometer for producing the phase plate. The measurements were compared and analyzed between the three aberrometers.

2.1.1 cSLO with High-Magnification Objective Lens

cSLO is a non-invasive imaging technique that scans the retina with a laser beam, enabling high-resolution retinal imaging. The cSLO principle is explained in detail in chapter 1. The cSLO device used in this study is the SPECTRALIS from Heidelberg

Engineering GmbH, Heidelberg, Germany. This device can be used for conventional fundus imaging as well as ultra-widefield retinal imaging by simply changing the objective lenses. In this study, the cSLO was used with a high-magnification objective (HMO) lens which has an 8° FOV as shown in Figure 2.1. The laser beam diameter of the standard objective is 3 mm, the HMO lens is 6 mm, and the working distance is 25 mm and 54 mm, respectively. The standard objective lens is most commonly used in clinics for fundus imaging.

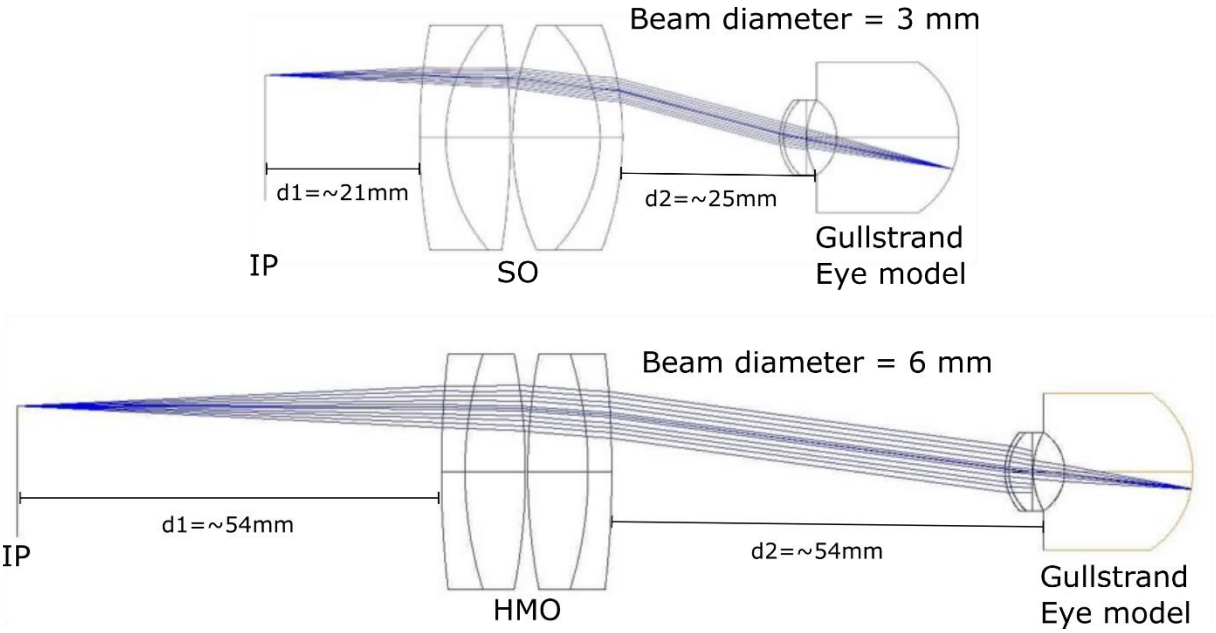

Figure 2.1. Overview of SPECTRALIS standard objective (f = 30 mm, maximum scan angle 30°) and HMO lens (f = 60 mm, maximum scan angle 8°). IP- Intermediate image plane, SO- SPECTRALIS standard objective lens, HMO- high-magnification objective, d1- distance from the intermediate plane to objective lens, d2- distance from the objective lens to the scan pupil

2.1.2 Measurement of Ocular Aberrations

Table 2.1. Ocular measurements

Volunteers	Pupil Diameter (mm)	Defocus (µm)	Astigmatism (µm)	HOAs (µm)
V1 (OD)	6.68	1.85	0.77	0.48
V2 (OD)	7.58	1.62	0.36	0.52
V3 (OS)	5.59	-0.59	0.41	1.45
V4 (OD)	7.18	5.52	2.17	0.78
V5 (OD)	7.91	21.84	1.28	0.43

As described in chapter 1, the wavefront technique allows for precise measurement of optical aberrations in the human eye. Clinically available aberrometers can be used to measure the ocular aberrations of an eye (Table 2.1) and produce a customized phase plate. In this study, we used a commercially available aberrometer, the iDesign from Abbott Medical Optics, USA. This instrument combines aberrometer and corneal topography measurements and the wavefront sensor component is a Shack-Hartmann wavefront sensing type. The ocular aberrations measurements were performed at the

Eye clinic Heidelberg (Augenpraxisklinik Heidelberg, Germany) by trained physicians who dilated the pupils for the aberration measurements. Using the measured ocular aberrations (Zernike coefficients), a customized phase plate was produced.

2.1.3 Custom Phase Plate with Zernike coefficients

The phase plate is a custom wavefront-optimized lens that compensates for wavefront aberrations. By compensating for the aberrations of the optical system and the human eye, diffraction-limited imaging can be achieved, significantly improving the image quality. The phase plates are produced using a "mask structured ion exchange (MSI)" technique and manufactured based on the Zernike coefficients of the measured ocular aberrations (as shown in Figure 2.2). The phase plate is the inverse of the aberrated wavefront and will make the aberrated wavefront flat. Figure 2.3 illustrates how the phase plate can compensate for aberrations and result in a flat wavefront.

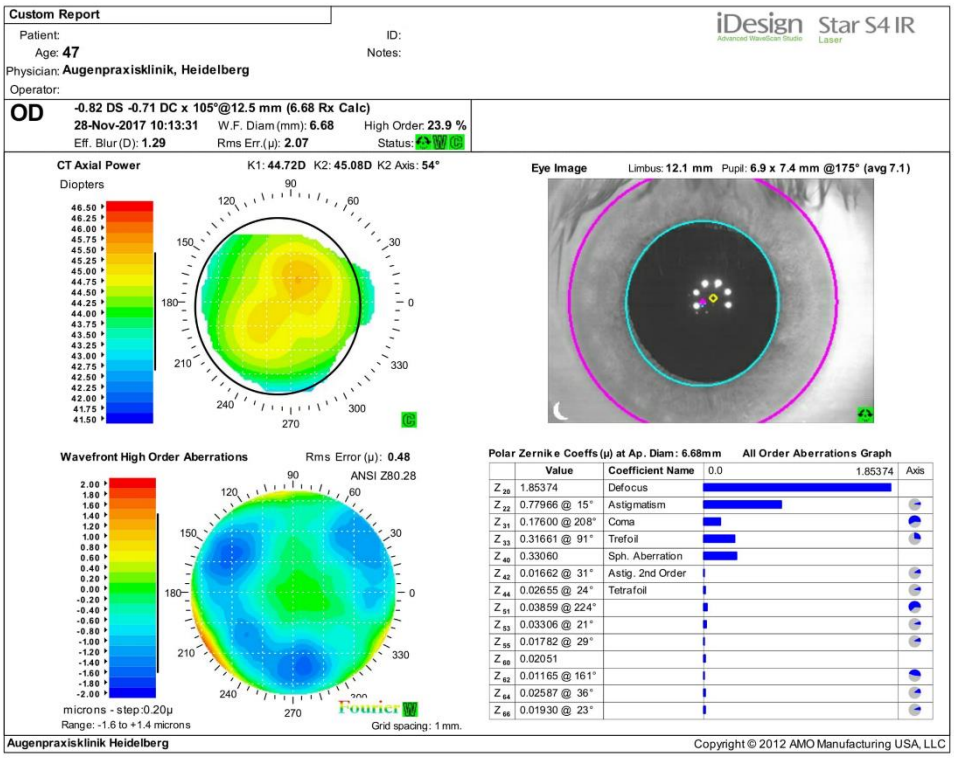

Figure 2.2. Custom report of ocular aberrations measurement from a volunteer with iDesign.

For this study, the phase plates were manufactured by SMOS, Walldorf, Germany, using MSI technology. The manufacturing process is a "One-to-One" procedure where the wafer plate has a dimension of 4 inches, and the mask is of a similar size. The mask is patterned with approximately one hundred different patterns, one distinct for each customized phase plate. The metal mask is written with a laser-writer and processed in a microlithographic procedure. The overall mask-writing process takes 4.5 hours. Then, the mask is positioned in front of the wafer plate inside the oven, and the ion-exchange process takes place. The procedure lasts 24 hours, including cutting and mounting the phase plates.
The size of the phase plate is 10 x 10 mm, with the aberration compensation zone (or active zone) of 8 mm (circular) and a thickness of 2 mm (Figure 2.4). Most aberrometers can measure the aberrations over 2 to 7 mm pupil diameter, and in this case, the

active area of 8 mm is extended with the Zernike coefficients from the border. For instance, if the ocular aberrations are only measurable for a 6 mm pupil diameter, then the phase plate will have a 6 mm active zone in the center, which will represent the ocular aberrations, and the remaining 2 mm of the active zone will be filled with the Zernike's value at the 6 mm border. The laser beam diameter of the HMO lens is 6 mm, and outside the 6 mm would not affect the beam path unless the phase plates are misaligned.

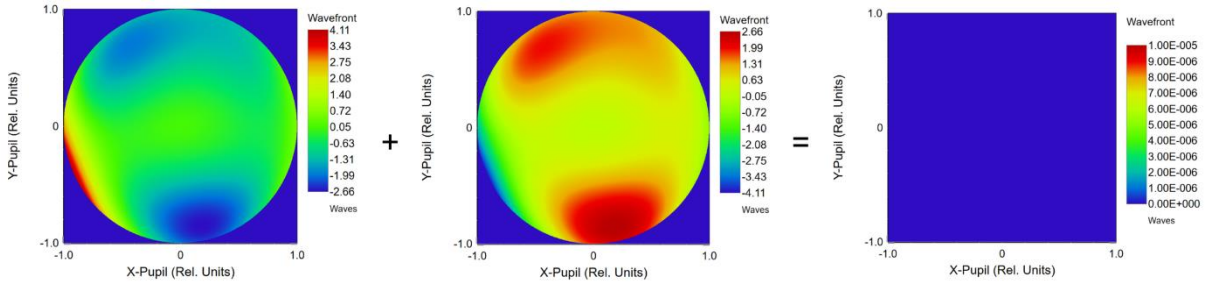

Figure 2.3. Wavefront compensation with phase plate. Wavefront map of the aberrated eye (left image), wavefront map of the phase plate (middle image), and the resulting wavefront map (right image)

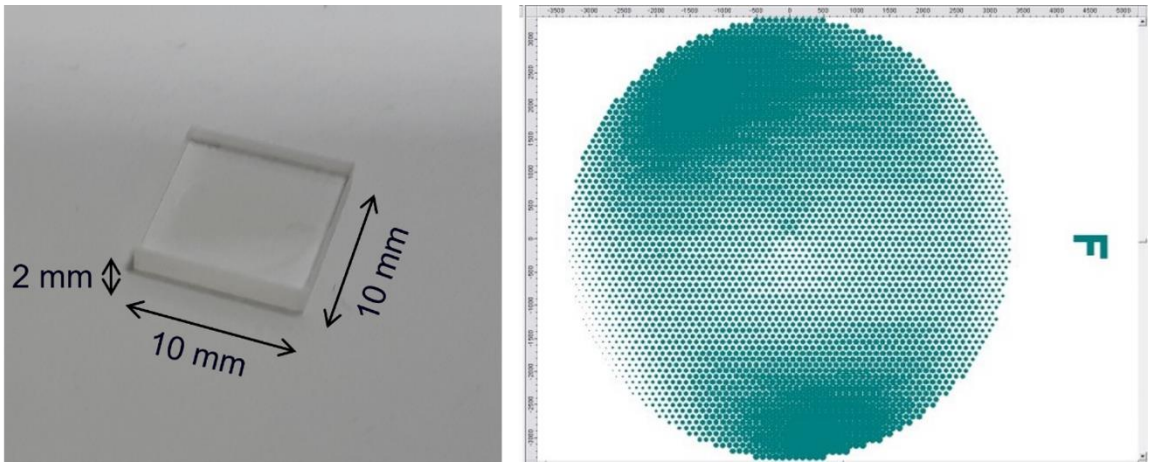

Figure 2.4. Photograph of the phase plate (a). Wavefront map on the phase plate (b). “F” marking on the phase plate indicates the axis of the eye at 0 degree.

2.1.4 Mask Structured Ion Exchange Technique

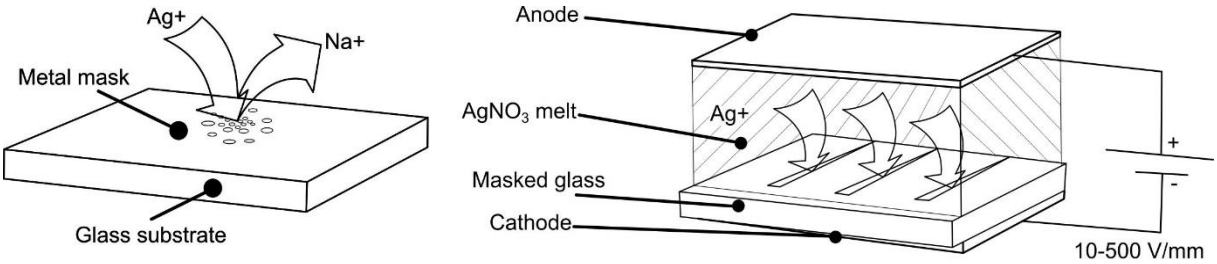

Figure 2.5. Mask structured ion exchange technique. A thermal diffusion: exchange of Na^+ by Ag^+ ions (left image), field-assisted process: Ag^+ ion current (right image)[159]

In most cases, traditional mechanical methods known as micro-optics (i.e., milling or lapping) are not suitable for creating microstructures and, particularly, micro-optical elements below a certain size. In the sub-millimeter range and down to the size of several tens of microns, most processes are applied by using natural micro forces to self-organize matter in a specific manner.

The mask structured silver-sodium ion exchange in glass is a powerful method for creating high precision refractive micro-optical components. The MSI technique is used to produce the phase plates. A planar glass substrate is covered with a titanium layer on both sides. One side is structured using a photolithographic process to create well-defined apertures for the ion migration into the glass material, while the other side remains unstructured. The diffusion process takes place in a melt of $AgNO_3$, where silver ions exchange with sodium ions from the melt (Figure 2.5 left image). For the field-assisted process (Figure 2.5 right image), an additional electric field is applied between the silver salt melt (anode) and the bottom of the glass (cathode), which affects a current of silver ions into the glass[159].

2.1.5 Measurement of a Phase Plate

The wavefront sensor (SHSLab, Optocraft GmbH, Germany) with the SHSworks software (Version 11.021.4) was used to verify the phase plates and the aberration compensation. Each phase plate was fixed in a customized 3D-printed phase plate holder and an optical rail. The wavefront map, PSF, and MTF of the aberration plate and the compensation plate were measured individually at first. Then, the aberration compensation was measured by positioning the aberration plate and the compensation plate together in the optical path (Figure 2.6). The aberration plate adds eye aberrations to the imaging beam, while the compensation plate counteracts these aberrations with their inverse. A stationary laser beam without scanning was used in this setup to measure the wavefront, PSF, and MTF.
Likewise, an USAF target with an eye model was used to determine the improvement in image quality with phase plates (Figure 2.7). In this setup, a scanning laser was used with an artificial eye model with an USAF target.

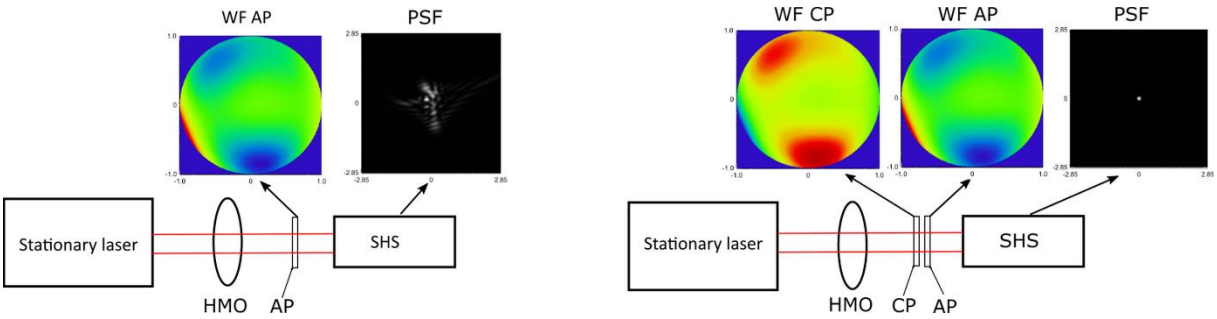

Figure 2.6. Measurement of aberration plate (left image) and with compensation plate (right image) with SHS. HMO- high-magnification objective, AP- aberration plate, CP- compensation plate, WF- wavefront, PSF- point spread function, SHS- Shack-Hartmann sensor.

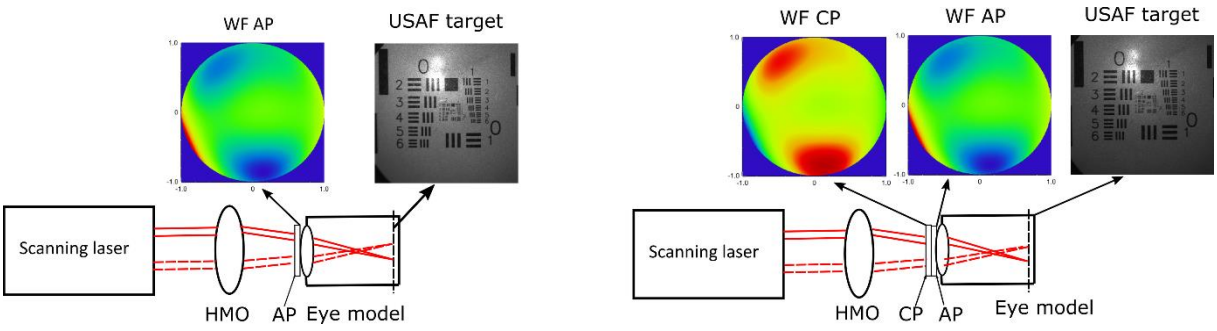

Figure 2.7. Image quality measurement with the USAF target. The aberration plate introduces aberrations in the imaging beam (left image), and with the compensation plate, the induced aberrations are compensated (right image)

2.2 Results

2.2.1 Evaluation of Phase Plate through Zemax Simulation

With the measured ocular aberrations, the Zemax simulations were carried out to characterize the effect of aberration compensation using phase plates. The simulations were performed on the ocular measurements to evaluate the impact of a phase plate in correcting ocular aberrations. One example is demonstrated in this section. The Zernike coefficients from the iDesign measurement were used to simulate the wavefront map, PSF, and MTF in Zemax. The piston, tilt and defocus are avoided for the simulation study since the piston and tilt correspond to lateral displacements of the image rather than the image degradation. The wavefront map simulated in Zemax is shown in Figure 2.8 and is compared to the aberrometer measurement. The RMS error value and the wavefront map from the Zemax simulation match the aberrometer measurement. Figure 2.9 shows the corresponding PSF and MTF of the eye before and after aberration compensation. The PSF and MTF clearly show that the aberrations severely impact the imaging quality, and there will be a significant improvement if these aberrations are compensated.

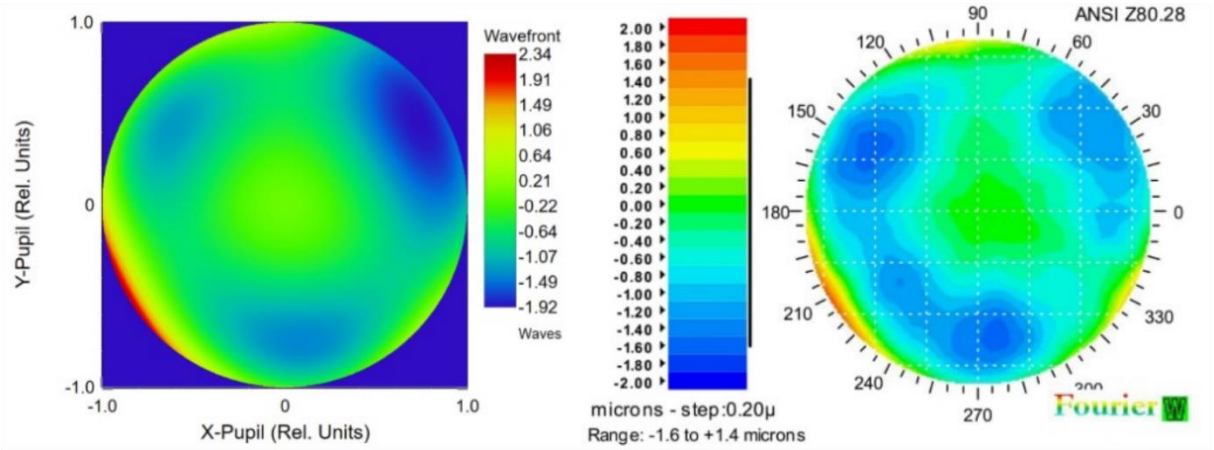

Figure 2.8. Zemax simulation of wavefront map with HOAs without defocus and astigmatism (left image). Wavefront map of HOAs from aberrometer (right image). RMS = 0.48 microns

2.2.2 Assessment of Aberration Compensation through Bench Testing

An aberration plate and a compensation plate were produced for three volunteer eyes to assess the aberration compensation. The aberration plate comprises the Zernike coefficients of the eyes aberration and introduces aberrations to the imaging beam (reflects eye aberrations). The compensation plate includes the inverse of the eyes aberration and compensates for aberrations induced by the aberration plate. The wavefront sensor and the SHSworks software were used for the bench test. Using the Shack-Hartmann sensor (SHSLab) at 815 nm wavelength, the wavefront map, PSF, and MTF of the aberration plate and the compensation plate were measured individually at first. Then the aberration compensation was measured by positioning the aberration plate and the compensation plate together in the optical path (Figure 2.10). The aberration and compensation plate were placed apart at approximately 15 mm, which is expected to resemble the retinal imaging condition in subjects. One example is shown in Figure 2.10 (Volunteer 1), which illustrates the reduction of ocular aberrations by the customized phase plate. However, residual aberrations were noticed in the bench test. The RMS error of the aberration plate, measured with SHS, was 0.56 microns. After adding the compensation plate (0.43 microns) to the optical path, the RMS

decreased to 0.08 microns, corresponding to ~85% of compensation. The amount of aberration compensation with phase plates in test eyes is shown in Table 2.2, and the Strehl ratio was calculated with a simple empirical expression, $S = [1 - 2(\pi\omega)^2]^2$ where ω is the RMS deviation of the measured wavefront in wavelengths.

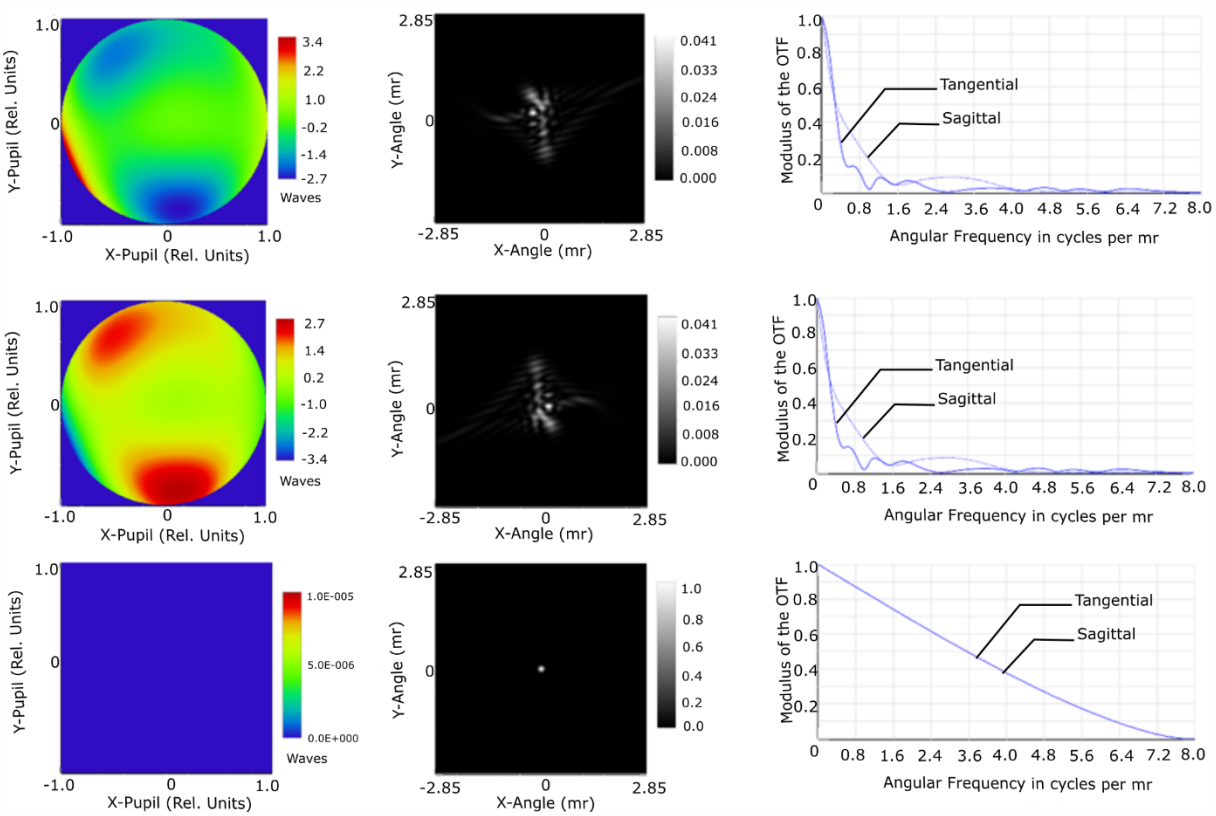

Figure 2.9. Simulation of wavefront maps (left column), PSFs (middle column), and MTFs (right column) in Zemax. Wavefront map, PSF, and MTF of an aberrated eye (top row), phase plate (middle row), and the result of aberration compensation (bottom row).

Table 2.2. Aberration compensation through phase plates

Volun-teers	Eye data		Rescaled to 5 mm PD	Aberration plate RMS (μm)	Compensation plate RMS (μm)	Residual RMS (μm)	Strehl ratio
	PD (mm)	RMS (μm)	RMS (μm)				
V1 (OD)	6.68	0.92	0.47	0.56	0.43	0.08	0.76
V2 (OD)	7.58	0.61	0.25	0.24	0.26	0.07	0.82
V3 (OS)	5.59	1.44	1.26	1.15	0.87	0.41	< 0.05

* The table shows RMS values based on the measurement of astigmatism and HOAs only and excludes defocus and tilt. The eye measurements were taken using commercial aberrometers, while the aberration plate and compensation plate were measured using a SHS in a laboratory setup. The phase plate measurements were taken with an approximate pupil size of 5 mm, and the rescaled RMS values of the eye measurements are also included in the table. PD- Pupil diameter, RMS- Root mean square.

From Table 2.2, it can be seen that the aberration compensation with phase plate is effective for volunteers 1 and 2. However, for volunteer 3, only minor improvement was noticed due to inaccuracies in the RMS values of the aberration and compensation plates. The RMS of the compensation plate for volunteer 3 was 0.87 microns, while

the RMS of the aberration plate was 1.15 microns. This discrepancy in the RMS values was identified during this phase of the study and reported to the phase plate manufacturer for further optimizations.

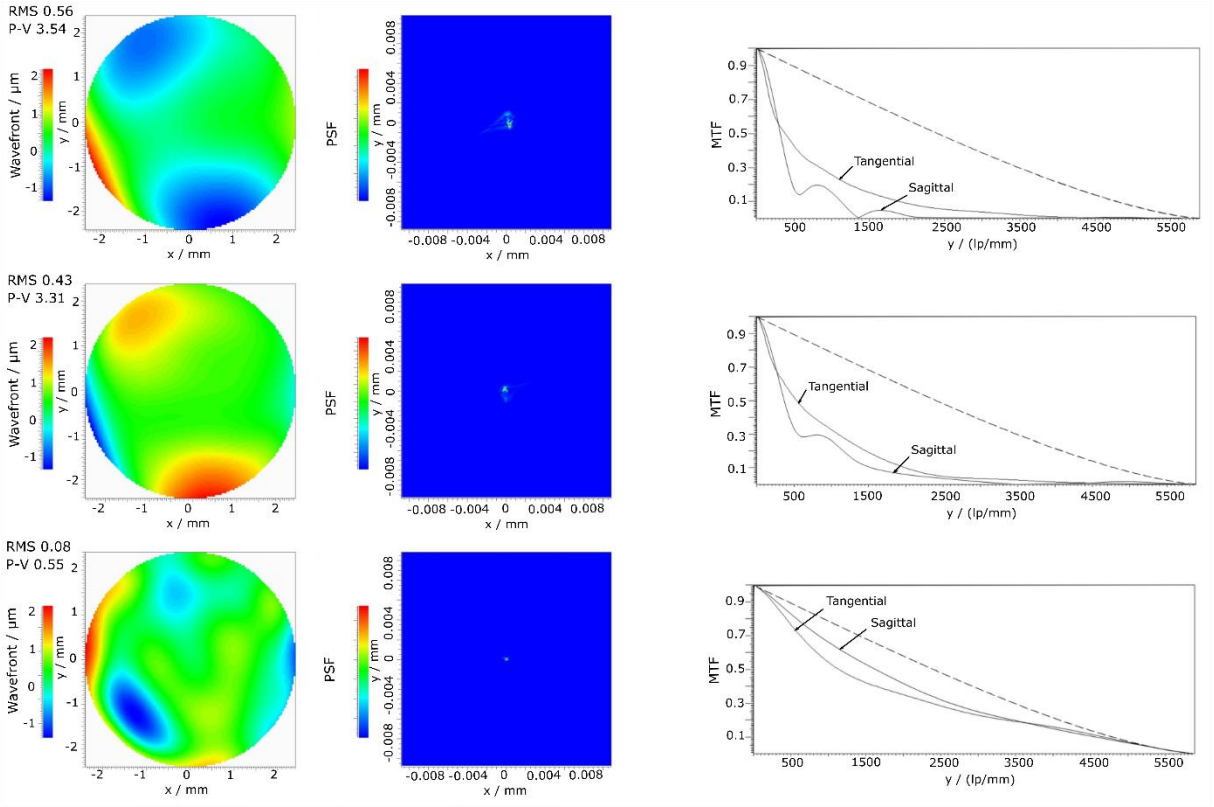

Figure 2.10. Wavefront map (left column), PSF (middle column), and MTF (right column) of aberration plate (top row), compensation plate (middle row), and the result of aberration compensation (bottom row) measured with SHS.

2.2.3 Image Quality Assessment through Bench Testing

The cSLO with HMO lens was used to measure the impact of the image quality with the use of a USAF target and an eye model. The aberration and compensation plates as mentioned in section 2.1.5, were used in this test. An example of the test results is shown in Figure 2.11. At first, the USAF target was acquired with the cSLO (Figure 2.11b), and then the target image was acquired by adding the aberration plate (V3, RMS- 1.15 microns) in front of the eye model. The aberration plate introduced wavefront aberrations, and the image acquired after adding the aberration plate was distorted (Figure 2.11c). Later, the compensation plate (V3, RMS- 0.87 microns) was positioned next to the aberration plate at approximately 15 mm apart to compensate for the induced aberrations. After the insertion of the compensation plate, an improvement in image quality was noticed (Figure 2.11d). It is clear from the results (Figure 2.11) that the eye aberrations have a significant impact on image quality, and better image quality can be achieved with aberration compensation. The numbers on the target can be read more easily after aberration compensation (Figure 2.11d), and the resolving power of the USAF target was improved from 4.49 lp/mm (Figure 2.11c) to 10.08 lp/mm (Figure 2.11d) with the use of compensation phase plates. The intensity profiles (Figure 2.11f, 2.11g, and 2.11h) also show an increase in gray value after aberration compensation, which indicates an improvement in contrast. The gray value refers to the intensity values of the pixels and the contrast of an image can be inferred from the gray values. A significant improvement, in contrast, is noticed after compensating for the

aberrations with a compensation plate. However, the image quality was better with HMO lens (Figure 2.11b) than after aberration compensation (Figure 2.11d). This could be due to differences between the RMS value of the aberration plate and the compensation plate. To avoid this in the future, the manufacturing process for the phase plates will be improved in the next set of plates, as communicated with the phase plate manufacturer. The aberrations present in the eyes of volunteers 1 and 2 were too minimal to determine any improvement in image quality.

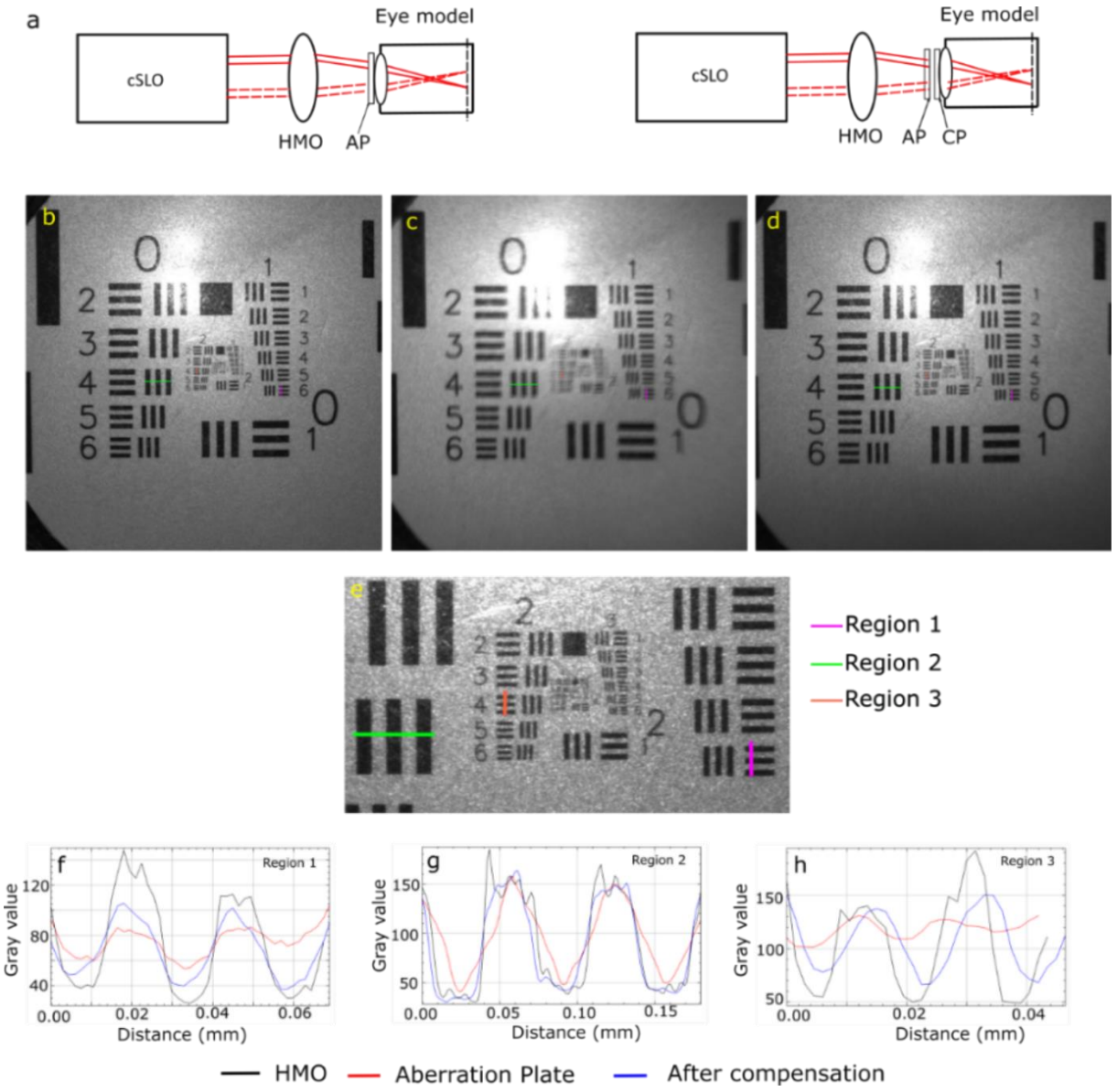

Figure 2.11. Schematic setup of cSLO with HMO lens, phase plate, and eye model to evaluate the image quality (a). USAF target image with cSLO (no plates) (b), aberration plate (c), and after adding compensation plate (d). Zoom-in image (e) of (b) shows three regions (pink, green, and orange). Intensity profiles in three areas pink (f), green (g), and orange (h). AP- Aberration plate, CP- Compensation plate

2.2.4 Measurement of Lower-Order Aberrations Using Phase Plate

The lower-order aberrations for retinal imaging can be compensated with eyeglasses in a clinical routine, but these eyeglasses can introduce artifacts. To avoid these artifacts, phase plates that only compensate for lower-order aberrations can be beneficial. A bench test was conducted to verify that the phase plate can be produced equivalent to the measured RMS. The results from sections 2.2.2 and 2.2.3 were communicated

to the phase plate manufacturer, and improvements in the manufacturing processing was requested. Here, a simple phase plate with only astigmatism of 2.17 microns at a 97-degree axis for a pupil diameter of 7.18 mm was requested (Volunteer 4). The manufacturer improved the process further and produced a simple phase plate with only astigmatism.
The phase plate has an inverse wavefront map of the eye to counteract the eye aberrations. Figure 2.12 shows the wavefront map of the astigmatic eye (simulated in Zemax) and the resultant wavefront map of the phase plate with SHS. The measured RMS value in the phase plate was 1.11 microns instead of 2.17 microns. It is to be noted that the 2.17 microns of the eye are for a pupil diameter of 7.18 mm, whereas the phase plate measurement with SHS is only for a diameter of 5.25 mm. The phase plate RMS value at 7 mm pupil with SHS is 1.911 microns. We noticed that with a larger beam diameter, a clipping of the beam occurred with the SHS setup. The SHS measurement beam at 7 mm is not circular due to clipping, and therefore the phase plates were measured at 5.25 mm diameter. Then rescaled to the respective eye pupil diameter to verify the RMS of phase plates to eye aberrations. For example, rescaling the eye pupil diameter to 5 mm would lead to an RMS error of 0.95 microns (original 2.17 microns at 7.18 mm). And the RMS of the phase plate at 5.25 mm is 1.11 microns. This shows that the phase plates can be manufactured equivalent to the measured ocular aberrations. The phase plate equivalence can be verified by rescaling the pupil diameter since the SHS cannot measure aberrations at a larger diameter (See Appendix).

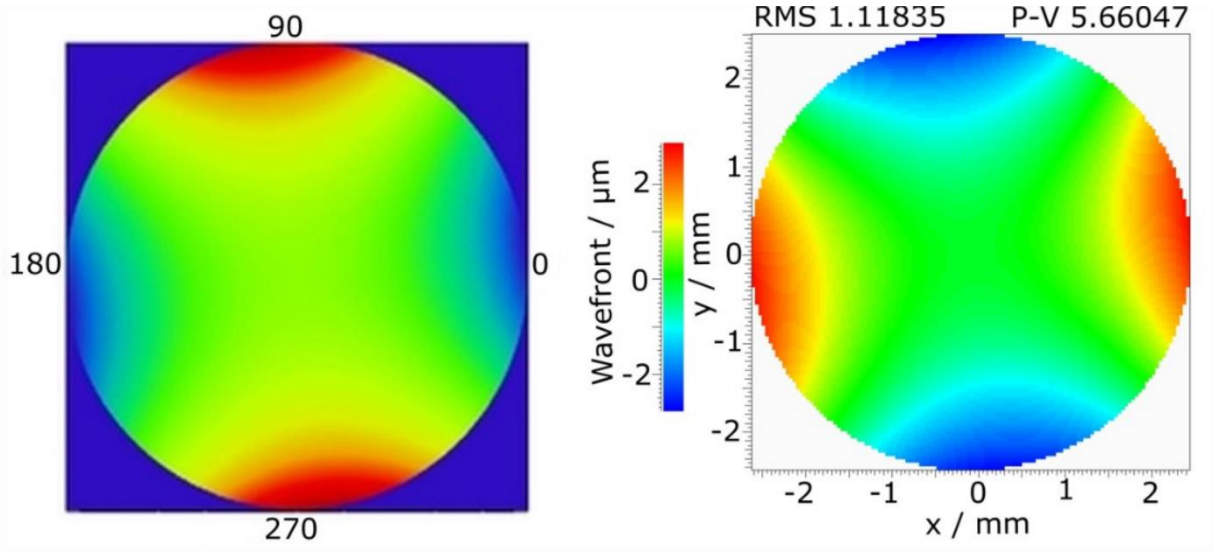

Figure 2.12. Wavefront map of the astigmatic eye simulated in Zemax (left image), and the wavefront map of the phase plate (right image) measured with SHS.

2.2.5 Positioning and Integration of Phase Plates in cSLO Devices

Positioning the phase plate in the cSLO is crucial since the custom phase plate's position and orientation determine its performance. A key factor for achieving the optimum degree of compensation is the proper positioning of the phase plates in the reference frame. Any misalignments would reduce the performance of the compensation unit[160]. This section evaluates the positioning of the phase plates in cSLO with an HMO lens because positioning is key for aberration compensation. The ideal position of phase plates is the conjugate to the eye's pupil. However, in a clinical setup, the phase plates cannot be positioned at the conjugate plane to the pupil unless the manufacturer of the device implements the changes. The phase plates are custom designed for each

individual, and the camera head or design of the clinical cSLO device cannot be changed or adapted for this study or easily in any clinical routine. Furthermore, non-contact ophthalmic imaging should be achieved for patient comfort and experience. Considering these factors, the phase plate adapter was designed to easily integrate the phase plates in any clinical practice. The optical simulation in Zemax was also performed to determine the impact of positioning phase plates at a different plane than the eye's pupil plane. After careful evaluation, the phase plates were positioned at the scan pupil of the laser beam, i.e., close to the eye's pupil. This way, the performance of aberrations compensation with phase plates can be adequate and minimizing the burden of implementation in clinical practice.
The cSLO device used in this study has the laser beam parallel after the HMO lens since the eye optics (crystalline lens) serve as the objective lens. Thus, we positioned the phase plate at the scan pupil of the laser beam to avoid any decentration of the plate to the scanning laser beams. The laser beam size at the scan pupil is 6 mm. With this setup, lateral displacement can be avoided (Figures 2.13). Furthermore, since the phase plates are custom designed, the in-plane rotational residual aberrations can be avoided if the phase plates match the axis of the eye (Figure 2.14). However, the residual aberrations with the axial displacement cannot be avoided since the phase plates are positioned 10-15 mm away from the eye's pupil. The phase plate retinal imaging is non-contact, and the residual aberrations due to the axial displacement are evaluated with the setup shown in section 2.2.2. The axial displacement of the phase plates did not affect the performance much, and we noticed a residual aberration of approximately 0.10 µm (±0.05).

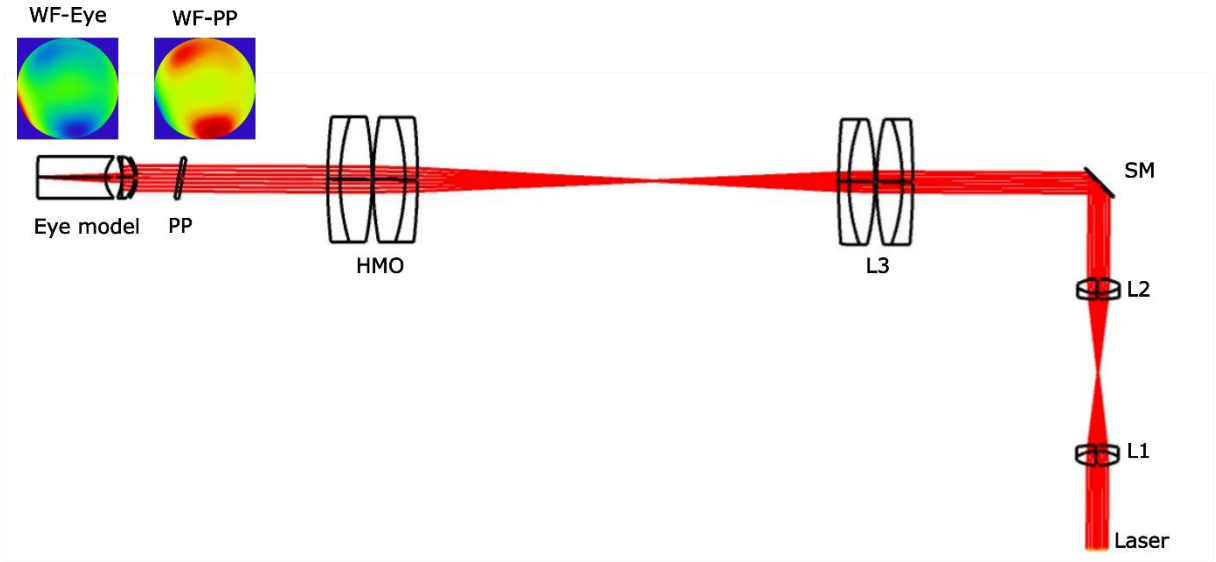

Figure 2.13. Schematic representation of cSLO with HMO lens and phase plate. WF- wavefront, PP- phase plate, L1, L2, L3 – Lenses, SM- scanning mirrors, HMO- high-magnification objective.

The phase plate is of size 10 x 10 x 2 mm, and the diameter of the aberration compensation zone is 8 mm (circular). A phase plate adapter was designed to place the phase plate in the scan pupil of the laser beam, i.e., precisely at 54 mm from the objective lens. The phase plates were fitted onto an HMO lens with a custom-made external (conical) adapter (Figures 2.15 and 2.16). The length of the adapter is 55 mm, and the phase plates are positioned precisely at the exit pupil of the scanning laser beam. The external adapter can be rotated manually for precise adjustment. For retinal imaging, the resultant phase plate is placed at 10-15 mm in front of the eye by carefully moving the cSLO system close to the eye. The external adapter has a magnetic ring, and the HMO lens has magnets which would ensure a firm holding of the adapter. Also, the

markings in the phase plate and the adapters would help align the phase plates to the subject's axis.

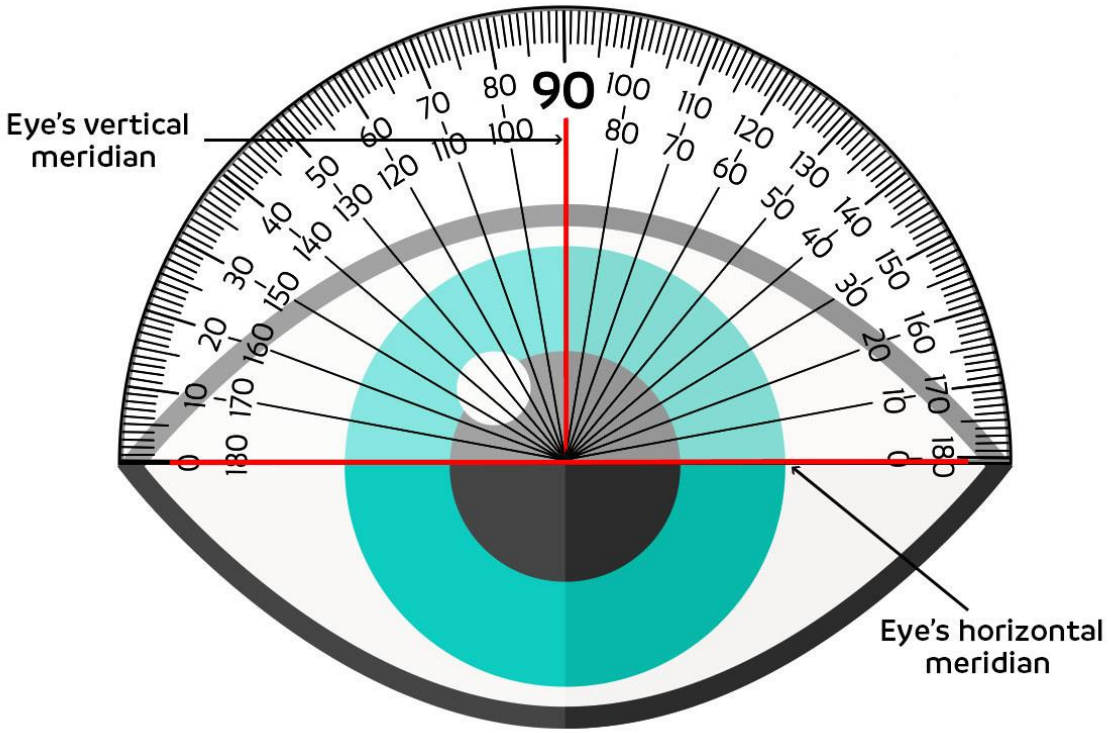

Figure 2.14. Axis of the eye[161]

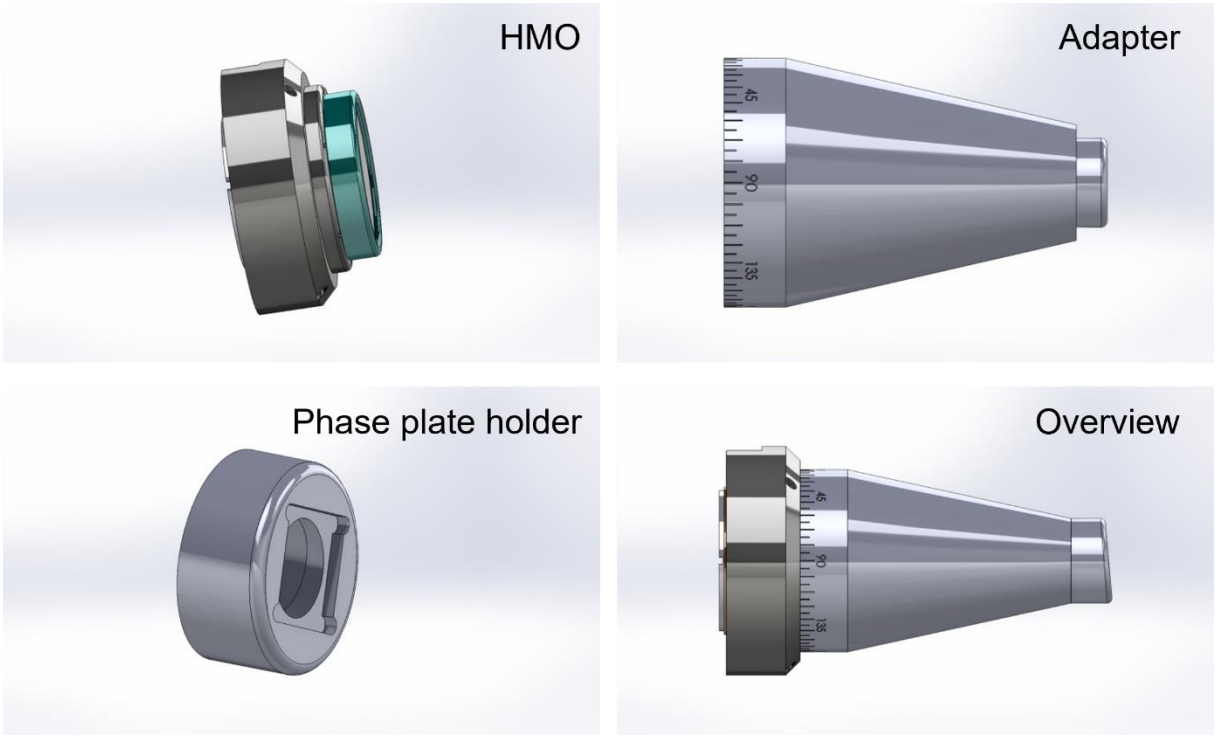

Figure 2.15. Computer-aided design (Dassault Systèmes SolidWorks Corporation, USA) of the HMO lens, adapter, and the phase plate holder.

Furthermore, the phase plate holder was designed with a 10-degree tilt to avoid reflections from the phase plates. The ideal place for a phase plate is at the conjugate plane

to the eye pupil and placing the phase plates strictly at the conjugate pupil inside the device would avoid tilt. This induces some residual aberrations due to the 10-degree tilt. Due to the optical design of the cSLO, the reflections from the phase plates can be achieved only at 10 degrees. Tilt does not affect the overall image quality; however, it is best to avoid it as much as possible. Although the adapter for holding the phase plates was designed carefully to avoid lateral displacements and rotational displacement, slight variable lateral displacements might happen due to manufacturing errors (for example, difficulty cutting the phase plate exactly centered 10 x 10 mm). Residual aberrations appear in case of substantial misalignment of the phase plates to the eye.

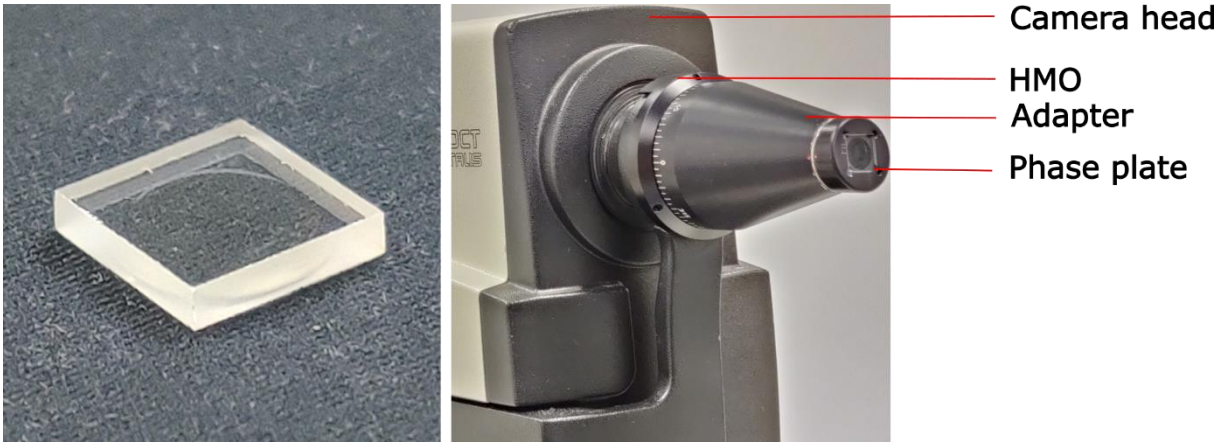

Figure 2.16. Photograph of a phase plate (left). Picture of external adapter fitted into cSLO and HMO lens with phase plate (right).

2.2.6 Ocular Aberrometer Evaluation

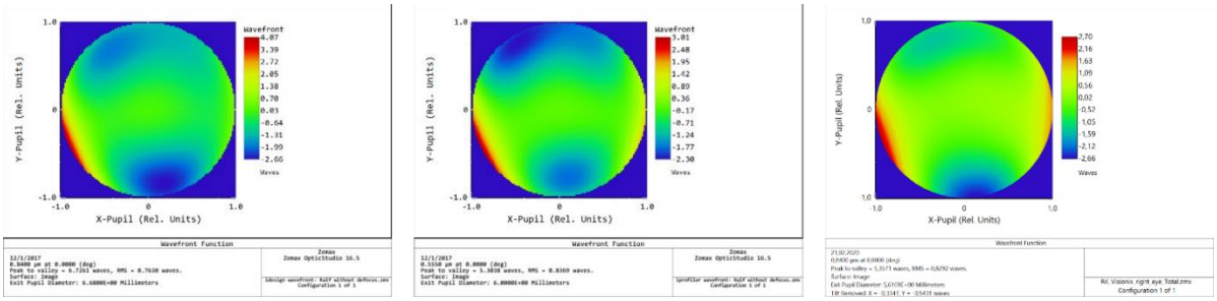

Figure 2.17. Wavefront map of HOAs with astigmatism but without the piston, tilt, and defocus from iDesign (left), iProfiler (middle), and Visionix (right) aberrometers (Volunteer 1).

Any aberrometers that can measure the ocular aberrations of an eye can be used to produce a custom phase plate. During this study, we had the opportunity to measure ocular aberrations from three different manufacturers and evaluated three aberrometers: iDesign (Abbott Medical Optics Inc., USA), iProfiler (ZEISS, Germany), and Visionix Vx110 (Luneau Technology Operations SAS, France). All three aberrometers are based on Shack-Hartmann wavefront sensors. The iDesign device uses 840 nm light, and can gather more than 1250 data points from up to 7.0 mm pupil diameter[162, 163]. The Visionix VX110 uses 800 nm light, and can gather more than 1500 data points for a 7.0 mm pupil diameter[164]. The iProfiler uses 555 nm light, and can gather up to 1500 data points for a 7.0 mm pupil diameter[165].
The RMS error and wavefront maps are evaluated to assess the aberration measurements for phase plates. The ocular aberrations obtained with the three aberrometers showed significant differences in total ocular aberrations such as defocus and HOAs (Table 2.3). However, only minor differences were noticed for astigmatism, coma, and

trefoil. Moreover, the wavefront map of the three aberrometers matches well, and one example is shown in Figure 2.17.

Table 2.3. Eye measurements with iDesign, iProfiler, and Visionix aberrometers.

Volunteers	iDesign				iProfiler				Visionix			
	PD (mm)	Total RMS (µm)	HOA RMS (µm)	Defocus (µm)	PD (mm)	Total RMS (µm)	HOA RMS (µm)	Defocus (µm)	PD (mm)	Total RMS (µm)	HOA RMS (µm)	Defocus (µm)
V1 (OD)	6.68	2.07	0.48	1.85	6.0	1.42	0.42	1.16	5.62	1.04	0.33	0.63
V2 (OD)	7.58	1.74	0.52	1.62	6.9	1.05	0.38	0.97	6.37	0.43	0.24	1.85
V5 (OD)	7.91	21.89	0.43	21.84	7.0	17.34	0.27	17.27	NA	NA	NA	NA

*NA- Not available, PD- Pupil diameter.

Table 2.4. Comparison of iDesign and Visionix Zernike's after rescaling the pupil size

	Volunteer 1 (OD)		Volunteer 2 (OD)	
	iDesign	Visionix	iDesign	Visionix
Rescaled Pupil diameter (mm)	5	5	6	6
Total RMS (µm)	0.87	0.74	0.80	0.35
LOA RMS (µm)	0.85	0.71	0.77	0.28
HOA RMS (µm)	0.19	0.22	0.21	0.21

Although the wavefront map matches well, the RMS error differs between the aberrometers. Effective correction of aberrations is possible if high levels of measurement accuracy can be achieved. In this study, we converted the aberrations to the same pupil size since each aberrometer measures the aberrations at different pupil sizes, which can influence the measurements. As an example, we converted the Visionix and iDesign data to 5- and 6-mm pupil sizes using the formulas described in the research article[166]. After rescaling the Zernike's to different pupil sizes, the RMS of HOA agrees well between the aberrometers. However, the RMS of the lower-order aberration has some discrepancies. This is due to the large defocus value between the devices (See Table 2.3). The RMS of the lower-order aberration is the root of the sum of squares of astigmatism and defocus. The defocus value leads to a vast difference in the RMS of lower-order aberration.

Also, we noticed that astigmatism and a few aberrations were measured at different angles between the aberrometers (Figures 2.18 and 2.19). Since the iDesign and Visionix measure the RMS at different axes, this could lead to a slight difference between the two devices.

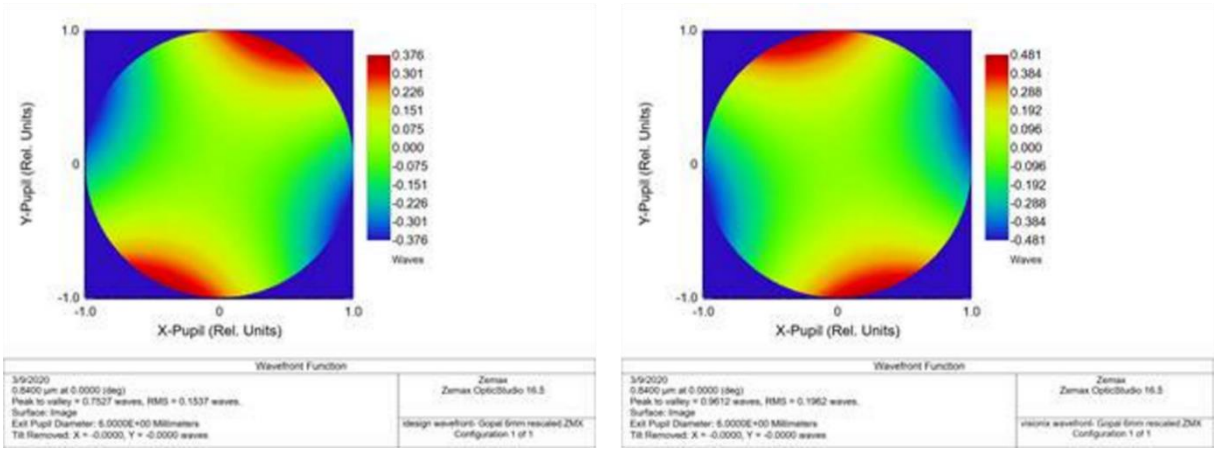

Figure 2.18. Comparison of astigmatism between iDesign and Visionix (Volunteer 2). Left: iDesign- RMS 0.1537 @ 68 degree, Right: Visionix- RMS 0.1962 @ 106 degree.

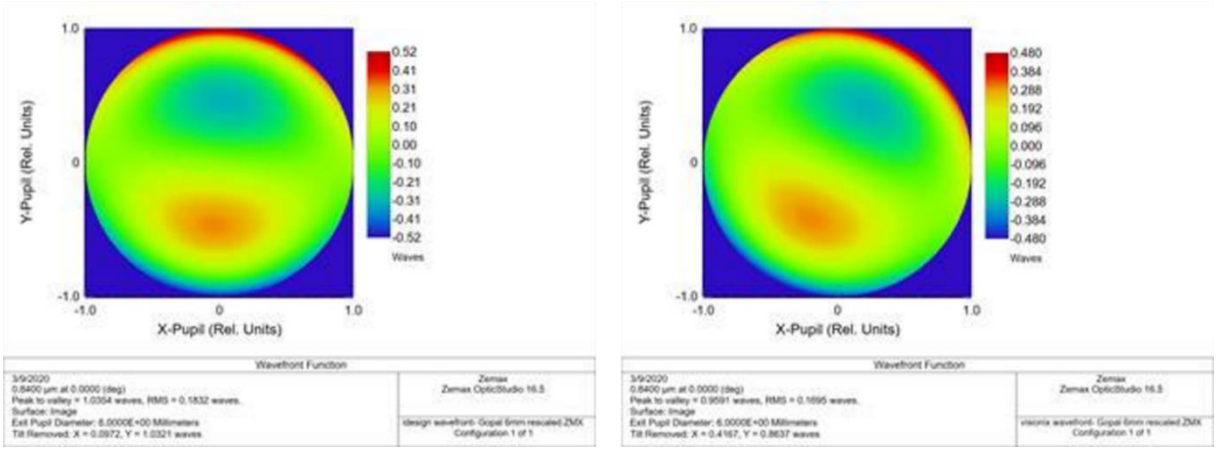

Figure 2.19. Comparison of coma between iDesign and Visionix (Volunteer 2). Left: iDesign- RMS 0.183 @ 85 degree, Right: Visionix- RMS 0.1695 @ 65 degree.

2.3 Conclusion and Discussion

In this study, a custom phase plate was designed and produced to compensate for ocular aberrations in the quest for improvement in retinal image quality. Simulations in Zemax were used to evaluate the performance of different design alternatives and determine the optimal position for the phase plate within the clinical cSLO device. The simulation results showed significant improvement in image quality, as seen in the PSF and MTF values. Alternative designs (trial phase plates) for custom phase plates were also evaluated in the simulation. But due to design complications, the practical implementation of the trial phase plates was not demonstrated in this study (See Appendix). The test also showed that phase plates can compensate for both lower and HOAs and improve the image quality. The aberration compensation was evident in two out of three volunteers, but there was inconsistency in one of the phase plates resulting in only minor improvement with aberration compensation. Despite this discrepancy, an improvement in retinal image quality was still noticed with the phase plates (Volunteer 3), indicating that even partial compensation (~60%) of aberrations can still result in improved image quality. Additionally, a bench test was conducted to confirm that the custom phase plate can be fabricated to match the measured RMS of lower-order aberrations. The results of the test indicated that the phase plates can be produced, but it is necessary to rescale the RMS to compare it with the SHS measurement (See Appendix for the formulas).

Although the study found that custom phase plates can effectively compensate for both lower and HOAs, the residual aberrations were still present in the phase plates that were considered of good quality (Volunteers 1 and 2). The study estimated that around 85% of aberrations can be compensated with a good-quality phase plate (See Table 2.2). The experiment validated the effectiveness of phase plates in compensating for aberrations. However, residual aberrations are unavoidable due to various factors such as the position of the phase plates, scanning angle, distance between the eye and phase plates, decentration (off-axis), and the precision of manufacturing the phase plates. For example, currently, the manufacturer cannot provide very high accuracy of cutting the glasses manually with a centricity better than a few 0.1 mm (approximately ±0.2 mm to ±0.3 mm). The study suggests that precise cutting of the phase plates would eliminate some of the residual aberrations, but this is difficult to achieve due to limitations in manual cutting and centricity of the phase plates.

The positioning of phase plates is crucial for effective aberration compensation and the phase plates were designed to position it close to the eye's pupil, at a distance of 10-15 mm from the eye. A detachable mechanical stopper will be added to the cSLO device base to prevent the phase plates from touching the patient's eye. The adapter design also included a tilt of 10 degrees to avoid reflections from the phase plates during imaging, even though it might have been avoided if the plates were placed at the conjugate pupil. Although tilt is not considered a true optical aberration[167], it is best to avoid it as much as possible. The axial displacement from the eyes and tilt of the phase plate would further introduce some residual aberrations. The bench test suggests that the axial displacement of the phase plates did not affect the performance much, and a residual aberration of approximately 0.10 µm (±0.05) was noticed. The lateral positioning followed by angular positioning are the key factors that affect the compensation performance, and our findings suggest that the axial displacements of 10-15 mm might not severely affect the performance of the compensation unit[160].

The adapter with custom phase plates would allow to easily plug in and out the phase plates in a clinical device. It is to be noted that although the adapter for holding the phase plates was designed carefully to avoid lateral displacements and rotational displacement, slight variable lateral displacements might happen due to manufacturing errors (for example, difficulty cutting the phase plate exactly centered 10 x 10 mm). The compensation loss is dependent on the specific aberration pattern of each subject as well as on the amount and type of misalignment. Also, the degree of compensation depends on how well the custom phase plates are manufactured (composition of eye aberrations in plates) and misalignments.

With the help of wavefront technology, the optical aberrations in the human eye can be precisely measured and expressed into a series of Zernike polynomials. The aberrometer comparison in this study showed significant differences in total ocular aberrations such as defocus and HOAs. This is in agreement with other studies as well[162, 163, 166]. However, only minor differences were noticed for astigmatism, coma, and trefoil. But the wavefront map of the three aberrometers matches well. We noticed that each aberrometer measures the aberrations at different pupil sizes, and these could influence the aberration measurements. Further, we noticed that astigmatism and a few aberrations were measured at different angles between the aberrometers, and this could lead to a slight difference in the RMS between different devices. The differences in the algorithm to locate the pupil center between devices might also lead to discrepancies. However, any ocular aberrometer can be used for manufacturing phase plates since the phase plates can be manually rotated to find the optimal position and the aberrations can be compensated for better image quality. It appears that the ocular aberrometers will be the preferred device to improve retinal image quality with phase

plates since corneal topography or corneal aberrations may not be suitable since the internal optics of the eye partially compensate for anterior surface corneal aberrations[168]. The aberrations of the eye's internal optics are the sum of the posterior corneal and the crystalline lens aberrations. Therefore, total ocular aberrations equal internal optics and anterior corneal aberrations. This significantly leads to a difference in the total and corneal aberrations measurements. Manufacturing phase plates with only corneal aberrations would significantly not improve retinal imaging since internal optics aberrations will not be compensated and might induce additional aberrations. Therefore, for retinal imaging with phase plates, total ocular aberrometers would be most suitable. However, it is valuable to evaluate the aberration compensation with different aberrometers including corneal and total ocular aberrations in the future study.
In summary, this study aimed to evaluate and establish a compact non-contact aberration compensation unit for a clinically established device, considering factors such as operator-friendliness, patient comfort and safety, and easy integration in a clinical device. The results showed that the phase plates can significantly improve image quality by compensating for HOAs such as coma and trefoil, which cannot be corrected by eyeglasses or sphero-cylindrical lenses. This improved image quality can lead to improved diagnosis and detection of retinal diseases, making it useful for clinicians and researchers to study the retina at a cellular level. The results of this study motivated us to demonstrate the performance of the phase plates in human eyes, in order to show the potential of the phase plates in improving retinal image quality by compensating for HOAs.

3 RETINAL IMAGING WITH CUSTOM PHASE PLATES

In this chapter, we explore the use of compact custom phase plates for retinal imaging in human eyes. Using a commercially available cSLO device, we demonstrate the impact of phase plates on retinal imaging at a cellular level. Recent advancements in the field of retinal imaging have made it possible to visualize retinal microstructures without the need for adaptive optics. However, in its current state, the cSLO with an HMO lens may be beneficial only for subjects with low levels of ocular aberrations and smaller pupil sizes, as larger pupil sizes expose more aberrations to the imaging beam. We investigate if the use of phase plates can serve as an inexpensive and simplified aberration correction system for retinal imaging and determine the limits of retinal imaging with phase plates by comparing the results to those obtained using an AOSLO device.

3.1 Materials and Methods

In this study, we implemented a custom-made phase plate in a cSLO (SPECTRALIS, Heidelberg Engineering GmbH, Heidelberg, Germany), fitted with a small angle visual field lens (HMO lens) to examine the retina. The study design was a monocentric, prospective, non-invasive cross-over study. The study was conducted at the University Eye clinic Bonn, Germany with ethics approval. Noninvasive retinal imaging with cSLO and HMO lens was conducted and evaluated to investigate the effect of phase plates in compensating the ocular aberrations and impact in retinal image quality. On visit 1, a trained clinician/ researcher obtained the ocular aberrations from the participants using a clinical aberrometer. Then a custom phase plate was produced for each test eye with the measured ocular aberrations. Then on visit 2, retinal imaging with and without phase plates using cSLO and HMO lens was carried out to evaluate the performance of phase plates and the retinal image quality. Lastly, retinal images recorded with AOSLO and compared to the retinal image quality of cSLO with and without phase plates.

3.1.1 Confocal Scanning Laser Ophthalmoscope

cSLO is a non-invasive imaging technique that scans the retina with a laser beam enabling high-resolution retinal imaging. With cSLO (SPECTRALIS), the depth of focus can be adjusted manually, and deeper tissue structures can be visualized. 3D images can be generated with the focal plane adjustment as well.
The SPECTRALIS is an indispensable instrument in the field of ophthalmology, combining cSLO and high-resolution OCT. It has been widely used to diagnose various retinal diseases. It is an expandable diagnostic imaging platform and adds value to imaging. It can be used for conventional fundus imaging to ultra-widefield retinal imaging by simply changing the objective lenses. Widefield imaging facilitates a comprehensive diagnosis beyond conventional fundus imaging. High-contrast fundus images can be acquired with a 30º FOV using a standard objective lens. The widefield images of the fundus can be achieved with an additional objective lens allowing for a 55º FOV capturing the macula, the optic nerve head, and areas beyond the vessel's arcades in a single image (Figure 3.1 left image). The ultra-widefield objective lens can capture an extremely wide FOV of 102º with evenly illuminated, high-contrast images even in the periphery (Figure 3.1 right image). Thus, with a single imaging platform, the image of different FOVs can be acquired using SPECTRALIS simply by changing the objective lenses.

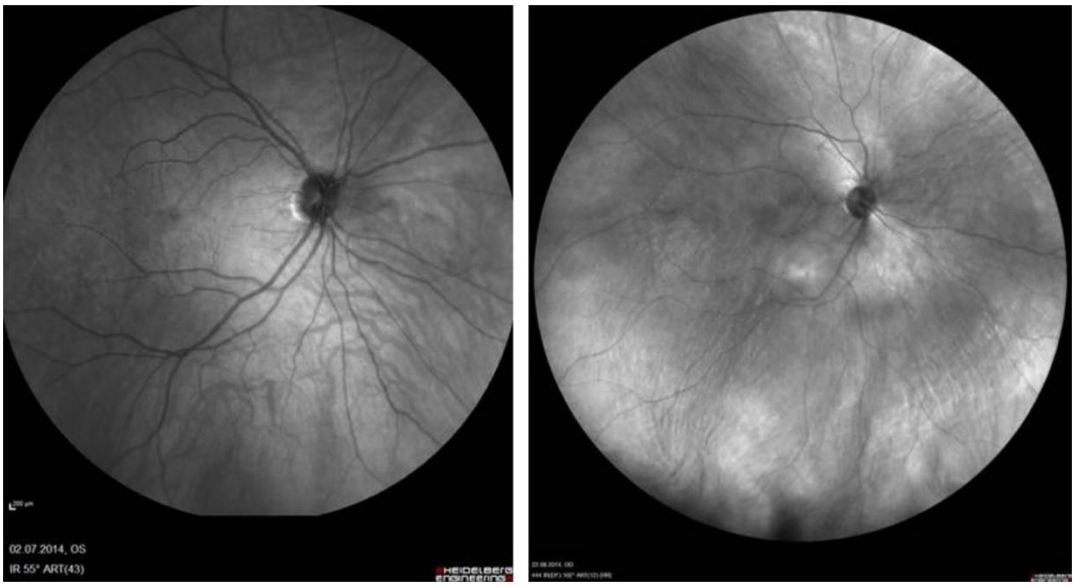

Figure 3.1. SPECTRALIS widefield (left image) and ultra-widefield (right image) retinal image of the right eye.

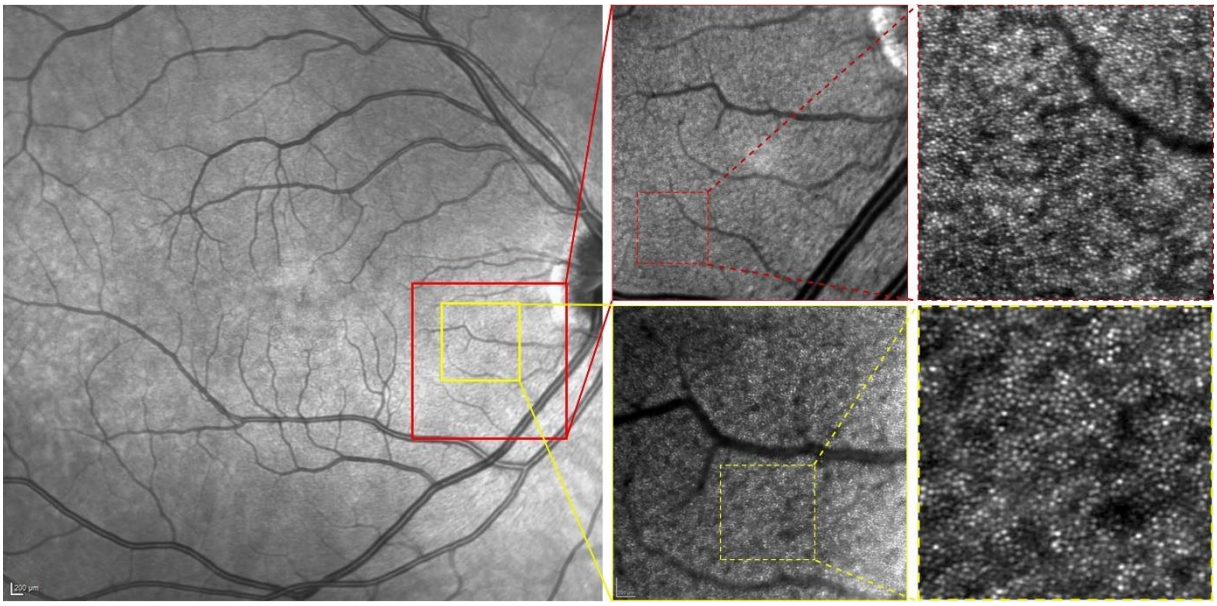

Figure 3.2. SPECTRALIS standard infrared reflectance image (30º FOV - left image) of the right eye. High-magnification retinal images with 8º (red box) and 4º (yellow box) FOV. Zoom-in images of 8º (red dotted line box) and 4º (yellow dotted line box) FOV showing cone photoreceptors.

Similarly, Heidelberg Engineering has developed a high-magnification lens for retinal imaging at 8º and 4º FOV. The HMO lens is an add-on objective lens that can be used with cSLO device to acquire high magnification retinal images (Figures 3.2, 3.3, 3.4, 3.5). The pixel densities are improved in X and Y directions with the HMO lens compared to the standard objective lens. The digital image readout for the high-resolution mode with an HMO lens for 8º and 4º FOV is 1536x1536 and 768x768 pixels. The 4-degree FOV is only an optical zoom-in of the 8-degree image and is not available in a clinical device yet. The 4-degree FOV can be activated only in research settings. Likewise, green imaging is available only in a research setting, and not commonly available in a clinical device. An additional blocking filter is integrated into the objective mount for laser safety. This filter strongly reduces the blue laser (486 nm). The infrared laser (815 nm), indocyanine green laser (786 nm), and green laser (518 nm) can be used for examination with an HMO lens in the reflectance mode and the angiography mode.

The cone photoreceptors can be visualized with the HMO lens in subjects with fewer ocular aberrations.

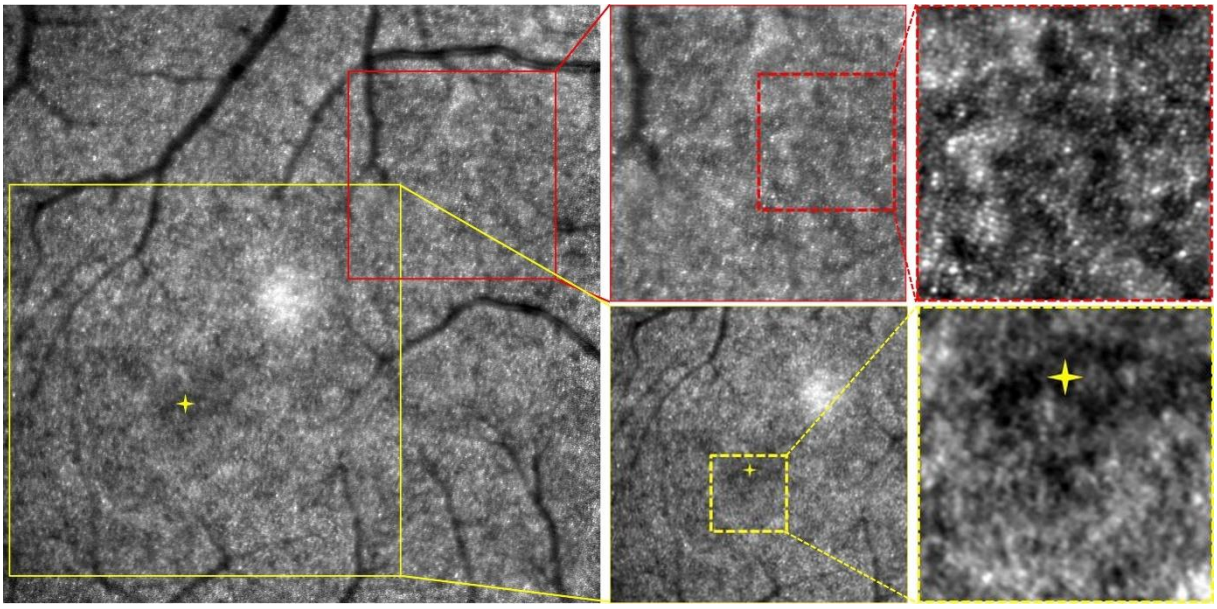

Figure 3.3. SPECTRALIS image of the fovea (4-point star) with 8º FOV (left image) showing cone photoreceptors at retinal eccentricities. Zoom-in images show cones photoreceptors at the retinal eccentricities (red boxes) and no photoreceptors at the fovea (yellow boxes).

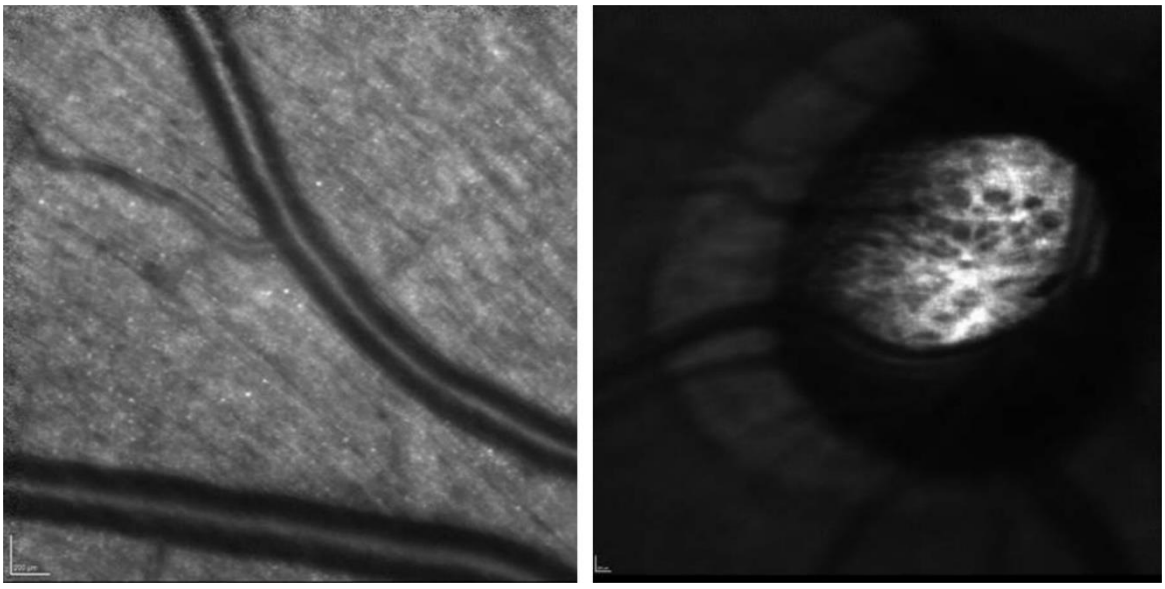

Figure 3.4. SPECTRALIS with HMO lens showing nerve fiber bundles (left image) and lamina cribrosa (right image)

For retinal imaging with phase plates, the phase plates were fitted onto an HMO lens with a custom-made external (conical) adapter (See Figure 2.16). The length of the adapter is 55 mm, and the phase plates are positioned precisely at the exit pupil of the scanning laser beam. The external adapter can be rotated manually for precise adjustment. The phase plates are placed at 10-15 mm in front of the eye by carefully moving the cSLO system close to the eye.

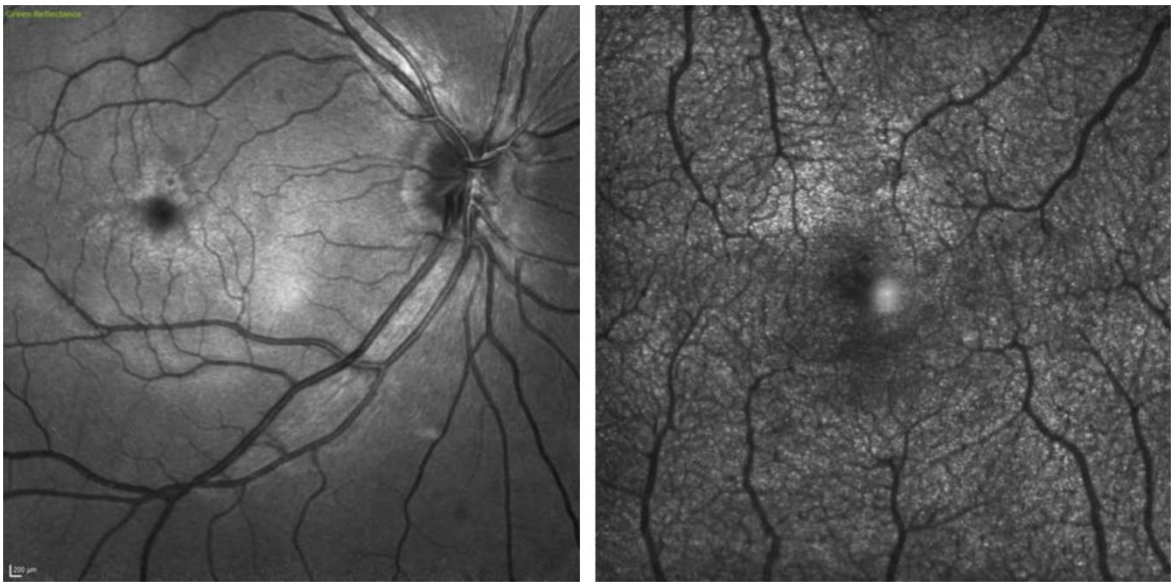

Figure 3.5. Green light retinal image with standard (30º FOV - left image) and high-magnification (8º FOV - right image) objective lenses.

3.1.2 Aberrometers

The ocular aberrations, including the Zernike coefficients, are needed to produce a custom phase plate. A clinically available aberrometer is used to measure the ocular aberrations of the subjects. Aberrometers record ocular wavefront data from several spots across the eye's pupil and provide a 2D map of its optical imperfections. The aberrometer can measure the Zernike polynomials up to the 6th order, which are included in the manufacturing process of the phase plate. For the aberrometer measurement, the participant's eyes are dilated by a physician. A trained clinician dilates the subjects' eyes with 1% Tropicamide and measures the ocular aberrations, including Zernike's coefficients, RMS error of lower and HOAs, and wavefront map. This information (pseudonymized) is then forwarded to the phase plate manufacturer.

3.1.3 Adaptive Optics Scanning Laser Ophthalmoscope

For a comparative approach, high-resolution retinal images were recorded using a custom build AOSLO at the University Eye Hospital Bonn[14, 169, 170]. The imaging wavelength is 842±25 nm light, bandpass filtered from the output of a supercontinuum laser (SuperK Extreme EXR-12, NKT Photonics A/S, Birkerød, Denmark). The illumination beam (7.2 mm diameter) was raster scanned across the retina by a resonant scanner in the horizontal (~15.9 kHz) and by a galvanometric scanner in the vertical direction (~30 Hz) pivoting about a plane conjugate to the eye’s pupil (Figure 3.6). Ocular wavefront aberrations were measured by a 23×23-lenslet Shack-Hartmann sensor (SHSCam AR-S-150-GE, Optocraft GmbH, Erlangen, Germany) and compensated by a 97-actuator continuous surface deformable mirror (DM 97-08, ALPAO, Montbonnot-Saint-Martin, France), operating at ~20 Hz closed-loop frequency. The light reflected by the retina was detected continuously by a PMT (H7422-50, Hamamatsu Photonics, Hamamatsu, Japan) located behind a confocal pinhole conjugate with the retina (pinhole diameter 20 µm = 0.47 Airy-disk diameters). The voltage output of the PMT, synchronized with the positional signals from the scanners, was used to render a 512×512-pixel imaging video at 30 frames per second. High signal-to-noise ratio images were created offline by stacking and averaging a number (n>100) of spatially aligned single frames of AOSLO videos.

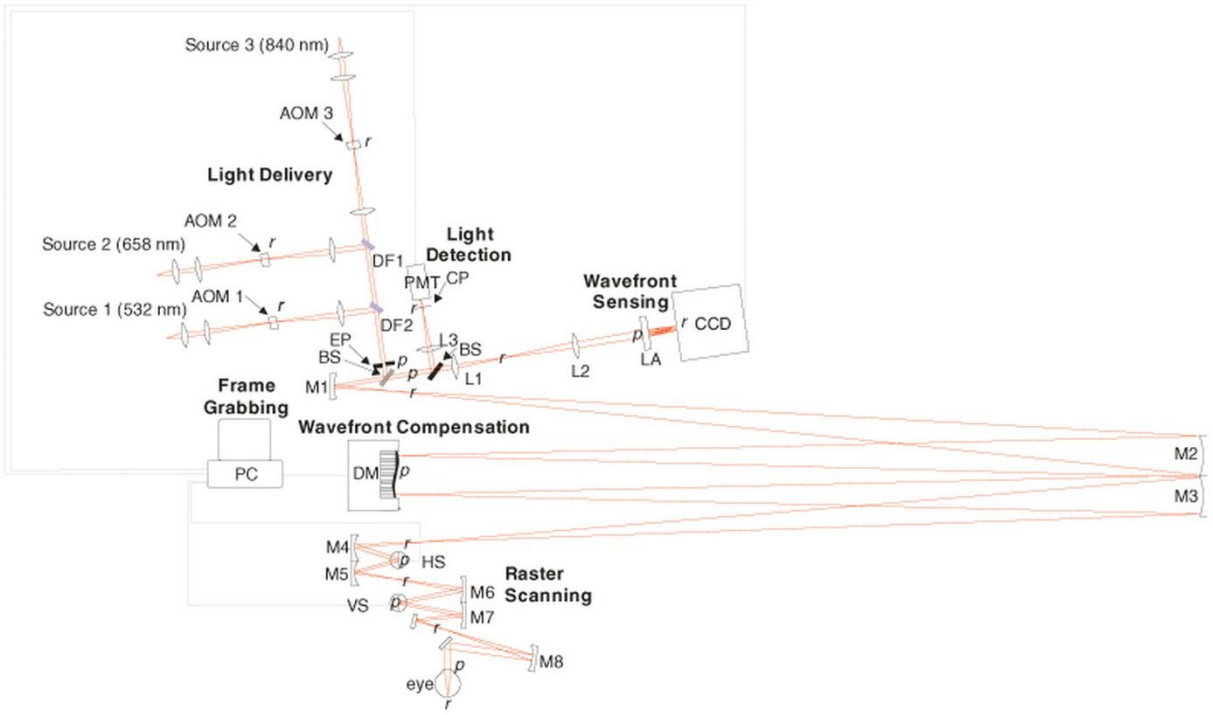

Figure 3.6. Schematic representation of AOSLO. L- lenses, M- mirrors, r and p – retinal and pupil conjugates in optical path length, AOM- acousto-optic modulator, DF- dichroic filter, EP- entrance pupil, BS- beam splitter, DM- deformable mirror, HS- horizontal scanner, VS- vertical scanner, LA- lens let array, CP- confocal pinhole, PMT- photomultiplier tube.

3.1.4 Study Participants

Six participants were included in this study. The ocular aberrations data were used to produce a custom phase plate. Out of the six participants, only one had HOAs and one had moderate astigmatism. For participant 1, two phase plates were produced: one to compensate only for astigmatism (lower order) and another to compensate for total ocular aberrations including astigmatism, to evaluate the potential use of phase plates in compensating for moderate astigmatism and defocus. The other four participants had minimal lower and HOAs. Furthermore, not all participants were able to participate in the AOSLO imaging session due to COVID-19 restrictions. Therefore, retinal imaging with AOSLO was performed only on four participants (P2, P3, P5, P6). Table 3.1 shows the RMS error of ocular aberrations measured with the clinical aberrometer and the RMS measured in the phase plates as shown in chapter 2. The aberrometer measures the aberrations at the given pupil diameter in millimeter.
During visit 2, retinal imaging with a 30-degree objective lens was acquired to assess the overall retinal quality. The images were acquired in the following sequence:

1. cSLO + HMO lens in non-mydriatic eyes
2. cSLO + HMO lens + phase plate in non-mydriatic eyes
3. cSLO + HMO lens in mydriatic eyes
4. cSLO + HMO lens + phase plates in mydriatic eyes

The participant's pupil was dilated after imaging sequence 2, and after a wait time of approximately 15-30 minutes, sequences 3 and 4 were carried out. Each imaging sequence lasted between 10-15 minutes. Although acquiring an image was instantaneous, more time was spent on readjustments and focus positioning for optimal visualization of the photoreceptor layers. A common approach with cSLO and HMO lens acquisition is to use an external light on the fellow eye to induce the consensual pupillary

reflex and enhance pupil constriction, improving the image quality[171]. However, in this study, external light was not used on the fellow eye to evaluate the effect of phase plates on smaller and larger pupil sizes. Each participant had one eye imaged at primary central, inferior, superior, nasal, and temporal locations with the internal fixation targets of the cSLO. The sensitivity and focus were manually adjusted to optimize the visualization of the photoreceptors subjectively. The automatic real-time tracking (ART) mode was used for each image, and no other offline registration or post-processing was performed on the images. Other parameters such as pupil diameter, ocular aberrations, and corneal topography were not measured on visit 2. The imaging took place in dim room lights, and subjects were encouraged to blink during the examination. The alignment and adjustment of cSLO + HMO lens and cSLO + HMO lens + phase plates were almost similar, except the working distance for cSLO + HMO lens is approximately 50-55 mm, whereas phase plates were 10-15 mm from the cornea. Additionally, the phase plate holder must be manually rotated to find an optimal position to make the cone photoreceptors look sharp and well-defined. In this chapter, the retinal images presented with cSLO, and HMO lens are mostly contrast-enhanced unless otherwise stated, to better visualization of cone photoreceptors. The contrast enhancement can be done with the cSLO device software HEYEX (Heidelberg Eye Explorer, Heidelberg Engineering GmbH, Germany).

Table 3.1. Aberrometer measurement of participant eyes and phase plates

Participants	**Aberrometer measurement of eye**						**Rescaling to ~6 mm PD**	**Measurement of PP**
	PD (mm)	Total RMS (µm)	Astig. RMS (µm)	Defocus (µm)	HOAs RMS (µm)	Astig.+HOAs RMS (µm)	Astig.+HOAs RMS (µm)	Astig.+HOAs RMS (µm)
P1 (OD)	7.18	5.99	2.17	5.52	0.78	2.32	1.60	1.62
P2 (OD)	7.58	1.74	0.37	1.62	0.52	0.49	0.36	0.39
P3 (OD)	6.68	2.07	0.78	1.85	0.48	0.92	0.76	0.85
P4 (OS)	5.59	1.56	0.41	-0.59	1.45	1.40	1.34	1.29
P5 (OD)	6.04	2.09	0.27	2.03	0.42	0.50	0.42	0.39
P6 (OD)	6.32	0.78	0.36	-0.58	0.37	0.51	0.33	0.37

[+]The SHS measured the phase plate at different diameters (approx. 6 mm), and the limitations were explained in chapter 2. By rescaling the diameter, the RMS of the phase plate and measured eye aberrations can be compared. Astig. - astigmatism, HOAs- higher-order aberrations, PD- pupil diameter, PP- Phase plate

3.2 Results

3.2.1 Retinal Imaging Compensating Lower-Order Aberrations

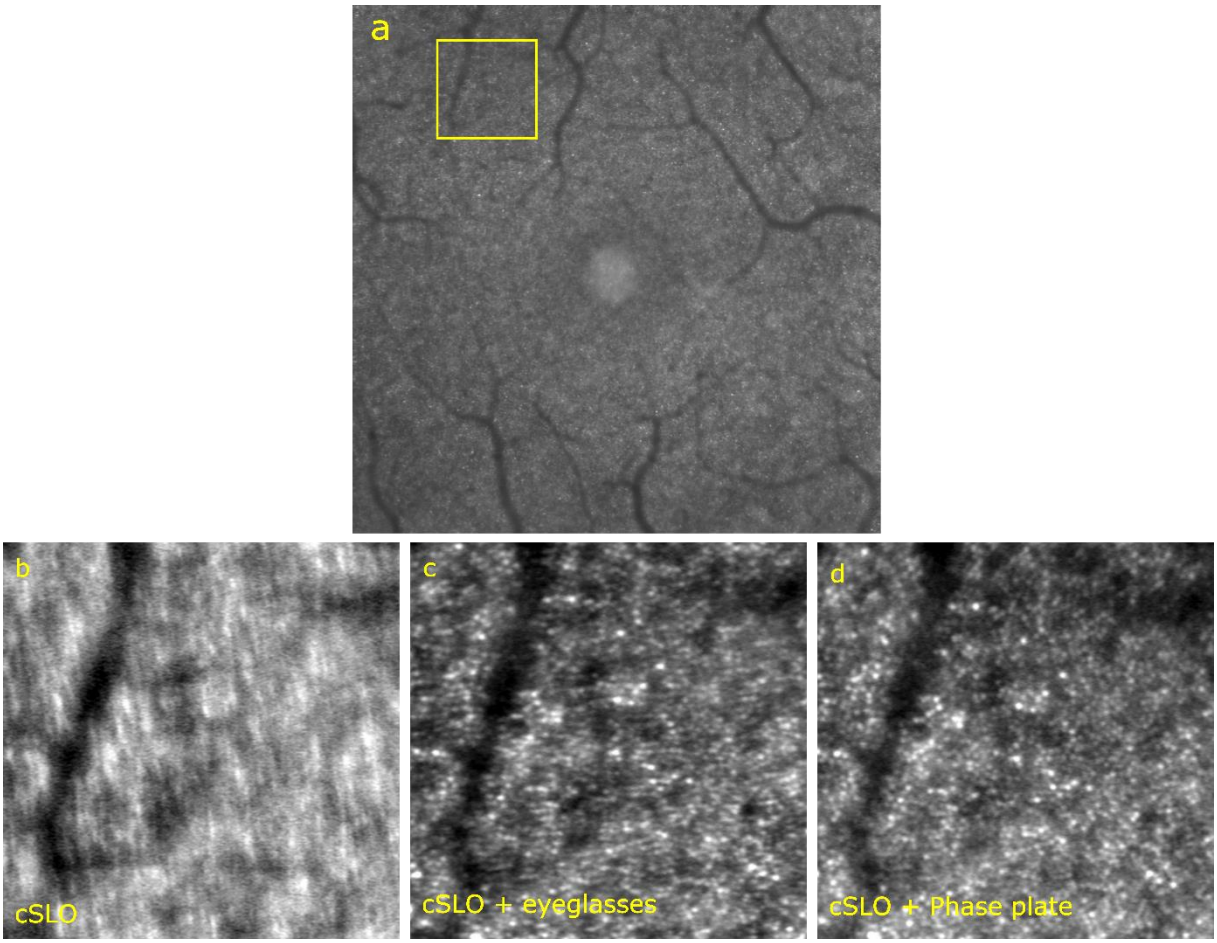

Figure 3.7. Comparison of retinal images assessing the lower-order aberration compensation. The 8 deg retinal image from participant 1 (a). The magnified retinal region without eyeglasses or phase plates (b), with eyeglasses (c), and with phase plates but without eyeglasses (d). The magnified images (b, c, and d) correspond to a 1.5 deg FOV.

In this study, retinal imaging in non-mydriatic eyes with the astigmatic plate (Participant 1) was performed to evaluate the lower-order aberration compensation with phase plates compared to conventional eyeglasses. Figure 3.7a shows the 8-degree FOV retinal image using a customized phase plate. The bright spot in the center of the image is a common central artifact caused by reflections from the internal optical surfaces of the cSLO and HMO lens. The region of interest is highlighted in yellow. Figure 3.7b shows the digitally zoomed-in 1.5-degree FOV retinal image without phase plates, Figure 3.7c is the zoomed-in 1.5-degree image from the same location but with the participant wearing their eyeglasses, and Figure 3.7d is the 1.5-degree FOV zoom-in image without eyeglasses and with a phase plate. The photoreceptors were not visible, and the image appeared distorted without eyeglasses or phase plates (Figure 3.7b). Nevertheless, the photoreceptors are evident with the phase plates, and a significant improvement in retinal images was noticed (Figure 3.7d). The photoreceptors were visible with eyeglasses too, and the retinal image quality with phase plates and eyeglasses for lower-order aberrations is comparable. This indicates that lower-order aberrations can be compensated by phase plates and improve retinal image quality in aberrated eyes, comparable to eyeglasses, even in small pupils.

3.2.2 Retinal Imaging Compensating Total Ocular Aberrations

Retinal imaging with and without phase plates in non-mydriatic eyes

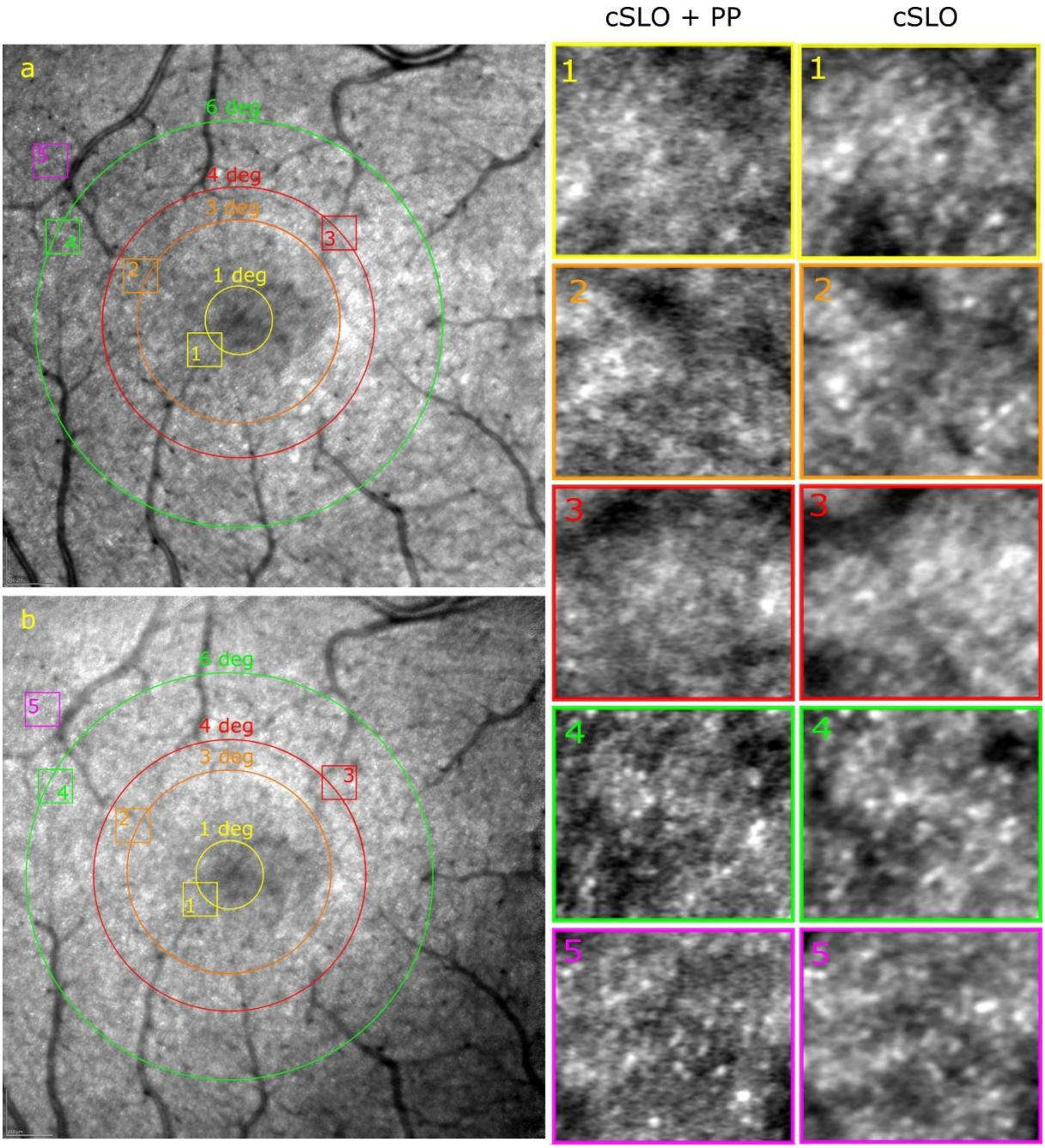

Figure 3.8. High-magnification retinal imaging without (a) and with phase plate (b) in a non-mydriatic eye of participant 5. The cone photoreceptors resolved at retinal eccentricities ≥ ~ 2 degrees. The retinal image with 8 deg FOV (a & b), and the digitally zoomed-in images correspond to a 0.5 deg FOV (image cutouts). PP- phase plates Scale bar- 200 µm

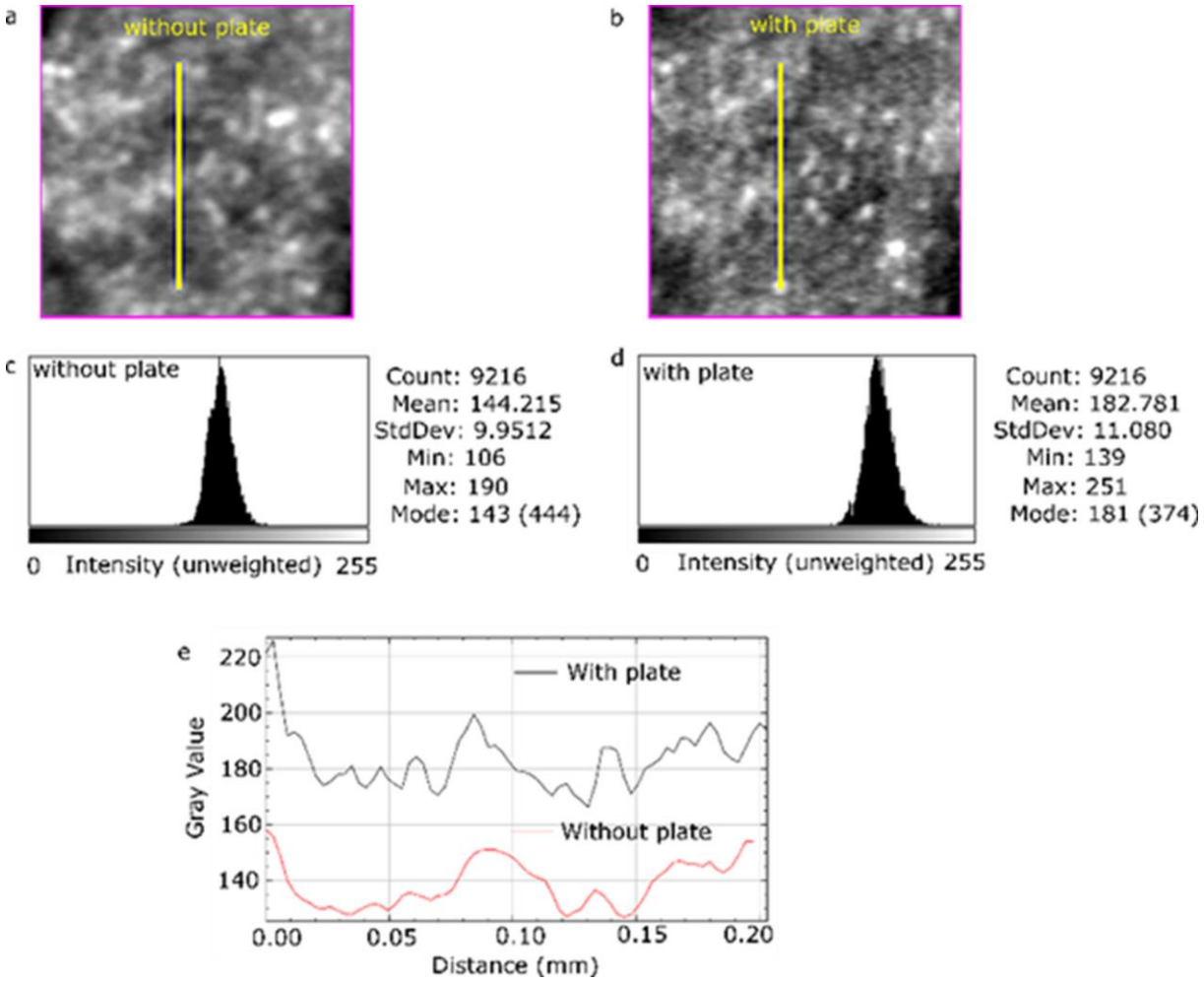

Figure 3.9. Comparison of retinal imaging without (a) and with (b) phase plates from Figures 3.8(5). Histogram of the image with and without phase plates (c and d). Line profile showing the intensity of pixels along the yellow line in the images (e). The digitally zoomed-in images (a and b) correspond to a 0.5 deg FOV.

The retinal imaging with and without phase plates in non-mydriatic eyes was acquired to assess the performance of the aberration compensation phase plates. It was assumed that the retinal image quality might not be affected by HOAs when the pupil size is 3 mm or smaller. Nevertheless, the impact of retinal image quality with phase plates in natural pupil size (approximately 3 mm to 5 mm without pupil dilation) was evaluated. Figures 3.8 show the retinal imaging with and without phase plates in the natural pupil (Participant 5). The retinal vasculatures and cone photoreceptors were visible with or without phase plates. A significant improvement in image quality with phase plates cannot be determined from Figures 3.8 because the aberrations might be minimal within smaller pupil sizes. The 8-degree FOV foveal image and the 0.5 deg FOV patches at 1-, 3-, 4-, 6- and 7- degree eccentricity from the foveal center with and without phase plates are shown in Figure 3.8. The cone photoreceptors were resolved at retinal eccentricities ≥ ~ 2 degrees with and without phase plates.

Figures 3.9a and 3.9b show the digitally zoomed-in images of the retinal images with and without phase plates from a retinal eccentricity of approximately 7 degrees from the fovea. Since the retinal image quality with phase plates could not be determined in a non-mydriatic eye, histograms and line profile plots were generated from one of the regions of interest. The histograms (Figures 3.9c, 3.9d) and intensity line profile plots (Figure 3.9e) highlight the contrast of the image before and after phase plates,

indicating a minor improvement in retinal image quality with phase plates, even in a non-mydriatic eye.

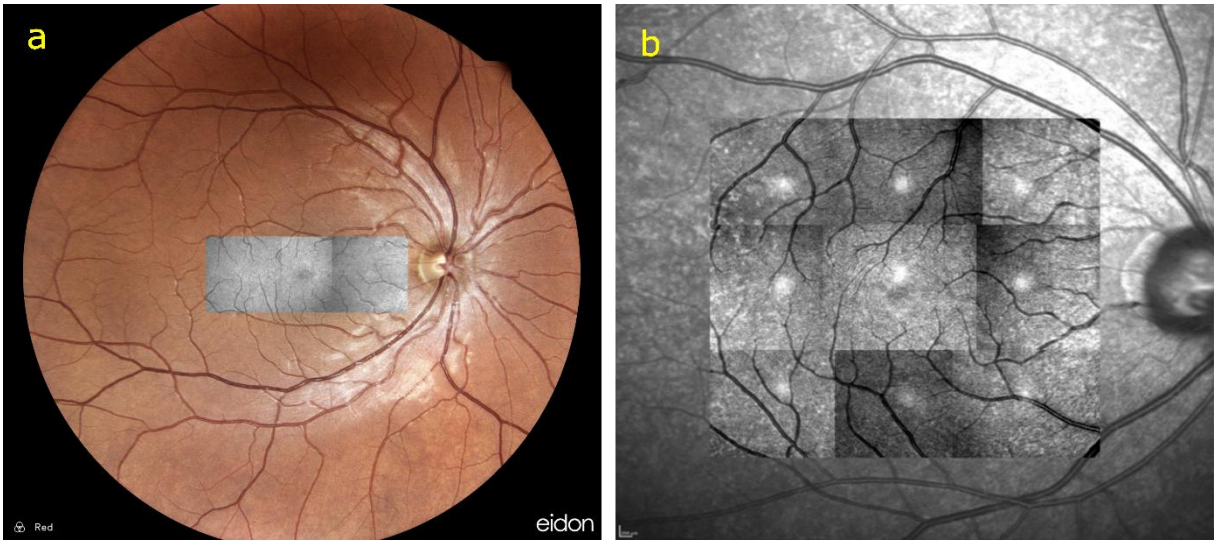

Figure 3.10. Overlay of cSLO with HMO lens retinal images without contrast enhancement on the EIDON fundus image from participant 5 (a). Overlay of 8-degree cSLO images from 9 target eye positions on the SPECTRALIS 30-degree FOV retinal image from participant 2 (b).

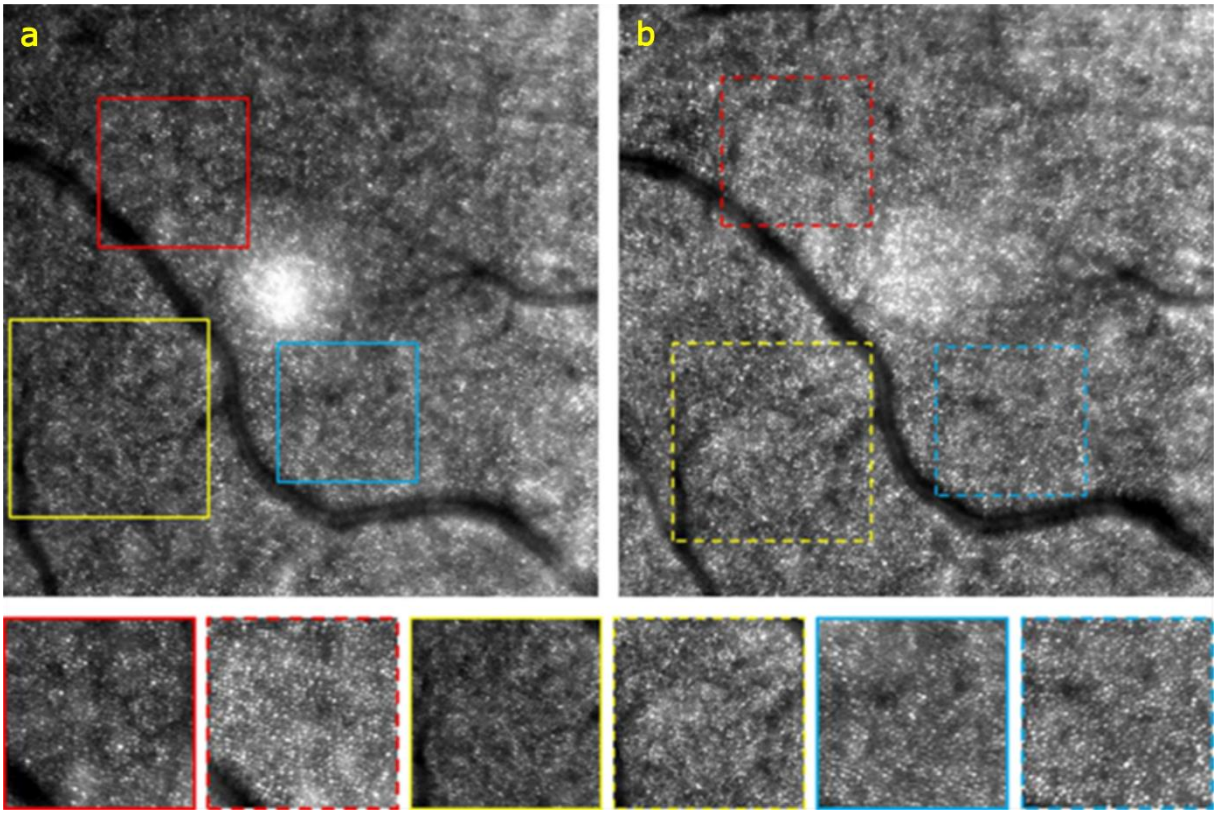

Figure 3.11. High-magnification retinal images in the non-mydriatic eye without (a) and with (b) phase plate (Participant 2). Comparison of retinal image quality without (solid line boxes) and with (dotted line boxes) phase plate.

Figure 3.10 shows an overlay of high-magnification retinal images (FOV 8 degrees) on fundus images. The 8-degree FOV retinal images from nasal, central, and temporal positions were stitched together and overlaid on the fundus image for a visual representation of cSLO retinal images with an HMO lens.

The retinal vasculatures and cone photoreceptors are visible with or without phase plates in non-mydriatic eyes from participant 2 (Figure 3.11). The improvement in contrast and visualization of cone photoreceptors with phase plates cannot be determined qualitatively since the improvement with phase plates is not substantial.

Retinal imaging with and without phase plates in mydriatic eyes

Figure 3.12 shows the retinal images from the nasal region with and without phase plates in a mydriatic eye (Participant 5). The digitally zoomed-in 2-degree FOV images from Figures 3.12a and 3.12b are shown in Figures 3.12c and 3.12d. The phase plates support improvement in the visualization of cone photoreceptors in mydriatic eyes (≥ ~ 7 mm). The cone photoreceptors are distinct from the phase plate retinal images (Figure 3.12d) compared to images acquired without a phase plate (Figure 3.12c). This shows that phase plates can compensate for HOAs and improve image quality in larger pupil sizes. Compared to the retinal images in non-mydriatic eyes (Figure 3.8), the aberration compensation and the improvement in contrast and image quality with the phase plate are more evident in mydriatic eyes. The cone photoreceptors and microvasculatures were also better resolved with phase plates in mydriatic eyes from other participants (Figures 3.13 and 3.14).

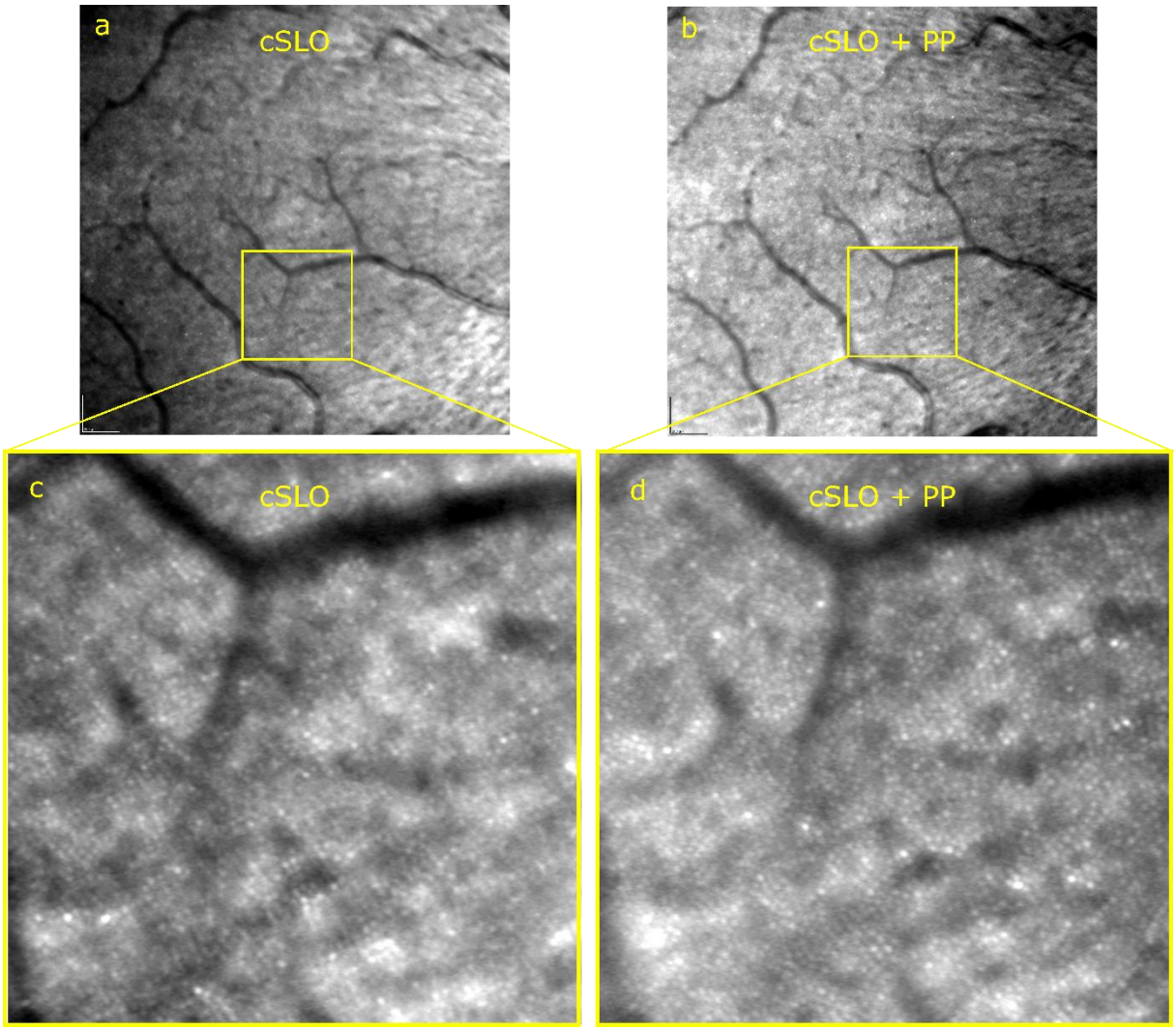

Figure 3.12. Comparison of retinal imaging without (a) and with phase plates (b) in mydriatic eye (Participant 5). The large image is the retinal image with 8 deg FOV (a and b), and the digitally zoomed-in images correspond to a 2 deg FOV (c and d). PP- Phase plate. Scale bar- 200 µm.

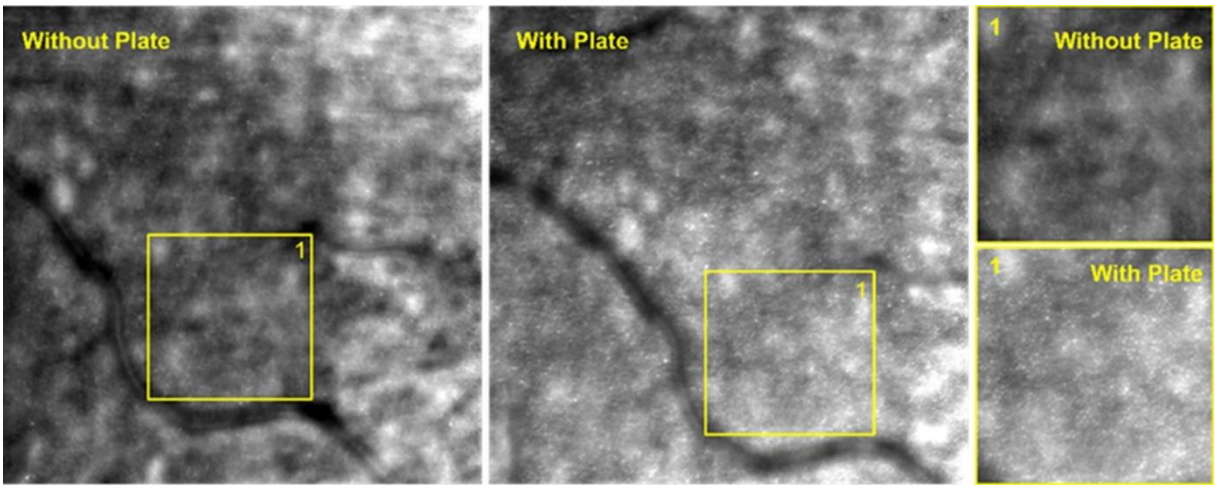

Figure 3.13. High-magnification retinal images of the test eye (Participant 2) without and with phase plate in the mydriatic eye. Comparison (boxes) of retinal image quality without and with a phase plate.

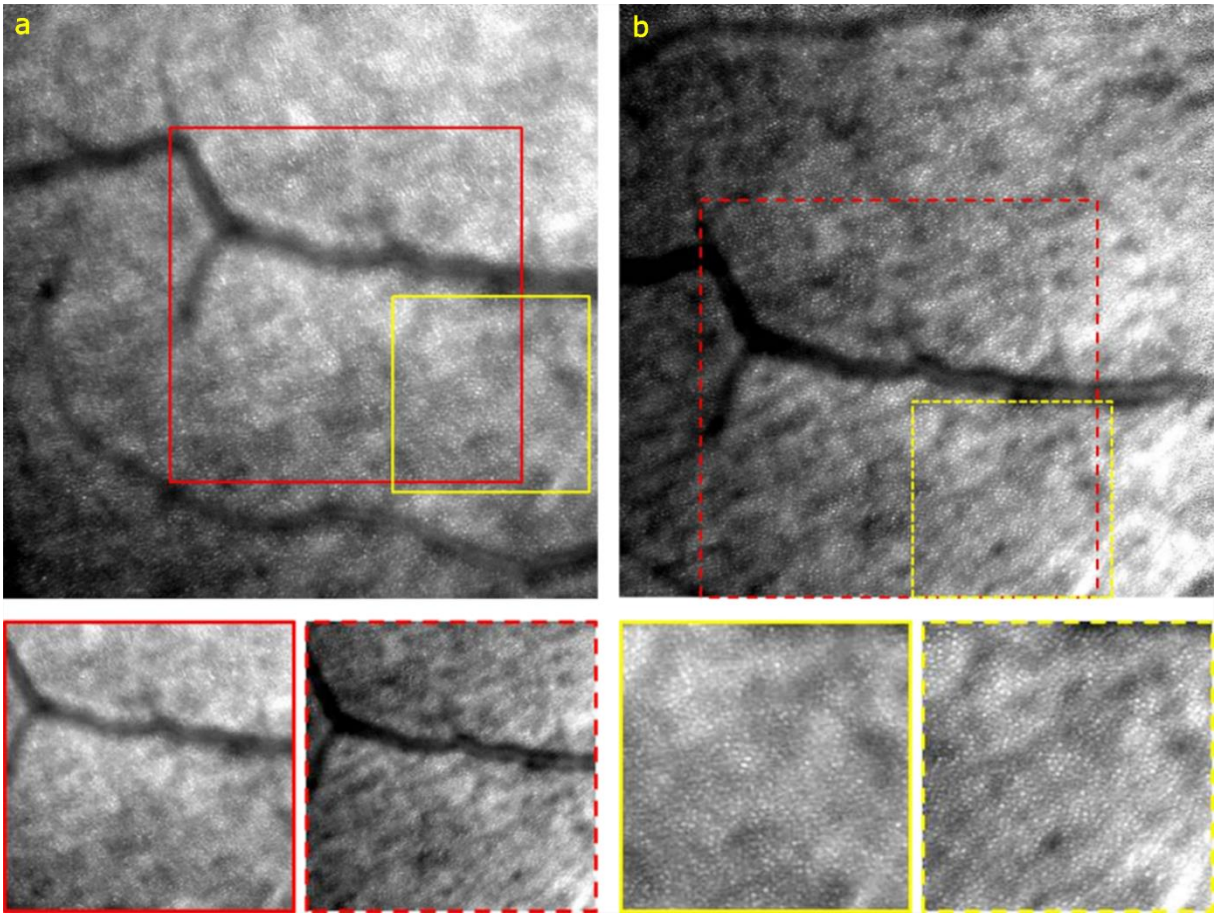

Figure 3.14. High-magnification retinal images in a mydriatic eye without (a) and with (b) phase plate (Participant 3). Comparison of retinal image quality without (solid line boxes) and with (dotted line boxes) phase plate.

The retinal imaging with and without phase plates from participant 4 did not resolve cone photoreceptors (Figure 3.15). Only the retinal vasculatures were visible in the images (Figure 3.15b and 3.15c). The 30-degree FOV retinal image with a standard objective lens is shown for comparison of retinal image quality to the cSLO and HMO lens (Figure 3.15a). The retinal vasculatures and image quality were better with the standard objective lens than with the HMO lens. The cSLO and HMO lenses with and

without phase plates could not resolve retinal microstructures. The histogram representation shows that the overall image quality is better with phase plates. Participant 4 had HOAs aberrations of 1.45 microns, but even after compensating for these aberrations with phase plates, the cone photoreceptors were not able to be visualized.

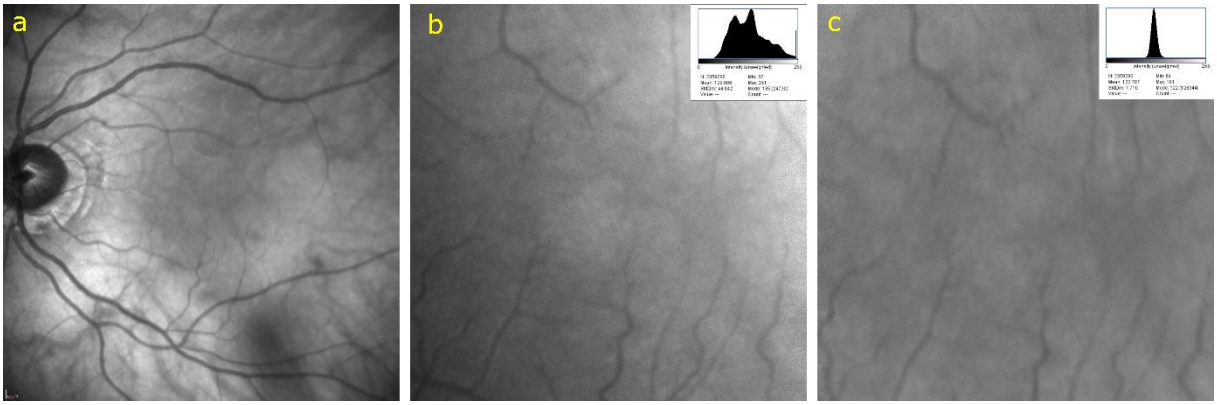

Figure 3.15. Comparison of retinal images without contrast enhancement in a mydriatic eye without and with phase plates from participant 4. A retinal image with 30-degree FOV without phase plate (a), 8-degree FOV without phase plate, and 8-degree FOV with phase plate (c). Histograms overlayed on the respective images (b & c).

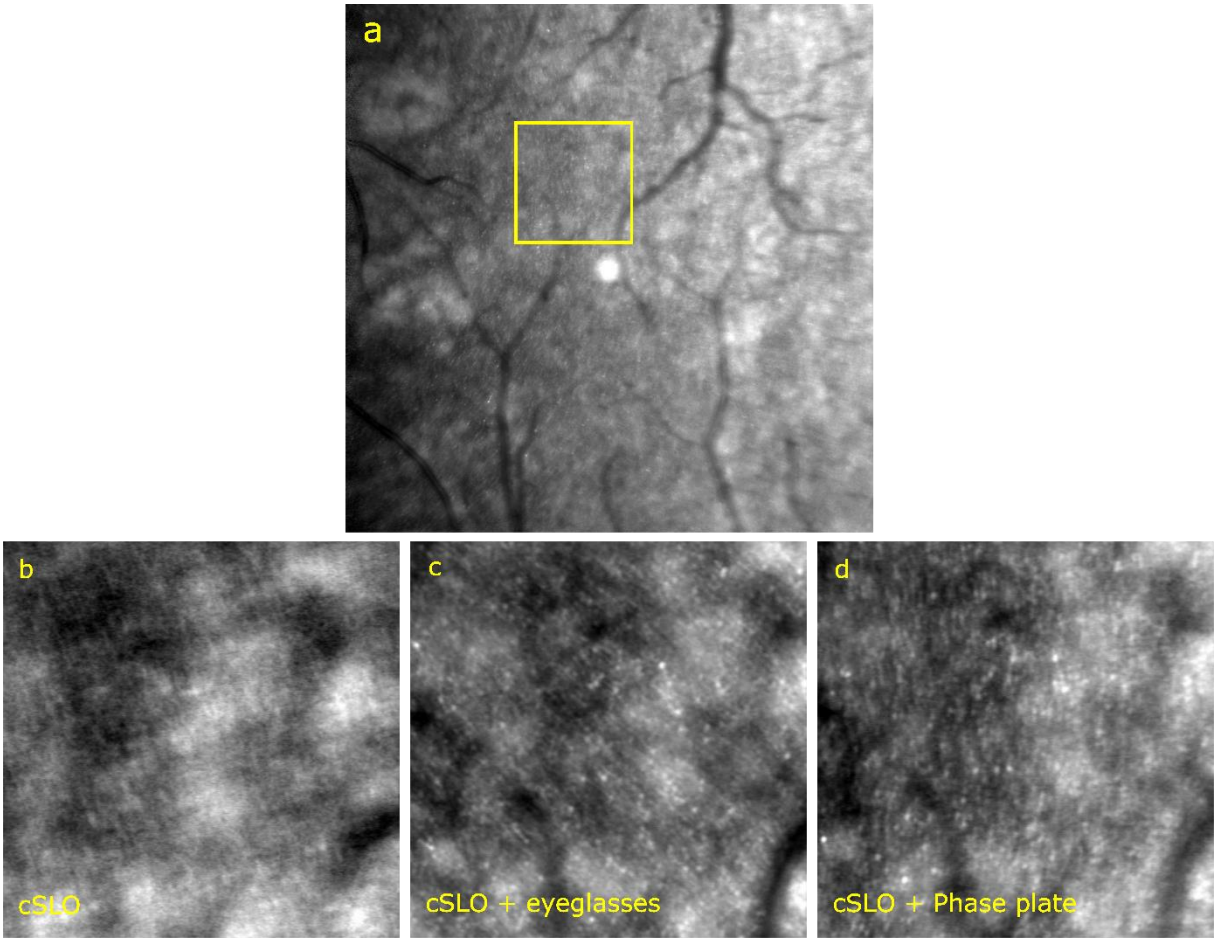

Figure 3.16. Comparison of retinal images assessing total ocular aberration compensation. The 8-degree retinal image from participant 1 (a). The magnified retinal region without eyeglasses or phase plates (b), with eyeglasses (c), and with phase plates but without eyeglasses (d). The magnified images (b, c, and d) correspond to a 1.7 deg FOV.

The retinal imaging compensating the total ocular aberrations is compared to the compensation with eyeglasses (Figure 3.16). The phase plate to compensate total ocular aberration for participant 1 was manufactured and tested in mydriasis eyes. Figure 3.16a shows the 8-degree FOV retinal image with a custom phase plate. The region of interest is highlighted in yellow, and Figure 3.16b shows the digitally zoomed-in 1.7-deg FOV retinal image without phase plates. Figure 3.16c is the zoomed-in 1.7-deg image from the exact location but with the participant wearing the eyeglasses, and Figure 3.16d is the 1.7-deg FOV zoom-in image without eyeglasses and with a phase plate. The photoreceptors were not visible, and the image appeared distorted without eyeglasses or phase plates (Figure 3.16b). The cone photoreceptors are evident with the phase plates, and a significant improvement in retinal images was noticed (Figure 3.16d). The photoreceptors were visible with eyeglasses too, but the retinal image quality with phase plates were slightly better compared to images with eyeglasses. The cone photoreceptors with phase plates were better visualized with phase plates. This shows that the lower and HOAs can be compensated by phase plates and improve the retinal image quality in aberrated eyes than eyeglasses in larger pupils.

Comparison of retinal images in mydriasis and non-mydriatic eyes

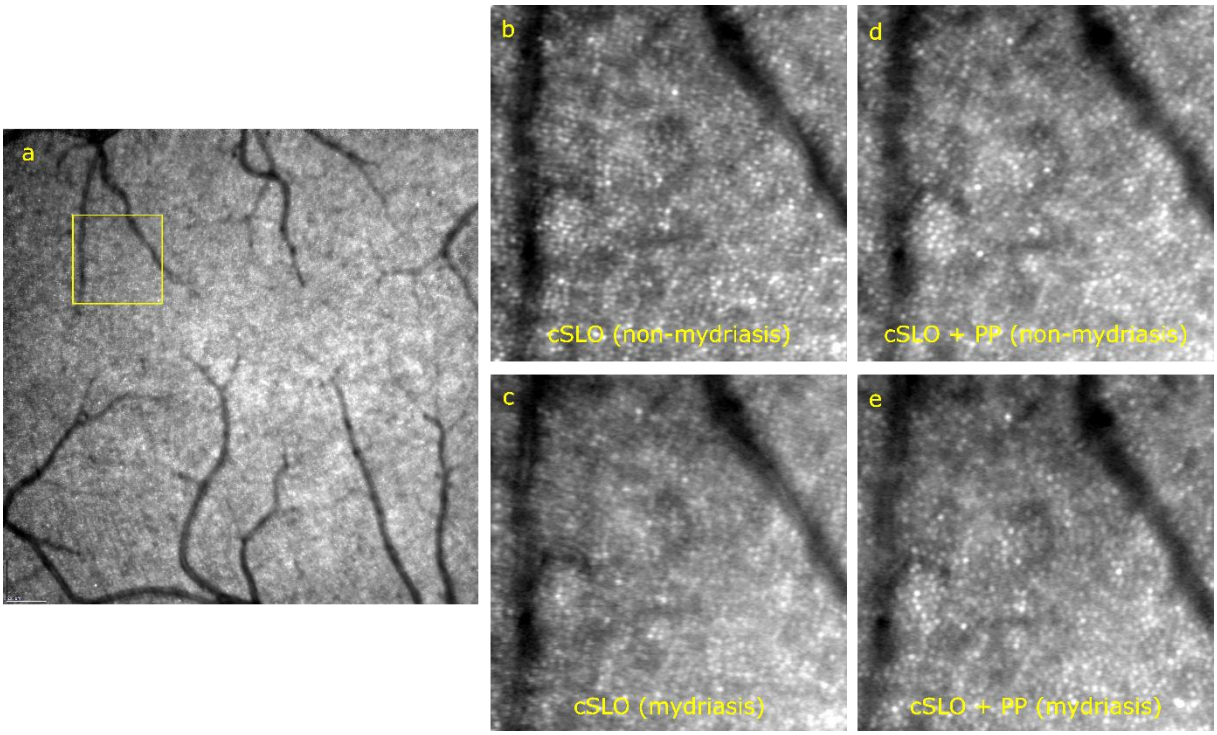

Figure 3.17. Comparison of retinal imaging with and without phase plates in mydriasis and non-mydriasis eye (Participant 5). High-magnification retinal image with 8 deg FOV from temporal area (a), and the digitally zoomed-in images correspond to a 1.5 deg FOV (b - e). PP- phase plates. Scale bar- 200 µm

The comparison of retinal images in mydriatic and non-mydriatic eyes is shown in Figure 3.17. Figure 3.17a is a high-magnification retinal image at a temporal region in a non-mydriatic eye with a phase plate for reference. Figures 3.17b and 3.17c are digitally zoomed-in images of a 1.5-degree FOV without a phase plate in a non-mydriatic and mydriatic eye. This clearly shows that HOAs affect the retinal image quality in the mydriatic eye compared to the non-mydriatic eye. The cone photoreceptors are better resolved in the non-mydriatic eye. Figures 3.17d and 3.17e are digitally zoomed-in images of a 1.5-degree FOV with a phase plate in a non-mydriatic and mydriatic eye. Comparing the retinal images without (Figure 3.17c) and with phase plates (Figure

3.17e) in the mydriatic eye, the improvement in retinal image quality is substantial with phase plates. However, the cone photoreceptors are equivalent, and sometimes better, in non-mydriatic (Figure 3.17a) than the mydriatic eyes (Figure 3.17e). The same results were noticed in other participants as well. Another example of mydriatic and non-mydriatic eyes is shown in Figure 3.18. The overall retinal image quality is better in smaller pupil sizes than in larger pupil sizes. The corrections of HOAs with phase plates in non-mydriatic eyes did not resolve the cone photoreceptors as well as in mydriatic eyes.

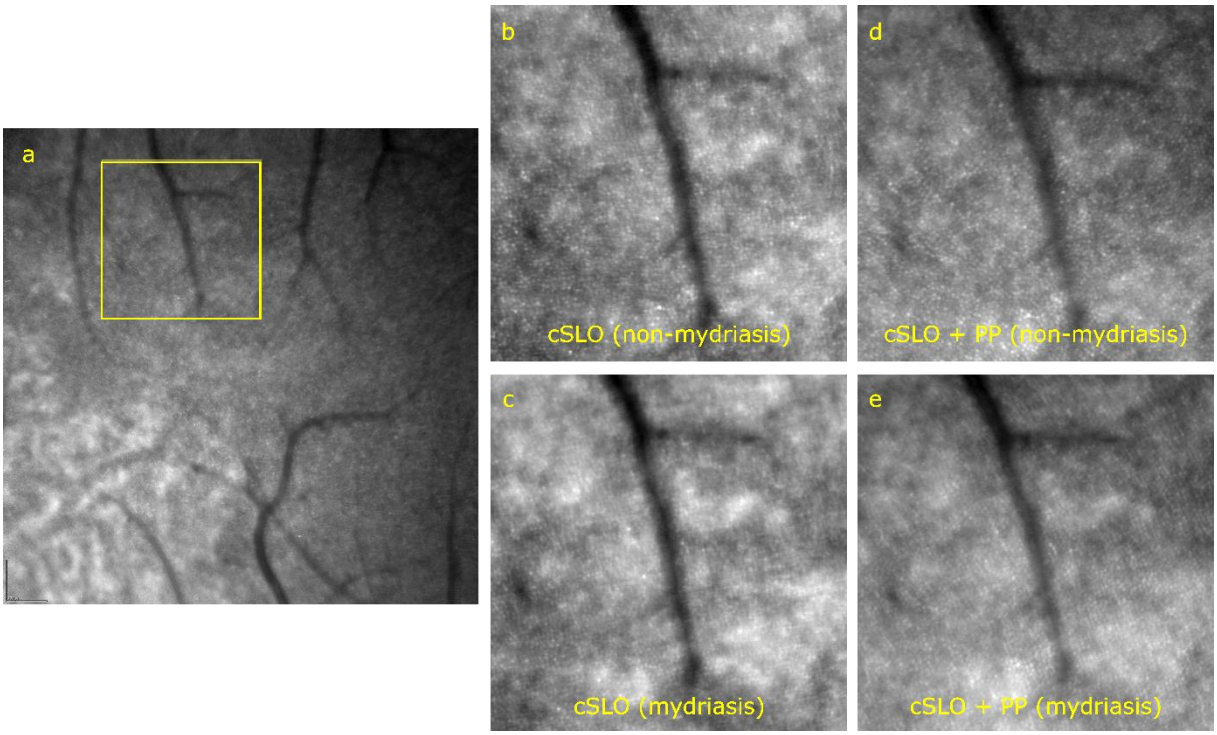

Figure 3.18. Comparison of retinal imaging with and without phase plates in mydriasis and non-mydriasis eye (Participant 6). High-magnification retinal image with 8 deg FOV from temporal area (a), and the digitally zoomed-in images (b - e). PP- phase plates. Scale bar- 200 µm

Retinal eccentricity and cone photoreceptor distribution

The impact of retinal image quality with phase plates in non-mydriatic eyes (approximately 3 mm to 5 mm without pupil dilation) is shown in Figure 3.19. The two 8-degree FOV images (central and temporal images) were stitched together in Figure 3.19. The central retina without and with phase plates revealed photoreceptors and microvasculatures. However, the improvement in image quality with phase plates is not evident. The cut-out image of the 8-degree FOV foveal image and digitally zoomed-in images at 2-, 4-, 6-, 8- and 10-degree eccentricity from the foveal center is shown in Figure 3.19. The cone mosaics were resolved at retinal eccentricities ≥ ~ 2 degrees with and without phase plates.

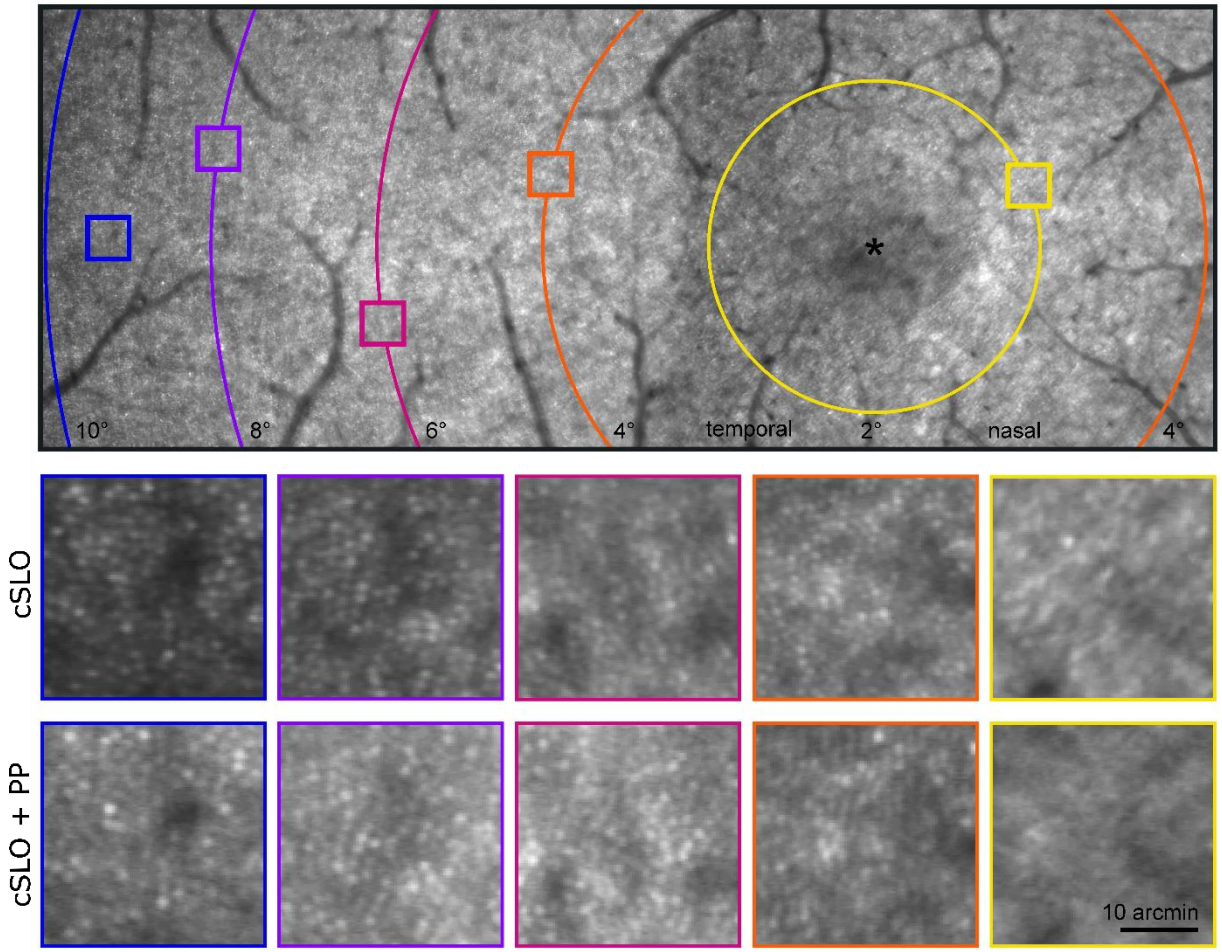

Figure 3.19. Comparison of high-magnification retinal imaging without and with phase plate in a non-mydriatic eye (Participant 5). The cut-out foveal image from two stitched 8 deg FOV (top row) and the digitally zoomed-in images without (middle row) and with (bottom row) phase plates at different retinal eccentricities. The cone mosaics are better resolved at retinal eccentricities ≥ ~ 2 degrees. PP- Phase plates

3.2.3 Comparing Retinal Imaging with Phase Plates and Adaptive Optics

Figure 3.20 shows a comparison of retinal images at different eccentricities obtained with and without phase plates in both mydriatic and non-mydriatic eyes, as well as with AOSLO in a mydriatic eye (Participant 5). The high-magnification retinal images shown in Figure 3.20 are digitally zoomed-in images from the 8-degree FOV. The cone photoreceptors and microstructures are predominantly visible in the parafoveal retina. A significant improvement in retinal image quality can be observed with phase plates in the mydriatic eye, demonstrating that phase plates can effectively compensate for HOAs and improve image quality in larger pupil sizes (≥ ~ 6 mm). In the non-mydriatic eye, the improvement in retinal imaging with a phase plate is evident, although the difference is minimal. The cone photoreceptors and vascular microstructures with and without phase plates are comparable to AOSLO images. However, foveal cone photoreceptors are only visualized in AOSLO images (Figure 3.21). While the resolution of cSLO with an HMO lens is not equivalent to AOSLO (where additional rod structure is visible), the center location of cone photoreceptors is identical. Cone photoreceptors were better visualized in parafoveal areas compared to perifoveal and foveal areas with cSLO and HMO lens (Figures 3.20 and 3.21).

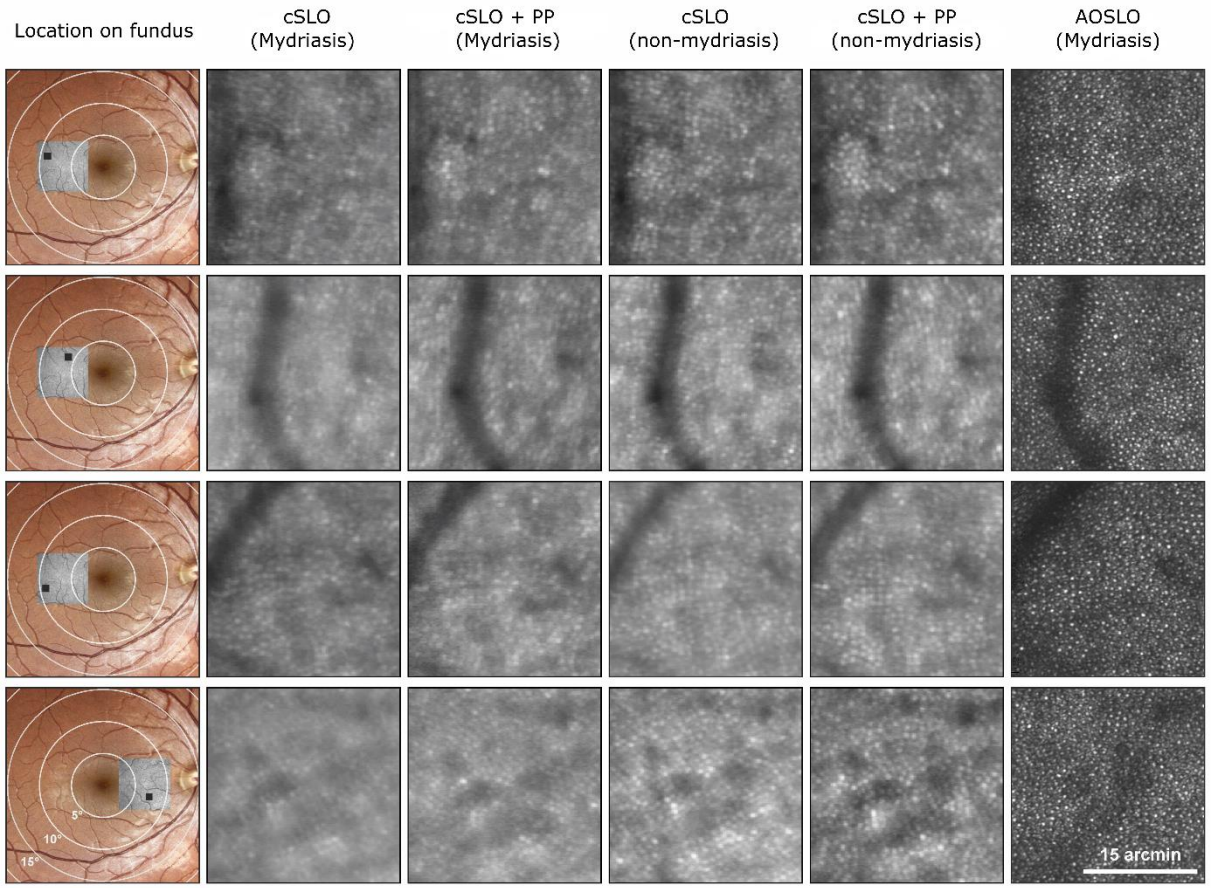

Figure 3.20. Comparison of high-magnification retinal images with cSLO device, cSLO with phase plates, and AOSLO in a mydriasis and non-mydriasis eye (Participant 5). PP- phase plates

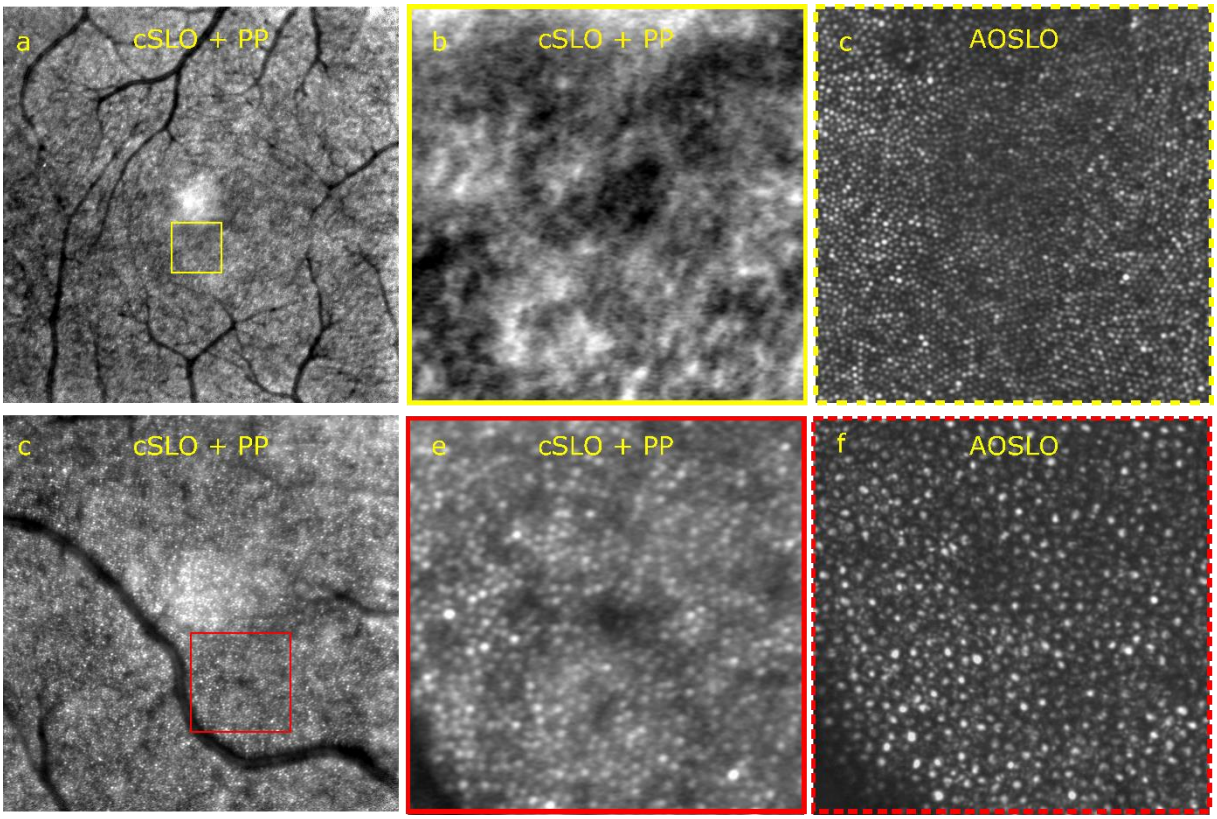

Figure 3.21. Comparison of high-magnification retinal images of cSLO with phase plates in non-mydriasis eyes and AOSLO retinal images in mydriasis eyes (Participant 2). FOV: a- 8 deg FOV; c- 4 deg FOV; b, c, d, e- 1 deg FOV. PP- Phase Plates

3.3 Conclusion and Discussion

In this study, we evaluated the feasibility of compact custom phase plates to improve the retinal image quality for patients suffering from ocular aberrations. We used a compact aberration compensation unit with "phase plates" on a clinical cSLO device. Our results showed that lower-order aberrations such as astigmatism can be well compensated with the custom phase plates produced by the MSI technique. The cone photoreceptors were resolved better with phase plates than without, and image quality was comparable to eyeglasses. In clinical practice, astigmatic patients' retinal images are typically acquired with eyeglasses, which can cause glare or reflections. To avoid this, phase plates can be used to obtain high-quality retinal images at a cellular level. However, we did not evaluate the impact of retinal imaging with contact lenses, and it may be worth further study to see how the axial displacement of eyeglasses (14 mm) affects image quality compared to contact lenses which sit on the corneal surface.
Furthermore, the performance of custom phase plates in compensating for total ocular aberrations, including both lower and HOAs, was evaluated in eyes with both mydriasis and non-mydriasis. The reason for this is to evaluate the impact of HOAs on image quality in larger pupil sizes and to achieve diffraction-limited imaging with the use of phase plates. When it comes to retinal imaging, the size of the pupil can greatly affect the quality of the images. A larger pupil size can improve the signal-to-noise ratio and increase the contrast of the images, which is crucial for seeing fine details and diagnosing certain retinal conditions or abnormalities. However, larger pupil sizes can also limit the resolution of the images due to diffraction. On the other hand, a smaller pupil size can minimize the effects of diffraction but still requires enough light to produce high-quality images. In this study, the effectiveness of using phase plates to achieve high-resolution retinal images was evaluated. The phase plates were used to compensate for aberrations and were expected to improve the resolution of the images. The results of retinal imaging with phase plates on eyes with mydriasis showed an improvement in image quality and distinct visualization of cone photoreceptors compared to images acquired without a phase plate. The use of phase plates resulted in a significant improvement in retinal image quality. This supports our hypothesis that phase plates can compensate for wavefront aberrations and produce high-quality and high-contrast images from eyes with aberrations. Despite careful examination, it was not possible to discern a difference in image quality between the images taken with and without phase plates in non-mydriasis eyes. Although the histogram and intensity profile suggest a minor improvement in contrast with the use of phase plates, a quantitative assessment is needed to confirm this and determine any improvement in resolution. Despite the lack of quantifiable improvement in image quality, the cone photoreceptors were visible at distances of ≥ 2 degrees from the fovea using a cSLO with an HMO lens. Comparing the retinal image quality between eyes with mydriasis and non-mydriasis, it is clear that there is an improvement in retinal image quality with mydriasis eyes, while it is not possible to determine the improvement with phase plates in non-mydriasis eyes. However, the cone photoreceptors were observed to be of equivalent or sometimes even better quality in non-mydriasis eyes compared to mydriasis eyes. Additionally, it was noted that the bright spot caused by the reflection from the HMO lens was reduced in mydriasis eyes compared to non-mydriasis eyes. This reflection is primarily caused by the size of the laser beam and can be eliminated through better lens coating or by subtracting the reflection digitally (See Appendix).
In participant 1, aberration compensation was performed using phase plates for only astigmatism (Figure 3.7) and total ocular aberrations (Figure 3.16). Both phase plates demonstrated that they could compensate for ocular aberrations and improve retinal

image quality. The cone photoreceptors were better visualized with the use of phase plates in both cases. In eyes with mydriasis, the cone photoreceptors were better resolved with phase plates compared to eyeglasses. The participant (P1) had a defocus of 5.52 microns, an astigmatism of 2.17, and an HOAs of 0.78 microns. Many deformable mirrors used in AOSLO systems have limitations in compensating for a large number of lower-order aberrations, and patients with a large amount of defocus and astigmatism need to wear eyeglasses or contact lenses to allow the deformable mirror to use its available stroke to compensate for HOAs. In this study, defocus is not included in the phase plates since it can be adjusted within the cSLO system. This supports that custom phase plates with cSLO device can compensate for a larger number of lower-order aberrations and the HOAs using a single plate. Overall, this technique can be used for clinical research without the need for adaptive optics and allows for a large field of view compared to adaptive optics.

It is known that both the size of the pupil and the wavelength of light can affect the diffraction limit of an optical system, which determines the resolution. In general, a larger pupil size can improve the resolution of the system, but there is a limit to the improvement that can be achieved, and the resolution will not improve further when the pupil size is larger than the diffraction limit. Similarly, a shorter wavelength of light can improve the resolution of the system, but there is a limit to the improvement that can be achieved, and the resolution will not improve further as the wavelength becomes shorter than the diffraction limit. The cSLO with HMO lens used in this study uses a laser of wavelength 815 nm (longer wavelength), and the retinal image quality was achieved better in non-mydriasis eyes. In general, a smaller pupil size results in higher spatial resolution and it allows for a more focused beam of light to illuminate the retina. But a smaller pupil size also reduces the amount of light that is detected, which can result in lower signal-noise-ratio and a decrease in contrast. From the results, it appears that better image quality visualizing the cone photoreceptors can be achieved with the NIR light with smaller pupil sizes for the cSLO and HMO lens in healthy subjects, and the current phase plates are not able to correct for aberrations in the peripheral parts of the eye.

Contrary to previous findings, the cSLO with an HMO lens was unable to acquire retinal images in the non-mydriatic eye of participant 4. Retinal imaging for this participant could only be achieved after dilating the pupil. This may be due to the participant eye having lower transparency than normal eyes, resulting in a poor signal-to-noise ratio and an inability to acquire an image without dilation. Even with dilated pupils, the cone photoreceptors were not resolved with or without the use of phase plates. Only the retinal vasculatures were visible in the images, making it difficult to determine any improvement in image quality. However, retinal images with and without pupil dilation were successfully obtained for the other five participants. Given the limited number of study participants and the small number of participants with HOAs, it is challenging to estimate the effectiveness of phase plates on the broader population of patients with ocular aberrations. However, the preliminary study results suggest that phase plates can compensate for aberrations and improve retinal image quality. We propose that using green light for retinal imaging and a larger pupil size may improve image quality and visualization of microstructures in participant 4. Green light minimizes scattering and absorption, making it particularly beneficial for imaging blood vessels and nerve fibers. Initial results from using green light with cSLO and HMO lens show an improvement in visualization of retinal microstructures in both non-mydriasis (Figure 3.22) and mydriasis eyes (Figure 3.23). The retinal vasculatures were better resolved with green laser imaging than with NIR laser imaging, particularly in mydriasis eyes. High-

resolution green light imaging may be beneficial for patients who cannot be imaged with NIR light, but further evaluation is needed in patients with HOAs and phase plates.

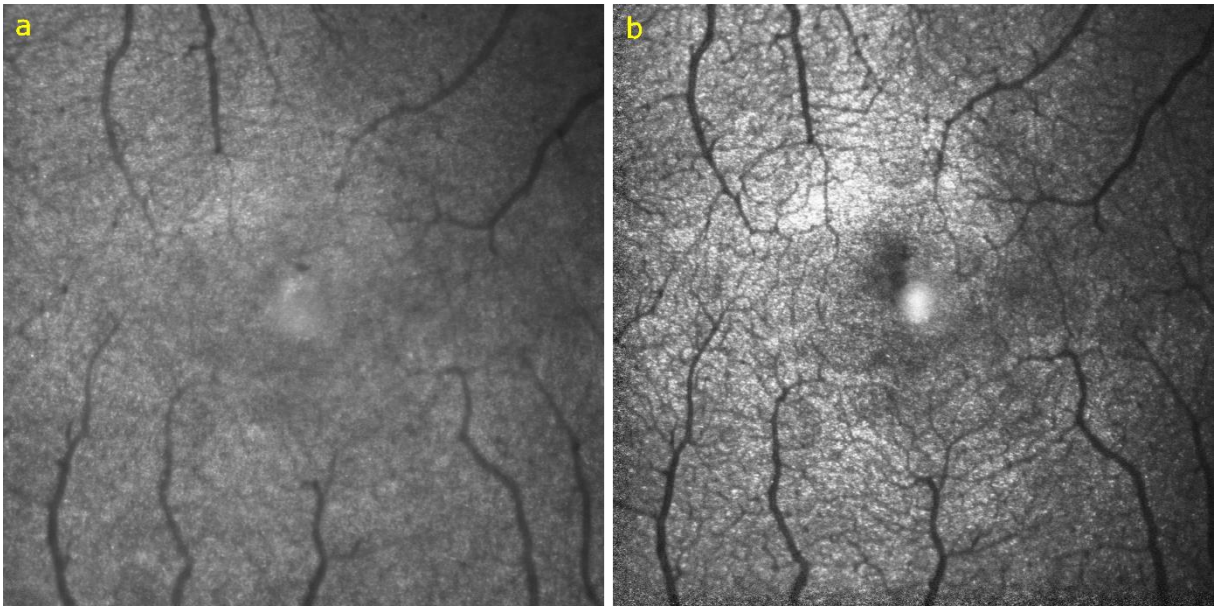

Figure 3.22. NIR laser (a) and green laser (b) retinal imaging on the non-mydriasis eye with cSLO and HMO lens from participant 3 (without contrast enhancement). FOV- 8 degree

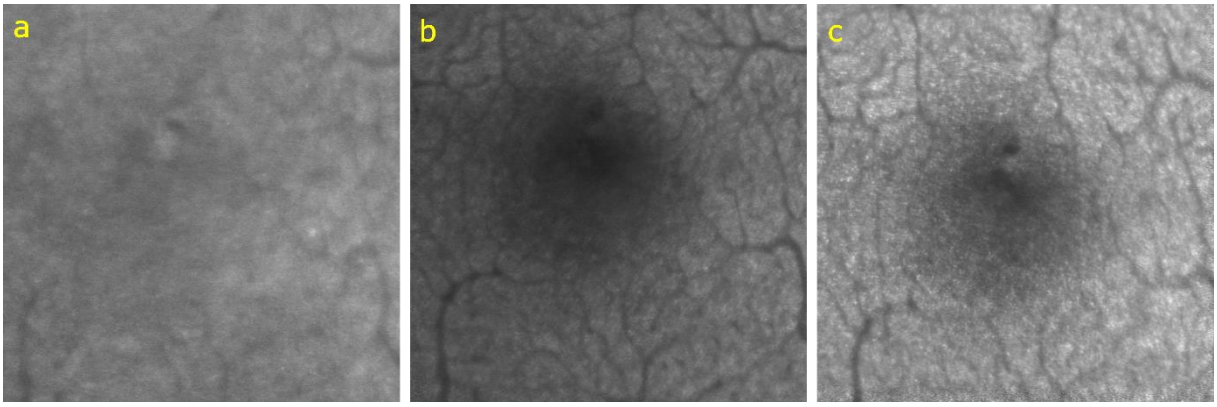

Figure 3.23. NIR laser (a) and green laser (b & c) retinal imaging with cSLO and HMO lens on the mydriasis eye from participant 3. FOV- 4 degree

In this study, we compared retinal imaging with a cSLO with and without phase plates to retinal imaging with an AOSLO. A hexagonal mosaic pattern of retinal shapes in parafoveal areas was visualized with cSLO and phase plates, supporting that cone photoreceptors can be visualized with cSLO with and without phase plates. However, direct comparison of these photoreceptors to AOSLO images cannot be made without further studying cone integrity and spacing metrics with cSLO and phase plates. The resolution of cSLO and HMO lens with or without phase plates is not equivalent to that of AOSLO, and the resolution is superior with AOSLO. The discrete patterns of photo-receptors in the fovea cannot be resolved with cSLO and phase plates. The cones are tightly packed in the fovea and require a lateral resolution of less than or equal to 1.8 microns, which the cSLO with HMO lens optical resolution does not meet even after correcting for HOAs with phase plates. This could also be due to the isoplanatic eye angle, which is 3 to 4 degrees, and the sampling density might not be sufficient to resolve small structures. Additionally, rod photoreceptors can be visualized with AOSLO, but not with cSLO and phase plates.

The AOSLO images are more detailed and capture retinal images at a higher resolution than cSLO with phase plates. The lower resolution of cSLO with HMO lens and phase plates may also lead to the appearance of neighboring cones as a single cone. The cone density and spacing of cone photoreceptors between cSLO with HMO lens and phase plates and AOSLO must be studied further to accurately assess pathology when compared to conventional clinical measures of retinal structure and function. One of the main advantages of AOSLO is its ability to correct dynamic aberrations, while phase plates can only correct static aberrations. The correction of dynamic aberrations is crucial, especially for larger pupils and HOAs. Dynamic aberrations are caused by tear films and even AOSLO sometimes struggles to correct high spatial aberrations caused by tear film breakup. A significant benefit of dynamic aberration correction with adaptive optics is that it can correct aberrations even when the pupil is off center to the imaging axis. In contrast, phase plates cannot correct pupils off center, for example when imaging the peripheral retina, the subject must rotate their eye and oblique aberrations might further degrade image quality. With blinking or artificial tears, better image quality can be achieved with phase plates, but it cannot be equivalent to AOSLO. The larger FOV (8°) with cSLO and phase plate to image the cone photoreceptors could be an advantage in a clinical routine. The advantages of phase plates are that it could be easily integrated into clinical systems since the phase plates are smaller in size, less complex, and not expensive compared to the AOSLO. In this study, a custom phase plate was manufactured at a cost of approximately 500 Euros, which could potentially be produced at a lower cost of around 100-200 Euros when manufactured in bulk. The time required to acquire images with phase plates is minimal (20-30 minutes) compared to AO systems (45 minutes to 1.5 hours with a bite bar). It is important to note that there are AOSLO systems that use standard head mounts, however, in this study, the custom AOSLO device used a bite bar. While the process of acquiring each image with a phase plate is instantaneous, it takes an additional 10-15 minutes per imaging session to find the optimal position by realigning and adjusting the focus to locate the photoreceptors.

There are limitations to this study that should be acknowledged. Although the improvement in visualization of cone photoreceptors was better with phase plates in mydriasis eyes, the difference in improvement cannot be determined in non-mydriasis eyes due to the qualitative analysis of images only. A quantitative analysis is crucial for interpreting the data objectively and unbiasedly. Image contrast can be quantified as a metric since there is a difference in contrast with and without phase plates in retinal images. A comparison of contrast between the images would have highly strengthened the work and confirmed the efficiency of phase plates. Further cone density and spacing metrics between the cSLO and AOSLO can be compared and quantified. It is also important to note that while phase plates have benefits, they are not suggested as a replacement for adaptive optics systems. Both AOSLO and cSLO with HMO lens and phase plates can be useful for the diagnosis and monitoring of eye conditions.

Another limitation of the study is the small number of participants enrolled. Additionally, most of the participants had minimal HOAs in their eyes. Out of the six participants, only one had significant HOAs and one had moderate astigmatism. The other four participants' eyes were considered healthy and normal. Despite this, the phase plates still showed improvement in visualizing cone photoreceptors in mydriasis eyes even in these healthy eyes. However, the phase plates failed to improve the visualization of cone photoreceptors in the HOAs participant's eye (P4). However, in a bench test, the same phase plate showed improvement in image quality (Figure 2.11). The phase plates were able to compensate for static aberrations, but it was not determined if this would be the case in a real eye. Additionally, the eye data of participant 4 may have

been too complex for aberration compensation with phase plates at the current stage of development. The participant had undergone a 9-diopter LASIK procedure, followed by a 2-diopter INTRACOR presbyopia correction, a subsequent Photorefractive keratectomy astigmatism correction, and a cataract procedure. Even with commercial aberrometers, it can be difficult to measure the aberrations in an eye with such a complex history. Due to restrictions caused by COVID-19, AOSLO images from this participant were not obtained which would have added value to the study. With only one participant with HOAs, it is difficult to determine the efficiency of phase plates in compensating for HOAs in human eyes. Further evaluation of HOAs and quantification is needed to better estimate the impact of phase plates in retinal imaging. However, if more participants with HOAs had been enrolled, it would have strengthened the results of the study.

Additionally, ocular aberration measurements are not typically part of retina clinical routines, making it challenging to identify potential participants with suitable HOAs. It requires integrating the aberrometer into the regular consultation and waiting until a subject with HOAs appears in the database, which is not practical and time-consuming. Due to these challenges and time limitations, the quantitative analysis and study of HOAs were not achieved in this study. However, given more time, these could have been achieved.

Another limitation of the study is that the pupil diameter was not measured during the retinal imaging, making it unknown what the pupil size of the participants was during imaging. Pupil size data is only available with ocular aberration measurements, and the phase plates were manufactured based on this pupil size data. Measuring the pupil size would have helped to determine the influence of phase plates in non-mydriatic eyes, as pupil size can vary significantly among subjects. The SPECTRALIS cSLO used in this study has an anterior segment lens that can measure pupil size, and this could have been used in this study. Pupil size is an important factor to consider when evaluating the impact of phase plates, and it should be taken into account in future research.

The positioning of the phase plates is crucial to compensate for aberrations. In this study, the phase plates were positioned at the exit pupil of the HMO lens, resulting in a 10-15 mm distance from the cornea, which could introduce residual aberrations. As discussed in chapter 2, for optimal results, the phase plates should be positioned at the eye's pupil plane. However, this is not possible with the current setup. The phase plate unit does not determine the pupil position, and the operator needs to align the camera with the pupil and move the camera forward. A careful alignment of the phase plates to the pupil center is crucial to minimize the residual aberrations and achieve optimal image quality.

Some of the limitations in achieving high-resolution images with cSLO and HMO lens include the confocal pinhole size and laser beam. The pinhole is used in confocal technique to reject out-of-focus light and improve the spatial resolution of the system. Reducing the pinhole size increases the spatial resolution and allows visualization of finer details, but also reduces the amount of light detected, resulting in lower signal-to-noise ratio and decreased contrast. To improve resolution for high-resolution retinal imaging of microstructures, a smaller pinhole size could be used. Currently, the cSLO uses a larger pinhole (100 µm) before the detector and replacing that with a smaller pinhole size (optimal: ~ 20 to 30 µm) would improve the resolution. Additionally, the beam diameter also has a significant impact on the spatial resolution and overall image quality. A smaller beam diameter will result in higher spatial resolution. The beam diameter of cSLO with HMO lens is 6 mm and reducing the beam diameter to 2.5 mm or lower at the eye pupil would optimize the spatial resolution[19]. The laser beam of size 6 mm

might not be optimal for high-resolution imaging since larger beam diameter yields poor diffraction-limited PSF. However, it should be noted that the beam diameter in cSLO changes with defocus adjustment, due to the optical setup of the device since the eye acts as the objective lens in cSLO imaging. The phase plates currently used do not include a defocus value, so the impact of not including the defocus needs to be evaluated further to study the impact of cSLO beam diameter at different focal lengths with phase plates. This evaluation could provide insight into potential improvements in the cSLO (SPECTRALIS) device to achieve better image quality.
During the study, a real-world scenario for custom phase plates was considered. In a clinical setting, phase plates could be used in the following way: The clinical team and researchers would identify eligible candidates. On the first visit, the participants would undergo screening with an aberrometer and cSLO with HMO lens to evaluate if good retinal imaging can be acquired without aberration correction. The aberrometer data would then be sent to the manufacturer/distributor to produce a custom phase plate. Once manufactured, the phase plates would be shipped to the respective clinics within one or two weeks. The patients would then be scheduled for a second visit for retinal examination with the custom-made phase plates. Since the phase plates are custom-made for each patient, they can carry their plates for follow-up visits instead of storing them at clinics. It's important to consider that ocular aberrations can change over time, especially for certain conditions such as age-related changes or development of certain diseases. Therefore, for a long-term treatment, it would be necessary to regularly re-evaluate the patients' ocular aberrations and potentially create new custom phase plates to ensure optimal imaging quality. This could be done by incorporating regular follow-up visits with aberrometer measurements as a part of the treatment plan.
The method of custom phase plates has been shown to be effective with the cSLO device, but there is still room for further improvements in the future. Some potential next steps could include:

- Conducting further studies to evaluate the effectiveness of retinal imaging with phase plates in patients with significant HOAs and quantifying the data. Incorporating offset values (residual aberrations due to distance from eye to phase plates, tilt of phase plates) into the phase plates during manufacturing. This was not done in the current study. Improving the manufacturing process to allow the phase plates to compensate for more waves. Currently, the phase plates can compensate for up to 17 waves at 635 nm, but this can be improved to 35 waves with a longer processing time[159]. Adding a wavefront sensor to the cSLO device to aid in aligning the phase plates to the eye's pupil center. An external aberrometer was used for ocular measurements in the current study, but a wavefront sensor would allow measuring both the system and eye aberrations together and including these aberrations in the phase plates. However, this would increase the cost of the cSLO device but would be beneficial for clinics that do not have a commercial aberrometer.
- The phase plates can be used to improve the lateral resolution of OCT imaging when used with a cSLO device equipped with an HMO lens. Currently, cSLO with HMO lens does not allow for OCT imaging because the reference arm is set for a standard objective lens but extending the reference arm would enable it. This would provide an advantage over commercially available AOSLO systems, for example, the RTX-1 (Imagine Eyes, Orsay, France) adaptive optics system which do not provide OCT imaging and have a smaller FOV (4 degree) compared to cSLO with HMO lens. Both, cSLO with HMO lens and RTX-1 cannot resolve foveal cones. Therefore, extending the HMO lens to OCT imaging will be an advantage for cSLO devices with multimodality options.

- The phase plates have the potential to be used in other imaging modalities such as two-photon imaging to enable sub-diffraction imaging and aberration-free imaging. They could also be evaluated for selective retinal therapy[172] (SRT) as the laser can be focused precisely on the retina by compensating for the aberrations of the human eye. Combining SRT with two-photon ophthalmoscopy and phase plates holds the potential to advance SRT treatment for future applications. The two-photon principle allows the laser to be focused more precisely on the RPE without radiating other retinal tissue layers. A new technique called Refractive Index Shaping[173] (RIS) has been developed, which uses femtosecond laser pulses to change the refractive characteristics of a polymeric material without cutting it. The RIS-lens is a gradient lens, with the related refractive index change generated by the instantaneous energy of the laser pulse, which is regulated by an acousto-optic modulator at approx. 1 MHz speed. The RIS procedure is accomplished in approximately 2 minutes. This technique could be used to manufacture phase plates at a rate of 50,000 to 100,000 per year on one laser station. Since the laser writer is identical to the clinical instrument for surgery RIS procedures (Perfect Lens, LLC, Irvine, CA), the installation of RIS-phase plate-manufacturing systems on clinical sites could be envisioned, allowing for rapid on-site manufacturing of custom phase plates.

The phase plate technique holds potential for future applications in various areas with further developments. In mydriasis eyes, the phase plates have the potential to correct for about 3/4 of aberrations that would be corrected by adaptive optics. However, the actual benefit of phase plates in non-mydriasis eyes is currently unclear apart from specific pathologic clinical cases like for instance abnormal corneal conditions like corneal transplants and keratoconus, and in patients with conventional laser refractive surgery and intraocular implants due to the presence of post-surgical HOAs[174-176].

The cSLO with HMO lens resolves photoreceptors, retinal nerve fiber layer bundles, and microvasculatures, which could provide a unique insight into the progression of certain retinal diseases like retinal degenerations[177-180], diabetes[181-183], and retinitis pigmentosa[184, 185]. It could also benefit patients with macular diseases since HOAs are higher in eyes with a macular disease than in eyes without a macular disease[186]. The clinical value of phase plates, adaptive optics, and generally improving SLO image quality, contrast, and resolution is uncertain now, but basic scientific and clinical research is currently trying to establish novel biomarkers and improved functional tests based on such imaging modalities. The cSLO with HMO lens and phase plates is a promising technique that could support research to establish biomarkers in a clinical setting. It could significantly improve retinal image quality and potentially greatly expand the high-resolution imaging of cone photoreceptors in HOAs. However, adequate testing and validation are necessary as proof of principle to achieve the same image quality with phase plates.

4 IN-VIVO TWO-PHOTON RETINAL IMAGING

The study aimed to evaluate the retina using NIR two-photon scanning laser ophthalmoscopy. The study included New Zealand white rabbits, albino rats, and brown Norway rats. The method used was two-photon imaging, which captured high-resolution, real-time images of retinal cells and their associated vasculature, as well as retinal vessels, nerve fiber layers, and non-pigmented retina with two-photon fluorescence angiography (FA) and the choroidal vasculature with two-photon indocyanine green angiography (ICGA). The study also determined the minimum laser power threshold required for two-photon fluorescence and demonstrated that high-resolution images can be acquired in real-time with a single light source without the need for additional filters for FA or ICGA. The study suggests that the combination of FA and ICGA using the two-photon ophthalmoscope can aid in characterizing retinal diseases in animal models and classifying types of choroidal neovascularization (CNV) in macular degeneration. Additionally, the prototype can be adapted to image the retina in rodents and rabbits.
Despite the widespread use of two-photon imaging in biomedical research, there have been few reports of its use for imaging the retinal microvasculature[187-189], and none for imaging the choroidal vasculature in animal models. The study aims to demonstrate the efficacy of using a 780 nm NIR femtosecond laser for these purposes. With this method, single TPEF images of the retina were achieved in a short time with a standard FOV of 20-30º, which is considered adequate for fundus imaging[190]. Another benefit of using the two-photon technique for retinal imaging is that it utilizes near-infrared (NIR) light, which is less harmful than visible light[191]. Several reports of two-photon imaging in animal models using different infrared wavelengths have been demonstrated[38, 107, 187, 190, 192-194], but limited data are available demonstrating the autofluorescence emission spectra of retinal layers. Comparatively, there is insufficient data on two-photon retinal imaging in rabbits and rats, despite their more common use as an experimental model in ophthalmic research. Overall, this study aims to provide an adequate evaluation of two-photon ophthalmoscopy as a fundus imaging method in animal models.

4.1 Materials and Methods

4.1.1 Animal Preparation

Six New Zealand white rabbits, six albino rats (Crl: CD (SD) IGS), and six brown Norway rats were used for two-photon autofluorescence imaging and two-photon FA. Four brown Norway rats were used for two-photon ICGA. Experiments were performed with one eye at a time, and the fellow eye served as the control. The experimental groups were anesthetized using isoflurane 1-3% inhalant. In addition, a drop of topical proparacaine anesthesia (Proparacaine Hydrochloride Ophthalmic solution USP, 0.5% Sterile) and a pupil dilator (0.5% tropicamide ophthalmic solution, USP) was administered to the eyes. Furthermore, sterile saline drops were administered to the test eye every 30 seconds to maintain hydration throughout the cornea.
Brown Norway rats and albino rats with jugular vein catheterization (Surgery code: JUGVEIN; Charles River Laboratories, Inc.) were used for two-photon retinal angiography. The fluorescein (10% AK- FLUOR, Akron) and indocyanine green (ICG) dyes (IC-GREEN with sterile aqueous solvent) were administered through the jugular vein catheter to characterize the retinal and choroidal vessels. For simultaneous two-photon FA and ICGA, the fluorescein and indocyanine green dyes, with a sterile aqueous

solvent of equal volume, were mixed in a single syringe and administered through the jugular vein catheter. For two-photon FA in rabbits, fluorescein (10% AK- FLUOR, Akron) was administered through an intravenous catheter at the marginal ear vein. The dosage was controlled according to the animal's body weight. All experiments were approved by the Institutional Animal Care and Use Committee (IACUC) at Loma Linda University and were performed under the Association for Research in Vision and Ophthalmology (ARVO) statement for the use of animals in ophthalmic and vision research.

4.1.2 Optical Setup of Two-Photon Scanning Laser Ophthalmoscope

Figure 4.1 shows the schematics of the experimental setup. A non-tunable customized compact femtosecond laser (MENDOCINO FIBER LASER, Model: FPL-05RFFHDB12; Calmar laser) with 780 nm, 270 fs, 50 MHz, and output powers tunable up to 500 mW was used as the light source for imaging. The linearly polarized light beam is deflected by mirrors (U-M1 and U-M2) into lenses L1 and L2 (1:1 telescope), responsible for precise focus for different scanning angles. Subsequently, the laser beam is raster scanned by a pair of galvanometric mirrors in x and y directions. The scan speed is achieved by operating the fast axis of the raster at its resonance frequency. The laser is finally focused on the retina through a set of achromatic lenses (L3, f = 50 mm and L4, f = 30 mm). The scan pupil of these lenses is placed on the pupil of the animal eye. L4 and the camera can be moved relative to one another through the focus knob (refractive adjustment). Thus, the visual acuity or focus on the retina can be precisely adjusted during recording. For example, given that most rat eyes are myopic by nature, decreasing the distance between L4 and the camera shorter can subsequently result in a divergent beam path, thereby providing an image of the retina with lesser aberrations. The tunable focal range (i.e., the distance between the camera and L4) is converted into diopters and displayed by the software (HEYEX, Heidelberg Engineering GmbH, Heidelberg, Germany).
TPEF from the retina is collected by lens L4 and passed through a dichroic mirror (Semrock, FF720-SDi01, Reflection band R_{avg} > 95% 750-875 nm, Transmission band T_{avg} > 85% 370-690 nm) and focused by a lens (L5) onto a photomultiplier tube. Backscattered laser light is further rejected by a short-pass barrier filter (Semrock, FF01-750/SP-25, Transmission band T_{avg} > 90% 380-720 nm, Blocking band OD_{avg} > 6, 750-1100 nm). The region of interest is scanned/ excited point by point using the raster. Since no TPEF is generated outside the focal volume, the confocal pinhole is eliminated. The second harmonic generation (SHG) can be captured using the same instrument by inserting a bandpass filter (Semrock, FF01-390/ 18-25, Transmission band T_{avg} > 90% 381-399 nm, center wavelength 390 nm and guaranteed minimum bandwidth 18 nm) in front of the photomultiplier tube.
Besides the fluorescence detection unit, the setup also provides the original confocal reflection mode of the Heidelberg Retinal Tomograph (HRT) by simply inserting a polarizing beam splitter followed by a quarter wave-plate (L/4) into the beam path. The reflected light from the retina is focused by another achromatic lens (L6) to an avalanche photodiode to generate backscattered light contrast. A confocal pinhole is slotted in front of the photodiode for better depth discrimination, conjugating to the focal plane. An electronic switch permits the change between confocal and two-photon detection modes while synchronizing to the scanning unit.

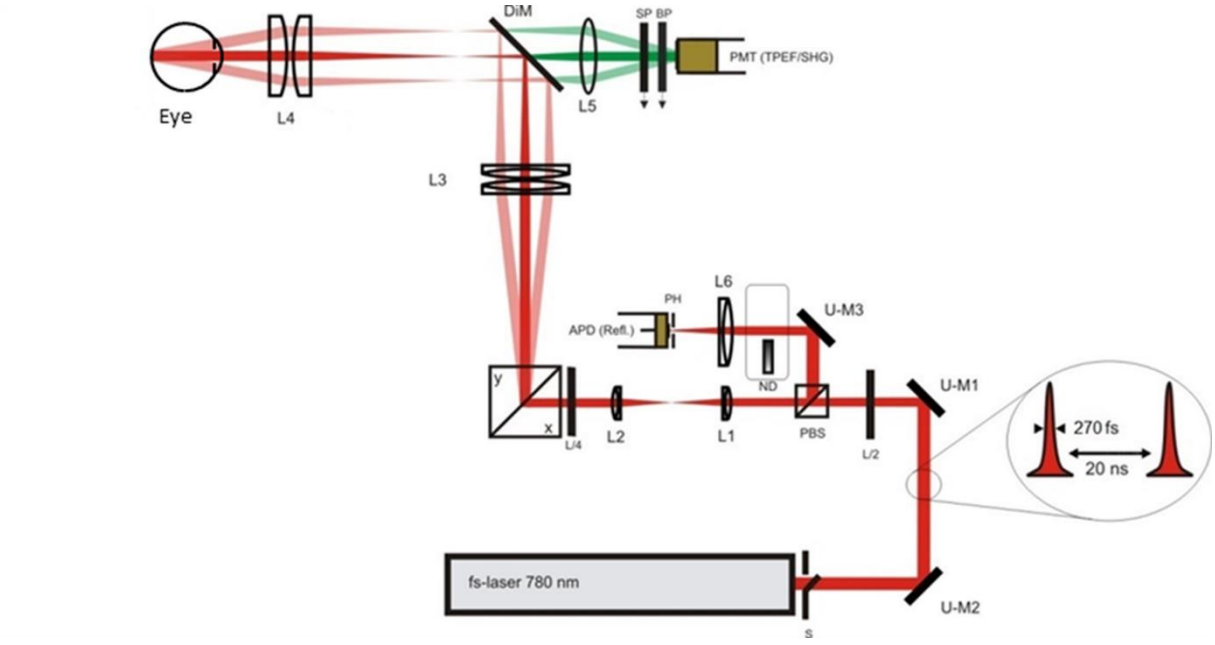

Figure 4.1. Optical setup of a two-photon ophthalmoscope based on a conventional scanning laser ophthalmoscope (Heidelberg Retinal Tomograph, HRT), the excitation path marked in red, and the fluorescence emission path marked in green. The incident and reflected light follow a coaxial path. M- mirrors, L- lenses, ND- neutral density filter, DiM- dichroic mirror, PBS- polarizing beam splitter, L/2- half wave-plate, L/4- quarter wave plate, APD- Avalanche photodiode, PMT- photomultiplier tube, SP- short pass barrier filter, BP- band pass filter.

Both the confocal reflectance and two-photon images can be captured using the same instrument in high-resolution mode and high-speed mode with 30° x 30°, 20° x 20°, and 15° x 15° transversal field-of-views (variable). Theoretically, the optical resolution of the system is 1.05 µm. The scanning frequency per frame in high-resolution mode is 5 Hz/ 7 Hz/ 9 Hz at 30°/ 20°/ 15° scan angle, whereas, in high-speed mode, the image acquisition frequency is 9 Hz/ 12.5 Hz/ 16 Hz at 30°/ 20°/ 15° scan angle respectively. Likewise, the digital image read out at the high-resolution mode is 1536 x 1536/ 1024 x 1024/ 768 x 768, and for the high-speed mode is 768 x 768/ 512 x 512/ 384 x 384. The scan time per image in high-resolution mode is 192 ms/ 128 ms/ 96 ms, and at high-speed mode is 96 ms/ 64 ms/ 48 ms. The tunable focal range is between -12 to +12 diopters (1 diopter corresponds to a focusing depth of 4 µm) spherical, and a video acquisition is possible with 6 frames per second. A stack of tomographic images (z-scans) can be automatically acquired, and the depth of the z-scan can also be adjusted. The signal-to-noise ratio of the images can be increased by frame averaging in real-time. The standard lens (L4; focal length, f = 30 mm; diameter, ϕ = 30 mm) from Heidelberg Engineering GmbH was used for rabbit retinal imaging, and an additional lens (f = 40/+25 diopter, ϕ = 40 mm) was used for rats to collect the two-photon signals. The additional lens reduces the beam diameter by 70%, which adapts the system to the shorter axial length of the rat eyes. The images were acquired in high-resolution mode with a 30° scan angle for fundus overview and a 20° and 15° scan angle for the detailed view of the retina.

4.2 Results

4.2.1 Two-Photon Autofluorescence Imaging

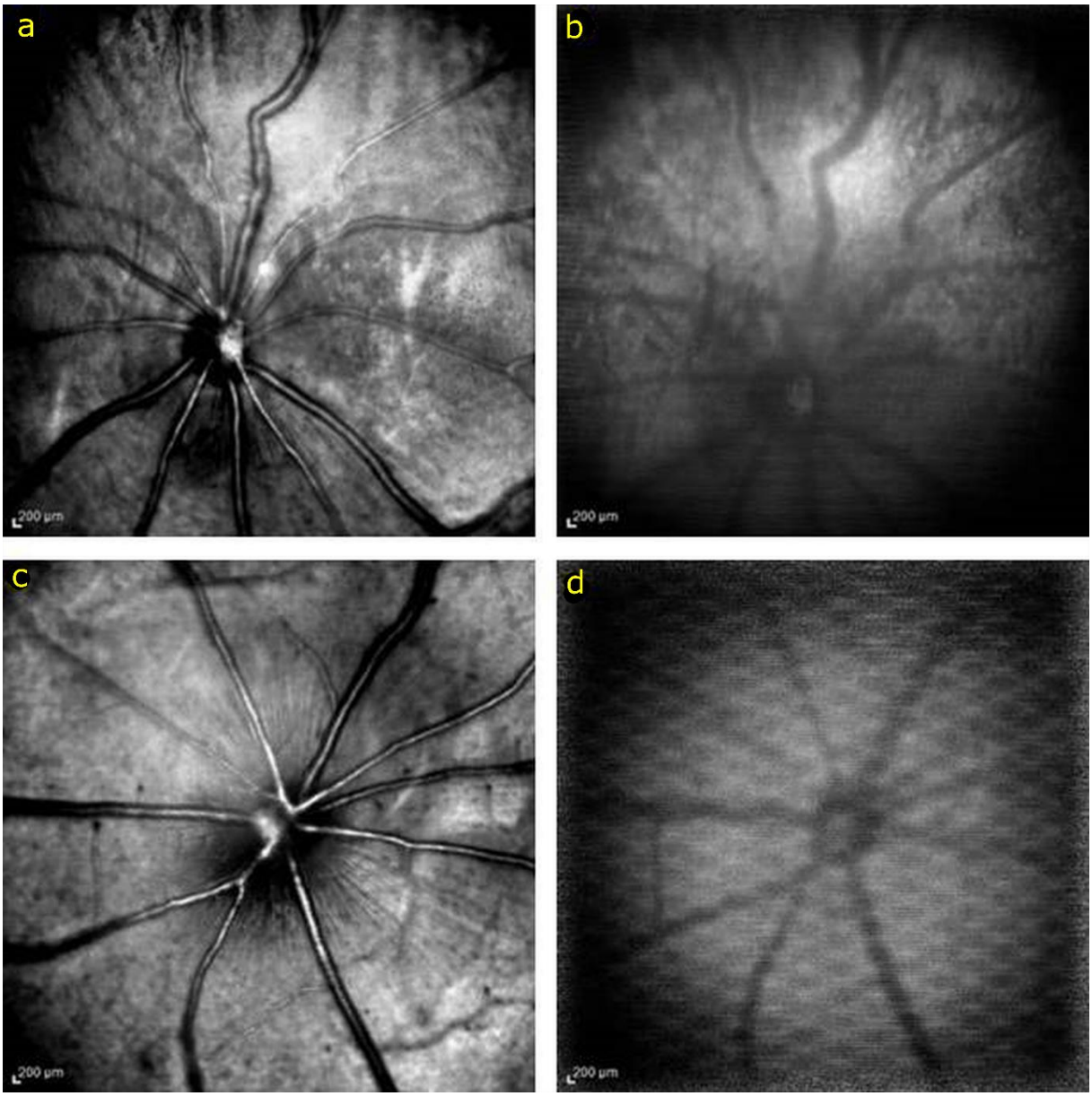

Figure 4.2. Confocal reflectance (a, c) and two-photon (b, d) autofluorescence imaging of retina from brown Norway rat. The two-photon autofluorescence imaging at ~320 mW laser power (b) and ~160 mW laser power (d). The autofluorescence images shown here were averaged through 40 frames in real-time scanning.

Figure 4.2 shows the confocal reflectance (Figure 4.2a, 4.2c) and two-photon autofluorescence (Figure 4.2b, 4.2d) images of brown Norway rat retina at a 30° scan angle. The two-photon autofluorescence was captured under real-time scanning within 100 seconds, and the blood vessels and other retinal cells emitting autofluorescence were seen. The autofluorescence retinal images (Figure 4.2b, 4.2d) represent the lipofuscin distribution in RPE. The pigmentation on the RPE layer and the choroid in the back of the eyes were also illuminated. To provide finer details, the retina was imaged with scan angles of 20º and 15° (smaller FOVs). The laser power threshold for two-photon autofluorescence imaging was also determined in this study. Since power measurement at the retina has limitations, power levels were measured at the cornea. The

minimum laser power required for autofluorescence was ~160 mW. The two-photon autofluorescence from the normal retina at ~320 mW and ~160 mW is shown in Figures 4.2b and 4.2d. The optic nerve head was dark due to the absence of lipofuscin, and the retinal vessels were dark due to the signal absorption by blood. The lipofuscin distribution in the RPE was mapped at ~320 mW (Figure 4.2b) and compared to the maps acquired at ~160 mW (Figure 4.2d). A weak but uniform autofluorescence distribution is noticed at ~160 mW, and at ~320 mW, other retinal cells emitting autofluorescence signals were visualized. Moreover, the electronic noise (lines) in Figure 4.2d showed that the overall signal-to-noise ratio was poor at lower power levels. In albino rats, no distinct autofluorescent signals were detected by two-photon imaging (Figure 4.3).

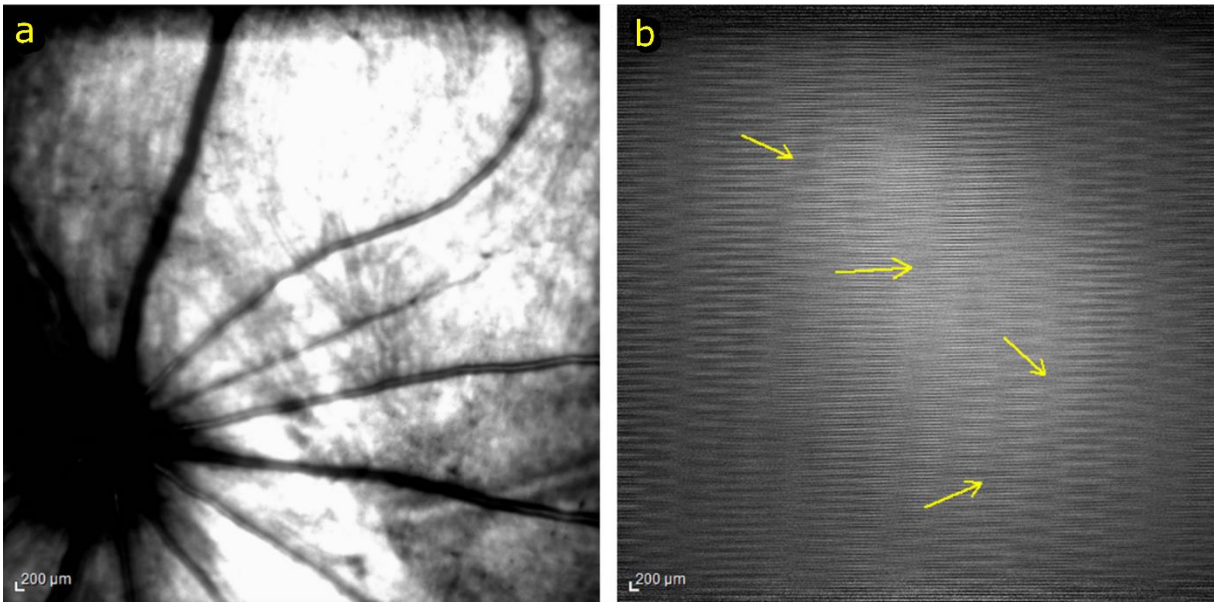

Figure 4.3. Confocal reflectance (a) and two-photon autofluorescence (b) imaging of albino rats. The two-photon image noticed the blood vessels, but no distinct autofluorescence was detected.

4.2.2 Two-Photon Fluorescein Angiography

Two-photon FA visualized the retinal vasculatures through the rabbit's and rat's eye pupils. The flow of fluorescein through the blood vessels was recorded in rabbits (Figure 4.4) and rats (Figure 4.5). The choroidal filling begins right after the injection within 3-5 seconds and is visible as a patchy pattern. Following the choroidal filling, the arteries were fluorescent, and the fluorescence images indicated the filling of veins. Later, the arteries and veins became homogeneously fluorescent. The maximum concentration of fluorescein within the choroid and retina occurs approximately 10-15 seconds after injection. In late phase FA, the fluorescence from the retinal vessels was weak, but the fluorescence images were obtained with further live frame averaging. The confocal reflectance and two-photon FA image (Figure 4.4a and 4.4b) of the New Zealand white rabbit at a 30° scan angle shows high contrast images of retinal vasculature. The bright white light on the confocal reflectance image (Figure 4.4a) was due to the surface reflection from nerve fibers. The two-photon FA demonstrated the architecture of the blood vessels owing to the increased penetration of NIR wavelengths. The non-pigmented retina with choroidal vessels was seen in two-photon FA with a 30° scan angle at ~160 mW (Figure 4.4b) and ~120 mW (Figure 4.4c). The nerve fiber layer, also autofluorescent, was seen near the optic disc. The detailed view of the retinal vasculature was achieved using a tighter 15° scan angle (Figure 4.4d). The minimum power required for two-photon FA was determined to be ~80 mW. The retinal vasculatures were also visible at ~55 mW, but the vasculatures were not distinct at this power

level. Distinct vasculatures were noticed only at ~ 80 mW. Also, the images' contrast and signal-to-noise ratio were better with higher laser power (See Figures 4.4b and 4.4c). Two-photon FA imaging also noticed electronic noise similar to the autofluorescence images at a lower power threshold.

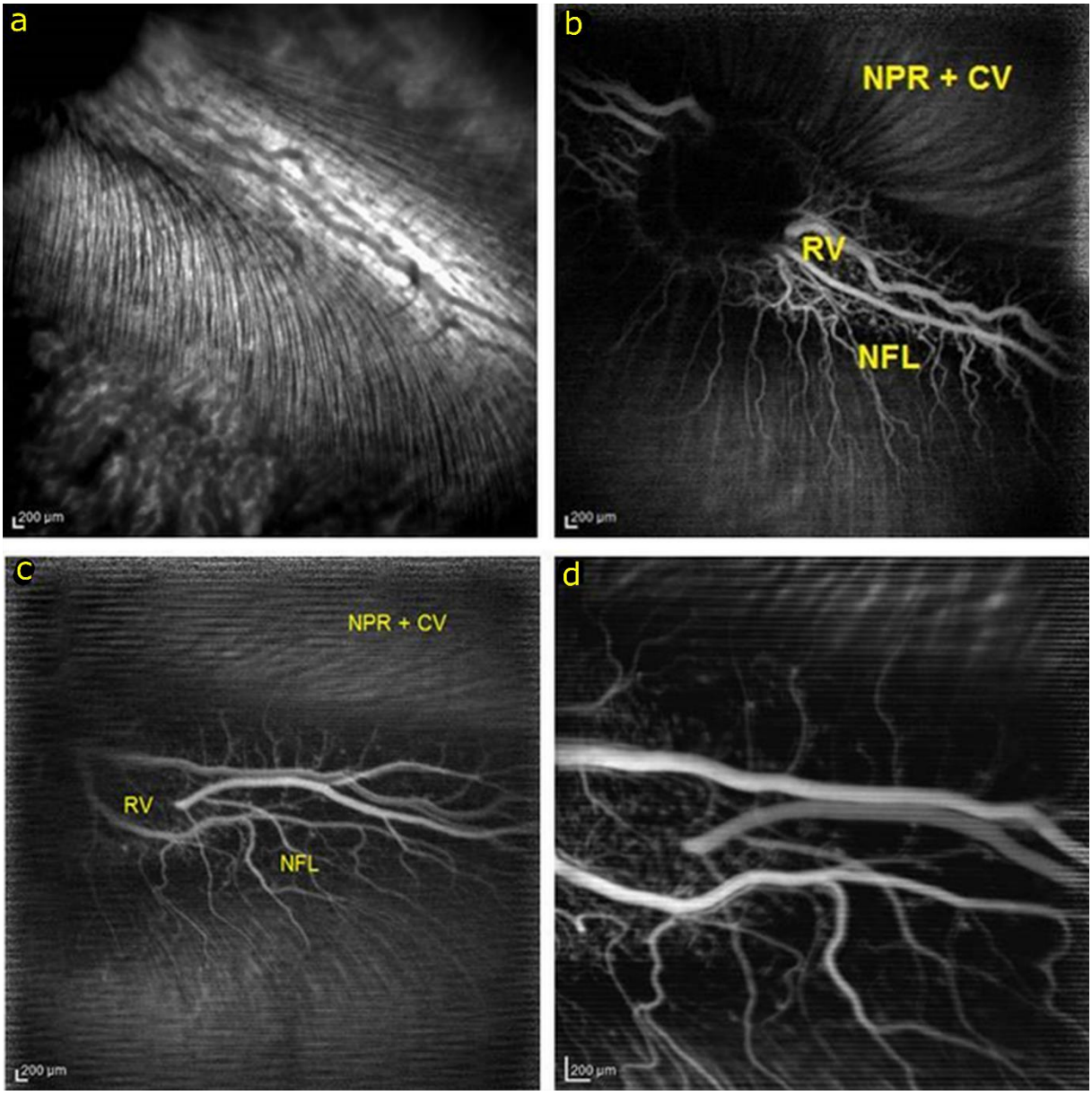

Figure 4.4. Confocal reflectance (a) and two-photon FA (b) of New Zealand white rabbit with 30° scan angle. The two-photon FA (c, d) of the rabbit retina for the scan angle 30° and 15°, the images were averaged for 20-40 frames. Retinal vessels (RV), nerve fiber layer (NFL), non-pigmented retina (NPR), and choroidal vessels (CV).

The power threshold for two-photon FA in rats was relatively similar to rabbits. The overall fundus image (Figure 4.5a) of the rat retina using the 30° scan angle at ~80 mW laser power showed the veins (Figure 4.5a, blue arrow) and arteries (Figure 4.5a, yellow arrow) that do not differ much in appearance. Dark spots (Figure 4.5a, red arrows) on the confocal reflectance image are the branching points and capillaries that run parallel to the laser. The nerve fiber layer is usually well visible in confocal reflectance mode, and the micro blood vessels and the choroid tissue behind that were determined using two-photon FA (Figure 4.5b, 4.5c, 4.5d). Two-photon FA image from the rat retina (Figure 4.5b) provided in-depth information on the blood vessel network

and surrounding tissue that fluorescein has highlighted. Also, two-photon FA yielded high-contrast images of the retinal capillaries and microvessel layers. The rat eyes' post fluorescence (Figure 4.5c and 4.5d) was also captured using two-photon FA at different time points. Two-photon FA after fluorescein injection was captured at 1 minute, 3 minutes, and 5 minutes to determine the perfusion time of fluorescein. The fluorescein was perfused through the micro vessels to the back of the retina, and by the end, most of the fluorescein was left behind in the tissues around the optic disc. This can be seen in Figure 4.5d, showing elevated levels of fluorescein around the optic disc after 5 minutes.

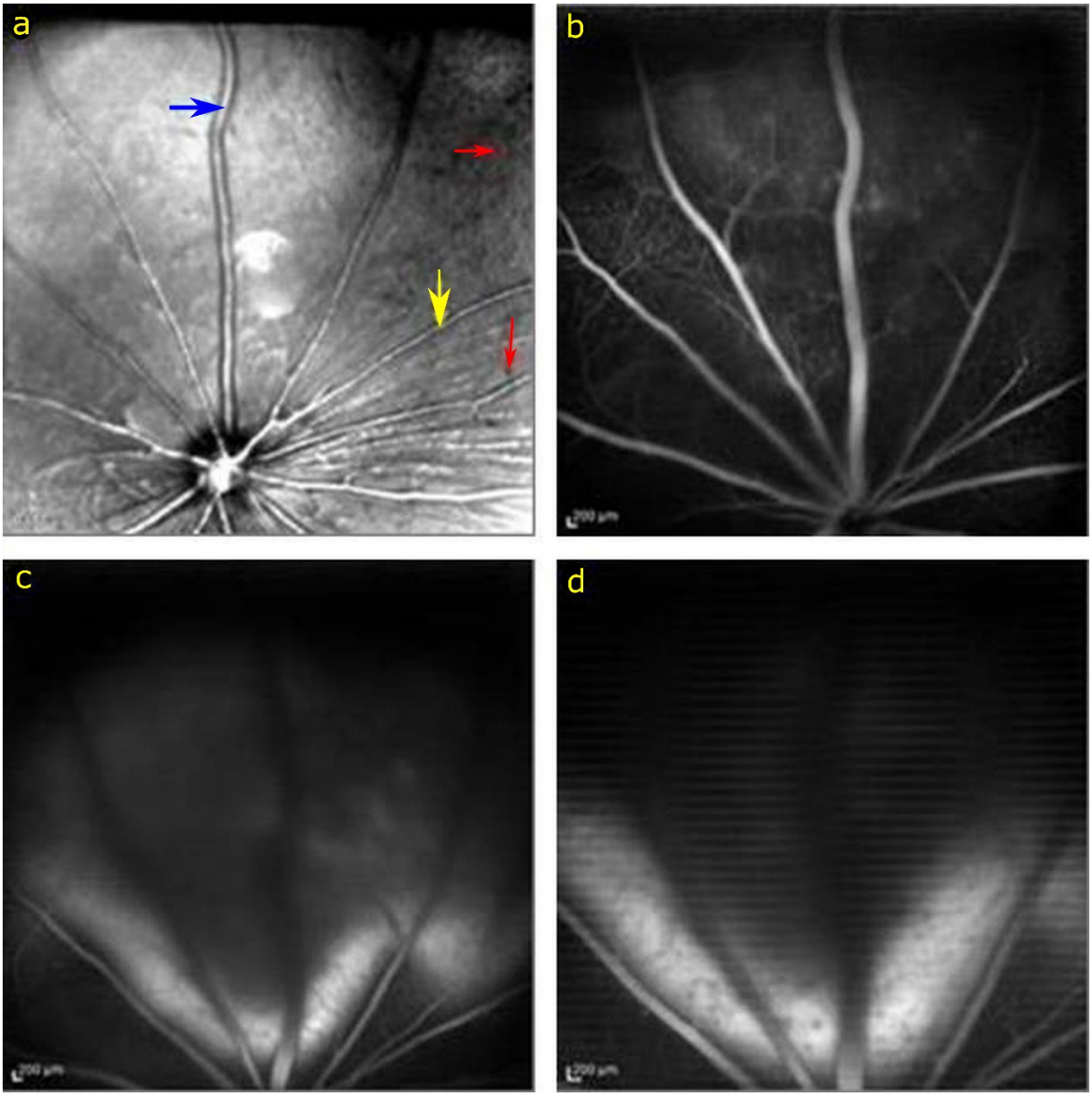

Figure 4.5. Confocal reflectance image (a) of the brown Norway rat with a 30° scan angle. Two-photon FA immediately after fluorescein injection (≤ 1 minute) at 20° scan (b), after 3 minutes at 30° scan angle (c), and after 5 minutes at 15° scan angle (d).

The flow of fluorescein through the blood vessels in brown Norway and albino rats is shown in Figures 4.6 and 4.7. Similar to rabbits, two-photon FA depicts the arterial and venous phases of fluorescein filling. The arteries were filled within 3-5 seconds after injection, and the arteriovenous filling lasted for approximately 10-15 seconds in pigmented rats (Figure 4.6). In mid-phase (2-4 minutes), the fluorescence diminishes

slowly, and with further averaging, the fluorescence images were captured. The late phase (7-10 minutes) demonstrated a graded elimination of dye from the retinal vasculatures. Comparatively, the albino rats depicted the same as pigmented rats, but the arteriovenous filling lasts only 3-5 seconds (Figure 4.7). High contrast images of retinal vasculatures and capillaries were noticed, but the filling of fluorescein in the vessels was faster than in pigmented rats.

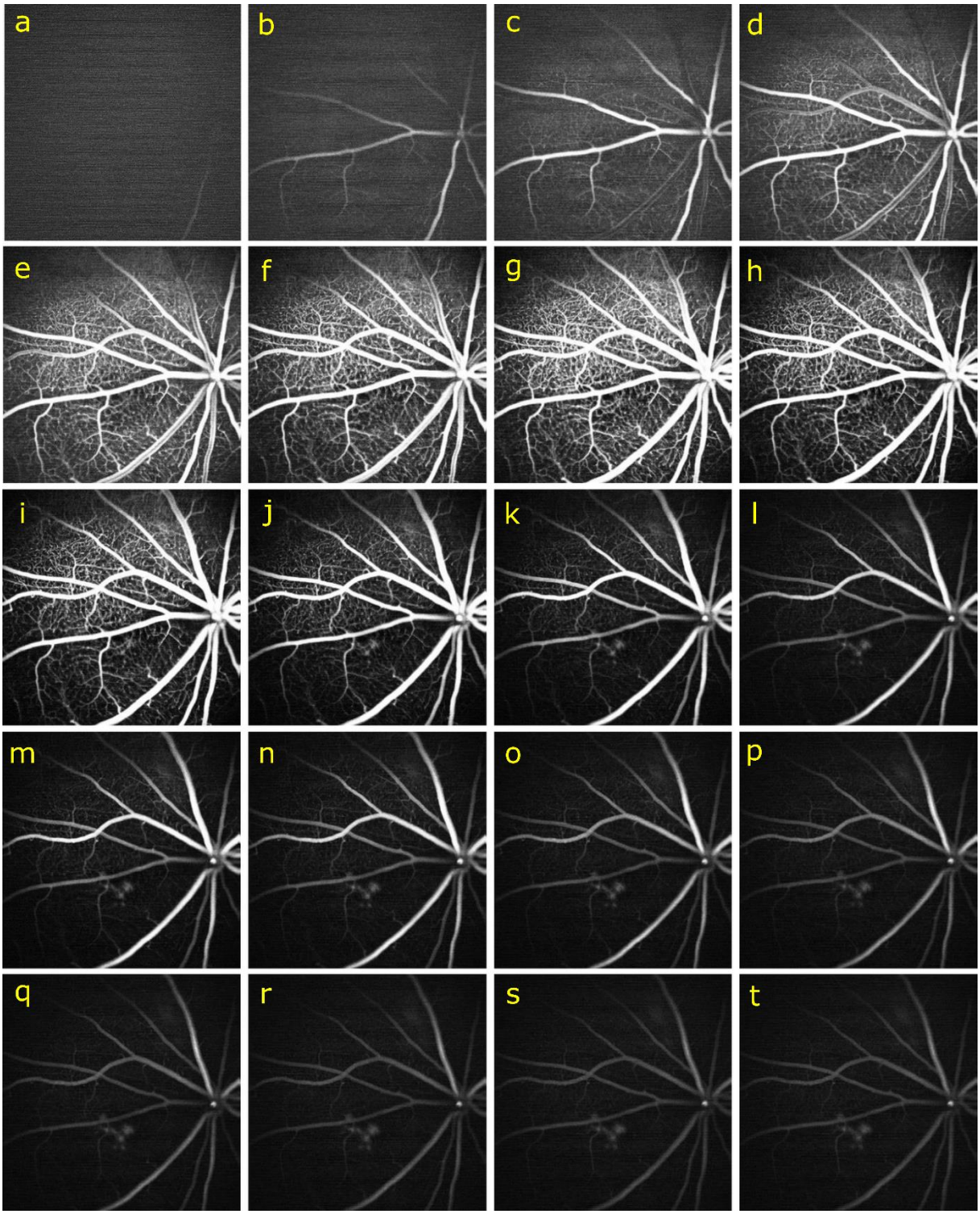

Figure 4.6. Two-photon FA of brown Norway rat retina with 30° scan angle. The two-photon video records 5 frames per second. The images shown here (a-t) were extracted from the video.

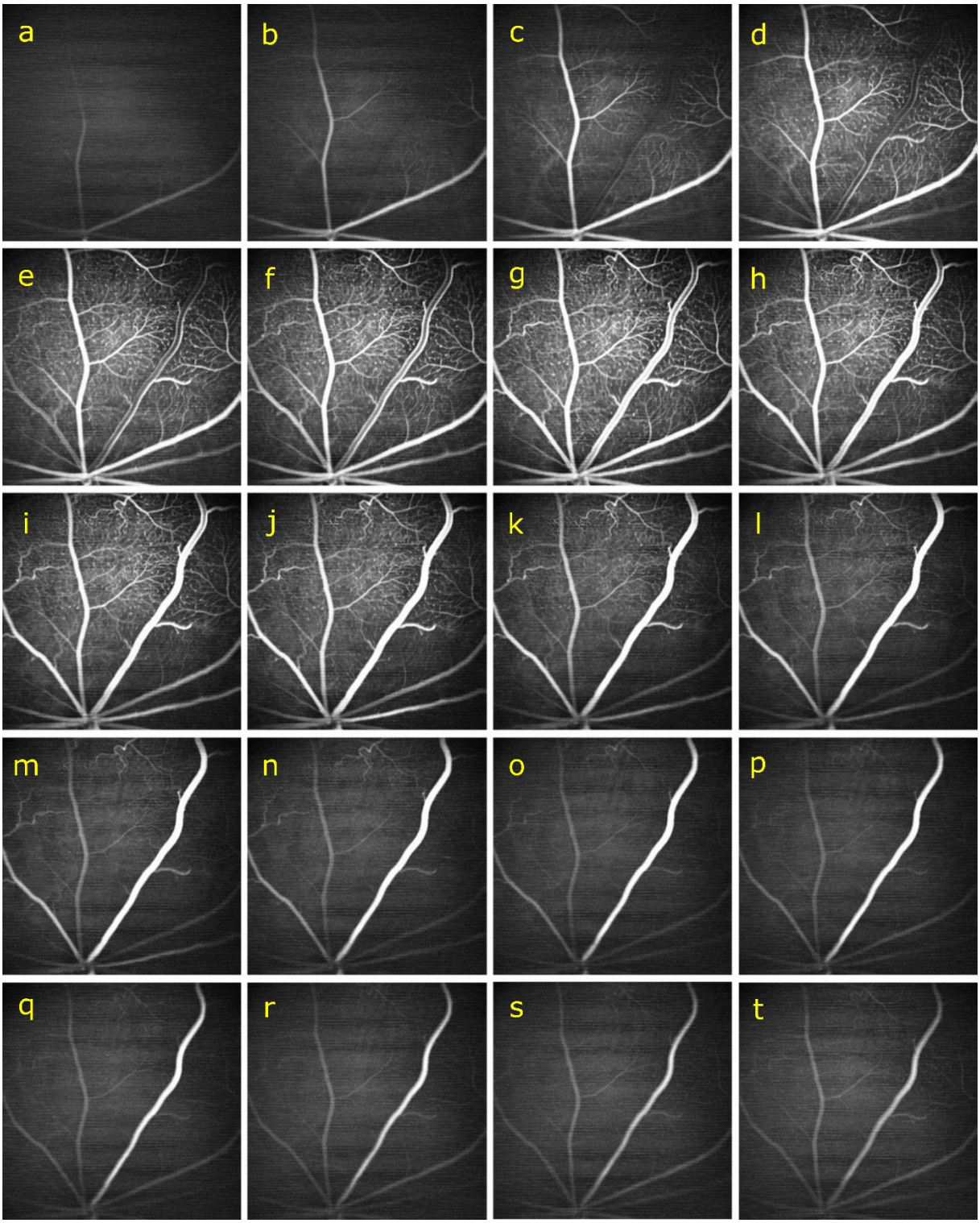

Figure 4.7. Two-photon FA of albino rat retina with 30º scan angle. The two-photon video records 5 frames per second. The images shown here (a-t) were extracted from the video.

4.2.3 Two-Photon Indocyanine Green Angiography

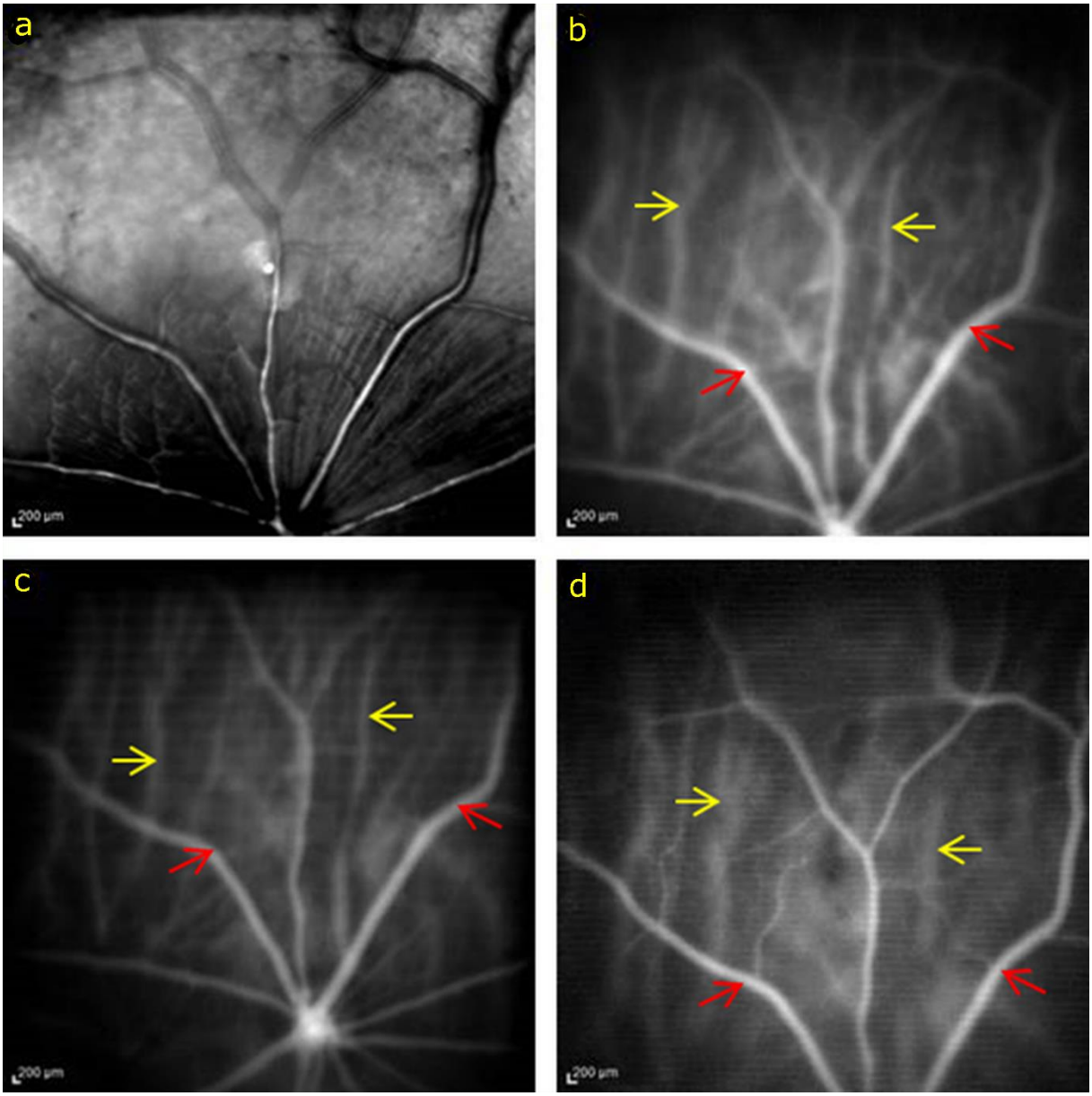

Figure 4.8. Confocal reflectance (a) image of the brown Norway rat with a 30° scan angle. Two-photon ICGA with 30° scan angle at the early phase (b), mid phase (c), and late phase (d). Red arrows represent retinal vessels, and yellow arrows represent choroidal vessels. The images were averaged through 40 frames.

ICGA images were acquired using the two-photon ophthalmoscopy. Real-time images were obtained even in the late phase. Three phases (early phase: 1-3 min, mid-phase: 5-15 min, and late phase: 18-22 min) of two-photon ICGA were recorded. The early phase (Figure 4.8b) demonstrated a bright blush of dye from the choroid, and the individual choroid vessels were well delineated. Both medium and large choroidal arteries were visualized beneath the hyperfluorescent retinal vasculature. The individual choriocapillaris was not well distinguished at this phase. A decrease in overall fluorescence was noticed in the mid-phase (Figure 4.8c), and the choroidal vessels became less distinct. The fluorescence from the retinal vessels also began to attenuate. The retinal and choroidal vessels fade in the late phase and are not visible with standard confocal ICGA. The same behavior was observed with two-photon imaging, but with frame averaging, the retinal and choroidal vessels at the late phase (Figure 4.8d) could still be

visualized. The two-photon signals from the choroid were seen for a longer time than regular ICGA. Due to the animal's movement under anesthesia and eye rotation, the two-photon ICGA images from early to late phases were not localized to the same spot. The confocal reflectance (Figure 4.8a) image was used as a reference image.

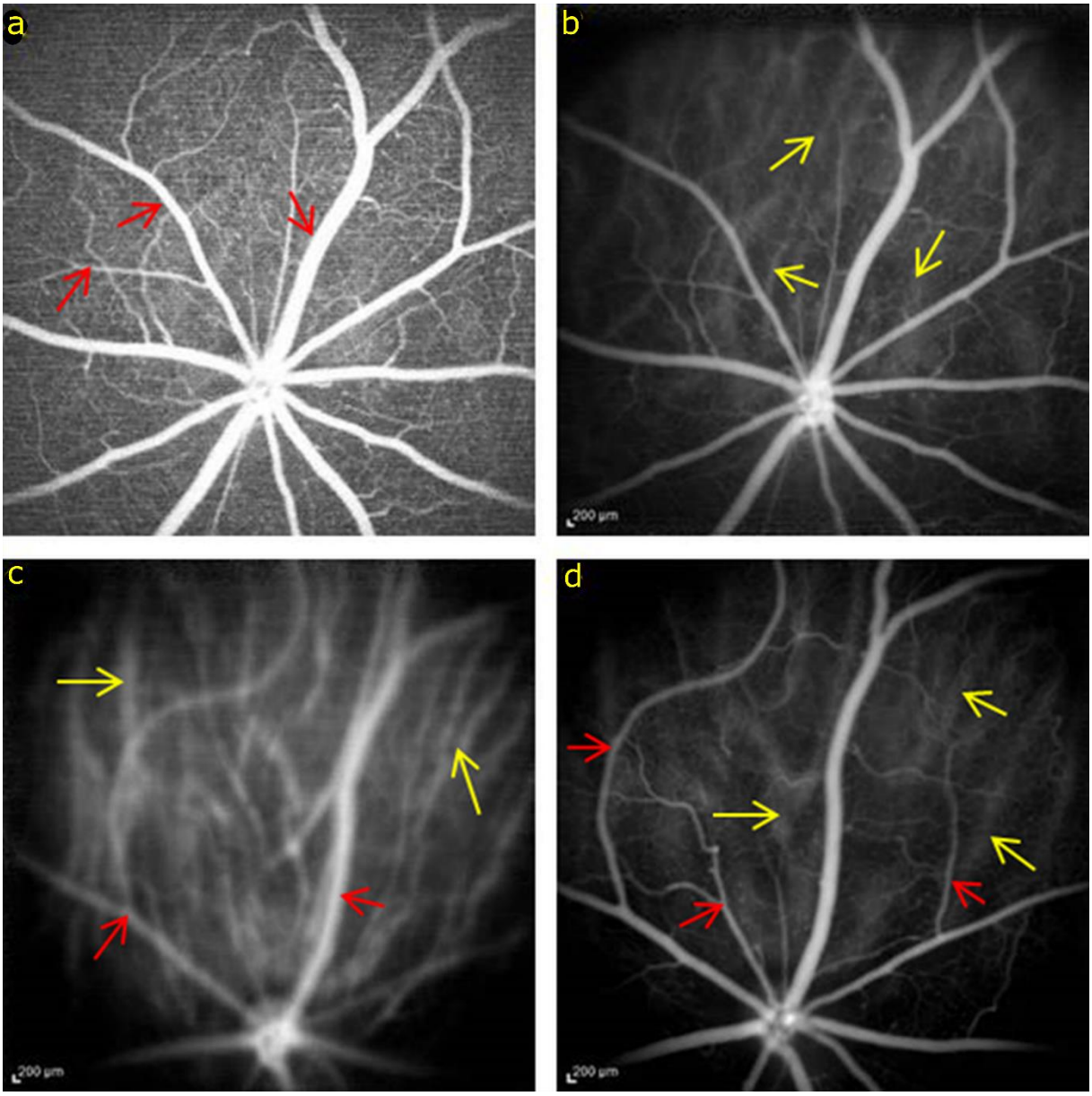

Figure 4.9. Simultaneous two-photon FA and ICGA revealed the retinal vessels (a, red arrows) immediately after the injection, and later the choroidal vessels (b, yellow arrows) were noticed. (c) The early phase two-photon ICGA, (d) the two-photon FA followed by two-photon ICGA. Red arrows represent retinal vessels, and yellow arrows represent choroidal vessels.

Furthermore, simultaneous two-photon FA and two-photon ICGA were performed to characterize the retinal and choroidal vessels with a single injection and a single light source (780 nm). Two-photon FA and two-photon ICGA were recorded to capture the immediate effect of the fluorescein and ICG flow through the vessels. The fluorescein filling of the arteriovenous phase in pigmented rats lasts for approximately 10-15 seconds, whereas with the mixture of fluorescein and ICG, the arteriovenous phase lasts approximately 40-60 seconds. High contrast images (Figure 4.9a) of retinal vasculatures were obtained. The retinal vessels and capillaries (Figure 4.9a) were seen immediately after the injection, and later the choroidal vessels (Figure 4.9b) were noticed

approximately 60 seconds later. Simultaneous FA and ICGA using two-photon ophthalmoscopy offer a longer duration of effective time than two-photon FA. The ICGA followed by FA (Figure 4.9c and 4.9d) and FA followed by ICGA exhibited both retinal and choroidal vasculatures, respectively. No significant differences were noticed in the overall detection of vasculatures. The ICGA was performed to observe the choroidal vessels (Figure 4.9c), and approximately 5 mins later, the fluorescein was administered to observe the retinal vessels (Figure 4.9d).

4.3 Conclusion and Discussion

We evaluated the efficacy of utilizing 780 nm, 270 fs, NIR laser for multimodal two-photon retina imaging. TPEF imaging at 780 nm allows multimodal fundus imaging in rabbits and rats with high quality and contrast. TPEF images of the retina with a FOV of 23° were reported in previous studies. For significant fundus imaging, 20º-30º FOV is required[190], which was established with our TPEF prototype (15º, 20º, and 30º). A uniform distribution of the autofluorescence signal was observed in pigmented rats (Figure 4.2), and no distinct autofluorescence signals were detected in albino rats. The retinal autofluorescence is mainly from RPE. Melanin and lipofuscin are two primary pigments in RPE for fundus autofluorescence. Stronger autofluorescence signals correlate with lipofuscin concentration. Although lipofuscin was present in albino rats, only weak autofluorescence signals with less detail of blood vessels were observed. The weak two-photon autofluorescence in albinos may be due to the absence of melanin or strong intraocular light scattering. Thus, the degree of pigmentation influences the two-photon autofluorescence imaging in pigmented and albino rats. On the contrary, by confocal imaging, no difference in signal intensities was noticed between the pigmented and albino mice[195]. Recently, Boguslawski et.al. reported an in vivo two-photon retinal imaging in human eyes in two healthy subjects with a safe laser power level of only 0.3 mW[196]. The fundus two-photon autofluorescence images from the human eyes (100 frames) observed similar to the autofluorescence images from rat eyes (100 frames) presented in this thesis.

One of the main challenges encountered in acquiring two-photon autofluorescence from rats was the optical quality of the rat eyes. The rat eyes are myopic; therefore, each rat eye's optical quality varies greatly. Other challenges include small pupil diameter along with the artifacts from respiration, muscle twitching, and heart rate of the rats under anesthesia[197]. The images reflected specific inevitable movements, yet we captured the two-photon autofluorescence from the rat's eyes. The images collected from one frame to the next were not fully aligned due to the breathing motion of the anesthetized rats. Therefore, some images were averaged through 20-40 frames for optimum image quality, but no additional post-processing was performed. In this study, contact lenses were not utilized. However, the use of contact lenses could have led to better image quality, corneal protection, less eye movement, and correction of refractive errors.

Two-photon FA was sufficient to resolve the microvasculature of the retina. Retinal vessels and capillaries were distinct with two-photon FA, and the same quality images were observed in both pigmented and albinos. The two-photon FA can overcome some of the limitations of conventional FA techniques in small animal models. For instance, FA in albinos with confocal imaging is affected by the background fluorescence from the choroid[195], which two-photon FA can eliminate since two-photon excitation eliminates the background fluorescence.

Two-photon ICGA was performed using the ICG dye labeling. The ICG dye has its principal singlet (S1) absorption maxima at 779 nm and emission maxima at 820 nm (Figure 4.10a). So, in principle, a laser at ~1552 nm is required for the two-photon

excitation of this dye, which is not positioned in the NIR tissue optical window. To overcome this, the second singlet (S2) state of the ICG can be excited by two photons with a laser wavelength of ~800 nm. A weak second singlet band with an excitation maximum at ~398 nm and emission maximum at ~695 nm exists[198], and these excitation and emission bands were used for two-photon ICGA. This process was verified by measuring the transmission spectra of the short-pass filter used in the setup (Figure 4.10b). The transmission range of the filter is 380-720 nm, and the filter completely blocks the emission wavelength above 750 nm (OD > 6). The filter has 95% transmission at the wavelength range of around 695 nm. The two-photon ICGA of the second singlet state in live animals was investigated for the first time.

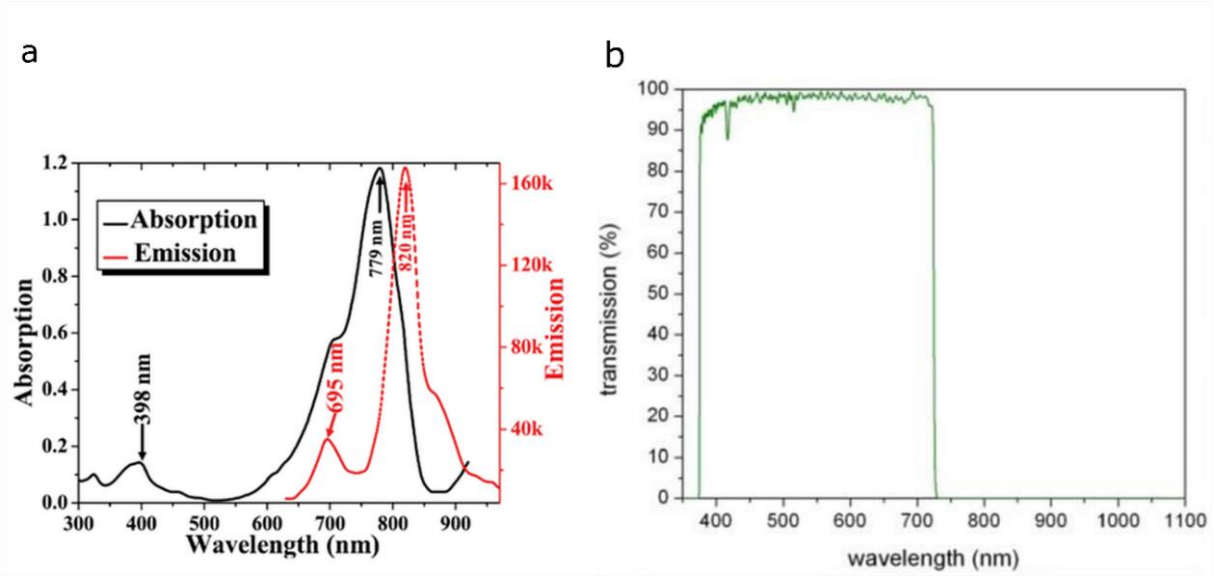

Figure 4.10. Absorption (solid line) and emission (dashed line) spectra of ICG (a)[198]. The measured transmission spectra of the short-pass filter (Semrock, FF01-750/SP-25) at normal incidence (b).

Although confocal imaging of fundus autofluorescence, FA, and ICGA has been safely used with single photon absorption of visible and NIR light in humans for decades without toxicity, it remains limited in its ability to resolve the entire extent of neovascularization completely. Two-photon FA and two-photon ICGA can overcome this issue owing to their superior penetration depth and the ability to control the focal plane. Two-photon FA and two-photon ICGA can be used to monitor and differentiate the types of CNV. Two-photon FA could provide 3D localization and the extent of neovascularization. Furthermore, dual light sources with different filters were used in conventional confocal imaging to capture the images of retinal and choroidal vessels. This study obtained images of retinal and choroidal vessels with a single light source, requiring no additional filters. In addition, simultaneous two-photon FA and ICGA were performed. Although simultaneous angiography by cSLO has been reported by many researchers[199, 200], no studies on two-photon imaging were reported. Our prototype captures the retinal and choroidal circulation using a single light source and a single injection. Usually, monitoring the retinal and choroidal circulations on animal models under anesthesia presents challenges due to prolonged duration. Simultaneously two-photon angiography could aid in monitoring the retinal and choroidal vessels with shorter exposure times. Two-photon retinal angiography with autofluorescence holds a promising perspective in animal models to determine and characterize retinal diseases.
The two-photon collection efficiencies of the standard lens (L4, f = 30 mm) and the additional lens (f = 40/ +25 diopter) for different scanning angles were evaluated. Two different species were selected to test the ability of the system to adapt to different

animal species. Also, limited data were available on two-photon retinal imaging in rabbits and rats. High contrast images of the retina were obtained from rabbits and rats. However, optical aberrations of animal eyes were inferred within the focal plane. The eye suffers from optical aberrations, which become significant at larger pupil sizes. This directly affects the resolution of the retinal image. The aberrations were comparatively smaller in rats than in rabbits due to the shorter axial length and strong convergence of light rays in the rat eye. In addition to optical aberrations, the numerical aperture of the animal eyes significantly impacts resolution. For in vivo retinal imaging, the resolution is limited by the optical quality of the animal eyes. The eye's numerical aperture limits the emitted signal's collection efficiency and determines the image's resolution. Compensating the eye aberrations by adaptive optics could effectively improve the quality of the retinal images[47]. Optical optimization for aberration correction is needed to scan the retina effectively. Comparing the numerical aperture of rat's and rabbits' eyes, a dilated rat's eye (~ 0.43 for 3 mm pupil size and 6 mm axial length) has a larger numerical aperture than the rabbit's eye (~ 0.25 for 7 mm pupil size and 18 mm axial length). Thus, with perfect aberration compensation, in vivo resolution of rat eyes could be improved approximately by a factor of two compared to rabbit eyes due to its larger numerical aperture. This could effectively resolve single retinal cells in rat eyes[201, 202].

The overall two-photon efficiency of the prototype can be increased by improving on two factors: the excitation wavelength and pulse duration. The excitation wavelength of 390 nm (two-photon process, excitation of 780 nm) though adequate to visualize the lipofuscin distribution and retinal vessels, may be suboptimal for fundus autofluorescence and two-photon FA, given the excitation maxima of lipofuscin (470 nm) and fluorescein (490 nm) respectively. Excitation with a 960 nm pulsed laser would effectively increase the two-photon excitation of lipofuscin and fluorescein by a factor of ten, yielding high-quality images in both pigmented and albino eyes. However, for two-photon ICGA, the 780 nm light source is the appropriate wavelength for two-photon excitation of the second singlet state (398 nm). Furthermore, a femtosecond laser with reduced pulse width would improve the two-photon efficiency since the shorter pulse width coupled with group velocity dispersion compensation would significantly increase the two-photon excitation-induced fluorescence[38]. The two-photon scanning laser ophthalmoscope in this study uses 270 fs laser pulse width. The pulse duration has an inverse relation to the power delivered by the system. Hence, the poor signal-to-noise ratio (electronic noise shown in Figure 4.2d) was noticed at lower laser power and a significantly increased image quality at higher laser power. By incorporating a laser with a pulse width of 70 fs, the prototype's efficiency can be increased, and imaging at lower power levels would be possible. The observed electronic noise at a lower power level can be suitably filtered out using standard post-processing algorithms.

The power threshold for two-photon autofluorescence and angiography with our prototype was determined. The minimum power required for two-photon autofluorescence imaging and angiography was about ~160 mW and ~80 mW, respectively. However, no potential photodamage was noticed due to the scanning laser beam even after multiple laser exposures. Thus, the two-photon prototype with current laser power can be safely used for experimental research in animal models. However, further improvement in light delivery is needed since the laser power used for two-photon imaging is higher than the clinical safety standards[126, 154, 203]. Therefore, further optimization of the two-photon ophthalmoscope to increase two-photon efficiency with safe laser power is much needed for clinical applications. The prototype is based on a commercially available HRT, so it could easily be adapted to image the retina of human eyes. A multimodal platform similar to the cSLO can be achieved with a two-photon SLO when the

safe use of femtosecond lasers for retinal imaging is established. Two-photon techniques might overcome some of the limitations which were not possible with confocal imaging techniques. High-quality images of retinal and choroidal vessels can be acquired in a real-time scan with a single light source, requiring no additional filter for FA or ICGA.

5 EVALUATING THE SAFETY OF TWO-PHOTON LASER RETINAL EXPOSURE

The NIR ultrashort pulsed lasers at high repetition rates are commonly employed for TPEF imaging since the pulsed laser beam enables efficient fluorophore excitation at higher scan rates, and the NIR light permits greater penetration depth, reduced scattering, and less phototoxic effects than visible light. Also, TPEF imaging can access endogenous fluorophores like NAD (P) H and retinoids[204, 205]; and excitation of these fluorophores by a single photon requires UV light, which is blocked by the anterior segment of the human eye[206]. Although TPEF imaging has been widely used to explore the retinal structures at a subcellular level in animal models, TPEF imaging in human eyes is crucial since the tissue responses to short pulses are unknown. Laser safety standards such as the ANSI Z136.1, IEC 60825-1, and ICNIRP guide to protecting the eye from hazardous laser exposures. These standards are based on numerous experimental studies and determine the MPE for the safe use of lasers. Despite that, the ultrashort pulsed laser safety in human eyes is still not well established due to insufficient biological data.
The effects of ultrashort pulsed laser on the retina with a stationary laser beam have been evaluated by numerous researchers to determine the safe use of these lasers for retinal imaging and treatment[207-211]. The pulsed laser generates peak powers that can cause potential mechanical, photochemical and thermal damage. The non-linear effects dominate with the ultrashort pulsed laser[153], and therefore, signals from fluorophore within the UV range can be generated within the retina by NIR pulsed laser. Thus, for the potential use of in vivo two-photon retinal imaging, the ultraviolet absorption effects including the photodamage must be considered and evaluated. However, few studies have evaluated the retinal safety of two-photon laser scanning ophthalmoscopes[212, 213]. Therefore, experimental studies on laser safety concerning exposure levels and a stationary vs. scanning laser beams would help better understand the biological effects of the pulsed lasers and support refining the MPE for the safety standards. We evaluated the effects of a pulsed laser (780 nm, 270 fs) on rat retinas for different power levels and exposure times. Although there are structural differences between rats and humans, this pilot study was carried out to determine the laser-tissue interactions in rodents since understanding the structural characteristics of the eye in different species is crucial. Also, rodents are widely used in ophthalmic research as retinal disease models, allowing for studying disease mechanisms and treatments.

5.1 Materials and Methods

5.1.1 Animal Preparation

Twelve brown Norway rats and twelve albino rats (Crl: CD (SD) IGS) with jugular vein catheterization were used for the experiment. Four brown Norway rats (pigmented) and four albino rats (non-pigmented) were exposed to the scanning laser beam, and eight brown Norway rats and eight albino rats to the stationary laser beam. Experiments were performed on one eye at a time, and the fellow eye served as a control. The experimental rats were anesthetized using isoflurane 1-3 % inhalant, and in addition, a drop of topical proparacaine anesthesia (proparacaine hydrochloride ophthalmic solution USP, 0.5 % sterile) and a pupil dilator (0.5% tropicamide ophthalmic solution, USP) were applied to the eyes. Furthermore, sterile saline drops were applied to the experimental eyes every 30 seconds to keep the cornea moisturized. The IACUC at

Loma Linda University approved the animal experiments. The experiments were carried out per the ARVO statement for the use of animals in ophthalmic and vision research.

5.1.2 Study Design

Table 5.1. Group 1: Experimental study design for scanning laser beam exposure

Strain	Laser power at cornea (mW)	Exposure time (seconds)	Scan angle (degrees)	Number of eyes
Brown Norway	160	100	30	1
			15	1
	160	300	30	1
			15	1
Albino	160	100	30	1
			15	1
	160	300	30	1
			15	1

Table 5.2. Group 2: Experimental study design for stationary laser beam exposure

Strain	Laser power at cornea (mW)	Exposure time (seconds)	Number of eyes
Brown Norway	7	60, 100, 300, 600	2[×]
	13	60, 100, 300, 600	2[×]
	80	100, 300	2[+]
	160	100, 300	2[+]
Albino	7	60, 100, 300, 600	2[×]
	13	60, 100, 300, 600	2[×]
	80	100, 300	2[+]
	160	100, 300	2[+]

[×] One eye is exposed to a single exposure time, and another is exposed to multiple exposure times. For example, two rat eyes were used for 7 mW laser beam exposure, of which one eye was exposed to a single exposure time (300 seconds), and another was exposed with multiple exposure times (60, 100, 300, and 600 seconds).
[+] Retina was exposed to only one single exposure time. For example, two rat eyes were used for stationary laser beam exposure at 80 mW laser power. One rat was exposed to 80 mW for an exposure time of 100 seconds, and another rat to 80 mW for 300 seconds.

Group 1: The retina was exposed to a scanning raster beam for two different time scales, 100 seconds, and 300 seconds at 160 mW for 30° and 15° scan angles. Four brown Norway rats and four albino rats were exposed to the scanning laser beam, as shown in Table 5.1.

Group 2: The retina was exposed to a stationary beam (spot size 5 µm) for different time scales, i.e., from 60 seconds to 600 seconds at 7 mW, 13 mW, 80 mW, and 160 mW laser power (Table 5.2). The threshold measurements for minimal visible lesions were determined using the stationary laser beam.
Before the laser exposure, a confocal reflectance image was acquired at a lower power level to determine the retinal location. The laser power levels were measured at the cornea since the power measurement at the retina has limitations. In rare incidents, the targeted eye drifts under the influence of anesthesia. In such instances, the exposure to the laser was blocked until the eye returned to its original position.

5.1.3 Two-Photon Laser Scanning Ophthalmoscope

The two-photon prototype has been described in detail in chapter 4. In brief, a compact femtosecond laser with 50 MHz repetition rate, 270 fs pulse width, 780 nm central wavelength, with tunable output power up to 500 mW, was used as a light source. The confocal reflectance imaging and two-photon imaging can be performed using the same instrument in the high-resolution mode and high-speed mode with 30° x 30°, 20° x 20°, and 15° x 15° transversal field of view. The scanning frequency per frame in the high-resolution mode is 5 Hz/7 Hz/9 Hz at 30°/20°/15° scan angle, whereas, in high-speed mode, the scan frequency is 9 Hz/12.5 Hz/16 Hz, respectively. The digital image readout for the high-resolution mode is 1536 × 1536, 1024 × 1024, 768 × 768; and for the high-speed mode, 768 × 768, 512 × 512, and 384 × 384. In real-time, the signal-to-noise ratio of the images was increased by frame averaging. For this study, the standard objective lens (focal length, f = 30 mm) with an additional objective lens (f = 40/+25 diopters) from Heidelberg Engineering GmbH was used to collect the two-photon signals. The additional objective lens reduces the beam diameter by 70%, adapting the system to the shorter axial length of the rat eyes. The images were acquired in high-resolution mode with a 30º scan angle for fundus overview and 20º and 15º scan angles for the detailed view of the retina.

5.1.4 Two-Photon Fluorescein Angiography

Fluorescein (10% AK-FLUOR, Akron) was administered through the jugular vein catheter for two-photon FA. The administered dose was correlated with the animal's body weight. The two-photon FA in animal models has been described in chapter 4. In brief, fluorescein was injected to visualize the retinal vasculature, and in the two-photon mode, the flow of fluorescein through the blood vessels was captured. The two-photon FA was performed to assess the potential retinal damage and to evaluate the efficacy of utilizing the two-photon FA in determining the light-induced damage.

5.1.5 Histology

The experimental rats were followed up for four days with confocal reflectance and two-photon FA and then euthanized humanely for histological analysis. The control and the experimental eye globes were enucleated and fixed in Davidson's solution for 24 hours and then embedded in paraffin. The retinal cross-sections of size 5 µm were cut from the paraffin-embedded eyes and transferred to the microscopic slides. The retinal sections were analyzed immediately under the light microscope, and after

careful evaluation, some retinal sections were selected for hematoxylin and eosin (H&E) staining. In parallel to the H&E-stained retinal sections, further sections from the same region were selected for the DeadEnd™ Fluorometric TUNEL (terminal deoxynucleotidyl transferase dUTP nick end labeling) assay. The TUNEL assay was performed according to the manufacturer's instructions (Promega Corporation, USA), and the retinal sections were mounted with VECTASHIELD® + DAPI to allow for staining of the nuclei. The TUNEL assay detects and quantifies apoptotic cell death by measuring the nuclear DNA fragmentation, a vital biochemical hallmark of apoptosis in many cell types[214]. The TUNEL assay is an established method to detect and quantify apoptotic cells due to light damage[215-217].

5.1.6 Microscopy

The light microscopic (Aperio scan scope, Leica Biosystems, Germany) images of the H&E-stained sections were captured to analyze the structural changes in the retina. The fluorescence microscopic (Olympus Corporation, Japan) images of the TUNEL stained retinal sections were captured to detect the apoptotic cells due to the laser exposure laser. Under a fluorescence microscope, the retinal sections were analyzed with 10×, 20×, and 40× objective lenses using a standard fluorescein filter at 520 nm to view the green fluorescence of fluorescein and at 490 nm for blue DAPI.

5.2 Results

5.2.1 Scanning Laser Beam Exposures

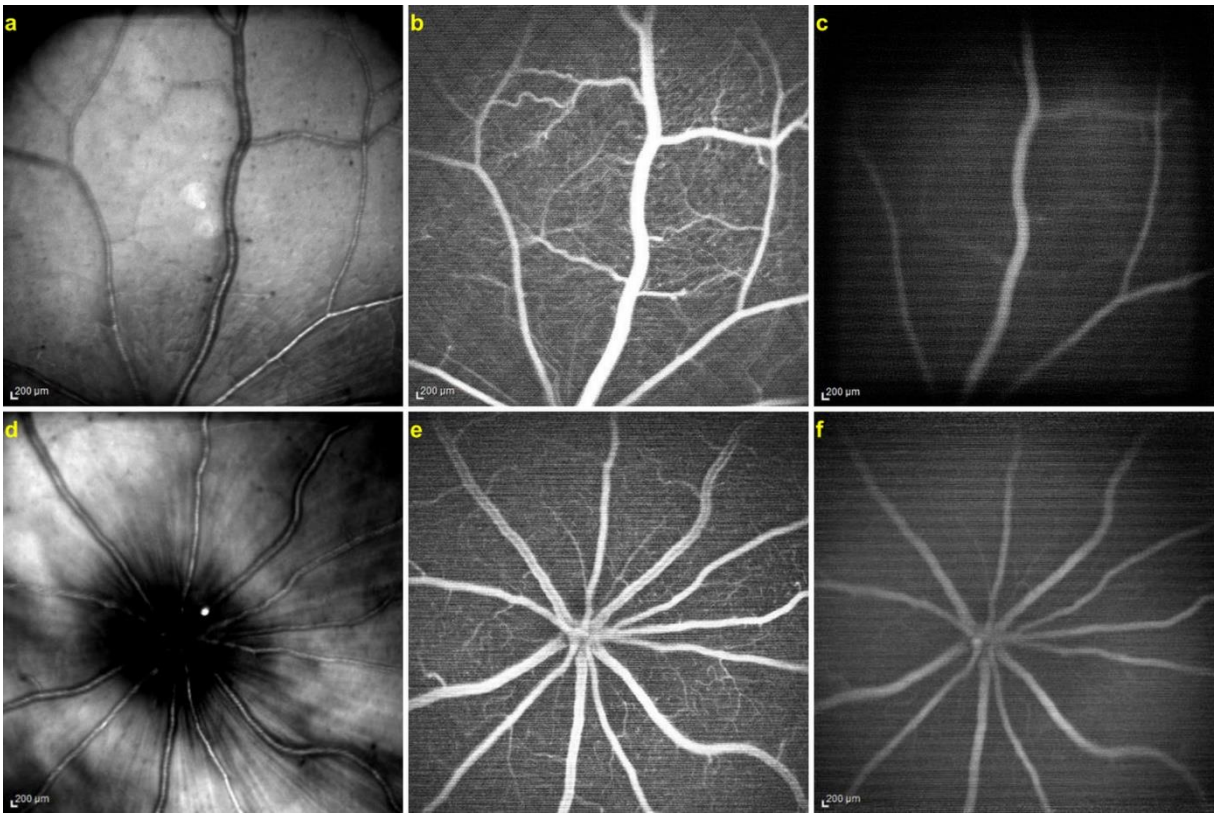

Figure 5.1. Scanning laser beam exposure for 300 seconds with a 30º scan angle at 160 mW laser power in brown Norway rats (a-c) and albino rats (d-f). The confocal reflectance image (a, d) of the laser-exposed retina. Early phase (b, e - 5 to 15 seconds after injection) and late phase (c, f - 7 to 10 minutes after injection) two-photon FA of the exposed retina.

Figure 5.1 shows the confocal reflectance and two-photon FA images of brown Norway and albino rats exposed to the scanning laser beam. The exposure settings were scanning angle 30°, exposure duration 300 seconds, and laser power 160 mW. The confocal reflectance image (Figures 5.1a and 5.1d) did not show any retinal abnormalities right after the laser exposure. The real-time two-photon FA from the early phase (Figure 5.1b and 5.1e) to the late phase (Figure 5.1c and 5.1f) showed neither hypofluorescence nor hyperfluorescence. Retinal capillaries were visible in the early phase of the fluorescein influx, and the fluorescein diminished slowly. The late phase demonstrated a graded elimination of dye from the retinal vasculature. The same results were observed for scanning laser beam exposure at a 15º scan angle, 160 mW laser power exposures for 100 seconds and 300 seconds.

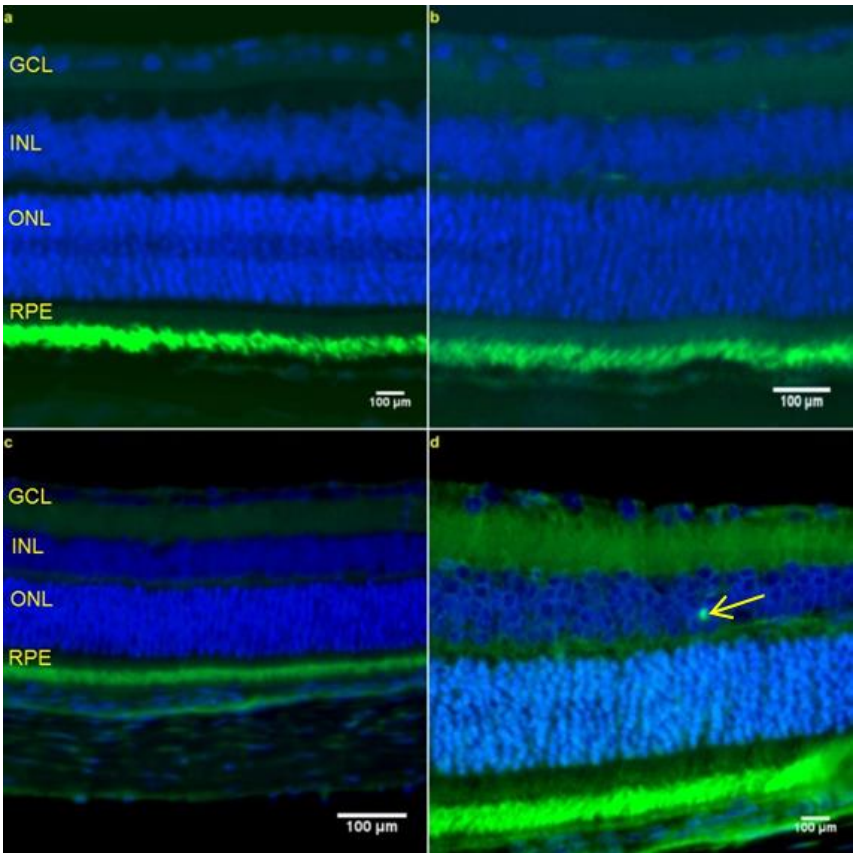

Figure 5.2. Fluorescence microscopic (TUNEL assay) images of brown Norway and albino retinal sections exposed to the scanning laser beam. The fluorescence image of the control (a, 20×) and the experimental eye (b, 10×) of the brown Norway rat retina; and the control (c, 10×) and the experimental eye (d, 20×) of the albino rat retina. The images shown here are the merged images of DAPI and green fluorescence and cropped for better visualization of the retinal cells. GCL - ganglion cell layer; INL - inner nuclear layer; ONL - outer nuclear layer; RPE - retinal pigment epithelium.

The retinal sections of the control and the experimental eye were analyzed using the fluorescence microscope, and neither significant changes in cell loss nor disruption in the retina or retinal swelling were noticed. Furthermore, the immunohistochemistry (TUNEL assay) analysis from the exposed retinal sections showed no cellular damage. Figure 5.2 shows the fluorescence images of the control and the experimental retina of brown Norway and albino rats. The green fluorescence noticed in Figure 5.2d (arrow) is an artifact of histology sections.

5.2.2 Stationary Laser Beam Exposures

Brown Norway rats

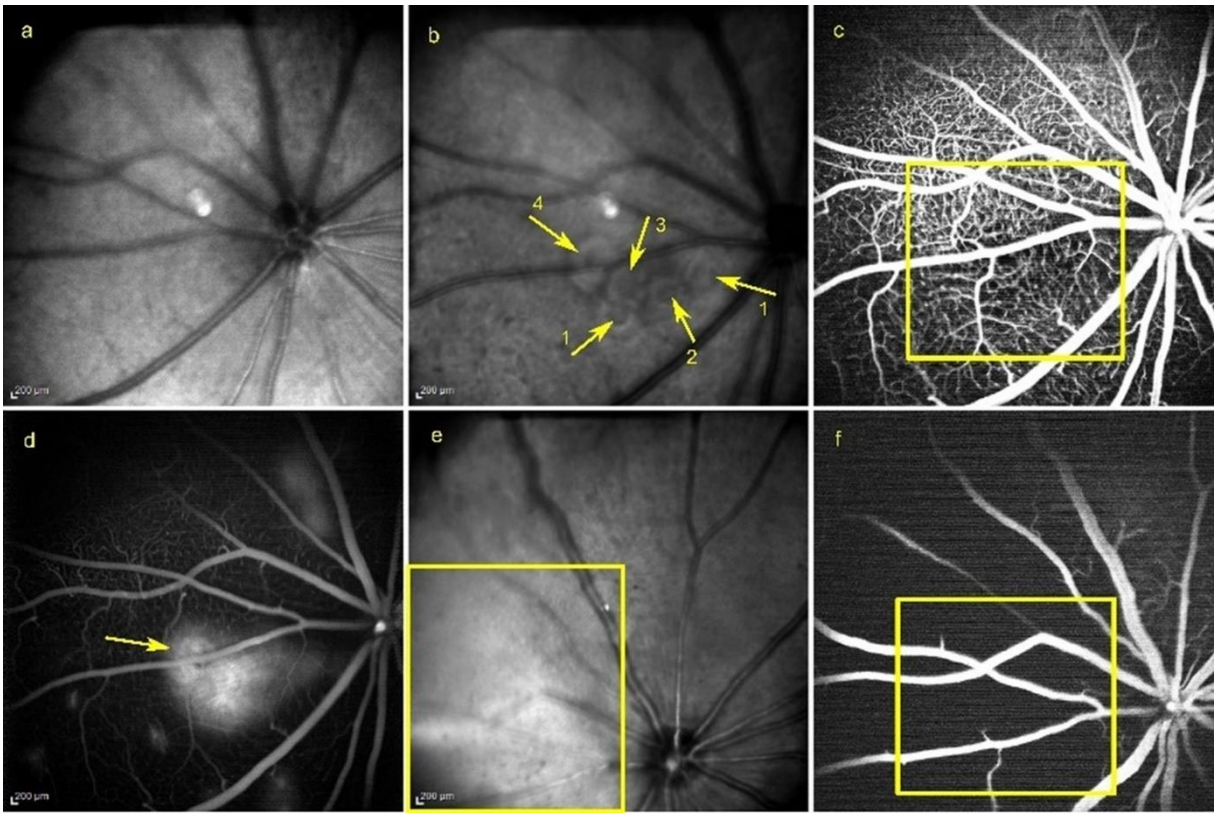

Figure 5.3. The stationary laser beam exposure in the brown Norway rat at 13 mW laser power. (a) confocal reflectance image before exposure, (b) confocal reflectance image after exposure to the laser at 13 mW for 60 seconds (arrow 1), 100 seconds (arrow 2), 300 seconds (arrow 3), and 600 seconds (arrow 4). The early phase (c) and late phase (d) two-photon FA, the hyperfluorescence (d, arrow) is seen in the laser-exposed area. (e) Confocal reflectance image of the laser-exposed retina on day 4. Early phase (f) two-photon FA of the exposed retina on day 4.

Figure 5.3 shows the confocal reflectance and two-photon FA images of the brown Norway rat's retina exposed to the stationary laser beam. The retina was exposed to 13 mW for 60 seconds (arrow 1), 100 seconds (arrow 2), 300 seconds (arrow 3), and 600 seconds (arrow 4) each on a single spot of the retina to determine the effects of the ultrashort pulsed laser (780 nm, 270 fs) to exposure durations. The stationary laser beam was the parked laser beam available in the service mode of the system. The confocal reflectance image of the retina was captured immediately after the exposure, and the visible retinal lesion induced by exposure to the stationary laser beam for different exposure times is shown in Figure 5.3b. With a longer exposure time, more radiation was absorbed, and hence there was an increase in the size of the lesion. After the exposure, a two-photon FA was performed, and the early phase to late phase angiograms were recorded. High-contrast retinal microvasculature was clearly seen in the early phase of two-photon FA (Figure 5.3c, yellow box), and in the late phase (Figure 5.3d, arrow) the hyperfluorescence was noticed on the laser-exposed retinal area. The irregularity in the nerve fiber layer and the absence of capillaries in the exposed area were noticed on day 4 (Figure 5.3e, 5.3f). In Figure 5.3e (yellow box), the confocal reflectance image of the retina shows high reflectivity and an irregular nerve fiber layer in the laser-exposed area. In contrast, the retina on the other side of the optic nerve (unexposed retina) did not show any structural changes or irregularities. Also, the early

two-photon FA on day 4 (Figure 5.3f, yellow box) showed the absence of capillaries in the laser-exposed retina.

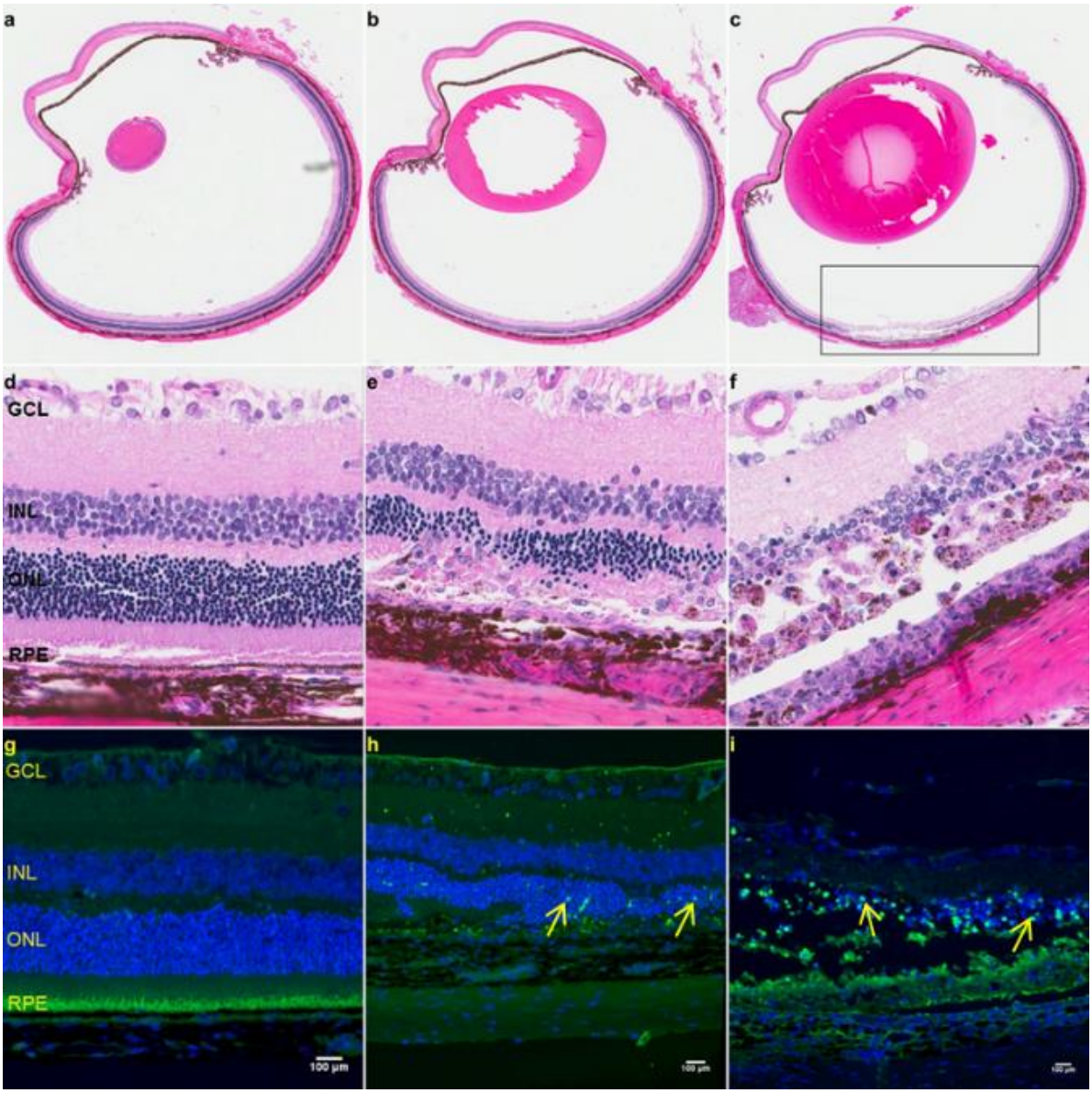

Figure 5.4. Light microscopic and fluorescence images of the retinal sections of the brown Norway rat exposed to a stationary laser beam at 13 mW laser power. H&E-stained retinal sections of the exposed retina at different sections from the periphery to the laser-exposed area. Retinal section (a, 4×) at the periphery; retinal section (b, 4×) approximately 50 microns from the periphery towards the optic nerve; and the retinal section of the exposed retina (c, 4×) close to the optic nerve. Close-up view of the retinal light-induced damages (d, e, f (from a, b, c)) acquired using a 40× objective lens. Fluorescence microscopic images of retinal sections (g, h, i of d, e, f) acquired using a 20× objective lens.

In addition, the H&E staining and TUNEL assays were performed on the retinal sections to evaluate the potential thermal damage to the retina. The retinal cross-sections were evaluated at different depths. The retinal sections close to the periphery of the eye globe did not show any structural damage to the retina (See Figure 5.4a, 5.4d, 5.4g), whereas the retinal sections closer to the exposed area showed disruption of the outer nuclear layer and the pigment epithelium (See Figure 5.4b, 5.4c, 5.4e, 5.4f, 5.4h, 5.4i). The retinal swelling, a disorganized outer segment with no RPE, and nuclear layer degeneration with a few apoptotic cells (Figure 5.4h and 5.4i, arrows) were noticed in the exposed area.

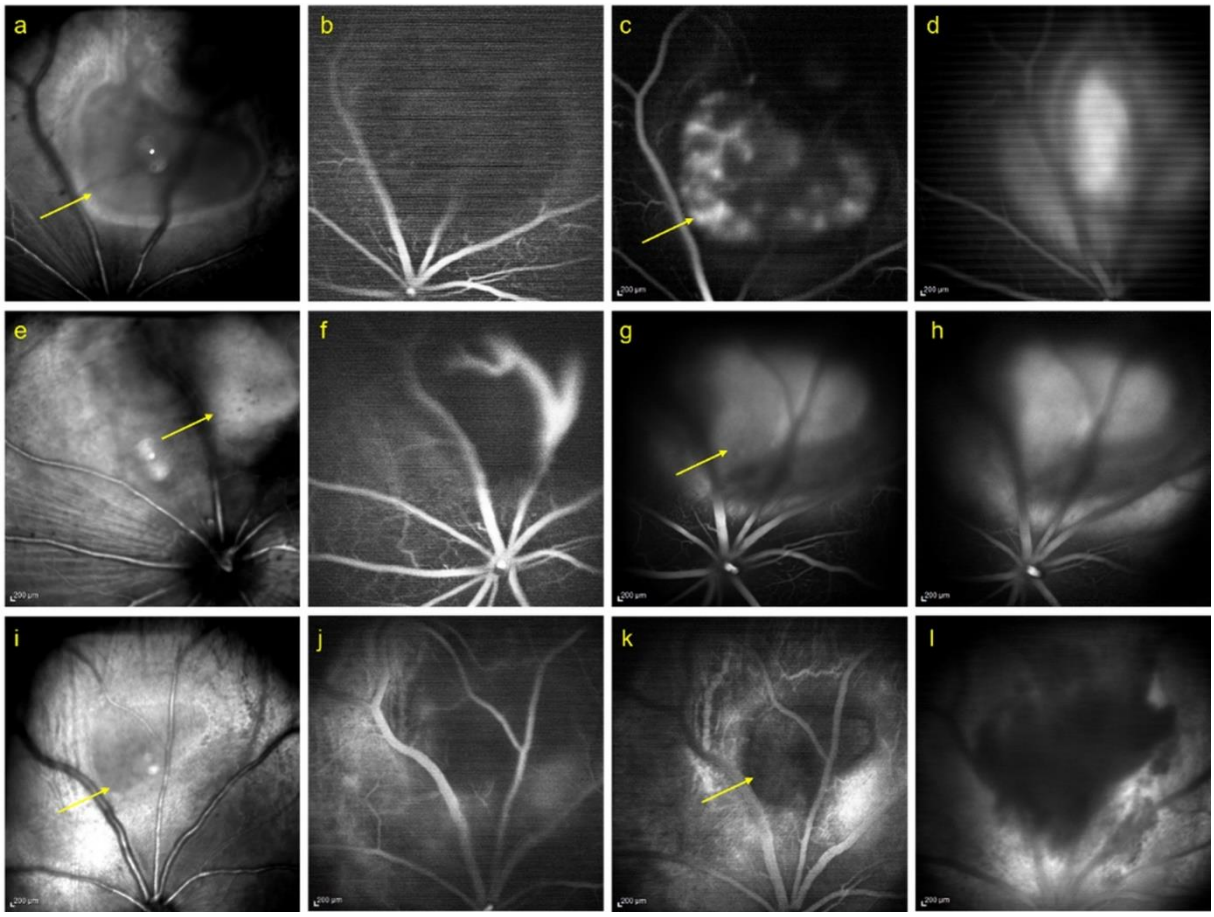

Figure 5.5. The effects of a stationary laser beam exposure on a brown Norway rat at 80 mW power for 100 seconds. (a) Confocal reflectance image of the exposed retina immediately after laser exposure (arrow). Two-photon FA at early (b), intermediate (c), and late (d) phases, showing hyperfluorescence (c, arrow) in the area of laser exposure. (e) Confocal reflectance image of the laser-exposed retina on day 1. Two-photon FA at early (f), intermediate (g), and late (h) phases on day 1. (i) Confocal reflectance image, (j) early phase, (k) intermediate, and (l) late phase two-photon FA of the exposed retina on day 4.

Figure 5.5 illustrates the results of confocal reflectance and two-photon FA on a brown Norway rat exposed to a stationary laser beam at 80 mW power for 100 seconds. The retinal lesion is clearly visible in the confocal reflectance image immediately after the exposure (Figure 5.5a) and appears to be surrounded by a zone of retinal whitening. The surrounding retinal tissue appears normal. The lesion appears to be larger than those resulting from exposure to 13 mW lasers. The exact appearance of the lesion is also dependent on the duration of exposure. The laser exposure at 80 mW caused retinal inflammation and scarring. Additionally, two-photon FA was utilized to evaluate the retinal blood vessels and revealed leakages in the vessels caused by the laser injury. In the two-photon FA images, the lesion is shown with hyperfluorescence (Figure 5.5c, arrow) and is surrounded by a zone of hypofluorescence, representing the area of retinal whitening caused by the burn. On day 1 and day 4, leakage of the dye from the blood vessels into the surrounding retina was observed, indicating damage to the blood-retinal barrier.

Figure 5.6 illustrates the effects of a stationary laser beam exposure on a brown Norway rat retina using 80 mW laser power for 300 seconds. As seen in the confocal reflectance imaging (Figure 5.6a), a dark spot on the retina is visible on the exposed area, surrounded by a zone of hyper-reflection. This is likely due to the accumulation of fluid in the retina. The 80-mW laser power at 300 seconds appears to severely

damage the retina and create a retinal hole. The laser-exposed spot in the retina appears dark in the early phase of two-photon FA (Figure 5.6b). The laser energy may have led to the collapse of blood vessels in that area, resulting in a dark or hypofluorescent area in the early phase of the two-photon FA. However, in the later stages of the two-photon FA, the exposed area appears hyperfluorescent. This could be because the dye has leaked through the hole, causing the area around it to appear hyperfluorescent. The retinal hole due to laser itself appears less distinct at the late phase two-photon FA (Figure 5.6c), indicating that the dye continues to leak, and the surrounding tissue becomes more hyperfluorescent. In H&E-stained images, the exposed retinal area appears irregular, and the surrounding tissue appears normal. The exposed area shows disruption of the outer nuclear layer and the pigment epithelium (Figure 5.6d, 5.6e). In fluorescence images, retinal swelling, disorganized outer segments with no RPE, and nuclear layer degeneration with a few apoptotic cells (Figure 5.6f) are noticed in the exposed area.

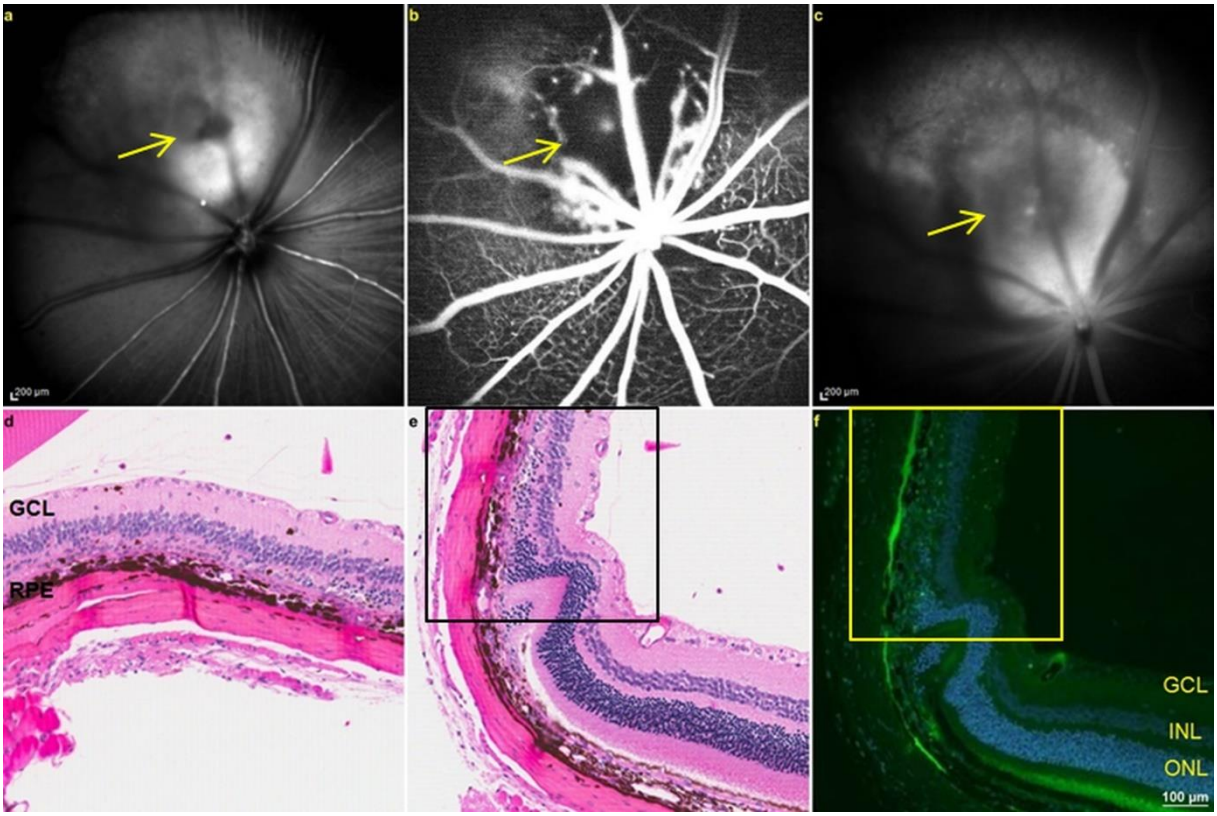

Figure 5.6. The effects of a stationary laser beam exposure on a brown Norway rat at 80 mW power for 300 seconds. (a) Confocal reflectance image of the retina immediately after laser exposure. (b) Early-phase and (c) late-phase two-photon FA. (d, e) H&E-stained retinal sections from the exposed area (black box). (f) Fluorescence image of the exposed area (yellow box).

Figure 5.7 illustrates the impact of laser exposure on a brown Norway rat at a power of 160 mW for 100 seconds. An apparent dark region in the retina was observed immediately after laser exposure (Figure 5.7b), revealing retinal hemorrhages. The 160 mW laser power leads to harm to the blood vessels in the retina, resulting in leakage of blood into the surrounding tissue. The early (Figure 5.7c) and mid-phase (Figure 5.6d) two-photon FA appeared dark due to the hemorrhage, and retinal vessels were visible from the surrounding area.

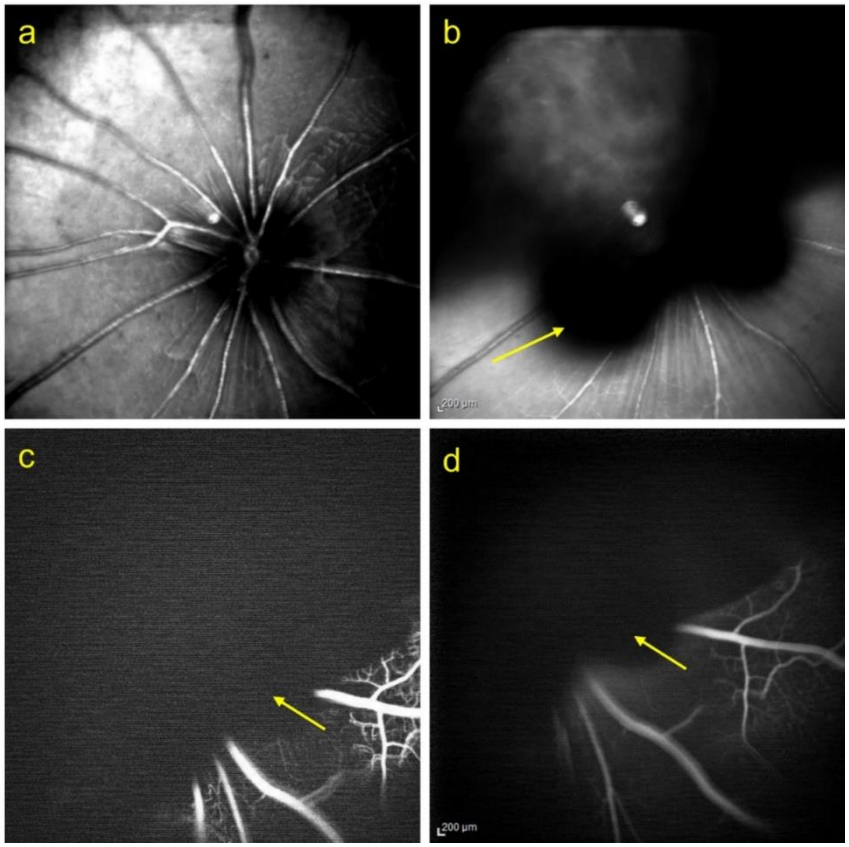

Figure 5.7. Stationary laser beam exposure in a brown Norway rat at 160 mW laser power for 100 seconds. (a) Confocal reflectance image before exposure, and (b) after exposure showing dark area (arrow) in the retina indicating retinal hemorrhages. (c) Early phase and (d) intermediate phase two-photon FA showing hypofluorescence (arrow) in the laser-exposed area due to blood leakage in the retina.

Albino Rats

Conversely, in albino rats, no potential damage was noticed for the stationary laser beam exposure at 7 mW, 13 mW, and 80 mW. No damages on the exposed retina were noticed even at 160 mW laser power exposure for 100 seconds. The damage occurs only at 160 mW laser power exposure for 300 seconds (Figure 5.8). The confocal reflectance (Figure 5.8a, 5.8b, 5.8e) and the two-photon FA images (Figure 5.8c, 5.8d, 5.8f) of the albino rat were acquired immediately to monitor the retinal damages due to the laser exposure. The hyperfluorescence (Figure 5.8d, arrow) was minimal in the exposed area compared to the brown Norway rats (See Figure 5.3d). Likewise, in the follow-up examination on day 4, neither change in the nerve fiber layer nor the absence of capillaries were noticed as in the brown Norway rat (See Figures 5.3f and 5.8f).

The TUNEL assay on the retinal sections of albino rats (Figures 5.9a and 5.9b) did not show any apoptotic cells due to the laser exposure. Neither cell death nor disruption in the retina was noticed. Few green fluorescence cells were noticed in the outer nuclear layer on the control and the experimental retinal sections (Figure 5.9a and 5.9b, yellow box). This could be due to the acute bright light exposure, which can damage the RPE and photoreceptors even in control eyes. Within the control group, light-induced damage can be multifactorial, including environmental conditions, genetic diseases, and aging. Animal environment, housing, and management are essential for maintaining laboratory animals' health and wellbeing, ensuring the reliable outcome of scientific investigations[218].

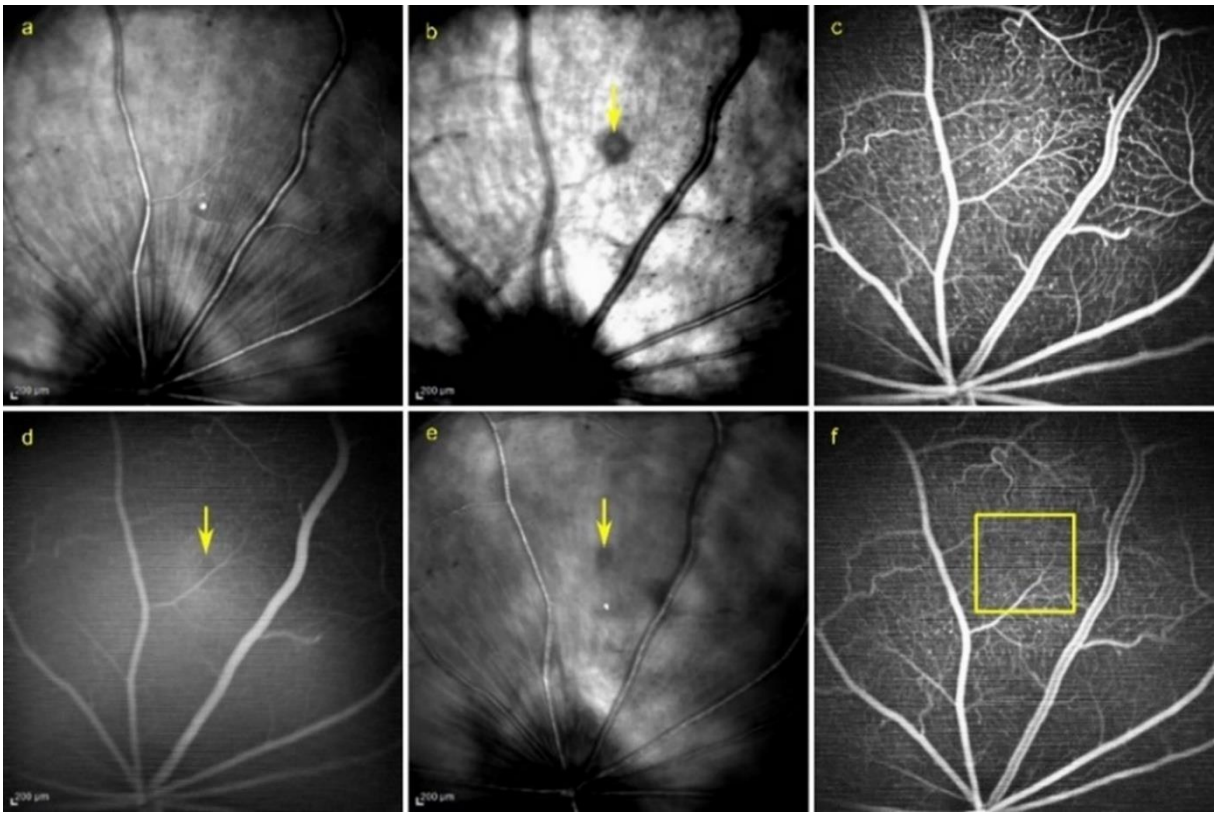

Figure 5.8. Stationary laser beam exposure in the albino rat at 160 mW laser power. Confocal reflectance image (a) before laser exposure, (b) confocal reflectance image after laser exposure, (c) the early phase, and (d) late phase two-photon FA. The hyperfluorescence (arrow) was noticed in the laser-exposed area. (e) Confocal reflectance and early phase (f) two-photon FA of the exposed retina on day 4.

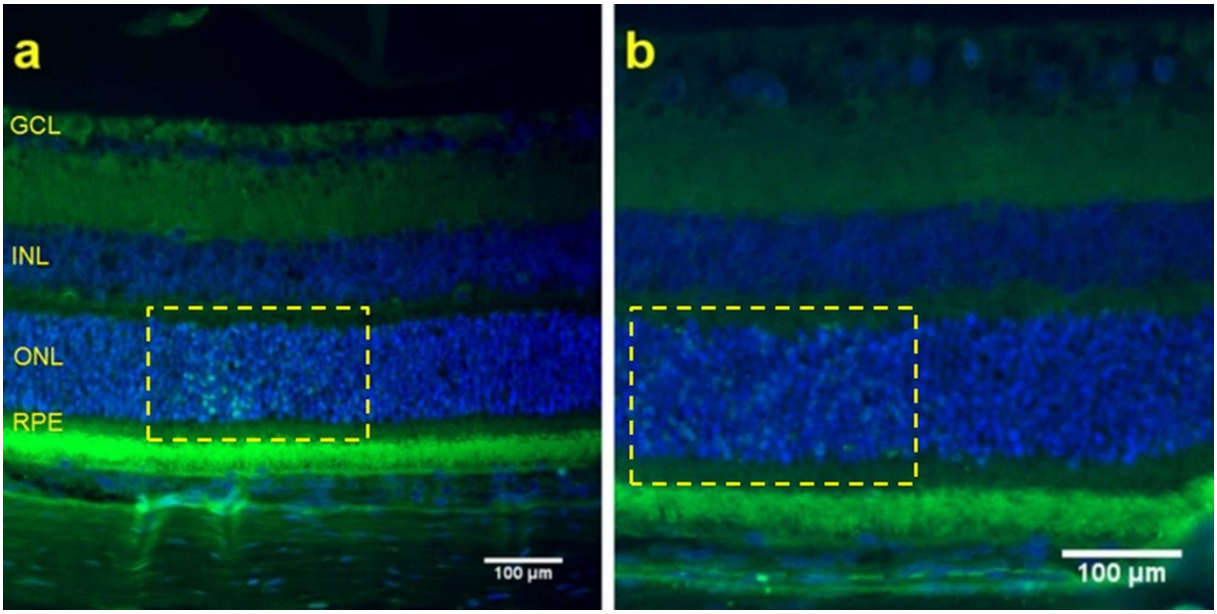

Figure 5.9. The fluorescence image of the control (a) and experimental (b) albino rat's retinal sections exposed to a stationary laser beam for 300 seconds at 160 mW laser power.

Retinal damage recovery

Brown Norway rat exposed to a stationary laser beam at 13 mW for a single exposure time was followed up for 4 days with no fluorescein injection to determine the recovery from light damage. Only confocal reflectance imaging and TUNEL assay were

performed on this rat to monitor the significant effects of light damage and structure recovery. The retina exposed to a stationary laser beam of 13 mW for 300 seconds is shown in Figure 5.10. The confocal reflectance image (Figure 5.10a) immediately after the laser exposure and the follow-up retinal image on day 4 (Figure 5.10b) visualize the retinal lesion (Figure 5.10a and 5.10b, arrows). However, no irregularities in nerve fiber layers were noticed on day 4. Also, the reflectivity from the laser-exposed area was not as severe as the retina exposed to the laser at multiple sessions (See Figure 5.3e). With a single laser exposure at 13 mW, the retinal damage did not progress and recovered itself without medications or the retinal health is not affected. Even the fluorescence image analysis did not show any irregularities or disruptions in the retina (See, Figures 5.4 and 5.10c).

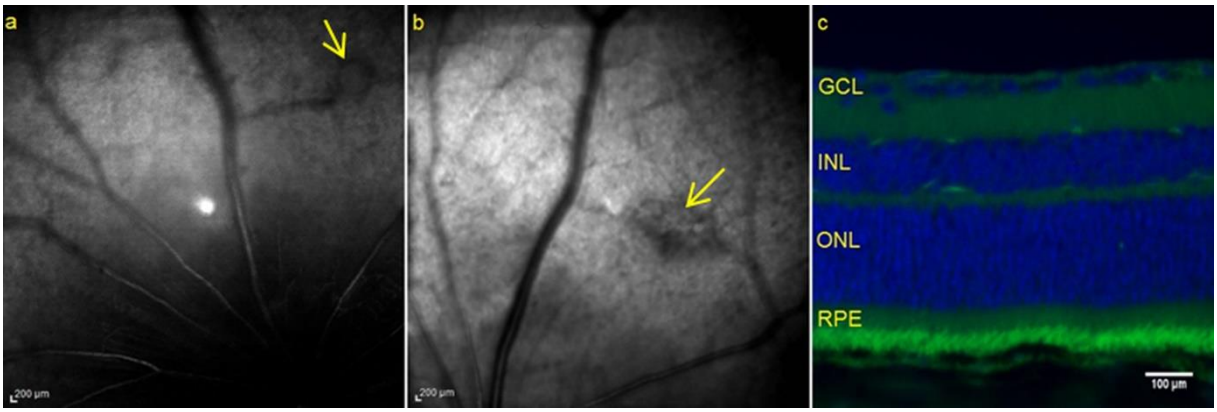

Figure 5.10. The confocal reflectance image (a) of the brown Norway retina exposed to the stationary laser beam of 13 mW for 300 seconds. (b) Confocal reflectance image on day 4 after laser exposure. The fluorescence image (c, 10×) of the exposed retina.

Although no irregularity in the nerve fiber layer or apoptosis was noticed in the exposed retinas due to the laser exposure in Figure 5.10c, different approaches must be performed better to locate the light damage on a cellular level. As for histology, it was difficult to locate the exact retinal lesion by a cross-section analysis. Therefore, the whole mount retinal analysis would be an efficient way to determine the effects of laser-induced damage for a single exposure. OCT would be another efficient method to look at the retinal lesions for cross-section analysis.

Immunohistochemistry analyses of the retina for multiple exposures to the scanning laser beam

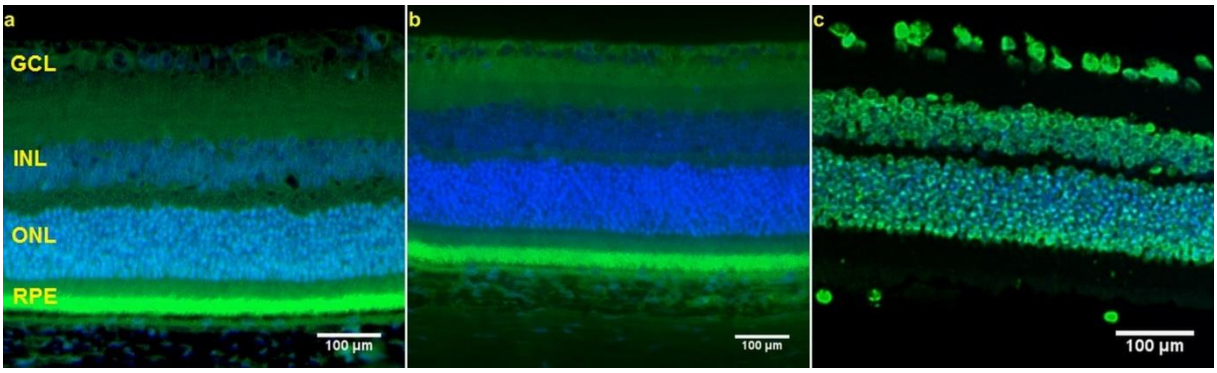

Figure 5.11. Fluorescence images of the control (a) and experimental (b) retina of brown Norway rat exposed to the two-photon scanning laser beam. The positive control test on the experimental eye (c). Blue fluorescence is the DAPI nuclei staining, and the green fluorescence is the TUNEL-positive nuclei staining. The bright green, fluorescent cells are the positive (apoptosis) cells, which is evident in the positive control retinal sections.

Fluorometric TUNEL analysis was performed on the rats that were used for two-photon autofluorescence imaging (See Chapter 4). The retinas were exposed to the scanning laser beam multiple times at 160 mW laser power. The imaging procedure in these rats took approximately 45-60 minutes. The fluorescence images of the brown Norway rat's retinas exposed to the scanning laser beam is shown in Figure 5.11a and 5.11b. The fluorescence microscopic analysis of these retinal sections reported no apoptosis or structural changes in the retina even after multiple exposures. Since no apoptosis was noticed in the exposed retinal sections, a positive control test was performed on retinal sections according to the manufacturer's instructions[214]. The apoptosis was clearly noticed (Figure 5.11c) on the positive control retinal sections. This shows that the scanning laser beam produces no considerable damage even after multiple exposures.

5.3 Discussion

5.3.1 Pigmented vs. Non-Pigmented Retinal Toxicity to Laser Exposures

A scanning laser beam returned no retinal toxicity in both animal models and was verified by confocal reflectance imaging, two-photon FA, and TUNEL assay. However, for stationary laser beam exposure, the retinal lesions were noticed at 13 mW for 60 seconds in brown Norway rats and only after exposure to 160 mW laser power for 300 seconds in albino rats. The number of TUNEL-positive cells was significantly higher in brown Norway rats compared to albino rats. Retinal swelling, a disorganized outer segment with no visible RPE, and nuclear layer degeneration were noticed in brown Norway retinal sections. In contrast, the albinos did not show any retinal damages at low laser power and only minimal damages at more prolonged exposure to high laser power. The albino rats had a higher laser safety threshold than the pigmented brown Norway rats due to the lack of melanin in the RPE layer. Absorption serves fundamentally in determining the potential toxicity of light on the retina.
Also, no potential thermal damages were noticed on the brown Norway rat retina exposed to the stationary laser beam of 7 mW, while the stationary laser beam exposure at 80 mW and 160 mW induced a retinal burn, pigmentary change, retinal detachment, and hemorrhage. These results infer the morphological changes related to tissue radiation interaction. This was primarily due to the absorption of radiant energy by melanin within the RPE and the choroidal melanocytes in brown Norway rats. But in albino rats, the laser-induced effects occurred because of multiple scattering, together with absorption within hemoglobin and possibly within tissue water[219].

5.3.2 Laser Safety Studies in Animal Models

Rodents have been predominantly used in ophthalmic research to study the disease progression and effect of therapies. Also, the rodents (rats 0.43) have larger numerical apertures compared to human eyes (0.20), and this possibly could resolve smaller retinal features[201]. Two-photon retinal imaging has been studied in different animal models, including rodents; however, for the laser safety study, rodents may not be the appropriate animal models due to several factors. The laser safety standards determine the MPE values through experimental studies in non-human primates since these eyes are closer to human eyes. Also, the retinal damage depends on the transmission of the laser radiation (ocular transmission in rats is 0.9 or greater at 780 nm), absorption, and the diameter of the laser spot at the retina. Multiphoton absorption by ultrashort pulsed laser must be ensured for safe retinal imaging. In rats, it might not be possible

to evaluate the UVA since the rat's cornea transmits UV radiation and supports its vision[220].
Laser safety guidelines specify that the diameter of the irradiance profile (D) at the retina determines the damaging potential of energy incident on the retina[221]. The retinal irradiance diameter can be calculated as $D = \alpha f_e$, where α is the source angle and f_e is the effective focal length of the eye (rats, f_e = 3.37 mm, humans, f_e = 17 mm). The retinal irradiance diameter for the small source (α = 1.5 mrad) in rats (5 µm) is 3 times lower than the human eyes (25 µm). Therefore, the energy required to create the damage must be lower in rats than in humans since the irradiance diameter is smaller in rats. However, in this study, the visible retinal lesions were noticed in brown Norway rats only at 13 mW laser power which is 2.3-fold higher than the safety standard (See section 5.3.3). This could be due to the retinal-laser spot diameter's influence and animal species differences. Also, rats have higher refractive power and HOAs, influencing the spot diameter. Therefore, accurate analysis of the potential retinal damage in different animal species needs to be carefully evaluated and correlated for safe two-photon imaging in humans.

5.3.3 Laser Safety Analysis according to IEC 60825-1:2014

Laser safety analysis of a stationary laser beam

Laser wavelength, λ = 780 nm; repetition frequency, F = 50 MHz; pulse duration, t = 270 fs.

$C_4 = 10^{0.002(\lambda-700)} = 1.445$ for the spectral region 700 to 1050 nm; $C_6 = 1$ since the beam is emitted for a small source.

Pupil aperture with a diameter of 7 mm $A_p = (\pi \cdot 7\text{mm}^2/4) = 0.385\ \text{cm}^2$ or $0.000038465\ \text{m}^2$

For repetitively pulsed lasers, the following conditions should be tested to determine the MPE.

Condition 1: The exposure from any single pulse shall not exceed the single-pulse MPE. Thus, the radiant exposure for the time period 270 fs is: $\text{MPE}_{\text{single}} = 1 \cdot 10^{-3}\ \text{Jm}^{-2}$

MPE in terms of average power: $\text{MPE}_1 = \text{MPE}_{\text{single}} \cdot \text{F} \cdot \text{A}_\text{p} = 1.92\ \text{W}$

Condition 2: The average exposure for a pulse train of exposure duration T shall not exceed the MPE for a single pulse of duration T. A reasonable estimate of hazardous chance exposure time can be taken as 10 s. t = 10 s

$$\text{MPE}_\text{T} = 18\ \text{t}^{0.75} C_4 \text{Jm}^{-2} = 146.26\ \text{Jm}^{-2}$$

Since there are $N = F \times T = (50 \times 10^6) \cdot 10 = 5 \times 10^8$ pulses in 10 s period, the average irradiance criteria result in a single pulse radiant exposure: $\text{MPE}_{\text{single-average}} = \text{MPE}_\text{T}/\text{N} = 2.92 \cdot 10^{-7}\ \text{Jm}^{-2}$

In terms of average power: $\text{MPE}_2 = \text{MPE}_{\text{single-average}} \cdot \text{F} \cdot \text{A}_\text{p} = 562\ \mu\text{W}$

Condition 3: The average exposure from pulses within a pulse train shall not exceed the MPE for a single pulse multiplied by the correction factor C_5 (where $C_5 = 5 \cdot N^{-0.25}$). The maximum exposure duration for 700 nm wavelength is T_2 = 10 s for $\alpha \leq \alpha_{min}$

Since the laser operates at high repetition, the multiple pulses appearing within the period of T_i (T_i = 5 µs) are counted as a single pulse to determine N, and the radiant exposure of the individual pulses is added to compare with the MPE of T_i. Hence, the effective pulse repetition frequency is $\text{F}_\text{E} = 1/\text{T}_\text{i} = 1/5\ \mu s = 2 \times 105\ \text{Hz}$

MPE for a pulse duration T_i is $\mathrm{MPE}_{\text{single-eff}} = 2 \cdot 10^{-3} C_4\ \mathrm{Jm}^{-2} = 2.89 \cdot 10^{-3}\ \mathrm{Jm}^{-2}$

The effective number of pulses in 10 s is: $N_E = T \cdot F_E = 10 \cdot (2 \cdot 10^5) = 2 \cdot 10^6$

For N_E pulses, each of duration T_i in 10 s period the radiant exposure under this criterion would be: $\mathrm{MPE}_{\text{train}} = \mathrm{MPE}_{\text{single-eff}} \cdot 5\ (N_E)^{-0.25} = 2.89 \cdot 10^{-3} \times 5\ (2 \cdot 10^6)^{-0.25} = 3.84 \cdot 10^{-4}\ \mathrm{Jm}^{-2}$

Conditions 1 and 2 are applicable to the pulse of energy, Q, while condition 3 is applicable to the pulse of energy = $Q \times T_i \times F$. Hence, dividing the $\mathrm{MPE}_{\text{train}}$ by $T_i \times F$ enables the comparison of three MPEs. $\mathrm{MPE}_{\text{train, single pulse}} = \mathrm{MPE}_{\text{train}} / (T_i \times F) = 1.5 \cdot 10^{-6}\ \mathrm{Jm}^{-2}$

In terms of average power: $\mathrm{MPE}_3 = \mathrm{MPE}_{\text{train}} \cdot F \cdot A_p = 2.6\ \mathrm{mW}$

Comparing the three MPEs, condition 2 yields the most restrictive, and therefore the single pulse MPE for the two-photon prototype must be 562 µW. The MPE in laser safety guidelines is 10 times lower than the damage threshold.

Laser safety analyses for an extended source

Here the total illuminated field is considered an extended source. The repetition rate PRF_f of the scan field equals the frame rate; PRF_f = 5 Hz and 9 Hz for 30º and 15º scan angles.

The angular subtense of the scan field is 525 × 525 mrad and 262.5 × 262.5 mrad for 30º and 15º scan angles, respectively. Duration of the field illumination, t_f = 192 ms and 96 ms for 30º and 15º scan angles.

Condition 1: The exposure from any single pulse (frame) within a pulse train (frame rate) shall not exceed the MPE for a single pulse (frame).

$$C_6 = \alpha_{\max}/\alpha_{\min}, \text{ where } \alpha_{\max} = 200 \cdot t_f^{0.5}\text{mrad for } \alpha > \alpha_{\max}$$

$$C_6 = 58.42 \text{ for } 30^\circ, \text{ and } 41.31 \text{ for } 15^\circ \text{ scan angle}$$

$$\mathrm{MPE}_{\text{single}} = 7 \cdot 10^{-4} C_4 C_6 t_f^{0.75} \mathrm{J} = 17\ \mathrm{mJ} \sim 89\ \mathrm{mW} \text{ for } 30^\circ \text{ scan angle}$$

$$\mathrm{MPE}_{\text{single}} = 7 \cdot 10^{-4} C_4 C_6 t_f^{0.75} \mathrm{J} = 7\ \mathrm{mJ} \sim 75\ \mathrm{mW} \text{ for } 15^\circ \text{ scan angle}$$

Condition 2: The average power for a pulse train (frame rate) of emission duration T shall not exceed the power corresponding to the MPE for a single pulse. Here are two different scan times considered for evaluation: T_2 = 100 s and 300 s

$$C_6 = \alpha_{\max}/\alpha_{\min}, \alpha_{\max} = 100\ \mathrm{mrad} \text{ since } t > 0.25\ \mathrm{s}, \text{ therefore, } C_6 = 66.7$$

$$\mathrm{MPE}_{\text{Thermal}} = 7 \cdot 10^{-4} C_4 C_6 T_2^{-0.25} \mathrm{W} = 21\ \mathrm{mW} \text{ for } 100\ \mathrm{s}$$

$$\mathrm{MPE}_{\text{Thermal}} = 7 \cdot 10^{-4} C_4 C_6 T_2^{-0.25} \mathrm{W} = 16\ \mathrm{mW} \text{ for } 300\ \mathrm{s}$$

$$\mathrm{MPE}_{\text{Thermal}} = 7 \cdot 10^{-4} C_4 C_6 T_2^{-0.25} \mathrm{W} = 5.1\ \mathrm{mW} \text{ for } 30000\ \mathrm{s} \text{ (intentional long-term viewing)}$$

Since α > 100 mrad, C_5 = 1. Therefore, condition 3 will result in the same as condition 1. The thermal limits for the two-photon prototype can be interpolated from condition 2, which is 21 mW and 16 mW for 100 and 300 s. For intentional long-term viewing, the study prototype's output power must be 5 mW. The laser safety guidelines developed the standard for the human eye with a focal length of 17 mm and a pupil size of 7 mm. Therefore, the MPE for the rat's retinal imaging can be obtained by scaling the MPE using the square of the ratio of the effective focal length of the rat and human eyes[222].

5.3.4 Retinal Damage Evaluation with Two-Photon ICGA

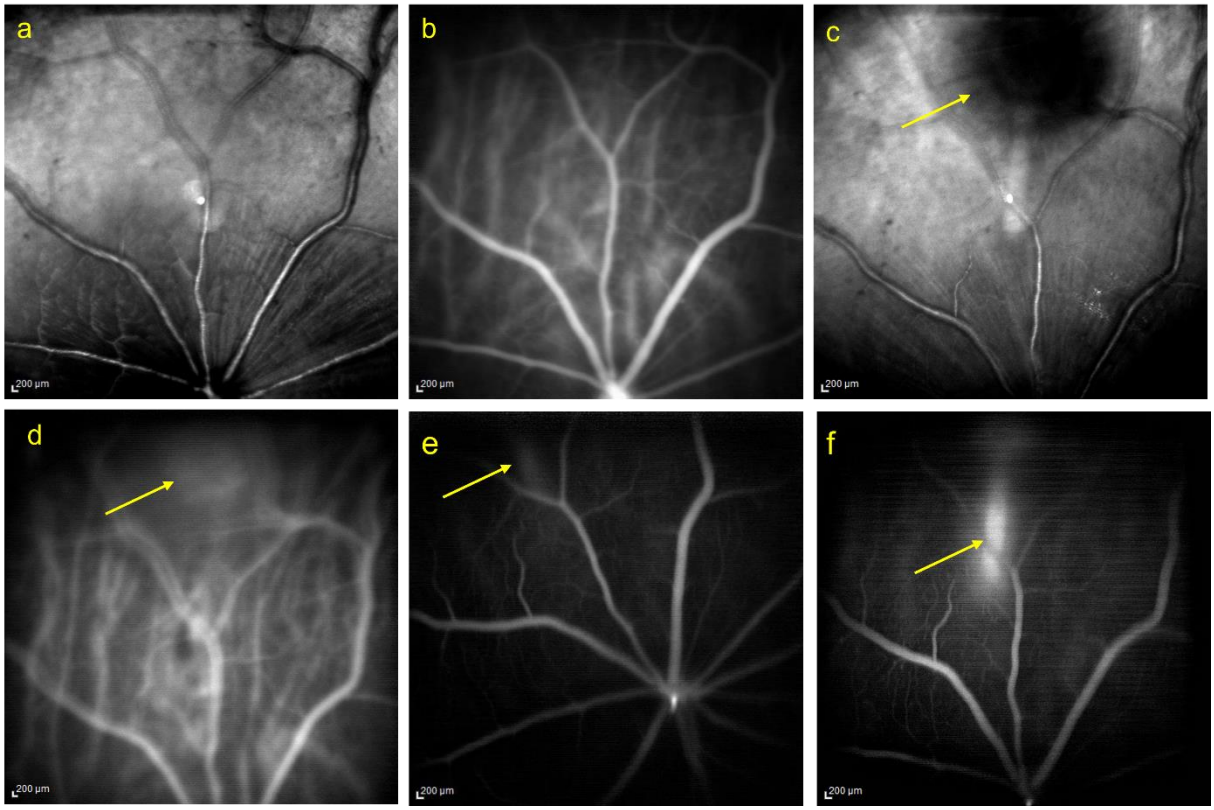

Figure 5.12. Confocal reflectance image (a) and early phase two-photon ICGA (b) of the brown Norway rat with 30° scan angle before laser damage. Confocal reflectance (c) and mid-phase two-photon ICGA (d) of the retinal laser damage with 160 mW for 5 seconds (yellow arrows). Early (e) and mid-phase (f) two-photon FA after ICGA of the laser damage.

The retinal laser damage was evaluated with two-photon ICGA imaging in one brown Norway rat eye. The retina was exposed to a stationary laser beam of 160 mW for 5 seconds. The confocal reflectance, two-photon autofluorescence, two-photon FA, and ICGA were recorded to capture the immediate effect of the laser damage, and the animal was followed for one week. Figure 5.12 shows the confocal reflectance (Figure 5.12a and 5.12c) and two-photon ICGA (Figure 5.12b and 5.12d), and two-photon FA images (Figure 5.12e and 5.12f) of the brown Norway rat's retina before and after exposure to the stationary laser beam. The confocal reflectance image of the retina was captured immediately after the exposure, and the visible retinal lesion induced by exposure to the stationary laser beam for different exposure times is shown in Figure 5.12c. After the exposure, two-photon ICGA was performed, and the early phase to late phase angiograms were recorded. High-contrast retinal and choroidal vasculatures were seen in the mid-phase (Figure 5.12d, arrow) two-photon ICGA, and hyper fluorescence was noticed on the laser-exposed retinal area. The retinal leakage was noticed at two-photon FA (Figure 5.12e and 5.12f).
The irregularity in the nerve fiber layer and the absence of capillaries in the exposed area were noticed on day 3 (Figure 5.13c, 5.13d) and day 7 (Figure 5.13g and 5.13h). The fluorescence signal was strong and distributed throughout the fundus. In Figure 5.13b (yellow arrow), the two-photon autofluorescence image of the retina shows high reflectivity in the laser-exposed area at a laser power of ~120 mW. In contrast, on day 1 after exposure, the retina showed no reflectivity with two-photon autofluorescence imaging. Also, the early two-photon FA on day 3 and day 7 showed the absence of capillaries in the laser-exposed retina. The two-photon autofluorescence image on day

7 showed increased background fluorescence compared to day 1 and day 3. The background autofluorescence was acquired at ~120 mW laser power.

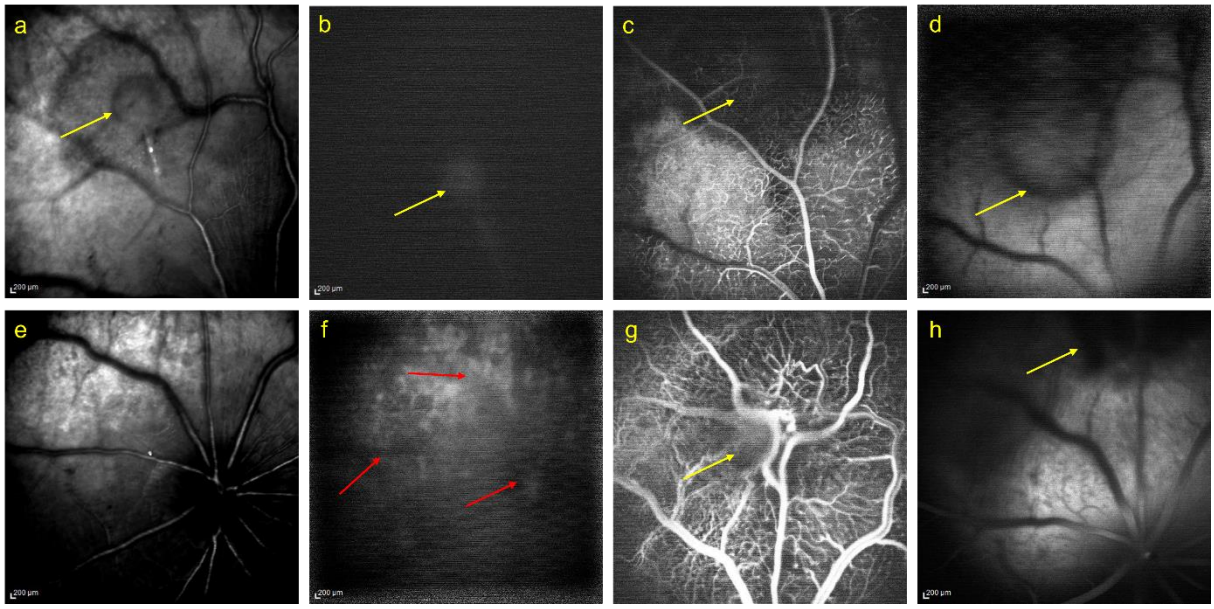

Figure 5.13. Confocal reflectance image (a), two-photon autofluorescence image (b), early (c), and late (d) two-photon FA of the laser damage on day 3. Confocal reflectance image (e), two-photon autofluorescence image (f), early (g) and late (h) two-photon FA of the laser damage on day 7.

We determined in our imaging study that the minimum laser power required for two-photon autofluorescence with our prototype was ~160 mW (Chapter 4). Here, we noticed a two-photon autofluorescence signal at ~120 mW on days 3 and 7. This fluorescence signal was not observed from rat eyes that were used only for imaging with two-photon FA or two-photon ICGA. It was not even observed in rats that were exposed to a stationary laser beam and followed for days with two-photon FA (example Figures 5.3, 5.6, and 5.8). It indicates that this could be due to the ICG dye deposits within the retina. IEC 60825-1 laser safety standard states that if an intense beam of laser light is focused on the retina, only a small fraction of light (up to 5%) will be absorbed by the visual pigment's rods and cones; and most of the light will be absorbed by the melanin in the RPE[126]. The absorbed energy will cause local heating and will burn both the pigment epithelium and adjacent light-sensitive rods and cones. This supports that the RPE was damaged with the 160-mW laser power. Furthermore, retinal toxicities studies have shown that the RPE can internalize the NIR ICG in vitro[223]. Pankova et al. also demonstrated a technique termed "delayed near-infrared analysis (DNIRA)" that permits the detection of RPE with cSLO and ICG dye and is apparent only after ICG injection[224]. Similar to this study, a strong background fluorescent was observed with two-photon imaging after injecting the ICG dye in damaged eye. However, DNIRA study used ICG dye only once, and angiography was not performed again during the study. But in this study, although ICG dye was injected once, a two-photon FA was performed on days 3 and day 7. Therefore, we cannot directly compare this to DNIRA study results. Further the observation was tested and noticed only in one eye and cannot determine the effects from one eye. However, the findings seem to be substantial and two-photon autofluorescent signal after ICG dye would help us detect and monitor the RPE damage and recovery. The relationship might be helpful to assess the retinal light damage with the femtosecond lasers and identify the retinal toxicity.

5.3.5 Future Directions

The power threshold required for the two-photon autofluorescence imaging with our prototype was determined to be 160 mW and is two orders of magnitude higher than the safety standards. Although no potential thermal damage was noticed due to the scanning laser beam, further improvement in light delivery is needed for the two-photon ophthalmoscope in clinical applications. Implementing adaptive optics to the current two-photon prototype would improve light delivery by a factor of four. Also, adaptive optics has emerged as an empowering technology for retinal imaging enabling diffraction-limited and holds potential for non-invasive detection and diagnoses of eye diseases. However, the cost and complexity of adaptive optics ophthalmoscopes with a limited field of view currently impede their clinical use[2]. The HMO lens (Heidelberg Engineering GmbH, Germany) with phase plates has the potential to establish aberration free retinal imaging at a cellular level in a clinical application by simplifying its incorporation in the prevailing systems. The combination of HMO lens with the phase plates could resolve ocular microstructures without using a complex adaptive optics system for an 8-degree FOV. Furthermore, a femtosecond laser with a reduced pulse width would improve the two-photon efficiency since the shortest pulse width coupled with group velocity dispersion compensation would significantly increase the two-photon excitation-induced fluorescence[38]. Thus, employing a shorter pulse width laser (~55 fs) with adaptive optics unit to the prototype will offer high-resolution retinal imaging sustaining the laser safety standards.

5.4 Conclusion

This study concludes that using a two-photon scanning laser ophthalmoscope for in-vivo retinal imaging is safe in rats. No potential thermal damage was observed due to the scanning laser beam at high laser power and multiple exposures. The high contrast two-photon FA images effectively evaluated the light-induced retinal damage. Furthermore, the immunohistochemistry analysis supported the study by analyzing the damages at a cellular level. Since no potential thermal damage was noticed even at high laser power, the physiological and biological processes of the retina in rodents can be studied in vivo using the two-photon ophthalmoscope. However, the appropriate light safety standards must be well established to implement this technique in clinics. The retinal toxicity evaluation at different operating wavelengths and for shorter pulse widths (typically < 100 fs) in non-human primates could establish a broader sense of these safety standards. Shorter pulse widths have a direct relationship to the generated two-photon fluorescence; therefore, it is vital to establish the correlation of the shorter pulse widths to retinal phototoxicity.

6 SUMMARY

Retinal imaging is a crucial tool for physicians to diagnose and monitor a wide range of eye conditions, such as age-related macular degeneration, diabetic retinopathy, and glaucoma. However, current clinical retinal imaging instruments have limitations in resolution and contrast, making it difficult to visualize small structures and details within the retina, making it challenging to accurately diagnose and treat diseases. This thesis aimed to improve the retinal image quality for early detection and diagnosis of retinal diseases by evaluating two methods.

The first method evaluated in this thesis is the use of a "custom phase plate" to compensate for ocular aberrations and improve retinal image quality in a clinical device. A compact, non-contact compensation unit with phase plates was designed and established for the confocal scanning laser ophthalmoscope with a smaller field of view. The results showed that aberration compensation with phase plates improved contrast and image quality and were able to resolve retinal vasculatures and cone photoreceptors. However, phase plates were not able to resolve foveal cones and rod photoreceptors as well as an adaptive optics system. Phase plates are a pre-compensation that can only compensate for static aberrations, unlike adaptive optics which can compensate for dynamic aberrations. The advantages of phase plates over adaptive optics systems are their compact size, less complexity, shorter acquisition time, easy integration into a clinical device, and lower cost. Phase plates and adaptive optics systems can support research to establish biomarkers and functional tests in a clinical setup. The findings of this work have the potential to overcome the limitations of current clinical instruments in resolution and contrast. The phase plates can be used as a middle ground to visualize small structures and details within the retina for improved diagnosis and detection of retinal diseases for patients with HOAs. It has the potential for greater clinical accessibility at lower costs, offering the opportunity to significantly expand the options for high-resolution imaging of the cone mosaic. However, any potential risks of the methods and results need to be evaluated in a clinical study before being implemented in commercial medical devices.

The second method evaluated in this thesis focused on using a "two-photon" imaging technique in animal models. This technique holds potential for high-resolution imaging and was demonstrated to image large areas of the retina in real-time using near-infrared light. The efficacy of using a 780 nm and 270 fs laser for multimodal two-photon imaging was evaluated, and a significant field of view (15º, 20º, and 30º) similar to a confocal scanning laser ophthalmoscope was established. The retinal and choroidal vessels were visualized with two-photon angiography, and the retinal vessels and capillaries were distinct with two-photon fluorescence angiography. Additionally, two-photon Indocyanine Green Angiography was achieved for the first time by exciting a second singlet state at ~398 nm. The results concluded that high-quality retinal and choroidal vasculature images can be acquired with a single light source, which is not possible with current confocal techniques. However, the laser power required for two-photon autofluorescence and angiography with the current prototype exceeds the laser safety standards for human retinal imaging. Therefore, further improvement in the prototype is needed to achieve the same quality and resolution with laser power levels within safety limits.

The safe use of retinal imaging with two-photon excitation in human eyes is crucial, as the effects of ultrashort pulsed lasers on the retina are relatively unknown due to inadequate biological data. Furthermore, the thesis evaluated the safe use of two-photon

imaging for retinal imaging in animal models. The animal retinas were exposed to various laser exposure levels with stationary and scanning laser beams to better understand the biological effects of the pulsed lasers and to support refining the maximum permissible exposure levels. The results showed that using two-photon scanning lasers for in-vivo retinal imaging is safe in rats, and no potential thermal damage was noticed due to the scanning laser beam at high laser power and multiple exposures. High contrast two-photon fluorescence angiography images effectively aid in assessing retinal light damage. The study results support that two-photon retinal imaging can be safely used for in vivo retinal imaging in animal models. However, for the implementation of this technique in human eyes, appropriate light safety standards must be well established.

7 BIBILOGRAPHY

1. Helmholtz, H: *Beschreibung Eines Augen-Spiegels,* Berlin, Heidelberg, Springer Berlin Heidelberg, 1851.
2. Marcos, S, Werner, JS, Burns, SA, Merigan, WH, Artal, P, Atchison, DA, Hampson, KM, Legras, R, Lundstrom, L, Yoon, G, Carroll, J, Choi, SS, Doble, N, Dubis, AM, Dubra, A, Elsner, A, Jonnal, R, Miller, DT, Paques, M, Smithson, HE, Young, LK, Zhang, Y, Campbell, M, Hunter, J, Metha, A, Palczewska, G, Schallek, J, Sincich, LC: Vision science and adaptive optics, the state of the field. *Vision Research,* 132, 2017. https://doi.org/10.1016/j.visres.2017.01.006
3. Rossi, EA, Granger, CE, Sharma, R, Yang, Q, Saito, K, Schwarz, C, Walters, S, Nozato, K, Zhang, J, Kawakami, T, Fischer, W, Latchney, LR, Hunter, JJ, Chung, MM, Williams, DR: Imaging individual neurons in the retinal ganglion cell layer of the living eye. *Proc Natl Acad Sci U S A,* 114**:** 586-591, 2017. https://doi.org/10.1073/pnas.1613445114
4. Webb, RH, Hughes, GW, Delori, FC: Confocal scanning laser ophthalmoscope. *Appl Opt,* 26**:** 1492-1499, 1987. https://doi.org/10.1364/AO.26.001492
5. Huang, D, Swanson, EA, Lin, CP, Schuman, JS, Stinson, WG, Chang, W, Hee, MR, Flotte, T, Gregory, K, Puliafito, CA: Optical coherence tomography. *Science,* 254**:** 1178-1181, 1991. https://doi.org/10.1126/science.1957169
6. Fercher, AF, Hitzenberger, CK, Drexler, W, Kamp, G, Sattmann, H: In vivo optical coherence tomography. *Am J Ophthalmol,* 116**:** 113-114, 1993. https://doi.org/10.1016/s0002-9394(14)71762-3
7. Swanson, EA, Izatt, JA, Hee, MR, Huang, D, Lin, CP, Schuman, JS, Puliafito, CA, Fujimoto, JG: In vivo retinal imaging by optical coherence tomography. *Opt Lett,* 18**:** 1864-1866, 1993. https://doi.org/10.1364/ol.18.001864
8. Liang, J, Williams, DR: Aberrations and retinal image quality of the normal human eye. *Journal of the Optical Society of America A,* 14, 1997. https://doi.org/10.1364/josaa.14.002873
9. Guirao, A, Porter, J, Williams, DR, Cox, IG: Calculated impact of higher-order monochromatic aberrations on retinal image quality in a population of human eyes. *J Opt Soc Am A Opt Image Sci Vis,* 19**:** 620-628, 2002. https://doi.org/10.1364/josaa.19.000620
10. SMIRNOV, MS: Measurement of the wave aberration of the human eye. *Biofizika,* 6**:** 776-795, 1961.
11. van den Brink, G: Measurements of the geometrical aberrations of the eye. *Vision Research,* 2, 1962. https://doi.org/10.1016/0042-6989(62)90028-7
12. Porter, J, Queener, HM, Lin, JE, Thorn, K, Awwal, A: *Adaptive Optics for Vision Science: Principles, Practices, Design, and Applications*, 2005.
13. Liang, J, Williams, DR, Miller, DT: Supernormal vision and high-resolution retinal imaging through adaptive optics. *Journal of the Optical Society of America A,* 14, 1997. https://doi.org/10.1364/josaa.14.002884
14. Roorda, A, Romero-Borja, F, Donnelly Iii, W, Queener, H, Hebert, T, Campbell, M: Adaptive optics scanning laser ophthalmoscopy. *Opt Express,* 10**:** 405-412, 2002. https://doi.org/10.1364/oe.10.000405
15. Burns, SA, Elsner, AE, Sapoznik, KA, Warner, RL, Gast, TJ: Adaptive optics imaging of the human retina. *Progress in Retinal and Eye Research,* 68**:** 1-30, 2019. https://doi.org/10.1016/j.preteyeres.2018.08.002

16. Pircher, M, Zawadzki, RJ: Review of adaptive optics OCT (AO-OCT): principles and applications for retinal imaging [Invited]. *Biomed Opt Express,* 8**:** 2536-2562, 2017. https://doi.org/10.1364/BOE.8.002536
17. Pircher, M, Götzinger, E, Sattmann, H, Leitgeb, RA, Hitzenberger, CK: In vivo investigation of human cone photoreceptors with SLO/OCT in combination with 3D motion correction on a cellular level. *Opt Express,* 18**:** 13935-13944, 2010. https://doi.org/10.1364/OE.18.013935
18. Merino, D, Loza-Alvarez, P: Adaptive optics scanning laser ophthalmoscope imaging: Technology update. *Clinical Ophthalmology.* 2016.
19. LaRocca, F, Dhalla, A-H, Kelly, MP, Farsiu, S, Izatt, JA: Optimization of confocal scanning laser ophthalmoscope design. *Journal of Biomedical Optics,* 18, 2013. https://doi.org/10.1117/1.jbo.18.7.076015
20. Vohnsen, B, Iglesias, I, Artal, P: Directional imaging of the retinal cone mosaic. *Opt Lett,* 29**:** 968-970, 2004. https://doi.org/10.1364/ol.29.000968
21. Wade, AR, Fitzke, FW: In vivo imaging of the human cone-photoreceptor mosaic using a confocal laser scanning ophthalmoscope. *Lasers and Light in Ophthalmology,* 8, 1998.
22. Konstantinou, EK, Mendonça, LSM, Braun, P, Monahan, KM, Mehta, N, Gendelman, I, Levine, ES, Baumal, CR, Witkin, AJ, Duker, JS, Waheed, NK: Retinal Imaging Using a Confocal Scanning Laser Ophthalmoscope-Based High-Magnification Module. *Ophthalmology Retina.* 5 ed., 2021.
23. Mendonça, LSM, Braun, PX, Martin, SM, Hüther, A, Mehta, N, Zhao, Y, Abu-Qamar, O, Konstantinou, EK, Regatieri, CVS, Witkin, AJ, Baumal, CR, Duker, JS, Waheed, NK: Repeatability and Reproducibility of Photoreceptor Density Measurement in the Macula Using the Spectralis High Magnification Module. *Ophthalmology Retina,* 4, 2020. https://doi.org/10.1016/j.oret.2020.04.021
24. Elahi, S, Miere, A, El Ameen, A, Souied, EH: In vivo visualization of variable photoreceptor alteration in a case of peripapillary congenital hypertrophy of the retinal pigment epithelium using spectralis ® high magnification module. *American Journal of Ophthalmology Case Reports,* 20, 2020. https://doi.org/10.1016/j.ajoc.2020.100952
25. Vasseur, V, Arej, N, Alonso, AS, Lafolie, J, Philibert, M, Vignal-Clermont, C, Mauget-Faÿsse, M: Spectralis High Magnification Module imaging in a case of Multiple Evanescent White Dot Syndrome. *American Journal of Ophthalmology Case Reports,* 19, 2020. https://doi.org/10.1016/j.ajoc.2020.100727
26. Wells-Gray, EM, Choi, SS, Bries, A, Doble, N: Variation in rod and cone density from the fovea to the mid-periphery in healthy human retinas using adaptive optics scanning laser ophthalmoscopy. *Eye (Lond),* 30**:** 1135-1143, 2016. https://doi.org/10.1038/eye.2016.107
27. Denk, W, Strickler, JH, Webb, WW: Two-photon laser scanning fluorescence microscopy. *Science,* 248, 1990. https://doi.org/10.1126/science.2321027
28. Helmchen, F, Denk, W: Deep tissue two-photon microscopy. *Nat Methods,* 2**:** 932-940, 2005. https://doi.org/10.1038/nmeth818
29. Masters, BR, So, PT: Antecedents of two-photon excitation laser scanning microscopy. *Microsc Res Tech,* 63**:** 3-11, 2004. https://doi.org/10.1002/jemt.10418
30. So, PT, Dong, CY, Masters, BR, Berland, KM: Two-photon excitation fluorescence microscopy. *Annu Rev Biomed Eng,* 2**:** 399-429, 2000. https://doi.org/10.1146/annurev.bioeng.2.1.399
31. Han, M, Giese, G, Schmitz-Valckenberg, S, Bindewald-Wittich, A, Holz, FG, Yu, J, Bille, JF, Niemz, MH: Age-related structural abnormalities in the human retina-

choroid complex revealed by two-photon excited autofluorescence imaging. *J Biomed Opt,* 12**:** 024012, 2007. https://doi.org/10.1117/1.2717522

32. La Schiazza, O, Bille, JF: High-speed two-photon excited autofluorescence imaging of ex vivo human retinal pigment epithelial cells toward age-related macular degeneration diagnostic. *J Biomed Opt,* 13**:** 064008, 2008. https://doi.org/10.1117/1.2999607
33. Maeda, A, Palczewska, G, Golczak, M, Kohno, H, Dong, Z, Maeda, T, Palczewski, K: Two-photon microscopy reveals early rod photoreceptor cell damage in light-exposed mutant mice. *Proc Natl Acad Sci U S A,* 111**:** E1428-1437, 2014. https://doi.org/10.1073/pnas.1317986111
34. Bindewald-Wittich, A, Han, M, Schmitz-Valckenberg, S, Snyder, SR, Giese, G, Bille, JF, Holz, FG: Two-photon-excited fluorescence imaging of human RPE cells with a femtosecond Ti:Sapphire laser. *Invest Ophthalmol Vis Sci,* 47**:** 4553-4557, 2006. https://doi.org/10.1167/iovs.05-1562
35. Borghuis, BG, Marvin, JS, Looger, LL, Demb, JB: Two-photon imaging of nonlinear glutamate release dynamics at bipolar cell synapses in the mouse retina. *J Neurosci,* 33**:** 10972-10985, 2013. https://doi.org/10.1523/JNEUROSCI.1241-13.2013
36. Imanishi, Y, Batten, ML, Piston, DW, Baehr, W, Palczewski, K: Noninvasive two-photon imaging reveals retinyl ester storage structures in the eye. *J Cell Biol,* 164**:** 373-383, 2004. https://doi.org/10.1083/jcb.200311079
37. Sharma, R, Yin, L, Geng, Y, Merigan, WH, Palczewska, G, Palczewski, K, Williams, DR, Hunter, JJ: In vivo two-photon imaging of the mouse retina. *Biomed Opt Express,* 4**:** 1285-1293, 2013. https://doi.org/10.1364/BOE.4.001285
38. Palczewska, G, Dong, Z, Golczak, M, Hunter, JJ, Williams, DR, Alexander, NS, Palczewski, K: Noninvasive two-photon microscopy imaging of mouse retina and retinal pigment epithelium through the pupil of the eye. *Nature Medicine,* 20, 2014. https://doi.org/10.1038/nm.3590
39. Kamali, T, Fischer, J, Farrell, S, Baldridge, WH, Zinser, G, Chauhan, BC: Simultaneous in vivo confocal reflectance and two-photon retinal ganglion cell imaging based on a hollow core fiber platform. *J Biomed Opt,* 23**:** 1-4, 2018. https://doi.org/10.1117/1.JBO.23.9.091405
40. Lombardo, M, Lombardo, G: Wave aberration of human eyes and new descriptors of image optical quality and visual performance. *Journal of Cataract and Refractive Surgery,* 36, 2010. https://doi.org/10.1016/j.jcrs.2009.09.026
41. Lawless, MA, Hodge, C: Wavefront's role in corneal refractive surgery. *Clinical and Experimental Ophthalmology,* 33, 2005. https://doi.org/10.1111/j.1442-9071.2005.00994.x
42. Razmjou, H, Peyman, A, Moshfeghi, S, Kateb, H, Naderan, M: A comparison between wavefront-optimized and wavefront-guided photorefractive keratectomy in patients with moderate-to-high astigmatism: A randomized clinical trial. *Journal of Current Ophthalmology,* 34**:** 194-194, 2022. https://doi.org/10.4103/joco.joco_18_21
43. Li, SM, Kang, MT, Wang, NL, Abariga, SA: Wavefront excimer laser refractive surgery for adults with refractive errors. *Cochrane Database of Systematic Reviews.* 2020.
44. Burns, SA, Marcos, S, Elsner, AE, Bara, S: Contrast improvement of confocal retinal imaging by use of phase-correcting plates. *Optics Letters,* 27, 2002. https://doi.org/10.1364/ol.27.000400

45. Navarro, R, Moreno-Barriuso, E, Bará, S, Mancebo, T: Phase plates for wave-aberration compensation in the human eye. *Optics Letters,* 25, 2000. https://doi.org/10.1364/ol.25.000236
46. Yoon, G, Jeong, TM, Cox, IG, Williams, DR: Vision improvement by correcting higher-order aberrations with phase plates in normal eyes. *Journal of Refractive Surgery.* 5 ed., 2004.
47. Bille, JF, Agopov, M, Alvarez-Diez, C, Han, M, Korablinova, N, Von Pape, U, La Schiazza, O, Schwingel, M, Zhang, H, Müller, F: Compact adaptive optics system for multiphoton fundus imaging. *Journal of Modern Optics.* 4-5 ed., 2008.
48. Zhang, H, Agopov, M, La Schiazza, O, Bille, J: Rotating pairs of Zernike phase plates for compensating for the higher-order aberrations of the human eye. *Journal of Modern Optics.* 4-5 ed., 2008.
49. Jeong, TM, Yoon, G: Customized correction of wavefront aberrations in abnormal human eyes by using a phase plate and a customized contact lens. *Journal of the Korean Physical Society,* 49, 2006.
50. Gupta, A, El-Rami, H, Barham, R, Fleming, A, Hemert, JV, Sun, JK, Silva, PS, Aiello, LP: Effect of phase-plate adjustment on retinal image sharpness and visible retinal area on ultrawide field imaging. *Eye (Lond),* 33**:** 587-591, 2019. https://doi.org/10.1038/s41433-018-0270-5
51. Mitchell, P, Liew, G, Gopinath, B, Wong, TY: Age-related macular degeneration. *The Lancet,* 392**:** 1147-1159, 2018. https://doi.org/10.1016/S0140-6736(18)31550-2
52. Thomas, CJ, Mirza, RG, Gill, MK: Age-Related Macular Degeneration. *Medical Clinics of North America.* 2021.
53. Wang, Y, Zhong, Y, Zhang, L, Wu, Q, Tham, Y, Rim, TH, Kithinji, DM, Wu, J, Cheng, C, Liang, H, Yu, H, Yang, X, Liu, L: Global Incidence, Progression, and Risk Factors of Age-Related Macular Degeneration and Projection of Disease Statistics in 30 Years: A Modeling Study. *Gerontology*, 2021. https://doi.org/10.1159/000518822
54. Delori, FC, Dorey, CK, Staurenghi, G, Arend, O, Goger, DG, Weiter, JJ: In vivo fluorescence of the ocular fundus exhibits retinal pigment epithelium lipofuscin characteristics. *Invest Ophthalmol Vis Sci,* 36**:** 718-729, 1995.
55. Von Rückmann, A, Fitzke, FW, Bird, AC: Fundus autofluorescence in age-related macular disease imaged with a laser scanning ophthalmoscope. *Investigative Ophthalmology and Visual Science,* 38, 1997.
56. Schmitz-Valckenberg, S, Steinberg, JS, Fleckenstein, M, Visvalingam, S, Brinkmann, CK, Holz, FG: Combined Confocal Scanning Laser Ophthalmoscopy and Spectral-Domain Optical Coherence Tomography Imaging of Reticular Drusen Associated with Age-Related Macular Degeneration. *Ophthalmology,* 117, 2010. https://doi.org/10.1016/j.ophtha.2009.10.044
57. Holz, FG, Bellman, C, Staudt, S, Schütt, F, Völcker, HE: Fundus autofluorescence and development of geographic atrophy in age-related macular degeneration. *Investigative Ophthalmology and Visual Science,* 42, 2001. https://doi.org/10.1016/S0002-9394(01)01394-0
58. Lois, N, Halfyard, AS, Bunce, C, Bird, AC, Fitzke, FW: Reproducibility of fundus autofluorescence measurements obtained using a confocal scanning laser ophthalmoscope. *British Journal of Ophthalmology,* 83, 1999. https://doi.org/10.1136/bjo.83.3.276
59. The Physics Hypertextbook. *http:// hypertextbookcom/physics/waves/aberration.*

60. Campbell, FW, Green, DG: Optical and retinal factors affecting visual resolution. *The Journal of Physiology,* 181, 1965. https://doi.org/10.1113/jphysiol.1965.sp007784
61. Charman, WN: Wavefront technology: Past, present and future. *Contact Lens and Anterior Eye,* 28, 2005. https://doi.org/10.1016/j.clae.2005.02.003
62. Zhang, H: A Study of Aberrations in the Human Eye by Zernike Phase Plate Precompensation and Finite Element Modeling Methods. Dissertation. Medical Faculty Mannheim, University of Heidelberg. 2007. https://archiv.ub.uni-heidelberg.de/volltextserver/10239/
63. ANSI Z80.28-2022: Ophthalmics – Methods of Reporting Optical Aberrations of Eyes. https://blog.ansi.org/ansi-z80-28-2022-ophthalmics-optical-aberrations/#gref
64. Fundus photography. https://en.wikipedia.org/wiki/Fundus_photography
65. Webb, RH, Hughes, GW, Pomerantzeff, O: Flying spot TV ophthalmoscope. *Applied Optics,* 19, 1980. https://doi.org/10.1364/ao.19.002991
66. Webb, RH, Hughes, GW: Scanning laser ophthalmoscope. *IEEE Trans Biomed Eng,* 28**:** 488-492, 1981. https://doi.org/10.1109/TBME.1981.324734
67. Aumann, S, Donner, S, Fischer, J, Müller, F: Optical Coherence Tomography (OCT): Principle and Technical Realization. In: *High Resolution Imaging in Microscopy and Ophthalmology.* 2019.
68. Hee, MR, Izatt, JA, Swanson, EA, Huang, D, Schuman, JS, Lin, CP, Puliafito, CA, Fujimoto, JG: Optical Coherence Tomography of the Human Retina. *Archives of Ophthalmology,* 113, 1995. https://doi.org/10.1001/archopht.1995.01100030081025
69. Puliafito, CA, Hee, MR, Lin, CP, Reichel, E, Schuman, JS, Duker, JS, Izatt, JA, Swanson, EA, Fujimoto, JG: Imaging of Macular Diseases with Optical Coherence Tomography. *Ophthalmology,* 102, 1995. https://doi.org/10.1016/S0161-6420(95)31032-9
70. Rocholz, R, Corvi, F, Weichsel, J, Schmidt, S, Staurenghi, G: OCT Angiography (OCTA) in Retinal Diagnostics. In: *High Resolution Imaging in Microscopy and Ophthalmology.* 2019.
71. Schiazza, OL: Fast Two-Photon Excited Fluorescence Imaging for the Human Retina. Dissertation. University of Heidelberg. 2008. https://archiv.ub.uni-heidelberg.de/volltextserver/8532/
72. Minsky, M: Microscopy Apparatus. *US Patent 3013467,* 3013467, 1957.
73. Wilson, T, Shepparu, CJR, Löschke, K: Theory and practice of scanning optical microscopy. Academic Press, London 1984, 213 Seiten, 138 Abbildungen, Preis $ 39.50 ISBN 0-12-757760-2. *Crystal Research and Technology,* 20, 1985. https://doi.org/10.1002/crat.2170201211
74. White, JG, Amos, WB, Fordham, M: An evaluation of confocal versus conventional imaging of biological structures by fluorescence light microscopy. *The Journal of cell biology,* 105, 1987. https://doi.org/10.1083/jcb.105.1.41
75. Pawley, JB: Fundamental limits in confocal microscopy. In: *Handbook of Biological Confocal Microscopy: Third Edition.* 2006.
76. Liang, J, Grimm, B, Goelz, S, Bille, JF: Objective measurement of wave aberrations of the human eye with the use of a Hartmann–Shack wave-front sensor. *Journal of the Optical Society of America A,* 11, 1994. https://doi.org/10.1364/josaa.11.001949
77. Dreher, AW, Bille, JF, Weinreb, RN: Active optical depth resolution improvement of the laser tomographic scanner. *Applied Optics,* 28, 1989. https://doi.org/10.1364/ao.28.000804

78. Liang, J: A new method to precisely measure the Wave Aberrations of the Human Eye with a Hartmann-Shack Sensor. 1991.
79. Mrochen, M, Kaemmerer, M, Seiler, T: Wavefront-guided laser in situ keratomileusis: Early results in three eyes. *Journal of Refractive Surgery,* 16, 2000. https://doi.org/10.3928/1081-597x-20000301-03
80. Hermann, B, Fernández, EJ, Unterhuber, A, Sattmann, H, Fercher, AF, Drexler, W, Prieto, PM, Artal, P: Adaptive-optics ultrahigh-resolution optical coherence tomography. *Optics Letters,* 29, 2004. https://doi.org/10.1364/ol.29.002142
81. Battu, R, Dabir, S, Khanna, A, Kumar, A, Roy, A: Adaptive optics imaging of the retina. *Indian Journal of Ophthalmology,* 62**:** 60-60, 2014. https://doi.org/10.4103/0301-4738.126185
82. Roorda, A, Williams, DR: The arrangement of the three cone classes in the living human eye. *Nature,* 397, 1999. https://doi.org/10.1038/17383
83. Jacob, J, Paques, M, Krivosic, V, Dupas, B, Erginay, A, Tadayoni, R, Gaudric, A: Comparing parafoveal cone photoreceptor mosaic metrics in younger and older age groups using an adaptive optics retinal camera. *Ophthalmic Surgery Lasers and Imaging Retina,* 48, 2017. https://doi.org/10.3928/23258160-20161219-06
84. Hammer, DX, Ferguson, RD, Bigelow, CE, Iftimia, NV, Ustun, TE, Burns, SA: Adaptive optics scanning laser ophthalmoscope for stabilized retinal imaging. *Optics Express,* 14, 2006. https://doi.org/10.1364/oe.14.003354
85. Lu, J, Gu, B, Wang, X, Zhang, Y: Adaptive optics parallel near-confocal scanning ophthalmoscopy. *Optics Letters,* 41, 2016. https://doi.org/10.1364/ol.41.003852
86. Mujat, M, Ferguson, RD, Iftimia, N, Hammer, DX: Compact adaptive optics line scanning ophthalmoscope. *Optics Express,* 17, 2009. https://doi.org/10.1364/oe.17.010242
87. Zhang, Y, Rha, J, Jonnal, RS, Miller, DT: Adaptive optics parallel spectral domain optical coherence tomography for imaging the living retina. *Optics Express,* 13, 2005. https://doi.org/10.1364/opex.13.004792
88. Prieto, PM, Vargas-Martín, F, Goelz, S, Artal, P: Analysis of the performance of the Hartmann–Shack sensor in the human eye. *Journal of the Optical Society of America A,* 17, 2000. https://doi.org/10.1364/josaa.17.001388
89. Chamot, SR, Dainty, C, Esposito, S: Adaptive optics for ophthalmic applications using a pyramid wavefront sensor. *Optics Express,* 14, 2006. https://doi.org/10.1364/opex.14.000518
90. Iglesias, I, Ragazzoni, R, Julien, Y, Artal, P: Extended source pyramid wave-front sensor for the human eye. *Optics Express,* 10, 2002. https://doi.org/10.1364/oe.10.000419
91. Brunner, E, Shatokhina, J, Shirazi, MF, Drexler, W, Leitgeb, R, Pollreisz, A, Hitzenberger, CK, Ramlau, R, Pircher, M: Retinal adaptive optics imaging with a pyramid wavefront sensor. *Biomedical Optics Express,* 12, 2021. https://doi.org/10.1364/boe.438915
92. Muramatsu, M, Eiju, T, Shirai, T, Matsuda, K: Application of a liquid crystal spatial light modulator on optical roughness measurements by a speckle correlation method using two refractive indices. *Optics and Laser Technology,* 29, 1997. https://doi.org/10.1016/S0030-3992(97)00019-4
93. Shirai, T, Takeno, K, Arimoto, H, Furukawa, H: Adaptive Optics with a Liquid-Crystal-on-Silicon Spatial Light Modulator and Its Behavior in Retinal Imaging. *Japanese Journal of Applied Physics,* 48**:** 070213-070213, 2009. https://doi.org/10.1143/JJAP.48.070213

94. Thibos, LN, Bradley, A: Use of liquid-crystal adaptive-optics to alter the refractive state of the eye. *Optometry and Vision Science,* 74, 1997. https://doi.org/10.1097/00006324-199707000-00028
95. Cope, WT, Wolbarsht, ML, Yamanashi, BS: The corneal polarization cross. *Journal of the Optical Society of America,* 68, 1978. https://doi.org/10.1364/JOSA.68.001139
96. Van Blokland, GJ, Verhelst, SC: Corneal polarization in the living human eye explained with a biaxial model. *Journal of the Optical Society of America A,* 4, 1987. https://doi.org/10.1364/josaa.4.000082
97. Van Blokland, GJ, Van Norren, D: Intensity and polarization of light scattered at small angles from the human fovea. *Vision Research,* 26, 1986. https://doi.org/10.1016/0042-6989(86)90191-4
98. Burns, SA, Tumbar, R, Elsner, AE, Ferguson, D, Hammer, DX: Large-field-of-view, modular, stabilized, adaptive-optics-based scanning laser ophthalmoscope. *Journal of the Optical Society of America A,* 24, 2007. https://doi.org/10.1364/josaa.24.001313
99. Doble, N, Williams, DR: The application of MEMS technology for adaptive optics in vision science. *IEEE Journal on Selected Topics in Quantum Electronics,* 10, 2004. https://doi.org/10.1109/JSTQE.2004.829202
100. Zhang, Y, Poonja, S, Roorda, A: MEMS-based adaptive optics scanning laser ophthalmoscopy. *Optics Letters,* 31, 2006. https://doi.org/10.1364/ol.31.001268
101. Fernandez, EJ, Vabre, L, Hermann, B, Unterhuber, A, Povazay, B, Drexler, W: Adaptive optics with a magnetic deformable mirror: applications in the human eye. *Optics Express,* 14, 2006. https://doi.org/10.1364/oe.14.008900
102. Zou, W, Qi, X, Burns, SA: Wavefront-aberration sorting and correction for a dual-deformable-mirror adaptive-optics system. *Optics Letters,* 33, 2008. https://doi.org/10.1364/ol.33.002602
103. Li, C, Sredar, N, Ivers, KM, Queener, H, Porter, J: A correction algorithm to simultaneously control dual deformable mirrors in a woofer-tweeter adaptive optics system. *Optics Express,* 18, 2010. https://doi.org/10.1364/oe.18.016671
104. Ferguson, RD, Zhong, Z, Hammer, DX, Mujat, M, Patel, AH, Deng, C, Zou, W, Burns, SA: Adaptive optics scanning laser ophthalmoscope with integrated wide-field retinal imaging and tracking. *Journal of the Optical Society of America A,* 27, 2010. https://doi.org/10.1364/josaa.27.00a265
105. Morgan, JIW, Dubra, A, Wolfe, R, Merigan, WH, Williams, DR: In vivo autofluorescence imaging of the human and macaque retinal pigment epithelial cell mosaic. *Investigative Ophthalmology and Visual Science,* 50, 2009. https://doi.org/10.1167/iovs.08-2618
106. Rossi, EA, Rangel-Fonseca, P, Parkins, K, Fischer, W, Latchney, LR, Folwell, MA, Williams, DR, Dubra, A, Chung, MM: In vivo imaging of retinal pigment epithelium cells in age related macular degeneration. *Biomedical Optics Express,* 4, 2013. https://doi.org/10.1364/boe.4.002527
107. Sharma, R, Williams, DR, Palczewska, G, Palczewski, K, Hunter, JJ: Two-photon autofluorescence imaging reveals cellular structures throughout the retina of the living primate eye. *Investigative Ophthalmology and Visual Science,* 57, 2016. https://doi.org/10.1167/iovs.15-17961
108. Feeks, JA, Hunter, JJ: Adaptive optics two-photon excited fluorescence lifetime imaging ophthalmoscopy of exogenous fluorophores in mice. *Biomedical Optics Express,* 8, 2017. https://doi.org/10.1364/boe.8.002483
109. Tang, JAH, Granger, CE, Kunala, K, Parkins, K, Huynh, KT, Bowles-Johnson, K, Yang, Q, Hunter, JJ: Adaptive optics fluorescence lifetime imaging

ophthalmoscopy of in vivo human retinal pigment epithelium. *Biomedical Optics Express,* 13, 2022. https://doi.org/10.1364/boe.451628
110. Mondal, PP, Diaspro, A: *Fundamentals of fluorescence microscopy: Exploring life with light*, 2014.
111. Kubitscheck, U: *Fluorescence Microscopy: From Principles to Biological Applications: Second Edition*, 2017.
112. Göppert-Mayer, M: Über Elementarakte mit zwei Quantensprüngen. *Annalen der Physik,* 401, 1931. https://doi.org/10.1002/andp.19314010303
113. Kamali, T, Farrell, SRM, Baldridge, WH, Fischer, J, Chauhan, BC: Two-Photon Scanning Laser Ophthalmoscope. In: *High Resolution Imaging in Microscopy and Ophthalmology.* 2019.
114. Kaiser, W, Garrett, CGB: Two-photon excitation in CaF2: Eu2+. *Physical Review Letters,* 7, 1961. https://doi.org/10.1103/PhysRevLett.7.229
115. Zipfel, WR, Williams, RM, Webb, WW: Nonlinear magic: Multiphoton microscopy in the biosciences. *Nature Biotechnology.* 2003.
116. Imanishi, Y, Lodowski, KH, Koutalos, Y: Two-photon microscopy: Shedding light on the chemistry of vision. *Biochemistry.* 2007.
117. Wang, W, Liu, Y, Xi, P, Ren, Q: Origin and effect of high-order dispersion in ultrashort pulse multiphoton microscopy in the 10 fs regime. *Applied Optics,* 49, 2010. https://doi.org/10.1364/AO.49.006703
118. Denk, W, Piston, DW, Webb, WW: Multi-photon molecular excitation in laser-scanning microscopy. In: *Handbook of Biological Confocal Microscopy: Third Edition.* 2006.
119. Theer, P, Hasan, MT, Denk, W: Two-photon imaging to a depth of 1000 microm in living brains by use of a Ti:Al2O3 regenerative amplifier. *Opt Lett,* 28**:** 1022-1024, 2003. https://doi.org/10.1364/ol.28.001022
120. Centonze, VE, White, JG: Multiphoton excitation provides optical sections from deeper within scattering specimens than confocal imaging. *Biophysical Journal,* 75, 1998. https://doi.org/10.1016/S0006-3495(98)77643-X
121. Gerritsen, HC, De Grauw, CJ: Imaging of optically thick specimen using two-photon excitation microscopy. *Microscopy Research and Technique,* 47, 1999. https://doi.org/10.1002/(SICI)1097-0029(19991101)47:3<206::AID-JEMT6>3.0.CO;2-H
122. Konig, K: Multiphoton microscopy in life sciences. *Journal of Microscopy.* 2000.
123. Squirrell, JM, Wokosin, DL, White, JG, Bavister, BD: Long-term two-photon fluorescence imaging of mammalian embryos without compromising viability. *Nature Biotechnology,* 17, 1999. https://doi.org/10.1038/11698
124. Tan, YP, Llano, I, Hopt, A, Würriehausen, F, Neher, E: Fast scanning and efficient photodetection in a simple two-photon microscope. *Journal of Neuroscience Methods,* 92, 1999. https://doi.org/10.1016/S0165-0270(99)00103-X
125. Diaspro, A, Bianchini, P, Vicidomini, G, Faretta, M, Ramoino, P, Usai, C: Multi-photon excitation microscopy. *BioMedical Engineering OnLine,* 5**:** 36-36, 2006. https://doi.org/10.1186/1475-925X-5-36
126. Iec: ISH 2 - IEC 60825 Safety of laser products – Part 1: Equipment classification and requirements. *International Standard,* IEC 60825, 2014.
127. Ham, WT, Mueller, HA, Sliney, DH: Retinal sensitivity to damage from short wavelength light. *Nature,* 260, 1976. https://doi.org/10.1038/260153a0
128. Wu, J, Seregard, S, Algvere, PV: Photochemical Damage of the Retina. *Survey of Ophthalmology.* 2006.
129. Youssef, PN, Sheibani, N, Albert, DM: Retinal light toxicity. *Eye.* 2011.

130. Birngruber, R, Hillenkamp, F, Gabel, VP: Theoretical investigations of laser thermal retinal injury. *Health Physics,* 48, 1985. https://doi.org/10.1097/00004032-198506000-00006
131. Moritz, AR: Studies of Thermal Injury: III. The Pathology and Pathogenesis of Cutaneous Burns. An Experimental Study. *Am J Pathol,* 23**:** 915-941, 1947.
132. Boulton, M, Rózanowska, M, Rózanowski, B: Retinal photodamage. *Journal of Photochemistry and Photobiology B: Biology,* 64, 2001. https://doi.org/10.1016/S1011-1344(01)00227-5
133. Hillenkamp, F: Laser radiation tissue interaction. *Health Physics,* 56, 1989. https://doi.org/10.1097/00004032-198905000-00002
134. Jacques, SL: Laser-tissue interactions: Photochemical, photothermal, and photomechanical. *Surgical Clinics of North America.* 1992.
135. Birngruber, R, Hefetz, Y, Roider, J, Schmidt, U, Fujimoto, JG, Puliafito, CA: Spatial confinement of intraocular picoseconds-photodisruption effects. *Ophthalmologe,* 90**:** 387-390, 1993.
136. Brinkmann, R, Hüttmann, G, Rögener, J, Roider, J, Birngruber, R, Lin, CP: Origin of retinal pigment epithelium cell damage by pulsed laser irradiance in the nanosecond to microsecond time regimen. *Lasers in Surgery and Medicine,* 27, 2000. https://doi.org/10.1002/1096-9101(2000)27:5<451::AID-LSM1006>3.0.CO;2-1
137. Jacques, SL, McAuliffe, DJ: THE MELANOSOME: THRESHOLD TEMPERATURE FOR EXPLOSIVE VAPORIZATION AND INTERNAL ABSORPTION COEFFICIENT DURING PULSED LASER IRRADIATION. *Photochemistry and Photobiology,* 53, 1991. https://doi.org/10.1111/j.1751-1097.1991.tb09891.x
138. Leszczynski, D, Pitsillides, CM, Pastila, RK, Anderson, RR, Lin, CP: Laser-beam-triggered microcavitation: A novel method for selective cell destruction. *Radiation Research,* 156, 2001. https://doi.org/10.1667/0033-7587(2001)156[0399:LBTMAN]2.0.CO;2
139. Vogel, A, Busch, S, Jungnickel, K, Birngruber, R: Mechanisms of intraocular photodisruption with picosecond and nanosecond laser pulses. *Lasers in Surgery and Medicine,* 15, 1994. https://doi.org/10.1002/lsm.1900150106
140. Vogel, A, Capon, MRC, Asiyo-Vogel, MN, Birngruber, R: Intraocular photodisruption with picosecond and nanosecond laser pulses: Tissue effects in cornea, lens, and retina. *Investigative Ophthalmology and Visual Science,* 35, 1994.
141. Vogel, A, Schweiger, P, Frieser, A, Asiyo, M, Birngruber, R: [Mechanism of action, scope of the damage and reduction of side effects in intraocular Nd:YAG laser surgery]. *Fortschr Ophthalmol,* 87, 1990.
142. Michels, M, Lewis, H, Abrams, GW, Han, DP, Mieler, WF, Neitz, J: Macular phototoxicity caused by fiberoptic endoillumination during pars plana vitrectomy. *American Journal of Ophthalmology,* 114, 1992. https://doi.org/10.1016/S0002-9394(14)71792-1
143. Jaffe, GJ, Irvine, AR, Wood, IS, Severinghaus, JW, Pino, GR, Haugen, C: Retinal Phototoxicity from the Operating Microscope: The Role of Inspired Oxygen. *Ophthalmology,* 95, 1988. https://doi.org/10.1016/S0161-6420(88)33065-4
144. Jaffe, GJ, Wood, IS: Retinal phototoxicity from the operating microscope: a protective effect by the fovea. *Archives of ophthalmology.* 1988.
145. M Albert, ED, Jakobiec W B Saunders Philadelphia, FA, Mellerio, J: Basic Sciences. 1994.

146. Gorgels, TGMF, Van Norren, D: Ultraviolet and green light cause different types of damage in rat retina. *Investigative Ophthalmology and Visual Science,* 36, 1995. https://doi.org/10.1097/00006982-199616040-00022
147. Busch, EM, Gorgels, TGMF, Van Norren, D: Temporal sequence of changes in rat retina after UV-A and blue light exposure. *Vision Research,* 39, 1999. https://doi.org/10.1016/S0042-6989(98)00233-8
148. Ham, WT, Ruffolo, JJ, Mueller, HA, Clarke, AM, Moon, ME: Histologic analysis of photochemical lesions produced in rhesus retina by short-wavelength light. *Investigative Ophthalmology and Visual Science,* 17, 1978.
149. Tso, MOM, Fine, BS: Repair and late degeneration of the primate foveola after injury by argon laser. *Investigative Ophthalmology and Visual Science,* 18, 1979.
150. Ham, WT, Mueller, HA: The Photopathology and Nature of the Blue Light and Near-UV Retinal Lesions Produced by Lasers and Other Optical Sources. In: *Laser Applications in Medicine and Biology.* 1989.
151. LaVail, MM, Gorrin, GM: Protection from light damage by ocular pigmentation: Analysis using experimental chimeras and translocation mice. *Experimental Eye Research,* 44, 1987. https://doi.org/10.1016/S0014-4835(87)80050-7
152. Hope-Ross, MW, Mahon, GJ, Gardiner, TA, Archer, DB: Ultrastructural findings in solar retinopathy. *Eye (Basingstoke),* 7, 1993. https://doi.org/10.1038/eye.1993.7
153. Ziegelberger, G: Icnirp guidelines on limits of exposure to laser radiation of wavelengths between 180 nm and 1,000 μm. *Health Physics,* 105, 2013. https://doi.org/10.1097/HP.0b013e3182983fd4
154. Laser Institute of America, LIA: ANSI Z136.1: American National Standard for Safe Use of Lasers. *SPIE Medical Imaging*, 2007.
155. Jayabalan, GS, Kessler, R, Fischer, J, Bille, JF: Compact Adaptive Optics Scanning Laser Ophthalmoscope with Phase Plates. In: *High Resolution Imaging in Microscopy and Ophthalmology.* 2019.
156. Jayabalan, GS, Bille, JF: The Development of Adaptive Optics and Its Application in Ophthalmology. In: *High Resolution Imaging in Microscopy and Ophthalmology.* 2019.
157. Jayabalan, GS, Wu, YK, Bille, JF, Kim, S, Mao, XW, Gimbel, HV, Rauser, ME, Fan, JT: In vivo two-photon imaging of retina in rabbits and rats. *Experimental Eye Research,* 166, 2018. https://doi.org/10.1016/j.exer.2017.04.009
158. Jayabalan, GS, Bille, JF, Mao, XW, Gimbel, HV, Rauser, ME, Wenz, F, Fan, JT: Retinal safety evaluation of two-photon laser scanning in rats. *Biomedical Optics Express,* 10, 2019. https://doi.org/10.1364/boe.10.003217
159. Baehr, J, Brenner, K-H: Applications and potential of the mask structured ion exchange technique (MSI) in micro-optics. *Gradient Index, Miniature, and Diffractive Optical Systems III.* 2003.
160. Bará, S, Mancebo, T, Moreno-Barriuso, E: Positioning tolerances for phase plates compensating aberrations of the human eye. *Applied Optics,* 39, 2000. https://doi.org/10.1364/ao.39.003413
161. Axis of the eye. https://www.feelgoodcontacts.com/eye-care-hub/what-does-axis-mean-on-my-prescription
162. Cook, W, McKelvie, J, Wallace, H, Misra, S: Comparison of higher order wavefront aberrations with four aberrometers. *Indian Journal of Ophthalmology,* 67, 2019. https://doi.org/10.4103/ijo.IJO_1464_18
163. Prakash, G, Jhanji, V, Srivastava, D, Suhail, M, Rong, SS, Bacero, R, Philip, R: Single session, intra-observer repeatability of an advanced new generation

Hartmann-Shack Aberrometer in refractive surgery candidates. *Journal of Ophthalmic and Vision Research.* 2015.
164. Carracedo, G, Carpena-Torres, C, Batres, L, Serramito, M, Gonzalez-Bergaz, A: Comparison of Two Wavefront Autorefractors: Binocular Open-Field versus Monocular Closed-Field. *Journal of Ophthalmology,* 2020, 2020. https://doi.org/10.1155/2020/8580471
165. Zeiss i.Profiler. https://www.zeiss.com/vision-care/us/eye-care-professionals/equipment/refraction/iprofiler.html
166. Visser, N, Berendschot, TT, Verbakel, F, Tan, AN, de Brabander, J, Nuijts, RM: Evaluation of the comparability and repeatability of four wavefront aberrometers. *Invest Ophthalmol Vis Sci,* 52**:** 1302-1311, 2011. https://doi.org/10.1167/iovs.10-5841
167. Malacara, D: *Optical Shop Testing: Third Edition*, 2006.
168. Artal, P, Guirao, A, Berrio, E, Williams, DR: Compensation of corneal aberrations by the internal optics in the human eye. *Journal of Vision,* 1, 2001. https://doi.org/10.1167/1.1.1
169. Domdei, N, Linden, M, Reiniger, JL, Holz, FG, Harmening, WM: Eye tracking-based estimation and compensation of chromatic offsets for multi-wavelength retinal microstimulation with foveal cone precision. *Biomedical Optics Express,* 10, 2019. https://doi.org/10.1364/boe.10.004126
170. Domdei, N, Domdei, L, Reiniger, JL, Linden, M, Holz, FG, Roorda, A, Harmening, WM: Ultra-high contrast retinal display system for single photoreceptor psychophysics. *Biomedical Optics Express,* 9, 2018. https://doi.org/10.1364/boe.9.000157
171. Wynne, N, Heitkotter, H, Woertz, EN, Cooper, RF, Carroll, J: Comparison of Cone Mosaic Metrics From Images Acquired With the SPECTRALIS High Magnification Module and Adaptive Optics Scanning Light Ophthalmoscopy. *Translational Vision Science & Technology,* 11**:** 19-19, 2022. https://doi.org/10.1167/tvst.11.5.19
172. Považay, B, Brinkmann, R, Stoller, M, Kessler, R: Selective Retina Therapy. In: *High Resolution Imaging in Microscopy and Ophthalmology.* Cham, Springer International Publishing, 2019, pp 237-259.
173. Sahler, R, Bille, JF, Enright, S, Chhoeung, S, Chan, K: Creation of a refractive lens within an existing intraocular lens using a femtosecond laser. *Journal of Cataract and Refractive Surgery.* 8 ed., 2016.
174. Padmanabhan, P, Basuthkar, SS, Joseph, R: Ocular aberrations after wavefront optimized LASIK for myopia. *Indian Journal of Ophthalmology,* 58, 2010. https://doi.org/10.4103/0301-4738.64139
175. McAlinden, C, Moore, JE: Comparison of higher order aberrations after LASIK and LASEK for myopia. *Journal of Refractive Surgery.* 1 ed., 2010.
176. Hashemi, H, Khabazkhoob, M, Jafarzadehpur, E, Yekta, A, Emamian, MH, Shariati, M, Fotouhi, A: Higher order aberrations in a normal adult population. *Journal of Current Ophthalmology,* 27, 2015. https://doi.org/10.1016/j.joco.2015.11.002
177. Boretsky, A, Khan, F, Burnett, G, Hammer, DX, Daniel Ferguson, R, Van Kuijk, F, Motamedi, M: In vivo imaging of photoreceptor disruption associated with age-related macular degeneration: A pilot study. *Lasers in Surgery and Medicine,* 44, 2012. https://doi.org/10.1002/lsm.22070
178. Duncan, JL, Zhang, Y, Gandhi, J, Nakanishi, C, Othman, M, Branham, KEH, Swaroop, A, Roorda, A: High-resolution imaging with adaptive optics in patients

with inherited retinal degeneration. *Investigative Ophthalmology and Visual Science,* 48, 2007. https://doi.org/10.1167/iovs.06-1422
179. Wolfing, JI, Chung, M, Carroll, J, Roorda, A, Williams, DR: High-Resolution Retinal Imaging of Cone-Rod Dystrophy. *Ophthalmology,* 113, 2006. https://doi.org/10.1016/j.ophtha.2006.01.056
180. Paques, M, Meimon, S, Rossant, F, Rosenbaum, D, Mrejen, S, Sennlaub, F, Grieve, K: Adaptive optics ophthalmoscopy: Application to age-related macular degeneration and vascular diseases. *Progress in Retinal and Eye Research.* 2018.
181. Lombardo, M, Parravano, M, Lombardo, G, Varano, M, Boccassini, B, Stirpe, M, Serrao, S: Adaptive optics imaging of parafoveal cones in type 1 diabetes. *Retina,* 34, 2014. https://doi.org/10.1097/IAE.0b013e3182a10850
182. Soliman, MK, Sadiq, MA, Agarwal, A, Sarwar, S, Hassan, M, Hanout, M, Graf, F, High, R, Do, DV, Nguyen, QD, Sepah, YJ: High-resolution imaging of parafoveal cones in different stages of diabetic retinopathy using adaptive optics fundus camera. *PLoS ONE,* 11, 2016. https://doi.org/10.1371/journal.pone.0152788
183. Nesper, PL, Scarinci, F, Fawzi, AA: Adaptive optics reveals photoreceptor abnormalities in diabetic macular ischemia. *PLoS ONE,* 12, 2017. https://doi.org/10.1371/journal.pone.0169926
184. Gale, MJ, Harman, GA, Chen, J, Pennesi, ME: Repeatability of adaptive optics automated cone measurements in subjects with retinitis pigmentosa and novel metrics for assessment of image quality. *Translational Vision Science and Technology,* 8, 2019. https://doi.org/10.1167/tvst.8.3.17
185. Tojo, N, Nakamura, T, Fuchizawa, C, Oiwake, T, Hayashi, A: Adaptive optics fundus images of cone photoreceptors in the macula of patients with retinitis pigmentosa. *Clinical Ophthalmology,* 7, 2013. https://doi.org/10.2147/OPTH.S39879
186. Bessho, K, Bartsch, DUG, Gomez, L, Cheng, L, Koh, HJ, Freeman, WR: Ocular wavefront aberrations in patients with macular diseases. *Retina,* 29, 2009. https://doi.org/10.1097/IAE.0b013e3181a5e657
187. Alexander, NS, Palczewska, G, Stremplewski, P, Wojtkowski, M, Kern, TS, Palczewski, K: Image registration and averaging of low laser power two-photon fluorescence images of mouse retina. *Biomedical Optics Express,* 7, 2016. https://doi.org/10.1364/boe.7.002671
188. Bar-Noam, AS, Farah, N, Shoham, S: Correction-free remotely scanned two-photon in vivo mouse retinal imaging. *Light: Science and Applications,* 5, 2016. https://doi.org/10.1038/lsa.2016.7
189. Schejter, A, Farah, N, Shoham, S: Two-photon in vivo imaging of retinal microstructures. *Multiphoton Microscopy in the Biomedical Sciences XIV.* 2014.
190. Stremplewski, P, Komar, K, Palczewski, K, Wojtkowski, M, Palczewska, G: Periscope for noninvasive two-photon imaging of murine retina in vivo. *Biomedical Optics Express,* 6, 2015. https://doi.org/10.1364/boe.6.003352
191. Zuclich, JA, Schuschereba, ST, Zwick, H, Boppart, SA, Fujimoto, JG, Cheney, FE, Stuck, BE: A comparison of laser-induced retinal damage from infrared wavelengths to that from visible wavelengths. *Lasers and Light in Ophthalmology,* 8, 1997.
192. He, S, Ye, C, Sun, Q, Leung, CKS, Qu, JY: Label-free nonlinear optical imaging of mouse retina. *Biomedical Optics Express,* 6, 2015. https://doi.org/10.1364/boe.6.001055
193. Palczewska, G, Golczak, M, Williams, DR, Hunter, JJ, Palczewski, K: Endogenous fluorophores enable two-photon imaging of the primate eye.

Investigative Ophthalmology and Visual Science, 55, 2014. https://doi.org/10.1167/iovs.14-14395
194. Peters, S, Hammer, M, Schweitzer, D: Two-photon excited fluorescence microscopy application for ex vivo investigation of ocular fundus samples. *Advanced Microscopy Techniques II.* 2011.
195. Paques, M, Simonutti, M, Roux, MJ, Picaud, S, Levavasseur, E, Bellman, C, Sahel, JA: High resolution fundus imaging by confocal scanning laser ophthalmoscopy in the mouse. *Vision Research,* 46, 2006. https://doi.org/10.1016/j.visres.2005.09.037
196. Boguslawski, J, Palczewska, G, Tomczewski, S, Milkiewicz, J, Kasprzycki, P, Stachowiak, D, Komar, K, Marzejon, MJ, Sikorski, BL, Hudzikowski, A, Głuszek, A, Łaszczych, Z, Karnowski, K, Soboń, G, Palczewski, K, Wojtkowski, M: In vivo imaging of the human eye using a 2-photon-excited fluorescence scanning laser ophthalmoscope. *Journal of Clinical Investigation,* 132, 2022. https://doi.org/10.1172/JCI154218
197. Balaban, RS, Hampshire, VA: Challenges in small animal noninvasive imaging. *ILAR Journal,* 42, 2001. https://doi.org/10.1093/ilar.42.3.248
198. Pu, Y, Shi, L, Pratavieira, S, Alfano, RR: Two-photon excitation microscopy using the second singlet state of fluorescent agents within the "tissue optical window". *Journal of Applied Physics,* 114, 2013. https://doi.org/10.1063/1.4825319
199. Freeman, WR, Bartsch, DU, Mueller, AJ, Banker, AS, Weinreb, RN: Simultaneous indocyanine green and fluorescein angiography using a confocal scanning laser ophthalmoscope. *Archives of Ophthalmology,* 116, 1998. https://doi.org/10.1001/archopht.116.4.455
200. Holz, FG, Bellmann, C, Rohrschneider, K, Burk, ROW, Völcker, HE: Simultaneous confocal scanning laser fluorescein and indocyanine green angiography. *American Journal of Ophthalmology,* 125, 1998. https://doi.org/10.1016/S0002-9394(99)80095-6
201. Geng, Y, Greenberg, KP, Wolfe, R, Gray, DC, Hunter, JJ, Dubra, A, Flannery, JG, Williams, DR, Porter, J: In vivo imaging of microscopic structures in the rat retina. *Investigative Ophthalmology and Visual Science,* 50, 2009. https://doi.org/10.1167/iovs.09-3675
202. Gibson, EA, Masihzadeh, O, Lei, TC, Ammar, DA, Kahook, MY: Multiphoton Microscopy for Ophthalmic Imaging. *Journal of Ophthalmology,* 2011, 2011. https://doi.org/10.1155/2011/870879
203. Delori, FC, Webb, RH, Sliney, DH: Maximum permissible exposures for ocular safety (ANSI 2000), with emphasis on ophthalmic devices. *Journal of the Optical Society of America A,* 24, 2007. https://doi.org/10.1364/josaa.24.001250
204. Huang, S, Heikal, AA, Webb, WW: Two-photon fluorescence spectroscopy and microscopy of NAD(P)H and flavoprotein. *Biophysical Journal,* 82, 2002. https://doi.org/10.1016/S0006-3495(02)75621-X
205. Palczewska, G, Maeda, T, Imanishi, Y, Sun, W, Chen, Y, Williams, DR, Piston, DW, Maeda, A, Palczewski, K: Noninvasive multiphoton fluorescence microscopy resolves retinol and retinal condensation products in mouse eyes. *Nature Medicine,* 16, 2010. https://doi.org/10.1038/nm.2260
206. Glickman, RD: Ultraviolet phototoxicity to the retina. *Eye and Contact Lens.* 2011.
207. Ham, WT, Mueller, HA, Wolbarsht, ML, Sliney, DH: Evaluation of retinal exposures from repetitively pulsed and scanning lasers. *Health Physics,* 54, 1988. https://doi.org/10.1097/00004032-198803000-00011
208. Cain, CP, DiCarlo, CD, Rockwell, BA, Kennedy, PK, Noojin, GD, Stolarski, DJ, Hammer, DX, Toth, CA, Roach, WP: Retinal damage and laser-induced

breakdown produced by ultrashort-pulse lasers. *Graefe's Archive for Clinical and Experimental Ophthalmology,* 234, 1996. https://doi.org/10.1007/bf02343045

209. Rockwell, BA, Hammer, DX, Hopkins, RA, Payne, DJ, Toth, CA, Roach, WP, Druessel, JJ, Kennedy, PK, Amnotte, RE, Eilert, B, Phillips, S, Noojin, GD, Stolarski, DJ, Cain, C: Ultrashort laser pulse bioeffects and safety. *Journal of Laser Applications,* 11, 1999. https://doi.org/10.2351/1.521879
210. Cain, CP, Toth, CA, Noojin, GD, Stolarski, DJ, Thomas, RJ, Rockwell, BA: Thresholds for retinal injury from multiple near-infrared ultrashort laser pulses. *Health Physics,* 82, 2002. https://doi.org/10.1097/00004032-200206000-00014
211. Thomas, RJ, Noojin, GD, Stolarski, DJ, Hall, RT, Cain, CP, Toth, CA, Rockwell, BA: A comparative study of retinal effects from continuous wave and femtosecond mode-locked lasers. *Lasers in Surgery and Medicine,* 31, 2002. https://doi.org/10.1002/lsm.10067
212. Schwarz, C, Sharma, R, Fischer, WS, Chung, M, Palczewska, G, Palczewski, K, Williams, DR, Hunter, JJ: Safety assessment in macaques of light exposures for functional two-photon ophthalmoscopy in humans. *Biomedical Optics Express,* 7, 2016. https://doi.org/10.1364/boe.7.005148
213. Schwarz, C, Sharma, R, Cheong, SK, Keller, M, Williams, DR, Hunter, JJ: Selective S cone damage and retinal remodeling following intense ultrashort pulse laser exposures in the near-infrared. *Investigative Ophthalmology and Visual Science,* 59, 2018. https://doi.org/10.1167/iovs.18-25383
214. Promega corporation- Product, G: DeadEnd™ Fluorometric TUNEL System Technical Bulletin. *https://wwwpromegade/-/media/files/resources/protocols/technical-bulletins/0/deadend-fluorometric-tunel-system-protocolpdf.*
215. Schmitz-Valckenberg, S, Guo, L, Maass, A, Cheung, W, Vugler, A, Moss, SE, Munro, PMG, Fitzke, FW, Cordeiro, MF: Real-time in vivo imaging of retinal cell apoptosis after laser exposure. *Investigative Ophthalmology and Visual Science,* 49, 2008. https://doi.org/10.1167/iovs.07-1335
216. Contín, MA, Arietti, MM, Benedetto, MM, Bussi, C, Guido, ME: Photoreceptor damage induced by low-intensity light: Model of retinal degeneration in mammals. *Molecular Vision,* 19, 2013.
217. Wood, JPM, Shibeeb, OS, Plunkett, M, Casson, RJ, Chidlow, G: Retinal damage profiles and neuronal effects of laser treatment: Comparison of a conventional photocoagulator and a novel 3-nanosecond pulse laser. *Investigative Ophthalmology and Visual Science,* 54, 2013. https://doi.org/10.1167/iovs.12-11203
218. Organisciak, DT, Vaughan, DK: Retinal light damage: Mechanisms and protection. *Progress in Retinal and Eye Research.* 2010.
219. McHugh, D, England, C, Van Der Zypen, E, Marshall, J, Fankhauser, F, Fankhauser-Kwasnieska, S: Irradiation of rabbit retina with diode and Nd:YAG lasers. *British Journal of Ophthalmology,* 79, 1995. https://doi.org/10.1136/bjo.79.7.672
220. Henriksson, JT, Bergmanson, JPG, Walsh, JE: Ultraviolet radiation transmittance of the mouse eye and its individual media components. *Experimental Eye Research,* 90, 2010. https://doi.org/10.1016/j.exer.2009.11.004
221. Lund, DJ, Edsall, P, Stuck, BE, Schulmeister, K: Variation of laser-induced retinal injury thresholds with retinal irradiated area: 0.1-s duration, 514-nm exposures. *Journal of Biomedical Optics,* 12, 2007. https://doi.org/10.1117/1.2714810

222. Morgan, JIW, Hunter, JJ, Masella, B, Wolfe, R, Gray, DC, Merigan, WH, Delori, FC, Williams, DR: Light-induced retinal changes observed with high-resolution autofluorescence imaging of the retinal pigment epithelium. *Investigative Ophthalmology and Visual Science,* 49, 2008. https://doi.org/10.1167/iovs.07-1430
223. Chang, AA, Zhu, M, Billson, F: The interaction of indocyanine green with human retinal pigment epithelium. *Investigative Ophthalmology and Visual Science,* 46, 2005. https://doi.org/10.1167/iovs.04-0825
224. Pankova, N, Zhao, X, Liang, H, Baek, DS, Wang, H, Boyd, S: Delayed near-infrared analysis permits visualization of rodent retinal pigment epithelium layer in vivo. *J Biomed Opt,* 19**:** 76007-76007, 2014. https://doi.org/10.1117/1.JBO.19.7.076007

8 APPENDIX

Trial phase plates

In this study, a set of trial phase plates with different aberrations (astigmatic plates, coma plates, trefoil plates, spherical aberration plates) was evaluated in Zemax as a way to cover a large population of patients instead of using customized phase plates. However, the practical implementation of this approach was not demonstrated in this study due to design complications and the number of phase plates required to compensate for HOAs. While it is possible to use pairs of rotating phase plates to compensate for variable HOAs[48], the current design of the prototype requires manual rotation to find the optimal position, which may be complicated for operators in clinical settings without automation. The impact of implementing such phase plates in a clinical setting would be difficult without automation. Therefore, it was decided not to implement a set of trial phase plates in this study, but with further automation, this could be a step forward. Further research can be conducted to determine how many trial phase plates would be needed to cover a large population, and an aberration model can be established based on statistical data.

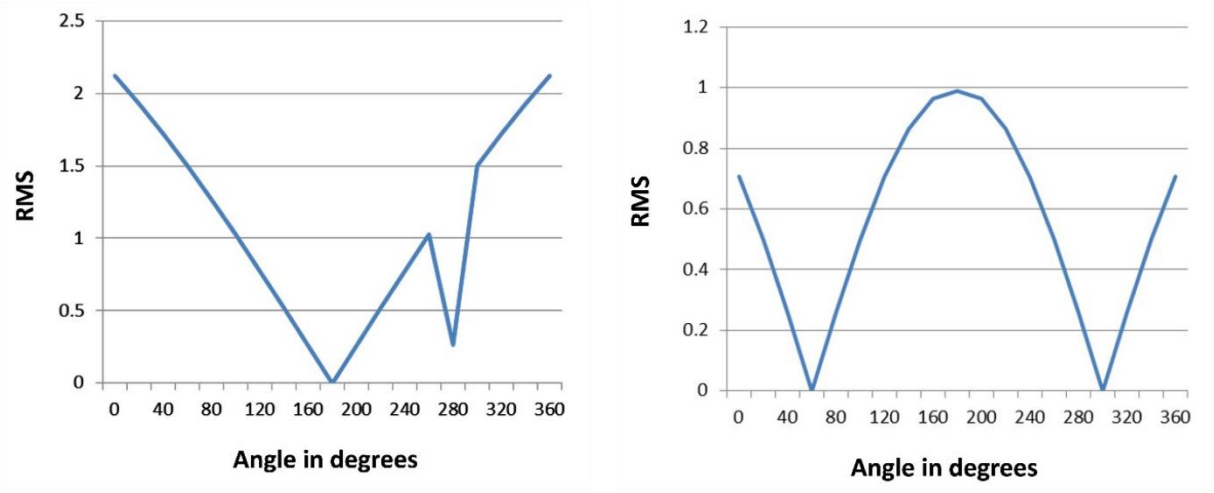

Figure 8.1. Variable aberration generation by rotating two phase plates. With two +0.5 microns coma plates, the RMS of 0 to 2 microns can be generated with rotation (left image). Likewise, with two +0.5 microns trefoil plates, the RMS of 0 to 1 micron can be generated (right image).

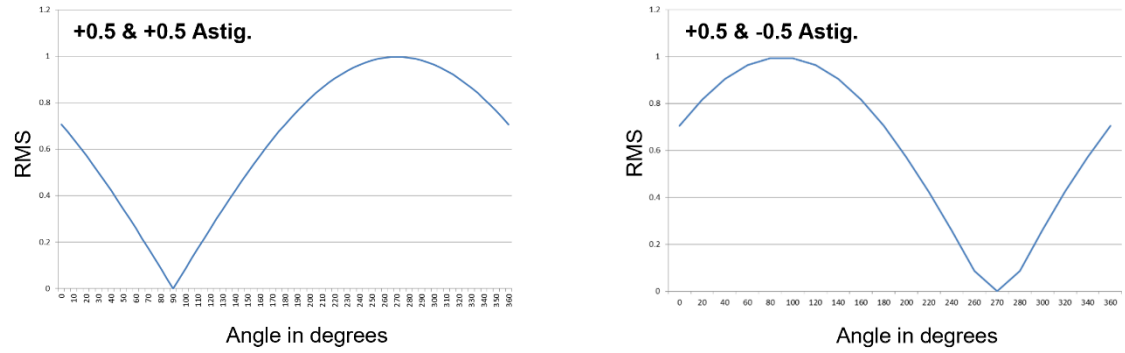

Figure 8.2. Variable aberration generation by rotating two astigmatism phase plates. With two +0.5 microns astigmatism plates, the RMS of 0 to 1 micron can be generated with rotation (left image). Likewise, with one +0.5- and -0.5-microns astigmatism plates, the RMS of 0 to 1 micron can be generated (right image).

The standard Zernike polynomial functions have been widely used to describe wavefront aberrations of the human eye. They are represented in the form of z_n^m, where "n" is the radial order and "m" is the azimuthal index. Zernike polynomials with the same radial order "n" but oppositely signed "m" are symmetric, meaning that one can be obtained by rotating the other by a given angle. It should be noted that the Zernike terms of the same radial order "n" and having the same magnitude of meridional indices "m" but with opposite signs can be redefined in terms of magnitude and axis. The magnitude coefficient "c_{nm}" and the axis coefficient "α_{nm}" can be calculated using the following equations:

$$C_{nm} = \sqrt{(C_n^{-m})^2 + (C_n^m)^2}$$

Equation 8.1

$$\alpha_{nm} = \frac{1}{m}\, tan^{-1}\left(\frac{C_n^{-m}}{C_n^m}\right)$$

Equation 8.2

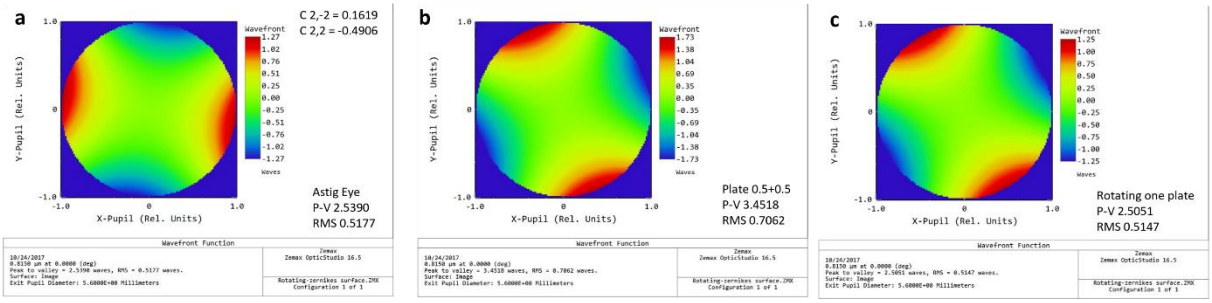

Figure 8.3. Wavefront map of the astigmatic eye with RMS 0.5177 microns (a), and the wavefront map with pair of astigmatic plate with 0.5 microns, RMS 0.7062 microns (b), the wavefront map generating RMS of 0.5147 microns by rotating one plate to each other (c).

Figure 8.3 illustrates a simulation using Zemax, which employs a pair of identical rotating Zernike phase plates to correct astigmatism in the human eye. The wavefront map of the astigmatic eye is displayed in Figure 8.3a, with an oblique astigmatism (C 2, -2) of 0.1619 microns and a vertical astigmatism (C 2, 2) of -0.4906 microns at 81 degrees, for a total of 0.5177 microns. Figure 8.3b shows the wavefront map of the two 0.5 microns astigmatism plates, creating an RMS of 0.7062 microns. However, the angle of astigmatism is different, and manual rotation of one plate is required to match the RMS of eye's aberration. By rotating one phase plate, a similar RMS error to the eye can be generated (Figure 8.3c). After locking this position, the pair of astigmatism plates can be placed in front of the eye to correct the eye's aberrations. The pair must be rotated together to correct the eye's aberration. This method can be used for larger populations, but it is complicated in practice. A Graphical user interface could aid in calculating the necessary phase plate selection and position by simply inputting the known aberrations of the patient. However, this has not been evaluated in this study and further automation would be needed for practical use.

Pupil rescaling

Table 8.1. Zernike's rescaling for the smaller pupil diameter.

				OD		
				Large pupil		small pupil
	dia [mm]			6.04		5
Zernike term	Order number					
0	0	piston		-0.013		-0.013
1_-1	1	ver Tilt		0.780		0.854
1_1	2	horiz Tilt		0.918		0.759
2_-2	3	obli Asti		0.229		0.166
2_0	4	defocus		2.034		1.134
2_2	5	vert Asti		0.144		0.103
3_-3	6	vert Trefoil		0.064		0.005
3_-1	7	vert Coma		-0.267		-0.119
3_1	8	horiz Coma		0.008		0.024
3_3	9	obli Trefoil		-0.046		-0.042
4_-4	10	obli Quadrafoil		0.055		0.015
4_-2	11	obli sec Asti		-0.010		-0.001
4_0	12	spherical Aberation		0.307		0.092
4_2	13	vert sec Asti		-0.004		0.013
4_4	14	vert Quadrafoil		-0.022		-0.012
5_-5	15			0.016		0.010
5_-3	16			0.033		0.028
5_-1	17			-0.033		-0.035
5_1	18			-0.022		-0.010
5_3	19			0.018		0.007
5_5	20			0.000		-0.002
6_-6	21			-0.034		-0.011
6_-4	22			0.012		0.004
6_-2	23			-0.004		-0.001
6_0	24			0.059		0.019
6_2	25			-0.017		-0.005
6_4	26			0.002		0.001
6_6	27			-0.015		-0.005
7_-7	28			0.008		0.002
7_-5	29			-0.005		-0.001
7_-3	30			-0.017		-0.005
7_-1	31			0.027		0.007
7_1	32			0.002		0.001
7_3	33			0.000		0.000
7_5	34			0.002		0.001
7_7	35			-0.016		-0.004
8_-8	36			0.000		0.000
8_-6	37			0.000		0.000
8_-4	38			0.000		0.000
8_-2	39			0.000		0.000
8_0	40			0.000		0.000
8_2	41			0.000		0.000
8_4	42			0.000		0.000
8_6	43			0.000		0.000
8_8	44			0.000		0.000
			LOA	2.052		1.151
			HOA	0.429		0.169
			Total	2.096		1.163

The Zernike data shown in table 8.1 were rescaled from larger pupil to smaller pupil using the formulas shown below[166]. The 8th-order Zernike terms were not shown in the table since the aberrometers can provide value only up to 7th order.

Formulas for Calculating the Zernike Expansion Coefficients for Smaller Pupil Sizes

n	*m*	New Expansion Coefficient
0	0	$b_{00} = a_{00} - a_{20}\sqrt{3}(1 - r_2^2 r_1^2) + a_{40}\sqrt{5}(1 - 3r_2^2 r_1^2 + 2r_2^4 r_1^4) - a_{60}\sqrt{7}(1 - 6r_2^2 r_1^2 + 10r_2^4 r_1^4 - 5r_2^6 r_1^6) + a_{80}\sqrt{3}(1 - 10r_2^2 r_1^2 + 30r_2^4 r_1^4 - 35r_2^6 r_1^6 + 14r_2^8 r_1^8)$
1	−1, 1	$b_{1m} = r_2 r_1[a_{1m} - a_{3m}\sqrt{8}(1 - r_2^2 r_1^2) + a_{5m}\sqrt{3}(3 - 8r_2^2 r_1^2 + 5r_2^4 r_1^4) - a_{7m}\sqrt{4}(2 - 10r_2^2 r_1^2 + 15r_2^4 r_1^4 - 7r_2^6 r_1^6)]$
2	−2, 0, 2	$b_{2m} = r_2^2 r_1^2[a_{2m} - a_{4m}\sqrt{15}(1 - r_2^2 r_1^2) + a_{6m}\sqrt{21}(2 - 5r_2^2 r_1^2 + 3r_2^4 r_1^4) - a_{8m}\sqrt{3}(10 - 45r_2^2 r_1^2 + 63r_2^4 r_1^4 - 28r_2^6 r_1^6)]$
3	−3, −1, 1, 3	$b_{3m} = r_2^3 r_1^3[a_{3m} - a_{5m}\sqrt{26}(1 - r_2^2 r_1^2) + a_{7m}\sqrt{8}(5 - 12r_2^2 r_1^2 + 7r_2^4 r_1^4)]$
4	−4, −2, 0, 2, 4	$b_{4m} = r_2^4 r_1^4[a_{4m} - a_{6m}\sqrt{35}(1 - r_2^2 r_1^2) + a_{8m}\sqrt{5}(9 - 21r_2^2 r_1^2 + 12r_2^4 r_1^4)]$
5	−5, −3, −1, 1, 3, 5	$b_{5m} = r_2^5 r_1^5[a_{5m} - a_{7m}\sqrt{43}(1 - r_2^2 r_1^2)]$
6	−6, −4, −2, 0, 2, 4, 6	$b_{6m} = r_2^6 r_1^6[a_{6m} - a_{8m}\sqrt{37}(1 - r_2^2 r_1^2)]$
7	−7, −5, −3, −1, 1, 3, 5, 7	$b_{7m} = r_2^7 r_1^7 a_{7m}$
8	−8, −6, −4, −2, 0, 2, 4, 6, 8	$b_{8m} = r_2^8 r_1^8 a_{8m}$

n, radial order; *m*, angular frequency; a_{nm}, old expansions coefficient; b_{nm}, new expansions coefficient; r_1, old pupil size; r_2, new pupil size.

Comparison of total ocular aberrations to corneal aberrations

Table 8.2. Comparison of total ocular aberrations with corneal aberrations.

Volunteer (OD)	iProfiler (total ocular)	ANTERION (corneal)
Pupil Diameter	4.9 mm	4.8 mm
Defocus, Z(2,0)	8.70 µm	1.5 µm
Obliq. Astigmatism, Z(2,-2)	0.02 µm	-0.1 µm
WTRATR Astigmatism, Z(2,2)	-0.69 µm	-0.8 µm
Vertical coma, +Z(3,-1)	0.01 µm	0.0 µm
Horizontal coma, Z(3,1)	0.02 µm	0.0 µm
Oblique trefoil, Z(3,-3)	-0.08 µm	0.0 µm
Horizontal trefoil, Z(3,3)	-0.14 µm	0.0 µm
Spherical aberration, Z(4,0)	-0.04 µm	0.1 µm

The aberrations in the eye's internal optics are a combination of posterior corneal and crystalline lens aberrations. The internal optics can partially correct for aberrations on the anterior surface of the cornea. Therefore, total ocular aberrations are a combination of internal optics and anterior corneal aberrations. In this study, we had the opportunity to use a corneal aberrometer on a few volunteers. The ANTERION from Heidelberg Engineering was used to measure the corneal aberrations. We compared corneal (topography) and ocular (Shack-Hartmann) aberrations to see if corneal aberrometers can be used as input for phase plates (Table 8.2). The RMS error of corneal

aberrations was higher than that of total ocular aberrations and showed opposite signs for some Zernike's. This could lead to additional aberrations in retinal images, so for retinal imaging with phase plates, it is better to use total ocular aberrometers. With the limited data, we cannot arrive at a conclusion. However, further research could be conducted to investigate if improvements in retinal imaging are possible with corneal aberration measurements.

Central reflection removal from the retinal image

The reflection from the high magnification retinal images can be removed by taking a background image and subtracting it from the acquired retinal image, as was done in this case (Figure 8.4). Other methods can also be used for this purpose.

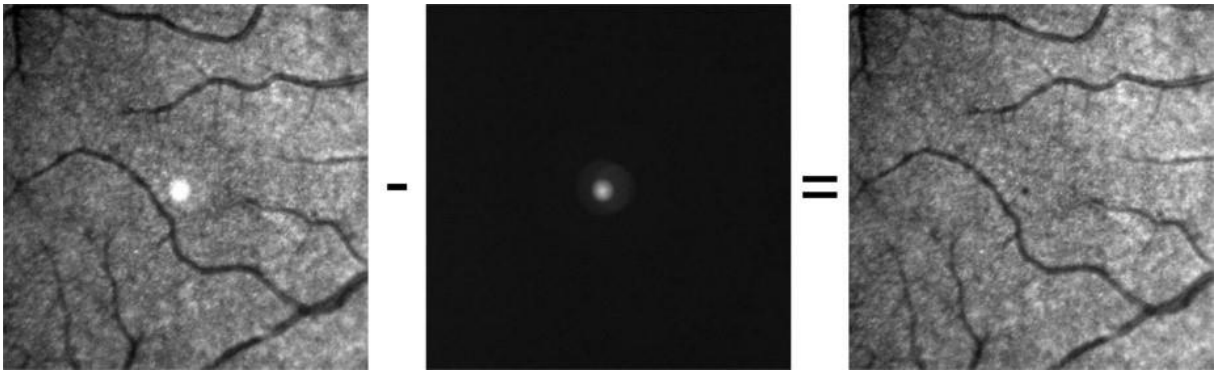

Figure 8.4. Retinal image (left image), background image (middle image), and the retinal image after background subtraction (right image)

9 CURRICULUM VITAE

PERSONAL INFORMATION

Name:	Jayabalan, Gopal Swamy
Date of Birth:	18.09.1988
Place of Birth:	Kumbakonam, India
Marital Status:	Married
Nationality:	Indian

EDUCATION

10/2014 – present	PhD study (Dr. sc. hum) University of Heidelberg, Germany
09/2017 – 08/2019	Academic employee Department of Radiation Oncology, University Medical Center Mannheim
12/2014 – 11/2016	Visiting scholar Loma Linda University, California, USA
09/2010 – 02/2013	M.Sc. Biomedical Engineering Medical Faculty Mannheim, University of Heidelberg, Germany
08/2006 – 05/2010	B.E. Biomedical Engineering Anna University, Chennai, India
06/2004 – 03/2006	High School diploma C K MAT HSS school, Kumbakonam, India

10 OWN PUBLICATIONS

This dissertation was primarily conducted at the Medical Faculty Mannheim of the University of Heidelberg in Germany, with additional research also being carried out at the University Eye Clinic in Bonn, Germany, and the Loma Linda University Eye Institute in the USA. The study was supervised by Prof. Dr. Josef F. Bille.

1. Jayabalan, GS, Kessler, R, Fischer, J, Bille, JF: Compact Adaptive Optics Scanning Laser Ophthalmoscope with Phase Plates. In: *High Resolution Imaging in Microscopy and Ophthalmology.* 2019.
2. Jayabalan, GS, Bille, JF: The Development of Adaptive Optics and Its Application in Ophthalmology. In: *High Resolution Imaging in Microscopy and Ophthalmology.* 2019.
3. Jayabalan, GS, Bille, JF, Mao, XW, Gimbel, HV, Rauser, ME, Wenz, F, Fan, JT: Retinal safety evaluation of two-photon laser scanning in rats. *Biomedical Optics Express,* 10, 2019.
4. Jayabalan, GS, Wu, YK, Bille, JF, Kim, S, Mao, XW, Gimbel, HV, Rauser, ME, Fan, JT: In vivo two-photon imaging of retina in rabbits and rats. *Experimental Eye Research,* 166, 2018.
5. Jayabalan, GS, Bille, JF: Confocal and multiphoton imaging of cornea, 2018.
6. Jayabalan G.S, Kessler R, Reiniger J.L, Ameln J, Holz F.G, Harmening W, Wenz F, Bille J.F. Evaluation of a Compact Non-Contact Compensation Unit for cSLO to Improve Retinal Image Quality. *In preparation for submission*.

11 ACKNOWLEDGEMENT

The successful completion of this dissertation would not have been possible without the invaluable support and guidance of several individuals who have played a crucial role in my research journey. I am deeply grateful to the following individuals for their unwavering encouragement, support, and contributions:

- Prof. Frederik Wenz for providing me with the opportunity to work under his supervision and for his invaluable guidance throughout the research process.
- Prof. Josef Bille for his exceptional mentorship, support and providing me with the opportunity to work in the exciting field of biomedical optics.
- Prof. Frank Holz and Dr. Wolf Harmening from Bonn University, Germany, for their invaluable input, interest and support in the phase plate study and the adaptive optics system.
- Dr. Ralf Kessler from Heidelberg Engineering, Germany, for his valuable advice and insightful discussions about the SPECTRALIS device.
- Dr. Jochen Bähr from Smart Micro-Optical Solutions, Walldorf, Germany, for his expertise in manufacturing the phase plates.
- Dr. Joseph Fan for his interest and support in two-photon technology, guidance during the joint project at Loma Linda University, and for providing me with valuable insights and advice.
- Dr. Howard Gimbel and Dr. Michael Rauser from Loma Linda University, USA, for their kind support during my visit as a visiting research scholar.
- Dr. Xiao Wen Mao, Department of Basic Sciences, Loma Linda University, for her support and valuable discussions on histological analysis.
- Dr. Ubaldo Soto, Department of Microbiology, Loma Linda University, for his expertise in fluorescence microscopy.
- John Hough, Department of Anatomy, Loma Linda University, for his assistance with tissue embedding and sectioning.
- Ms. Anke Keller, a former employee of Medical Faculty Mannheim, for her patience and care in preparing all the paperwork.
- Dr. Sophie Caujolle for proofreading the thesis and for the many tips.
- Augenpraxisklinik Heidelberg, Germany, for the ocular aberrometer measurements.
- Heidelberg Engineering GmbH, especially the late Dr. Gerhard Zinser, for supporting the project and for financial support.

I am also deeply grateful to all the colleagues, staff, and students at the various institutions I have been associated with, for their contributions and support.

I would like to express my deepest gratitude and appreciation to my family and friends, especially my parents, for their support and encouragement throughout my research journey. I would also like to express my deepest gratitude and love to my wife, Dr. Dhanvarshini Thennarasu, for her continuous support, encouragement, and love during the crucial stages of my research and writing process.